Mechanical Design, Development and Testing of Bioinspired Legged Robots for Dynamic Locomotion

Dissertation
der Mathematisch-Naturwissenschaftlichen Fakultät
der Eberhard Karls Universität Tübingen
zur Erlangung des Grades eines
Doktors der Naturwissenschaften
(Dr. rer. nat.)

vorgelegt von
M.Sc. Alborz Aghamaleki Sarvestani
aus Shiraz, Iran

Tübingen
2022

Gedruckt mit Genehmigung der Mathematisch-Naturwissenschaftlichen Fakultät der Eberhard Karls Universität Tübingen.

Tag der mündlichen Qualifikation:	17.11.2022
Dekan:	Prof. Dr. Thilo Stehle
1. Berichterstatter:	Dr. Alexander Badri-Spröwitz
2. Berichterstatter:	Prof. Dr. Martin Giese

I dedicate this thesis to many individuals that burn like a
candle to grow me in their light personally and scientifically,
and my love Farimah

Abstract

Animals perform complex locomotion tasks in the presence of large neurocontrol delays and low central command update rate. It is somewhat surprising that legged robots with high control frequencies and microsecond-range control delays are still unable to compete with legged animals in terms of agility, robustness, performance, and energy efficiency.

In the first part of this thesis, we observe the limitations of previous robotic legs and look into the animal leg to draw inspiration and improve robotic leg designs. We observed that when we flex certain joints in the dead animal leg, all other joints move in a coordinated manner, although there is no active central controller. We further observed that birds' legs structures were loadable or unloadable depending on foot segment orientation. From our observations, we developed a multi-segment leg that behaves like a spring-loaded leg during the stance phase and disengages its elasticity via foot extensor muscle (disengagement tendon) before the swing phase. Unlike previous robotic legs, the robot leg performs locomotion tasks with minimal actuator central control input. Furthermore, this novel robot achieves high speed and efficient locomotion with inexpensive, off-the-shelf hardware based on a Bioinspired leg design.

In the second part of this thesis, we take a deeper look into other disengagement tendon tasks under different gait speeds. The disengagement tendon is an extensor muscle for the foot joints. Besides disengaging parallel elasticity, this tendon charges locomotion energy during stance and releases energy during the transition from stance to swing. Therefore, disengagement helps the leg flex faster, have faster leg protraction at high speed, and operate at lower locomotion energy.

In the third part of this thesis, we use our novel leg design into a quadruped robot as a simplified physical model of a quadruped animal. We evaluate the effect of foot joint extensor muscle (disengagement) in quadrupedal trot gait. Unlike bipeds, leg loading is different between the front and hind leg in a quadruped robot. Quadruped animals such as dogs have less mobility in their distal joints for the hind leg compared to the front leg during trot gait. This difference is rooted in the development of extensor muscle at distal joints. We show this difference through our simplified physical model (robot). In walking scenarios, the hind leg foot segment rotates less under the same hip and knee position command due to trunk pitch down during the stance phase. As a result front leg recuperate energy nine times more than the hind leg via their extensor muscle. Since the hind leg does not benefit from the rotation of the foot segment during walking, it can be a source of why the hind leg in animals requires less mobility during walking.

In the last part of this thesis, we investigate the effect of parallel physical elasticity combined with active control in performance robotic leg under central controller delay. Animals locomote robustly and agile despite significant sensorimotor delays of their nervous system. Robot sensors and actuators can respond within a few milliseconds. However, with unknown touch-down timing, controllers of legged robots can become unstable, while animals are seemingly unaffected. We examine this discrepancy and suggest and implement a hybrid system consisting of a physical parallel elasticity and virtual leg length controller. Our system shows robustness in the presence of high sensorimotor delays and low control frequencies.

Kurzfassung

Tiere führen komplexe Fortbewegungsaufgaben in Anwesenheit großer neuronaler Regelungsverzögerungen und niedriger zentraler Befehlsaktualisierungsraten aus. Es ist daher überraschend, dass mit Beinen ausgestattete Roboter trotz hoher Ansteuerungsfrequenz und Regelungsverzögerungen im Mikrosekundenbereich immer noch nicht mit Tieren mithalten können in Bezug auf Beweglichkeit, Robustheit, Leistung und Energieeffizienz.

Im ersten Teil dieser Arbeit zeigen wir die Grenzen bisheriger Roboterbeine auf und untersuchen Tierbeine um daraus Inspirationen für ein verbessertes Design von Roboterbeinen zu ziehen. Wir stellen fest, dass sich beim Anwinkeln bestimmter Gelenke eines toten Tierbeins alle anderen Gelenke koordiniert bewegen, obwohl keine aktive Zentralansteuerung vorliegt. Außerdem haben wir beobachtet, dass Strukturen von Vogelbeinen, je nach Ausrichtung der Fußsegmente, belastbar oder nicht belastbar sind. Auf der Grundlage unserer Erkenntnisse haben wir ein Bein mit mehreren Segmenten entwickelt, welches sich in der Standphase wie ein gefedertes Bein verhält und seine Elastizität vor der Schwungphase über einen Fußstreckermuskel (Kopplungssehne) aufhebt. Unser Roboterbein führt im Gegensatz zu bisherigen Roboterbeinen Fortbewegungsaufgaben mit minimalem Zentralansteuerung-Aufwand der Aktuatoren aus. Darüber hinaus erreicht dieser neuartige Roboter eine hohe Geschwindigkeit und effiziente Fortbewegung mit kostengünstiger, handelsüblicher Hardware auf der Grundlage eines von der Natur inspirierten Beinentwurfs.

Im zweiten Teil dieser Arbeit befassen wir uns mit weiteren Aufgaben der Kopplungssehne bei unterschiedlichen Ganggeschwindigkeiten. Die Kopplungssehne ist ein Strecker für die Fußgelenke. Zusätzlich zur Kopplung parallel-elastischer Elemente, speichert diese Sehne die Bewegungsenergie während der Standhaltung und gibt die Energie beim Stand-Schwung Übergang wieder frei. Dieser Kopplungsmechanismus trägt dazu bei, dass sich das Bein schneller beugt, bei erhöhter Geschwindigkeit schneller streckt und mit geringerer Energie fortbewegt.

Im dritten Teil dieser Arbeit verwenden wir unseren neuartigen Beinentwurf für einen vierbeinigen Roboter als vereinfachtes physikalisches Modell eines vierbeinigen Tieres. Wir untersuchen die Wirkung des Fußgelenkstreckermuskels (Kopplung) beim vierbeinigen Trab. Im Gegensatz zu Zweibeinern, weist ein vierbeiniger Roboter eine unterschiedliche Beinbelastung zwischen dem Vorder- und dem Hinterbein auf. Bei Vierbeinern wie Hunden ist während des Trabgangs die Beweglichkeit der distalen Gelenke des Hinterbeins geringer als die des Vorderbeins. Dieser Unterschied ist auf die Entwicklung der Streckmuskeln an den distalen Gelenken zurückzuführen. Wir zeigen diesen

Unterschied anhand unseres vereinfachten physikalischen Robotermodells. Bei der Fortbewegung dreht sich das Fußsegment des Hinterbeins bei gleicher Hüft- und Knieposition weniger, da sich der Rumpf in der Standphase nach unten neigt. Infolgedessen gewinnt das vordere Bein über seinen Streckmuskel neunmal mehr Energie zurück als das hintere Bein. Da das Hinterbein beim Gang nicht von der Rotation des Fußsegments profitiert, kann dies eine Ursache dafür sein, warum das Hinterbein bei Tieren während des Fortbewegung weniger Beweglichkeit erfordert.

Im letzten Teil dieser Arbeit untersuchen wir die Auswirkung der physikalisch-parallelen Elastizität in Kombination mit aktiver Ansteuerung von leistungsfähigen Roboterbeinen mit zentraler Regelungsverzögerung. Tiere bewegen sich trotz erheblicher sensomotorischer Verzögerungen ihres Nervensystems robust und wendig. Folglich können Robotersensoren und -aktuatoren innerhalb weniger Millisekunden abgerufen werden. Bei unbekanntem Aufsetzzeitpunkt kann die Ansteuerung von Laufrobotern jedoch instabil werden, während Tiere davon scheinbar unbetroffen sind. Wir untersuchen diese Diskrepanz und entwickeln ein hybrides System, welches aus einem physikalisch-parallelen Elastizität und einem virtuellen Beinlängen-Regler besteht. Die Implementierung unseres Systems zeigt sich robust gegenüber großen sensomotorischen Verzögerungen und niedrigen Ansteuerungsfrequenzen.

Acknowledgments

- I want to thank my supervisor Dr. Alexander Badri-Spröwitz for the opportunity, support and feedback through my doctoral research.
- I would like to thank the IMPRS-IS for their administrative support.
- I want to thank the DLG team for sharing the last four years, Especially my lab buddy Felix for all the chats, discussions, laughs and dances in the lab.
- I want to thank my TAC Prof. Dr. Martin A. Giese and Prof. Dr. rer. nat. Syn Schmitt for their support on the university related matters, feedback and ideas during my doctoral research.
- I want to thank my parents for lighting the way and provide endless support in my path of perusing knowledge.
- at last I want to thank my other half my lovely wife, Farimah, for all emotional support during Ph.D. and life.

Contents

Chapter 1

Introduction

1.1 Motivation

This thesis has two main motivations. First, building a simplified physical model of animals to answer the shortcomings in the current robotic design, such as energy efficiency and robustness to sensorimotor delays to improve the robot and reach desirable biomimicking. Second, providing a tool to answer the biomechanical hypothesis in animals, which are impossible to answer due to the limitation of measuring forces and internal muscle interactions in alive animals. We believe that animals develop complex musculoskeletal legs to respond to complex locomotion tasks via mechanical embodied intelligence in the leg and reduce central nervous system load during rhythmic tasks such as locomotion. We are interested in discovering how this mechanically intelligent elements can help robots achieve higher performance and understand their function in animals.

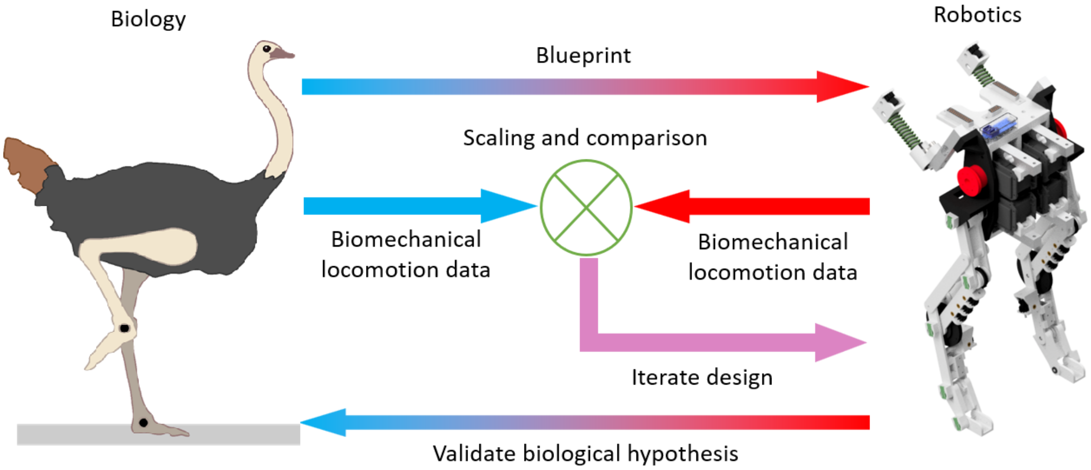

Figure 1.1: Iterative loop of robot design inspiration from biology and explaining animal biomechanics via robot as a physical platform.

1.2 Relevant Publications

All research in this thesis is based on these publications:

1. Aghamaleki Sarvestani*, A., Petereit, R., Badri-Spröwitz, A. RoboManul: Quadrupedal Robot with Passive Disengagement Mechanism for Efficient Locomotion. *In preparation* for **Nature Communication**
2. Aghamaleki Sarvestani*, A., Badri-Spröwitz, A. BirdBot 2: Investigating Parallel Elasticity Disengagement Mechanism Effect on Efficient Legged Locomotion. *In preparation* for **IEEE Transactions on Robotics**
3. Badri-Spröwitz*, A.T., Sarvestani*, A.A., Sitti, M., Daley M. 2021. BirdBot: Avian-inspired leg clutching achieves energy-efficient gait with minimalistic control. **Science Robotics**, 7(64), p.eabg4055.
4. Shafiee Ashtiani*, M., Sarvestani*, A.A. and Badri-Spröwitz, A., 2021. Hybrid parallel compliance allows robots to operate with sensorimotor delays and low control frequencies. **Frontiers in Robotics and AI**, 8, p.170.

1.3 Collaborators

The content of this work is developed in collaboration with Dr. Alexander Badri-Spröwitz. The work published in Chapter 3 was developed alongside Prof. Dr. Metin Sitti from the department of Physical Intelligence at the Max Planck Institute for Intelligent Systems and Prof. Dr. Monica Daley from the Ecology and Evolutionary Biology department, University of California, Irvine. The work published in Chapter 5 was developed with Robin Petereit master student at the Dynamic Locomotion Group at the Max Planck Institute for Intelligent systems. He helped unify measuring and control codes in raspberry pi and communication with the host computer and performed no disengagement tendon experiments. The work in Chapter 6 was developed alongside Milad Shafiee Ashtiani from the Dynamic Locomotion Group at the Max Planck Institute for Intelligent systems. He and the author performed all the experiments and simulations and data analysis together. The author is the first or co-first author in all publications presented in this thesis chapters.

1.4 Contribution and outline

I started my thesis work with a non-actuated initial prototype of the clutchable parallel elastic leg mechanism developed by Prof. Dr. Alexander Badri-Sprowitz. I adapted, modified, and extended the original leg mechanism by actuation, sensing, and adding the disengagement mechanism for robust and efficient disengagement of parallel elasticity and several morphological features. I then extended the improved and robust robot leg in two bipedal robots. This thesis take a closer look at the functionality of the tendon system for the proposed leg and how the disengagement tendon changes the energy efficiency of the bipedal robot. Then I implement the leg in a quadrupedal robot to investigate the leg's performance in the quadrupedal scenario and later answer the question of how extensor muscles in the animal can be benefited in the front and hind legs. In the end, we take a look into the functionality of parallel elasticity in the robotic system to overcome sensorimotor delays in robots and show how animals can benefit from it. The contribution in each chapter are as follow:

Chapter 2: In this chapter, we present previous leg mechanisms and discuss their advantage and disadvantages.

Chapter 3: In this chapter, we present the novel bioinspired leg design concept and implement it in a bipedal robot. Then we show how the simplified tendon network of an animal takes us closer to the real behavior of the animal. Then we measure the energy performance of the leg compared to other legs, especially the non-clutchable parallel elastic leg. Finally, by introducing this leg concept we reduce the energy consumption of the robot by 75 %.

Chapter 4: In this chapter, we take a deeper look into the functionality of the clutch activator tendon and in general clutching mechanisms, under different gait speeds. Clutching of parallel elasticity in the leg was realized by the foot extensor tendon, which we called disengagement tendon. Besides the clutch activator behavior, this tendon also acts as a spring and mechanically recuperates locomotion energy at low speed and reduces COT by 30 %. On the other hand, this tendon helps faster leg protraction during the swing phase for higher speed. It allows us to achieve up to 28 % higher speed with the same gait parameter.

Chapter 5: In this chapter, we expand the bipedal system to quadrupedal scenarios with a free pitching trunk. We want to observe the effect of the disengagement tendon on the front and hind legs and how they contribute to the performance of the quadrupedal robots. This study suggests that adding disengagement reduces the cost of transport by 20 % with the same gait parameter. Furthermore, adding the disengagement tendon reduces trunk pitch by up to 24 %. We also show that the front leg recuperates ten times higher energy than the hind leg. This study shows that animals need DE tendon in the front leg more than the hind leg. The hind leg can lift with the help of trunk pitch motion.

Chapter 6: In this chapter, we show that leg parallel elasticity is not only beneficial for reducing energy consumption during the stance phase but also helps systems to deal with sensorimotor delays. The elastic behavior of muscle allows the leg to respond instantaneously to ground perturbation. We use this paradigm and implement it in hybrid motor control at the knee and show that adding a physical spring alongside with virtual spring help the system to overcome 30 ms sensorimotor delay. High sensorimotor delay for fully actuated robot causes failure in locomotion tasks.

Chapter 2

Related works

2.1 Leg Models

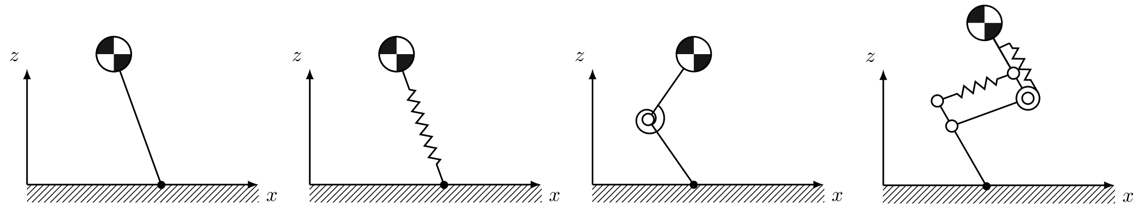

IP SLIP Two-segmented leg Biarticular three-segm. leg

Figure 2.1: The leg models.

Most leg designs are derivative and simplified versions of the animals' legs. Leg design in conventional robotics is a mixture of series and parallel segments, passive spring and damper with actuators to actuate leg mechanism. There are different ways of classifying different leg mechanisms. In this dissertation, we classified leg design based on morphology and actuation type. The first approach for classification is based on the leg model:

Inverted pendulum (IP): in this model, the leg is modeled as a massless single rigid segment that is actuated with the hip motor and all of the robot's mass is concentrated as a point mass at the hip [38] (2.1).

Spring-loaded inverted pendulum (SLIP): this model is similar to the inverted pendulum model, but instead of the rigid segment, it explains the behavior of the center of mass as a form of spring and mass system [31]. The SLIP model can accurately explain bipedal animals' center of mass behavior during walking and running accurately [82].

Two-segmented SLIP: this model is similar to the inverted pendulum model, but instead of a compression linear spring, we have a linear torsional spring knee which acts as a nonlinear spring in leg length direction [95].

Biarticular three-segmented: in this leg design, by adding a pantograph spring segment to the SLIP-like leg [208, 191, 209] we can shorten the leg independent of body motion and introduce more degree of freedom to the leg. [77, 70]. Moreover, [232] suggests the three-segmented leg as a pantograph structure for robots to resemble the main mammalian leg features.

Another approach is to classify the legs base on the type of actuation. The leg can be classified into two main categories: the spring-loaded leg and the fully actuated leg.

Spring loaded leg: these types of legs counter the leg's loading during stance via parallel elastic elements. These legs are usually inefficient during the swing phase due to co-contraction of knee motor with series elasticity(Fig. 2.2).

Fully actuated leg: these types of legs counter leg's loading during stance via their actuators and usually are inefficient during swing since the actuator needs to constantly consume energy to hold leg loading. Fully actuated legs are efficient during the swing phase since the actuator only needs to move segments inertia(Fig. 2.2).

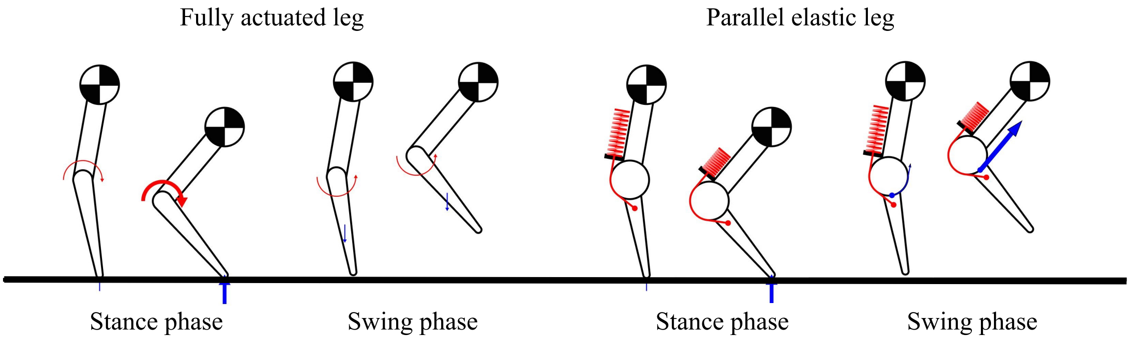

Figure 2.2: Two categories of leg designs based on the actuation.

2.2 Bipedal legged locomotion in robots

Agile legged locomotion in robots is a challenge [58, 107, 118, 237]. Legged animals outperform legged robots on locomotion performance [110]. Animals' complex leg mechanisms with multiple serial and parallel tendon networks allow them to mechanically respond to perturbation [55] and achieve coordination between joints during locomotion. A bipedal robot cannot run quickly, untethered, in natural environments over long distances. Yet, these activities are commonplace for terrestrial animals. Despite the apparent agility of running animals, legged locomotion is complex and requires control of leg-substrate interaction forces in the face of terrain variation and sensorimotor delays [156, 50, 215, 214].[1] However, due to leg simplicity and lack of elastic and damping units in the current robotic systems, tasks such as perturbation rejection joint coordination need to be realized with the joint actuators. As a result, the locomotion capacity of actuators is getting limited. Animals with a low-efficiency chemical to the mechanical conversion of energy [194] are still more efficient than robots with high-performance motors on normal terrain [105, 99]. Innovation is needed to design legged robots that achieve low energy consumption locomotion [162] with robust mechanics and simple control. For operational robustness, the system should be able to deal with external perturbations that occur faster than communication delays and actuator response times [150]. Hence, systems should minimize dependence on communication speed and sensor quality. One of the reasons is that robot morphology is simpler than animal morphology. The legged animals usually have more than four segments in their leg structure, giving them more mobility than their robotic counterparts since most robotic legs include two to four segments [28, 90, 207, 99].[1]

Figure 2.3: Joint ordination in ostrich during locomotion [21].

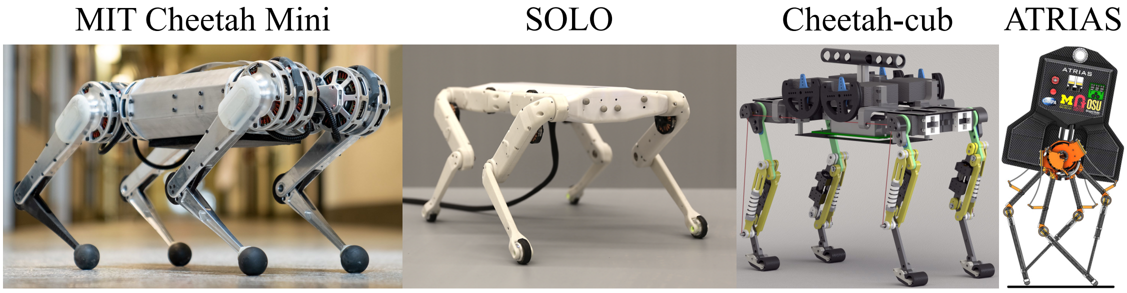

Figure 2.4: State-of-the-art robotic platforms [119, 90, 207, 99].

In biological systems, the prevailing theory suggests that legged animals coordinate joint actuation through antagonistic pairs of muscles controlled by spinal sensorimotor circuits, functioning as 'myotatic units' [154, 167, 204, 114, 17]. The myotatic

---

[1] This paragraph uses original or modified text from [21, 20]

unit concept is mimicked in robotics through the control of joint extension and flexion by separate actuators at each joint. Joint actuation is typically controlled through complex, optimized algorithms that rely on internal robot models and rapid sensory feedback loops [174]. Phase transitions are controlled through contact and load sensors at the feet or within the leg structure [99], or as 'proprioceptive' sensing within the actuator's electrical circuits [199]. With fast sensory feedback and communication, robots can smoothly transition through the gait cycle and react to unforeseen perturbations [106, 30]. However, the robustness and agility of legged robots remain limited. Animals vastly outperform current robots despite considerably slower sensing and information transfer rates [150, 90, 19]. The muscle unit can perform as an active unit that can produce force while acting as a serial and parallel spring, consuming the minimum amount of energy [81]. On the other hand, the robotic platform needs to invest energy to produce a virtual spring [198]. Previous evidence suggests the potential for embodied, intrinsic mechanics and inter-joint mechanical coupling in vertebrates' legs to simplify control [195, 196, 56, 50, 51, 54, 231, 143, 39, 59, 161].[1]

Multi-articular muscle-tendon coupling can facilitate energy transfer between joints and improve efficiency by allowing muscles to work closer to optimal length and velocity [64, 223, 115, 122]. As a result, researchers inspired by animals try to mimic muscle behavior during locomotion by adding physical spring [95, 207, 20] and damper [147]. Nonetheless, the role of multi-articular mechanisms in the control of animal locomotion remains poorly understood. A challenge for demonstrating the role of embodied, intrinsic mechanics in animal locomotion is that both active neural and intrinsic mechanical control occur simultaneously [52, 86, 156, 215]. This makes it nearly impossible to disentangle the contributions of each. Robot experiments provide an opportunity to directly demonstrate the function of intrinsic mechanical coupling, using a physical model of the salient musculoskeletal features to test hypotheses about biological function while also inspiring innovations in robot leg design [111, 107]. Many legged animals show coupled joint kinematics, mediated by multi-articular muscle-tendon units, suggesting that such mechanisms are an essential feature of leg design and control in terrestrial animals [132, 96, 59, 122]. Passive mechanical coupling of joints through multi-articular muscle-tendons without active central nervous system control has been directly observed in frogs, horses, and ratites [132, 59, 195, 196]. Bio-inspired robots and exoskeletons have demonstrated functional benefits of coupled joints by creating analogous structures using spring-loaded four-bar, pantograph, and multi-articular cable mechanisms [18, 233, 117, 207, 200, 220]. Multi-articular mechanisms enable lightweight leg designs, with the heavy actuators mounted proximally. For example, the Spring Flamingo robot has series of elastic actuators in its trunk, with leg joints actuated by long tendons routed over pulleys [168]. Such mechanically elastic legs also mimic the spring-like function observed in animal gaits [168, 207, 7, 9, 144]. The MIT Cheetah robot's leg mounts a stiff belt as an Achilles tendon spanning multiple joints in a tensegrity struc-

---

[1] This text uses original or modified text from [21, 20]

ture, which maximizes the leg's strength to weight ratio [15]. Kurokawa et al. designed a biarticular mechanism that couples ankle and toe movement, enabling the transfer of energy between leg joints for jumping [123]. Mechanically coupled actuators can reduce overall work and force demands and thereby improve energy efficiency in robots, exoskeletons and prosthetic devices [183, 22].[1]

Passive mechanical walking robots demonstrate locomotion principles with either no actuation or minimal actuation under open-loop control. Purely mechanical walkers convert potential energy from a slope into the center of mass and swing leg motion [141]. Related minimally actuated walkers achieve the lowest cost of transport among legged walking machines [43]. Mechanical walkers and their models illustrate principles for economic walking by identifying sources of energy loss and fluctuation, including inelastic collisions between the foot and the ground, redirecting the center of mass velocity at the foot impact, achieving ground clearance during the forward leg swing, carrying the robot's weight during the stance, and joint friction [141, 213, 44, 42, 43]. Though exceptionally energy efficient, passive mechanical walking robots remain limited to flat and smooth terrain and their stability is sensitive to initial conditions and small perturbations. They have low foot-ground clearance, and even small perturbations such as bouncing joint locks can be destabilizing [44].[1]

2.3 Leg parallel elasticity clutch systems

Some studies suggest that bird can lock their joint to stand completely passively or use a minimal amount of energy to stand [40, 196]. These observations result in adding parallel elasticity to the leg mechanism [207, 210]. Parallel elasticity (PE) helps the robots stand without consuming energy and benefits during the stance phase to carry the leg loading passively [11, 207] and reduce the system energy compared to the conventional robots that do not use PE and need to compensate robot mass [199, 103] actively. Although parallel elasticity is useful during the stance, it is energy-consuming in the swing phase [222]. The parallel elasticity is an antagonist with the leg length motor that shortens the leg to provide ground clearance during the leg swing forward. Researchers use mechanical clutches [129, 21] to switch off parallel elasticity in the flight phase to avoid co-contraction. By doing so, we can load the leg with passive elasticity without using motor energy to hold the robot upright. We can also lift the leg without co-contract PE and lose energy [165]. Clutches are mechanically activated or electrically activated [94]. The electrically activated clutches are susceptible to noise and ground detection delay, plus they consume energy to activate. However, the mechanically activated clutch acts instantly depending on ground contact and does not use external energy sources.

Most of the current clutches mechanisms are an artificial robotic solution to the problem, and they have limitations such as bulkiness [186] and high energy consumption of

---

[1] This paragraph uses original or modified text from [21, 20]

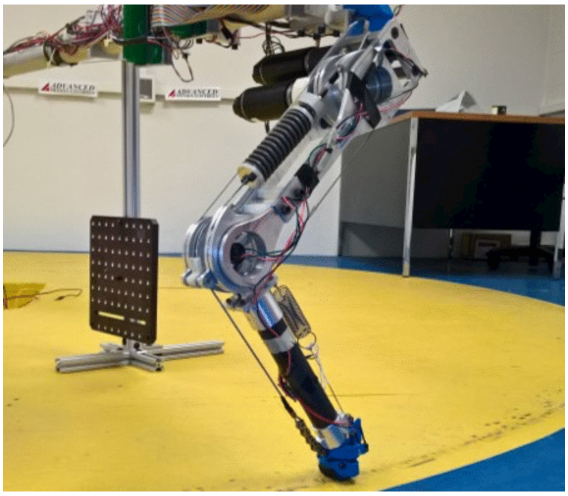

Figure 2.5: Switchable parallel elasticity [129].

power during activation [94]. In addition, some need precise sensing of ground contact. Most importantly, this system deactivated when PE is charged, causes the system to lose energy, reducing system performance and increasing robot power consumption.

2.4 Quadruped legged locomotion

Quadruped animals have a complex leg morphology [116]. Leg morphology for the front and hind leg evolved differently depending on morphology, the animal center of mass, segmentation, and muscle-tendon network [121, 229]. The front and hind legs can have different equivalent elements between the front and hind such as muscle size [229], segment length [240] or joint angular limits [134]. Another difference between the front and hind leg is in the distal mechanism of the leg [230].Dogs have a different range of motion for foot joints between the front and hind leg [72, 134]. The front leg creates up to 50 % more foot flexing rather than the hind leg during symmetric gait such as trot gait.
Studies show that distal leg muscles are recuperating locomotion energy [7, 10] during walking via a catapult mechanism [97, 230, 128]. A study by Wilson et al. [230] shows that foot flexion can help animals slack extensor muscles and protract faster during the swing phase.

Asymmetric leg design for front and hind in addition to hip torque cause pitch motion. Trunk pitching is an unwanted source of energy loss [219]. Most of the optimization algorithms for path planning of quadruped robots try to minimize body pitch which narrows the range of acceptable trajectory, which increase robot speed and efficiency.

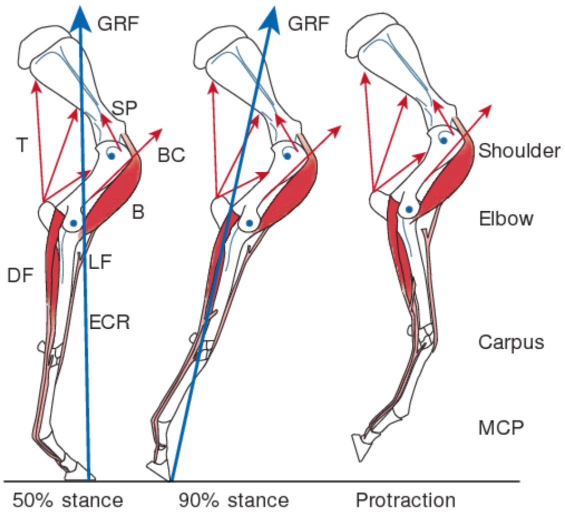

Figure 2.6: Leg catapult and rapid foot flexion in horse leg [230].

2.5 Legged locomotion in the presence of delay

.

Animals use muscle-tendon networks, which they control by spinal circuits, the brainstem, and with sensory feedback to produce joint torque and work for legged locomotion [74, 88, 25, 109, 212, 211]. The response time for muscle action caused by an external stimulus is related to axonal conduction velocity and animal body weight, and the resulting sensorimotor delay can be as slow as 41 ms in a 4 kg, cat-sized animal [76, 149]. House cats run with up to 5 Hz locomotion frequency [24]. At an assumed duty cycle of 0.4 the stance phase lasts 80 ms, and the animal would be sensor-blind for half its stance phase, i.e., during the entire force ramp-up time. We often assume feedback to be critical in challenging conditions like in rough terrain locomotion. However, running birds and other animals traverse hidden perturbations with ease, albeit limited sensorimotor capabilities [53, 66].[1]

Animal locomotion control is simplified by a morphology with tendons and muscles with intrinsic physical stiffness [6, 33]. Physical elasticities mounted serially like tendons can lead to under-actuation and reduced controllability. However, animals show no obvious signs of decline in robustness, responsiveness, or agility. Many muscle tendons are part of more extensive networks with parallel muscle-tendon units, requiring sensorimotor coordination [132, 100].[1]

Inspired by animal morphology and passive and active leg stiffness, legged robot designs often include mechanical springs [153, 14]. Series elastic actuation (SEA) can simplify control, improve robustness and interaction safety, and protect actuators from overloads [172, 180, 171, 102, 37, 105, 4]. Designs with parallel mounted springs and actua-

---

[1] This paragraph uses original or modified text from [20]

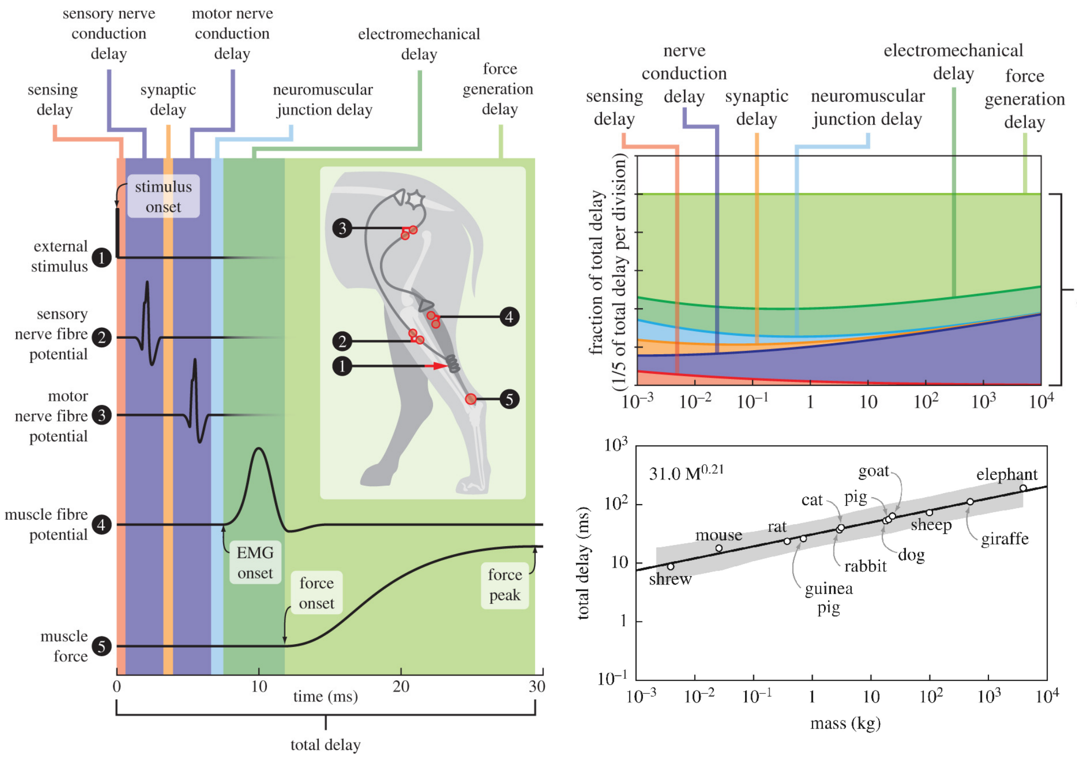

Figure 2.7: Sensorimotor delay source in animals and relation of sensorimotor delay with animals mass [149].

tors (parallel elastic actuation, PEA) can increase leg forces, improve locomotion energy efficiency, and reduce actuator loading [155, 92, 163, 238, 130, 216, 239, 184, 14]. Combined parallel and serial elastic designs have been proposed to reduce peak torques and improve locomotion applicability [89]. Leg stiffness is altered mechanically in several ways; decoupling actuator and spring action during the locomotion cycle can simplify control and improve energy efficiency [228, 208]. Variable elastic mechanisms augment physical stiffness for efficient actuation [41, 139, 36]. Until today, it remains challenging to effectively alter and rapidly manipulate compliance under high loads while keeping the mechanisms compact, robust, and lightweight.[1]

Serial and parallel elastic-legged robots can locomote by feed-forward control without system state knowledge from feedback [108, 152, 210, 191]. However, passive, compliant designs are under-actuated and show limited controllability. Parallel elastic designs can maintain good control authority; when controllability is more needed than spring-based natural dynamics, the actuator overrides the spring's action [226]. Usually, parallel elastic legs are designed with strong springs providing all the essential torques and forces. Consequently, strong, relatively heavy, and fast actuators are required to override

---

[1] This paragraph uses original or modified text from [20]

springs.[1]

Legged robots with proprioceptive actuation feature the highest control authority compared to the passive and partially actuated designs [199, 158, 62]. These legged machines are agile and fast. They jump high and land robustly [158, 91]. From a sensorimotor perspective, proprioceptive actuators require low communication and control delays in the range of a few milliseconds allowing a) high-frequency control above 500 Hz, b) accurate force and joint speed sensing, c) and precise touch-down sensing [30, 91, 127]. Not all conditions are always met, especially in unknown terrain and during harsh touch-downs, when actuator gains are changed, and when sensor noise indirectly causes feedback delays [99, 93].[1]

Robot force sensors are affected by leg impacts loading legs from zero to multiple body weights in a few ten milliseconds and leading to wobbling masses [83, 148]. Impact vibrations transfer to the sensor's mechanics and appear as sensor noise requiring processing [210, 91]. Low-noise leg force sensors are being developed, yet there remains a trade-off between sensitivity and specificity, sensor noise from impacts, and sensor weight and complexity [16, 104, 193, 91]. Noisy force data can be filtered to identify touch-down and leg loading uniquely, but filtering adds to the overall sensorimotor delay; for example, delays of 31 ms are documented to uniquely identify touch down with proprioceptive sensing [91]. Monitoring the deflection of physical joint elasticity provides alternative leg loading information, for example, for virtual model control [169]. Virtual damping assumes precise speed estimation, but numerically differentiating noisy signals requires filtering for sufficiently smooth signals, leading to feedback delay [73, 93]. Robot internal electrical communication delays are minimal. Contrary, teleoperation between operator and legged robot over long-distance can lead to significant feedback delays [225]. Dedicated force feedback control can robustly deal with limited delays; beyond that, control destabilizes [126, 203, 202]. The applicability of high-level locomotion planners is related to control the frequency and, therefore, also to sensorimotor delay; current planners run on time for control frequencies above 100 Hz [166, 138]. Legged robots intrinsically tolerating low control frequencies are therefore good candidates for complex online locomotion planners.[1]

2.6 CPG: Central Pattern Generator

WE implemented CPG, similar to [113, 207], to create hip and knee trajectories. These trajectories create rhythmic patterns based on the gait characteristic parameters such as hip and knee amplitude, hip offset, phase shift of legs, and duty factor. Robot actuator

---

[1] This paragraph uses original or modified text from [20]

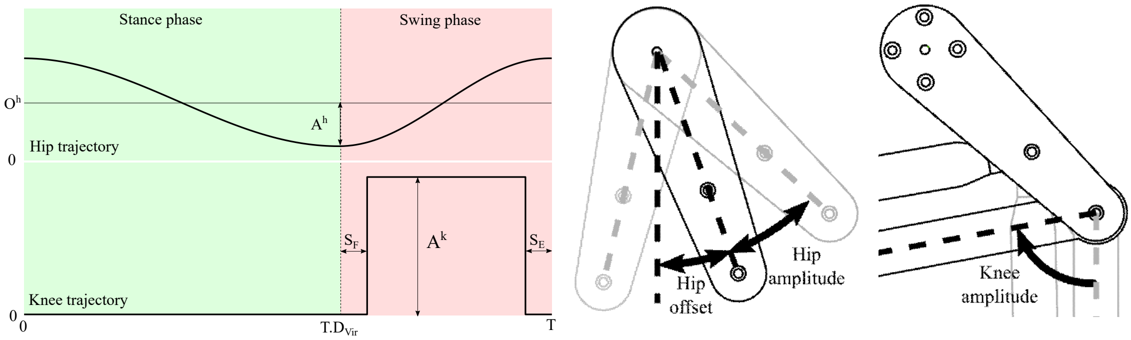

Figure 2.8: CPG desired trajectory.

trajectory will produce as follow:

$$\dot{\phi_i} = 2\pi f + \sum_{i \neq j} c_{ij} sin(\phi_j - \phi_i - \varphi_{ij}) \tag{2.1}$$

$$\dot{a_i^h} = \alpha(A_i^h - a_i^h) \tag{2.2}$$

$$\dot{o_i^h} = \alpha(O_i^h - o_i^h) \tag{2.3}$$

ϕ_i is the i-oscillator's phase; c_{ij} is the coupling matrix; f is the locomotion frequency; φ_{ij} is phase shifts matrix between the hip oscillators; a_i^h and A_i^h are the instantaneous and the commanded hip amplitude, respectively; o_i^h and O_i^h are the instantaneous and the commanded hip offset, respectively; α is a convergence gain. The commanded duty factor D adapts the phase Θ_i^h of the hip joint of leg i, leading to the hip actuator set position h_i:

$$\Theta_i^h = \begin{cases} \frac{\phi_i}{2D} & 0 \leq \phi_i \leq 2\pi D \\ \frac{\phi_i + 2\pi(1-2D)}{2(1-D)} & \end{cases} \tag{2.4}$$

$$h_i = a_i^h cos(\Theta_i^h) + o_i^h \tag{2.5}$$

The active flexion and extension of knee is coupled to the hip phase ϕ_i by the phase shift S_F and S_E, respectively:

$$S_F = 2\pi S_f(1 - D) \tag{2.6}$$

$$S_E = 2\pi S_e(1 - D) \tag{2.7}$$

Where S_f and S_e are the fraction of flexion and extension delay of the swing phase, respectively. The knee i actuator angle is set as k_i, with the commanded knee amplitude

A_i^k:

$$k_i = \begin{cases} 0 & 0 \leq \phi_i \leq 2\pi D + S_F \\ A_i^k & 2\pi D + S_F \leq \phi_i \leq 2\pi - S_E \\ 0 & 2\pi - S_E \leq \phi_i \leq 2\pi \end{cases} \tag{2.8}$$

Chapter 3

BirdBot-1 achieves energy-efficient gait through leg clutching

3.1 Contribution

Major indicates a contribution, without which the paper would probably not have been submitted.
Substantial contribution increase chance of acceptance.
Minor contribution improved the paper, but did not significantly change the form or content.

Author	Author position	Scientific ideas	Data generation	Analysis interpretation	Paper writing
Alexander Badri-Spröwitz	First	Major	Major	Major	Major
Alborz Aghamaleki Sarvestani	First	Major	Major	Major	Major
Metin Sitti	Second	Substantial	Minor	Minor	Minor
Monica Daley	Last	Major	Substantial	Substantial	Major
Title of paper		BirdBot achieves energy-efficient gait with minimal control using avian-inspired leg clutching			
Status in publication process		Published in Science Robotics			

Thesis author contribution based on [1].

Alborz Aghamaleki Sarvestani: conceptualization, methodology, software, validation, formal analysis, data curation, writing - original draft, visualization.

Content of this chapter is largely based on the below paper:

1. Badri-Spröwitz*, A.T., Sarvestani*, A.A., Sitti, M., Daley M. 2021. BirdBot: Avian-inspired leg clutching achieves energy-efficient gait with minimalistic control. **Science Robotics**, 7(64), p.eabg4055.

3.2 Abstract

Designers of legged robots are challenged with creating mechanisms that allow energy-efficient locomotion with robust and minimalistic control. Sources of high energy costs in legged robots include the rapid loading and high forces required to support the robot's mass during stance and the rapid cycling of the leg's state between stance and swing phase. Here, we demonstrate an avian-inspired robot leg design, BirdBot, that challenges the reliance on rapid feedback control for joint coordination and replaces active control with intrinsic, mechanical coupling, reminiscent of a self-engaging and disengaging clutch. A spring-tendon network rapidly switches the leg's slack segments into a loadable state at touchdown, distributes load among joints, enables rapid disengagement at toe-off through elastically stored energy, and coordinates swing leg flexion. A bistable joint mediates the spring-tendon network's disengagement at the end of stance, powered by stance phase leg angle progression. We show reduced knee-flexing torque to a tenth of what is required for a non-clutching, parallel-elastic leg design with the same kinematics, while spring-based compliance extends the leg in stance phase. These mechanisms enable bipedal locomotion with four robot actuators under feed-forward control, with high energy efficiency. The robot offers a physical model demonstration of an avian-inspired, multi-articular elastic coupling mechanism that can achieve self-stable, robust and economic legged locomotion with simple control and no sensory feedback. The proposed design is scalable, allowing the design of large legged robots. BirdBot demonstrates a mechanism for self-engaging and disengaging parallel elastic legs that are contact-triggered by the foots own lever-arm action.

3.3 Introduction

In this study, we test the hypothesis that an avian-inspired linkage mechanism can replace most of the neural circuitry required to control leg trajectory and transitions between stance and swing phases (Fig. 3.1). In an iterative design process, we develop a multi-joint linkage mechanism fully integrated into a bipedal robot's legs that achieves consistent inter-joint coordination and rapid, automatic phase transitions between stance and swing. The leg design is inspired by the muscle-tendon units of large ratite birds, such as the emu and ostrich, but the abstracted structural elements are common among ground-moving birds [227, 177, 189, 195, 27, 196, 190, 2, 39, 101, 50]. A multi-articular spring network guides the leg trajectory and provides a rapid transition between stance and swing using a mechanism reminiscent of a self-engaging and disengaging clutch.

BirdBot-1 showcases a foot contact-based, self-engaging leg spring clutch mechanism. It is minimally actuated with two actuators per leg— hip joint protraction and retraction and knee flexion actuators— controlled in feedforward mode. BirdBot-1 builds upon established mechanisms and principles including cable-and-pulley driven actuation, tendons routed over multiple joints ('multi-articular' tendons), clutching of leg forces, parallel and series leg elasticity during stance, and slack leg joints during swing. BirdBot-1's clutching mechanism engages and disengages robustly with no feedback control. Our design framework demonstrates how intrinsic leg mechanics can enable self-stable and economical gait with consistent phase transitions that are robust to variation in initial conditions.

We demonstrate the leg mechanism on a treadmill, held by a four-bar guide that allows free vertical and fore-aft horizontal translations, but limits sideways translation, pitch, yaw, and roll. We document the design process, mechanical features, and locomotor dynamics of BirdBot, which embodies mechanics and control elements conceived according to anatomical and functional features of avian locomotion [196, 101, 50].

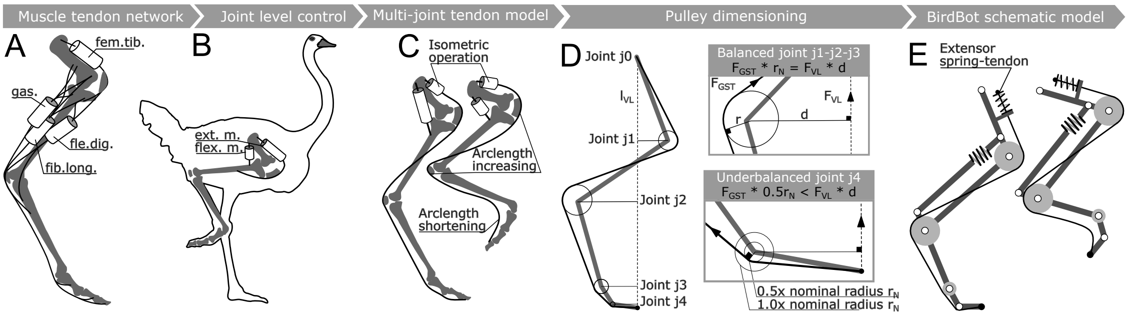

Figure 3.1: **Biologically inspired design of BirdBot's leg.** **(A)** Major muscle-tendon networks that contribute to coordinated stance leg extension and weight support in large ratite birds such as emu and ostrich. Figure inspired from [227]. **(B)** Classic theory suggests that joints are coordinated by flexor-extensor pairs at each joint, acting as myotatic units. However, in birds, distal joints are actuated by a multi-articular musculotendon network. Figure modified from [179]. **(C)** Mechanical analysis demonstrates that a solution exists for a single, multi-articular tendon to support stance loads, and also allow the leg to be fully flexed for swing. The increase in arclength from knee and ankle flexion is balanced by the shortened arclength at the distal distal joints, with tendon slack at the distal joints. The change from stance to swing configuration requires no net change in length, so it is feasible for a muscle acting in series to contract isometrically. **(D)** In BirdBot's leg design, we dimensioned all but the most distal pulleys to balance the external joint moment ($F_{\mathrm{VL}} \cdot d$) against internal joint moment ($F_{\mathrm{GST}} \cdot r_{\mathrm{N}}$). All joints share an equal global tendon force F_{GST}. The distal pulley radius is 0.5 times of the nominal pulley radius r_{N}. The under-balanced distal joint results in rapid digital extension into a flat-foot position under load. **(E)** Together, the multi-articular tendon and pulley design create a self-engaging clutch for the stance leg, which provides bodyweight support and distributes force and power among the joints. The foot's lever-action mechanically releases and slacks the multi-articular tendon in swing phase. BirdBot's leg design enables bipedal locomotion with minimalistic feed-forward control.

3.4 Methods

3.4.1 Robot prototype:

BirdBot is designed to be left-right symmetric. The robot's design parameters are provided in table 3.1, and its design is shown in Fig. 3.8 A and B. Most of the robot's trunk and leg parts are printed from Acrylonitrile Butadiene Styrene on a fused deposition printer (FDS, uPrint SE Plus). The nomenclature for segments and angles can be found in Fig. 3.2. Each leg features two springs. The global spring is mounted serially to the global tendon. We simplify the mounting of force sensors and mount the global spring to the robot's trunk, instead of, for example, the leg segment s01 (Fig. 3.2D). As a consequence, the global spring-tendon also spans over joint j0. A second, pantograph spring (Fig. 3.8A) is mounted within the segment s12p. The pantograph spring exerts forces when both parts of segment s12p are pulled apart, for example, when leg retraction torque is exerted at the hip joint [192]. Hence, the pantograph spring acts as a

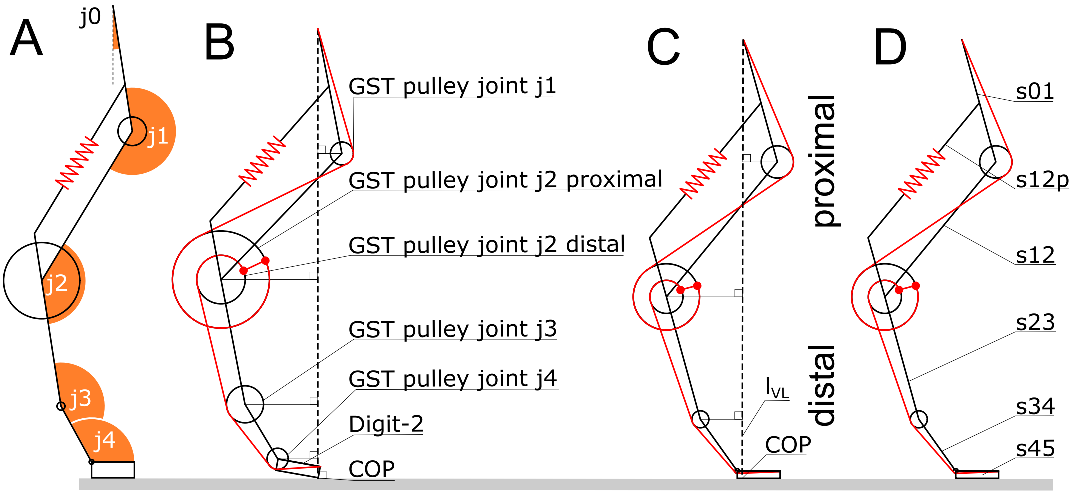

Figure 3.2: A) Definition of joint angles. Positive angles are measured in counter clock wise direction (CCW). B) As a first option, the pulley radii of the global spring tendon (GST) can be calculated assuming a single point contact of the digit-2. C) Alternatively, calculating balanced pulley radii can be based on a configuration with a full-contact digit-2 segment, and a center of pressure (COP) closer to joint J4. The virtual leg l_{VL} spans between hip j0 and the COP. We separated the global spring tendon into a proximal and a distal tendon, where the distal tendon uses higher tendon forces, and lower pulley radii. The proximal and distal global tendon are merged in the double-radius pulley of joint j2. The smaller pulley j4 radius allows a flatter digit-2 segment, where the j4 pulley does not touch ground. The joint's j4 pulley radius guiding the global spring-tendon is always under-dimensioned, see Fig. 3.1D for details. D) Leg segments, segment s23 is the tibiotarsus.

functional rotatory compliant element in response to hip torques. In emus, the gastrocnemius muscle is positioned similar to the spring-12p. Two off-the-shelf robot actuators (Dynamixel, MX-64 AT, RS485) actuate each leg; the hip actuator directly attaches to the leg and swings it forward (protraction) and backward (retraction). The knee actuator shortens the leg's knee joint j1 through the knee flexor tendon. Leg-lengthening is not actively supported, meaning the leg lengthens fully after swing phase, only supported by gravity and the leg's angular momentum. The robot's hip axes and knee flexor pulleys are connected to the trunk by large diameter, thin section ball bearings. Low friction bushings guide the remaining joint axes, which are cut from steel stock material.

Table 3.1: BirdBot's mechanical and mechatronic parameters. Abbreviations: global spring-tendon (GST), disengagement tendon (DET), extensor tendon (ET).

Component	[g]	Actuator model	MX-64 AT, RS485, Dynamixel
Robot mass	1725	Actuator stall torque	6 Nm
Trunk mass including actuators	1400	Actuator gear ratio	200:1
Actuator mass	165	Hard stop joint extension joint j3	160°
Force sensor mass	55	Global spring, model	SWY16.5-45, Misumi
Segment-01 mass	18	Global spring, stiffness	3.12 N/mm
Segment-12 mass	45	Slack length global spring	45 mm
Segment-23 mass	33	Spring segment s12p, model	P437, Misumi
Segment-34 mass	8	Stiffness spring segment s12p	5.9 N/mm
Segment-45 mass	6	Slack length spring segment s12p	35.5 mm
Leg mass	164	Tendon cable material & diameter	Liros D-Pro, 1 mm
	[mm]	Breaking force tendon cable	1950 N
Length segment-01	80	Force sensor GST, τ_{hip}, $\tau_{\text{knee(flex)}}$	TAL220, 100 N
Length segment-12	110		linearity ±0.05 %
Length segment-23	80	Joint position encoder	AS 5045, magnetic
Length segment-34	40	Ball bearing trunk actuator mount	6705 2RS, Misumi
Length segment-45	27	Joint bushing	JZF3, Misumi
Radius pulley GST joint j0	1.5		
Radius pulley GST joint j1	9		
Radius pulley GST joint j2 proximal	24		
Radius pulley GST joint j2 distal	12		
Radius pulley GST joint j3	2.5		
Radius pulley GST joint j4	1.5		
Radius pulley DET joint j3	5		
Radius pulley DET joint j4	1.5		
Hip height standing	290		
Radius pulley ET joint j2	17		
Radius pulley ET joint j3	5		
Radius pulley ET joint j4	1.5		
Radius pulley knee joint j1 flexor	8.5		
Radius pulley knee actuator	14		

3.4.2 Spring-tendon network:

A network of four tendons and spring-tendons is mounted to each leg, shown in Fig. 3.8B. The global spring-tendon splits into a proximal and a distal part (red). The disengagement flexor tendon supports j3 and leg disengagement (orange). The knee flexor tendon lifts the slack leg (blue). A last pair of tendons rotates both digits into digital-extension (digit-1 extensor, digit-2 extensor, light and olive green). Each tendon is tensioned through a tendon adjustment mechanism (TAM, Fig. 3.3). TAMs are custom-made, from a plastic worm gear driving a drum winding up the tendon, and work like a violin's string tensioning mechanism. The multi-articular global spring-tendon extends joints j1, j2, j3, and j4 against loads in leg length direction during stance phase (Fig. 3.8B). The global spring-tendon also spans over joint j0 to simplify mounting the spring's force sensor. The biarticular disengagement flexor tendon runs parallel to the global spring-tendon but spans only over the leg's two distal joints j3 and j4. When tensioned by joint j4 flexion through stance phase, the disengagement flexor tendon pushes joint j3 from one stable joint position, over its unstable, collinear position of segment s23 and digit-1 (Fig. 3.12C and D). The disengagement flexor tendon action 'collapses' joint j3 and with it the in-parallel mounted global spring-tendon. The disengagement flexor tendon does not insert into a spring; instead, we directly use the tendon's intrinsic elasticity, like a very stiff

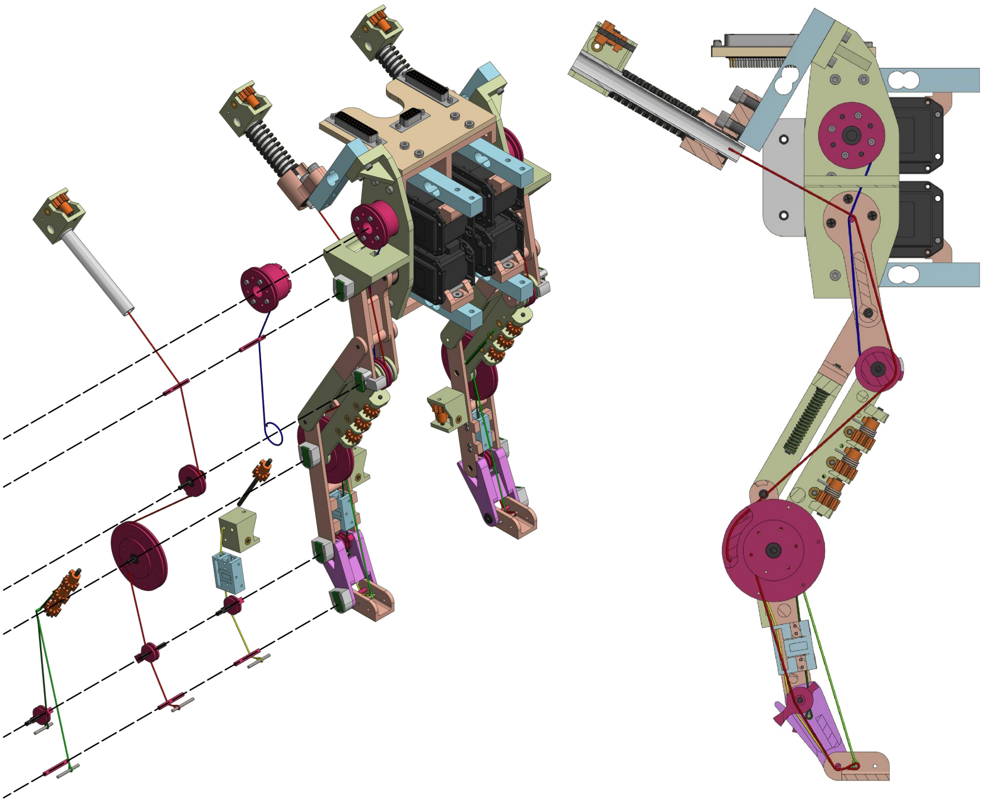

Figure 3.3: Tendon routing, adjustment mechanisms, and tendon insertions are shown in the explosion view on the left. 1) knee flexor tendon, 2) disengagement flexor tendon, 3) global spring tendon, proximal part, 4) global spring tendon, distal part, 5) extensor tendon digit-1, and 6) extensor tendon digit-2.

spring. We estimated the tendon's spring-like stiffness ($k = 60\,\text{N/mm}$) in its built-in configuration. The knee flexor tendon flexes the knee joint j1. Its proximal end inserts into the knee actuator pulley. The tendon is then routed over the hip j0 axis, into the knee flexing pulley, and finally into its TAM mounted to the s23 segment (Tibiotarsus, Fig. 3.8B, Fig. 3.2D). A pair of dorsiflexion tendons span over joints j2, j3, and j4. When joint j2 extends just before touchdown (Fig. 3.8B), the dorsiflexion tendons rotate digit-1 and digit-2 into a digital-extended position. The dorsiflexion tendon TAMs are integrated into segment s23. The disengagement flexor tendon and the global spring-tendon are mounted antagonistically to the dorsiflexion tendons, and hence we adjusted each tendons' slack carefully.

All tendons are made from 1 mm thick cables (Dyneema). Tendon ends are manually cut to length. The tendon's tail is inserted into the standing part of the tendon to create an eye. Both twines are lock-stitched together by hand.

The left and right leg global spring-tendons were initially set to zero slack length, with the robot's legs in the air and all the leg segments extended. The robot was placed on the ground, and the global spring-tendons were adjusted for an equal joint j1 angle between the left and the right leg. We adjusted the disengagement flexor tendons on the standing robot with femur segments set vertically by the hip actuator (joint j0, 0°. The tension of the disengagement flexor tendons was adjusted to a force of $F = 100\,\text{N}$, just before the joint j3 snap-through. The knee flexor tendon's slack was removed with the femur segment positioned vertically. Both dorsiflexion tendons were adjusted to create joint j4 digital-extension when joint j2 is extended. Knee and hip torque sensors and the global spring-tendon force sensor were calibrated with an external load cell. The robot's legs were placed horizontally to avoid the effect of gravity. The tendon buckle sensor was calibrated with a defined external load pulling on the disengagement flexor tendon.

3.4.3 Actuators and low-level actuator control:

Four off-the-shelf robot actuators drive the robot's legs (Dynamixel, MX-64 AT, Fig. 3.8A and B). One hip actuator per leg is mounted between the trunk and the femur segment s01; it directly moves the femur. The knee actuator flexes the knee joint j1 by pulling on the knee flexor tendon (Fig. 3.8B). We controlled the actuators in position mode, from a control PC with an update frequency of $f = 125\,\text{Hz}$. All four actuators are connected through a single RS485 communication bus. A U2D2 universal serial bus (USB) communication converter connects the communication bus via USB to the control PC. We modified the Matlab Dynamixel software development kit for this use (SDK, v.3.5.4). All control commands were sent as feed-forward signals. We generated locomotion control patterns with a Central Pattern Generator, similar to [113, 207]. We applied CPG control to generate smooth hip joint angle trajectories, which is important when initializing the gait patterns. Custom-designed CPGs require only few driving parameters, such as amplitude, offset, phase shift, and duty factor. The CPG was implemented on a PC in Matlab; the trajectories were sent to the actuators as feed-forward signals. Stride frequencies of $f = 1.0$ Hz and 1.5 Hz were set, resulting in robot speeds of 0.50 m/s and 0.75 m/s, respectively. The left and the right leg received phase-shifted but otherwise identical trajectories: We observe that the commanded duty factor ($D = 0.60$) differs from the observed duty factor ($D = 0.49$, $f = 1.5$ Hz stride frequency). A typical CPG output for one stride of a single leg is provided in Section 2.6. CPG parameters are provided in Table 3.2.

Table 3.2: The CPG parameters for gait 1 ($f = 1$ Hz) and gait 2 ($f = 1.5$ Hz).

Parameter	Gait 1	Gait 2	Parameter	Gait 1	Gait 2
f (Hz)	1	1.5	D_{vir}	0.6	0.6
A^h (°)	32	35	α	1	1
O^h (°)	22	30	S_f	0	0
A^k (°)	120	120	S_e	0.22	0.22

3.4.4 Instrumentation:

Each leg is instrumented with four sensors measuring force or torque. A custom-designed sensor measures the hip actuator's reaction torque. The reaction force F is measured by an off-the-shelf beam-type load cell (TAL220, 100 N), at a lever arm length of $l = 47$ mm, and we calculate the hip reaction torque $\tau = F \cdot l$ (Fig. 3.14B). A second, identically constructed sensor measures the reaction torque of the knee actuator, and we calculate the torque acting at the knee flexor tendon (Fig. 3.15A). The global spring-tendon's force is measured with an identical force sensor (Fig. 3.4). We measure the disengagement flexor tendon's force with a custom-designed tendon buckle sensor. All joint positions are measured with absolute magnetic encoders (AS 5045, AMS), recorded at $f = 333$ Hz, and time-stamped with a microcontroller board (Arduino Mega), individually for the right and left leg. Both microcontrollers were connected to a personal computer with USB. Force data was sampled by a data acquisition system (cDAQ-9189, National Instruments) at $f = 1$ kHz, with strain bridge input modules (NI-9237). A custom written LabVIEW program recorded the NI MAX module data, including the trigger line status. The current supplied to the actuators was captured with an external current sensor (LA 25, 25 A, LEM), mounted to a custom amplifier. The amplifier's voltage output signal was recorded with an analog-to-digital converter (NI-9205). The current sensor was calibrated with a 1 Ohm precision resistor. Current data was time-stamped and trigger synchronized. An external power supply provided the robot's actuator voltage (12.0 V) through a power cable.

Gait experiments were recorded with a high-speed camera (MiroLab 110, Phantom) at a frame rate of $f = 400$ fps, and still frames were extracted from video material for Fig. 3.10. High-speed videos were synchronized to the data based on an optical and electrical trigger event. Touchdown and toe-off events were determined manually from high-speed videos. Further videos and photos were recorded with a camcorder (FDR-AX 100, Sony) and a digital camera (D5500, Nikon).

The robot as shown on Fig. 3.4 walked on a recreational treadmill (model Christopeit TM500S), modified for speed control by setting a directly connected power supply voltage. The treadmill's speed was measured by a custom mounted encoder (AS 5045, AMS) and recorded by a microcontroller (Arduino Mega). A linear guide (Misumi SVR) was de-greased and loosened for minimal sliding friction. The slider is mounted to an overhead rail, $h = 0.53$ m above the belt. Rail and robot are connected by a parallel four-bar guide, with segment lengths $l = 0.51$ m and $l = 0.04$ m. The rail and four-bar restrict the robot to translations in the sagittal plane (fore-aft and up-down) and prohibit trunk pitching. The linear guide's position is measured by a pair of counter-mounted draw-wire sensors (Waycon LX-PA-20), read out by an analog-digital converter (NI 9205).

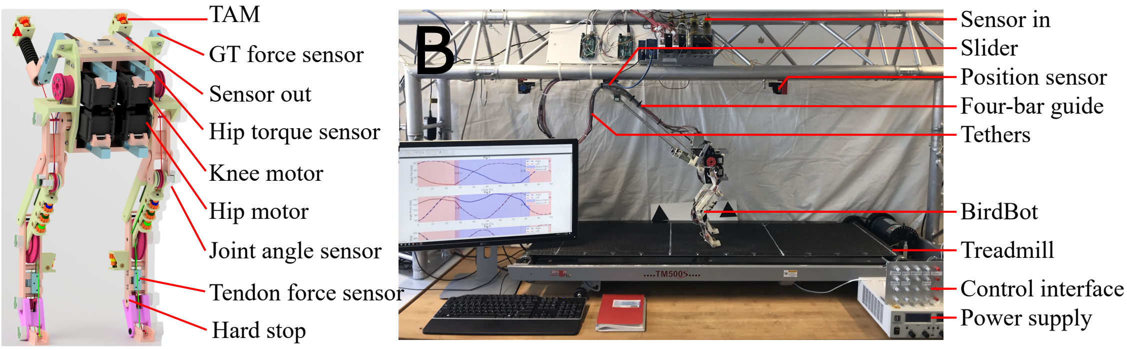

Figure 3.4: **A)** BirdBot components. **B)** Locomotion setup.

3.4.5 Calculation of Froude number, cost of transport:

We calculate the Froude number as

$$\mathrm{Fr} = v^2/gl \tag{3.1}$$

according to [5], were v is the robot's speed v in [m/s] on the treadmill, averaged over in sum 70 strides from 5 experiments with each 14 strides. The robot's standing hip height is $l = 0.29$ m, and the gravitational acceleration is $g = 9.81$ m/s^2. The mechanical power P [W] was calculated as the product of velocity v [m/s] and force F [N], or angular velocity $\dot{\alpha}$ [rad/s] and torque τ [Nm]. The robot's electrical (metabolic) cost of transport was calculated according to [217]. We measured the instantaneous current I [A] with current clamps for each actuator individually, calibrated the data, and kept the positive values only, from 70 strides. We then summed up the data of the four actuators, and derived the mean and standard deviation (table 3.5). We then calculated the net electrical

COT:

$$\mathrm{COT_{en}} = ((U \cdot I) - P_{\mathrm{SB}})/(m \cdot g \cdot v) \tag{3.2}$$

where we removed the standby actuator power $P_{\mathrm{SB}} = 4.8\,\mathrm{W}$. The actuator's manual specifies 100 mA standby current, which we confirmed by own measurement. The robot's weight mounted to the rail is $m = 1.73\,\mathrm{kg}$, the average robot speeds were $v = 0.50\,\mathrm{m/s}$ at $f = 1\,\mathrm{Hz}$ stride frequency, and $v = 0.75\,\mathrm{m/s}$ for $f = 1.5\,\mathrm{Hz}$ stride frequency. Cost of transport is normalized ([J/N/m]), to evaluate the energy efficiency during locomotion. However, animal locomotion data indicates that the cost of transport decreases with increasing animal mass m, also shown with the 'natural runner' down-sloping trend line in [217]. To compare BirdBot's cost of transport to legged hoppers, bipedal robots, and quadrupedal robots of different body mass, we first digitized Tucker's trend line (Figure 2 of [217]), which leads to the following cost of transport reference line (Fig. 3.16C, 100 % line);

$$\log[10](\mathrm{COT_{nr}}) = -0.3138 \cdot \log[10](m) + 0.2346 \tag{3.3}$$

We added indicator lines (25 %, 50 %, 100 %, 200 %, and 400 %) for a 'relative COT' (in [%]), calculated as the ratio between the natural runner's cost of transport and the robot's electrical net or total cost of transport to Fig. 3.16C, to indicate COT grouping of robots of different type and size:

$$\mathrm{COT_{re}} = \frac{\mathrm{COT_{nr}}}{\mathrm{COT_{en}}} \cdot 100\,\%. \tag{3.4}$$

The above cost of transport comparison is based on allometric relationships; we are comparing BirdBot to an average animal of the same body weight. Specific cost of transport values of similar-sized birds at similar locomotion speeds are 0.81 J/N/m (guinea fowl, 1.5 kg, between 0.5 and 3 m/s) [136], 1.30 J/N/m (leghorns, 2.0 kg, 0.7 m/s) [185], and 1.4 and 2.0 J/N/m (guinea fowl, 1.3 kg, 0.5 and 1.0 m/s) [142]. We show in table 3.6 the cost of transport (COT) of selected bipedal, quadrupedal, and single-legged hopping robots, latter indicated by an 'H'. The table content is the basis of Fig. 3.16C, figure data points are marked in bold. The cost of transport of natural runners of equal bodyweight is shown as the 100 % reference cost of transport line according to [217]. $\mathrm{COT_{et}}$ is the total electrical cost of transport. It includes the motor driver and communication power consumption. We calculate the net electrical cost of transport $\mathrm{COT_{en}}$ by subtracting the standby power from the total power. The mechanical cost of transport $\mathrm{COT_{me}}$ is calculated from the actuator's mechanical work [131]. BirdBot's net cost of transport is shown for a stride frequency of $f = 1.5\,\mathrm{Hz}$. We normalize the total, net, and the mechanical cost of transport with the natural runner's cost of transport: $\overline{\mathrm{COT_{et}}} = \mathrm{COT_{et}}/\mathrm{COT_{nr}}$, shown in [%]. Several brushless-motorized systems can recuperate negative power either into batteries, or connected motors. The ability for recuperation ('Recuperation') typically improves the system's cost of transport [200]. The guide-type is indicated as 'no' (mount) for freely running robots, 'planar' for robots that are limited to move within a plane, and 'planar+pitch' for robots that are limited to moving in a plane and are also pitch (rotation) locked. BirdBot is stabilized to run in a plane, and is pitch-locked. 'L' is leg length, 'm' is mass, 'v' is speed, and 'Fr' is Froude number. Number of legs are shown as 1, 2, or 4.

BirdBot has been instrumented for research purposes, increasing its weight beyond that necessary for locomotor function. Its force sensors, joint positions sensors, mounting reinforcements, and the cabling add up to about 0.5 kg. BirdBot consumes a total of 21.6 W (12 V, 1.8 A, at 0.75 m/s). Currently available Lithium polymer batteries weigh 0.22 kg (2000 mAh, 14.8 V, 4S configuration), DC to DC converter boards are available that weigh less than 50 g, allowing an onboard power supply with a mass of less than 0.3 kg. With the on-board power supply, but without its research instrumentation, BirdBot could run over 1 h at 0.75 m/s; 2000 mAh = 2 A current for 1 h, compared to the 1.8 A the actuators pull. Based on these estimates, we do not expect BirdBots cost of transport to change substantially with onboard power supply, as long as the robot is stripped of its research instrumentation.

The standard measurement for cost of transport in animals is the net cost of transport; cost of locomotion minus resting metabolic cost. The reasoning for this is to be able to systematically consider the costs involved with movement separate from other costs, which are likely to vary substantially depending on specific details about the power sources and onboard computational complexity of the robot. Hence, the robot's net cost of transport value can act as a consistent comparison to animals [200, 120, 129, 210]. A robot's standby power required depends its computing source, electronics, sensors, communication, and actuation type. This 'overhead' is not scaling linearly with robot size. For example, BirdBot's total power consumption at 1.5 Hz is 21.6(4) W, including the consumed standby electrical power from the electronics of four Dynamixel actuators (4.8 W, 22 % overhead). Oncilla robot's (4.5 kg) best $\mathrm{COT_{et}}$ gait consumes 109 W electrical power in total, including 19.6 W standby power (18 % overhead, [210]). MIT Cheetah 1 robot draws 21 W for its electronics and 377 W in total (5.6 % overhead, Table I, page 33, [200]). Although the total overhead varies, the relative overhead typically reduces for larger robots.

3.4.6 Cadaver studies

We measured the joint angle coupling in an emu cadaver by manually moving the Tibiotarsus in an unloaded leg while observing the coupled flexion and extension of the ankle and tarsometatarso-phalangeal joints (Fig. 3.6B). The bird's leg was held approximately horizontally. Reflective markers were attached to the skin of the leg's joints, and marker positions were captured in 3D with a motion capture system with multiple cameras, at 250 Hz (Qualisys). Qualisys Track Manager software was used to import and label markers, and identify consecutive flexion and extension cycles without marker occlusions.

Labeled marker positions were exported into a text file, and imported and processed in Matlab. Joint angles were calculated assuming a two-dimensional, horizontally oriented leg. The data was not filtered.

Emu cadavers were obtained from a prior study of Emu ontogenetic biomechanics [125] at the Royal Veterinary College (RVC) Structure and Motion Laboratory. The animals were housed and reared at the RVC and all procedures and humane euthanasia were conducted with ethical approval under at UK Home Office license: PPL707122. Cadavers were stored in a −20 °C freezer after euthanasia and thawed slowly to room temperature before experiments.

3.4.7 Data processing

Data was processed in Matlab (Mathworks). Joint speeds were derived from joint encoder data, applying the ‘sgolay_t’ Matlab function to joint position data (Author: Tiago Ramos, settings: N=4, F=51, DIM=1). Current data were filtered with a zero-phase digital filter (30 Hz low pass, 2nd order, 0.2 PassbandRipple).

Static knee joint torque in swing and stance : For static conditions, we calculated the torque required to extend the knee joint when standing on a single leg and holding the robot’s weight, and while lifting the lower leg. We simulated three different robot spring and actuator configurations (Fig. 3.5A to C). All three modeled robot configurations have an equal mass of $m = 1.73\,\text{kg}$, identical to BirdBot. The robots’ center of mass and their hip joints align vertically, and no hip torque is induced during standing. In the lifted leg scenario, the lower leg mass and the horizontal distance between its segments’ center of gravity and the knee joint are assumed to be identical for all three designs ($m_{\text{lower}} = 0.092\,\text{kg}$, $l_{\text{distance}} = 0.056\,\text{m}$).

Table 3.3: We modeled three static scenarios and show the leg joint torque required to shorten or lengthen the leg, either with an actuator or with a leg spring. The robots’ geometries were chosen for a comparable analysis. The robot leg designs behind the three scenarios (direct actuation, non-clutching parallel spring, BirdBot) are schematically shown in Fig. 3.5.

Joint action	Mechanism	Direct actuation	Non-clutched parallel spring	BirdBot
flexion	actuator	0.09 Nm	3.71 Nm	0.09 Nm
extension	actuator	0.42 Nm	—	—
extension	leg spring	n.a.	0.42 Nm	0.42 Nm

Single leg disengagement experiment : The joint positions at leg disengagement and leg-unloading were determined based on visual cues, tracked manually from high-speed

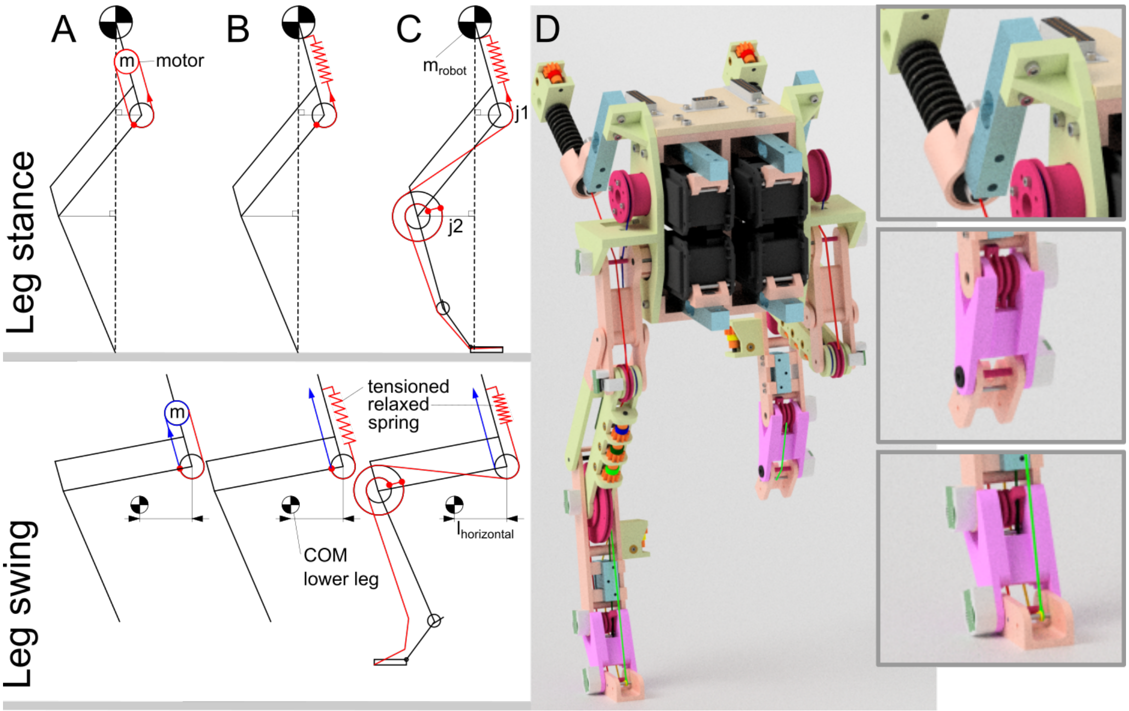

Figure 3.5: Schematic presentation of three leg configurations for the calculation estimating the *static load* applied at leg length actuator and the spring, to flex or extend the robot's leg joints. Results are shown in table 3.3. The three actuator and spring configurations are: A) Direct actuation, without a spring; B) Non-clutching, parallel spring configuration, similar to the leg design of [207], and C) BirdBot's leg design. D) Shows a rendered BirdBot with the right leg in stance, and the left leg in swing.

video footage. Angles were extracted in ImageJ software. The virtual leg angle was defined by the joint j0 and j4, and a third point at the trunk. For the leg with the disengagement flexor tendon mounted, we determined the disengagement leg angle when $\alpha_{\mathrm{j3}} > 180°$.

Disengagement tendon work calculation : We estimate a spring-like behaviour of the disengagement flexor tendon. We calculated the tendon's stiffness (k_{DET}) by measuring a known tendon force F_{DET} and the tendon's change in length $disengagementlta(l_{\mathrm{DET}})$, in its built-in state. For the plot Fig. 3.14A, we calculate the disengagement flexor tendon work W_{DET} from the recorded tendon force, and the change of tendon length l_{DET} wrapping around the pulleys of joint j3 and joint j4:

$$W_{\mathrm{DET}} = \frac{1}{2} F_{\mathrm{DET}} \cdot disengagementltal_{\mathrm{DET}} \tag{3.5}$$

Global spring-tendon (GST) work calculation : The work W_{GST} of the global spring-tendon is calculated from the tendon's force, which is identical to the spring force, and the spring stiffness:

$$W_{\mathrm{GST}} = \frac{1}{2}\frac{F_{\mathrm{GST}}^2}{k} \tag{3.6}$$

Statistics : Unless otherwise indicated, uncertainty bounds are provided as mean and standard deviation (mean ± SD). Data from continuous data plots is presented as mean and 95 % confidence interval (mean ± CI), averaged over 70 strides. Single leg disengagement data is presented as mean of 20 repetitions per leg configuration. Mean disengagement angles of $69 \pm 1.2°$ and $59 \pm 0.3°$ (mean ± SD) were recorded for the leg with and without the disengagement flexor tendon, respectively (Fig. 3.12). The 10° difference was statistically significant according to a Mann-Whitney U test, $\mathrm{n1} = \mathrm{n2} = 20$, $p = 0.01$. Correlation coefficients for j2 and j3 joint trajectories (Fig. 3.6) were calculated as $r = \mathrm{correff(j2, j3)}$ (Matlab), with 2001 data points from five joint extensions and flexions. The flexion correlation coefficient is $r_{\mathrm{flex}} = 0.99$, the extension correlation coefficient is $r_{\mathrm{ext}} = 0.96$ (Fig. 3.6C). Correlation coefficients $r > 0.8$ are considered an indicator for strong coupling.

3.5 Results

We use a robot leg design as a physical model to test the hypothesis that a rigorously designed multi-articular spring-tendon network can fully support locomotor loads during stance, coordinate the transfer of mechanical load among the joints, and enable automatic stance/swing phase transitions (Fig. 3.1). The distal segment's (foot) lever action and a global spring-tendon automatically switch the leg's joints into a loadable state during touchdown and mechanically distributes torques among joints during stance (Fig. 3.1D). A dedicated tendon disengagement mechanism supports stance-to-swing transition during toe-off by actuating a snap-through (bi-stable) joint using elastically stored energy. The global spring-tendon and the compliant four-bar linkage couple leg joints into coordinated leg flexion during swing and rapidly create foot ground clearance for swift leg protraction. BirdBot is designed as a proof-of-concept planarized bipedal robot, with high-geared (200:1 ratio), brushed-motor actuators that enable moderate frequencies and speeds (Froude number $\mathrm{Fr} = v^2/(gl) = (0.75\,\mathrm{m/s})^2/(9.81\,\mathrm{m/s}^2 \cdot 0.29\,\mathrm{m}) = 0.20$), but not fast running. The bio-inspired features, design process, and resulting gait mechanics are detailed below.

We measured the joint angular coupling in an emu cadaver leg by manually moving the tibiotarsus in an unloaded leg while observing the coupled flexion and extension of the ankle and tarsometatarso-phalangeal joints (Fig. 3.6A to C). Upon manually flexing and extending the ankle joint j2, we measured coupled motions at the tarsometatarso-phalangeal (TMP) joint j3. Strong coupled motion between the ankle and TMP is evidence based on an observed correlation coefficient of 0.96 for extension and 0.99 for flexion (Fig. 3.6C). In our measurements, the mechanical coupling arose only from passive tissue elasticity because the central nervous system was inactive. Sources of passive tissue connectivity in the avian limb include the proximal origins of major ankle extensors and digital flexors from the patellar tendofascial sheet at the knee [206], and ligament connectivity between distal joints including the intertarsal joint (Fig. 3.1A) [196, 195]. In particular, Schaller observed an ankle-locking mechanism based on ligament interactions in ostrich legs, although it remains unclear whether these passive structures alone can fully support body weight in these animals [196].

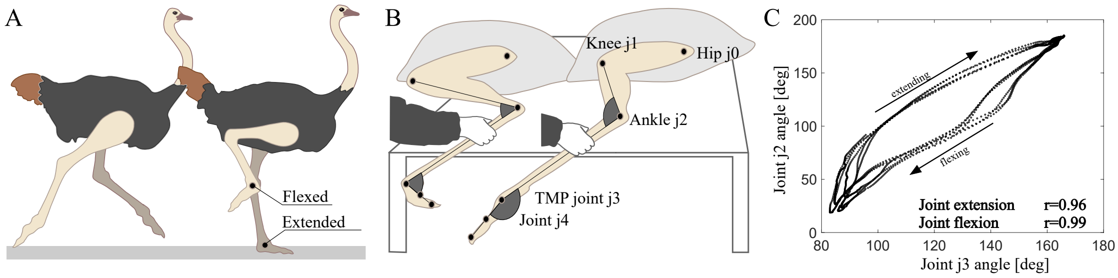

Figure 3.6: **Mechanical coupling of distal joints in the ratite leg.** **(A)** In the running ratite birds, the digits are digital-flexed in swing and digital-extended upon knee extension in preparation for stance. **(B)** The distal avian hindlimb exhibits passive mechanical joint coupling, which can be determined by manually flexing and extending the ankle joint, j2, and measuring coupled motions at the tarsometatarso-phalangeal (TMP) joint, j3. **(C)** Strong coupling exists between the two joints in both flexion and extension, demonstrated by correlation coefficients of $r = 0.99$ and $r = 0.96$, respectively.

To enable a rigorous approach for designing a ratite-inspired tendon network, we initially ‘linearise’ many of the biologically relevant structures. That is, we assume constant pulley radii and simple hinge joints (Fig. 3.1D and E), in place of nonlinear curved sesamoid surfaces and bone surface interactions that lead to a complex, translating center of rotation. Nonetheless, the robot tendon network retains the essential connectivity features of the avian limb. The spring-tendon network is designed to establish coupled joint kinematics in swing phase, flexing all joints to provide ground clearance, engage the global leg spring upon loading into stance phase, to support body weight, distribute torque and power among joints during stance, and disengage at the end of stance and rapidly transition the leg into the swing phase. The joint coupling during stance distributes the load among the individual joints, without the danger of catastrophic collapse at any single joint, and supports compliant leg compression under load for elastic energy cycling [7].

To achieve these mechanical features, we first introduce a single multi-articular spring-tendon structure connecting all leg joints (Fig. 3.1C). We design a z-like leg structure (Fig. 3.1D and E) commonly observed in vertebrates [87, 71, 234]. We further assume a planar configuration, without off-plane influence. Pulley radii r_{jx} of joint j_{x} are calculated to establish an equal effective mechanical advantage (EMA) [25] for all joints sharing the same multi-articular spring-tendon (‘global spring-tendon’, GST), with a force magnitude of $\left\|\vec{F}_{\mathrm{GST}}\right\|$:

$$\left\|\vec{F}_{\mathrm{VL}}\right\| \cdot d_{\mathrm{jx}} = \left\|\vec{F}_{\mathrm{GST}}\right\| \cdot r_{\mathrm{jx}} \tag{3.7}$$

$$r_{\mathrm{jx}} = \frac{\left\|\vec{F}_{\mathrm{VL}}\right\| \cdot d_{\mathrm{jx}}}{\left\|\vec{F}_{\mathrm{GST}}\right\|} \tag{3.8}$$

where $\vec{F}_{\mathrm{VL}}$ is the force along the virtual leg direction l_{VL} (Fig. 3.1D), and d_{jx} is the shortest distance between joint j_{x} and the virtual leg l_{VL}. Equation (3.7) balances joints j1 and j2 equally. For the shown, EMA-balanced configuration in Fig. 3.1D and E and a given a virtual leg length change, these joint’s angles change equally. Each joint’s torque balance depends on its pulley’s radius and the joint’s perpendicular distance to the virtual axis. Next, we introduce an imbalance between the torque loading of the distal joint j_{distal} (external), and its extension torque (internal). The imbalance serves to securely

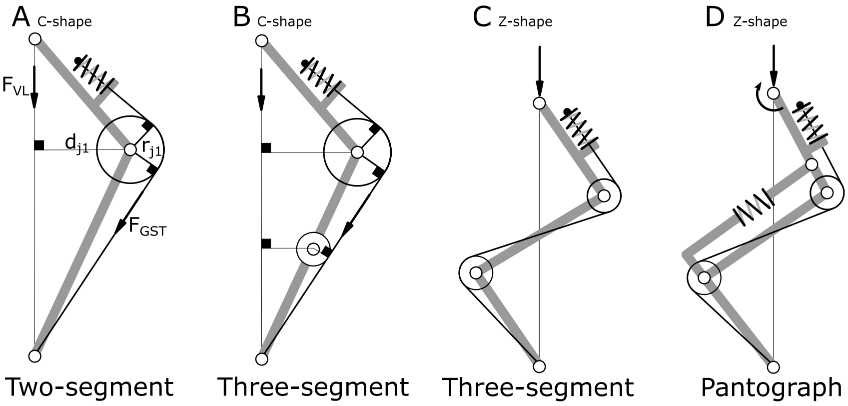

Figure 3.7: Schematic view of leg segment configurations. **A)** A two-segmented leg in a c-shape configuration. The joint’s j1 external and internal torques are balanced as products of pulley radius r_{j1} and spring tendon force GST, and loading force F_{VL} and moment arm distance d_{j1}. See Eq. (3.7) for details. **B)** An added second joint j2 creates a three-segmented leg, shown as c-shape configuration. In this configuration, joint torques are balanced, but the leg is unstable. The pulleys of joints j1 and j2 ’see’ the equal tendon force. **C)** An equivalent configuration to **B)**, but shown as a z-shape. **D)** The balanced, but unstable configurations in **B)** and **C)** are stabilized by an additional strut, leading to a spring-loaded pantograph configuration with a global tendon spanning joints j1 and j2. For BirdBot’s legs, we added two additional digit segments that share the global tendon force F_{GST}.

and compliantly 'lock' the leg structure under external load $\left\|\vec{F}_{\mathrm{VL}}\right\| > 0$. The imbalance is achieved by under-dimensioning the most distal joint's pulley radius relative to its nominal (balanced) value. In place of an EMA-balanced pulley (Eq. (3.7)) with nominal radius (r_{N}), an 'under-balanced' pulley with half the EMA-balancing radius is mounted:

$$r_{\mathrm{und}} = \frac{r_{\mathrm{N}}}{2} \tag{3.9}$$

$$\left\|\vec{F}_{\mathrm{VL}}\right\| \cdot d_{\mathrm{j,distal}} > \left\|\vec{F}_{\mathrm{GST}}\right\| \cdot r_{\mathrm{und}} \tag{3.10}$$

The under-balanced joint deflects faster, compared to the balanced joints. Consequently, when the leg is loaded, the distal joint rapidly collapses until the most distal segment touches the ground to establish a flat, foot-style contact (movie S7).

With the selected global spring's stiffness, the leg deflects by 10 % under three body weights, approximately to that observed in legged animals [32, 145, 67]. The resulting leg structure is balanced for static load but would destabilize when transitioned between leg postures, or when torques are applied. Therefore we further stabilize the leg by embedding a spring-loaded pantograph mechanism into the z-shaped leg structure (Fig. 3.1E, Fig. 3.8A), which also provides compliance in leg angle direction, benefiting energy economy [192].

The global spring-tendon coordinates the motion of all four leg joints during stance phase and rapid transitions to a slack, flexed position in swing (Fig. 3.8, Fig. 3.9, movie S7). When unloaded, the distal joint is released from its clutched, digital-extended position (Fig. 3.12). The global spring-tendon becomes slack and detached from the distal pulley, and all leg joints become loose. A Central Patter Generator (CPG) swing controller (Section 2.6) commands the knee actuator to flex the knee joint j1, leading to coordinated flexion of all four joints, coupled by the multi-articular and the compliant pantograph. Simultaneously, distal joints j3 and j4 rapidly rotate from their digital-extended position during stance to a pronounced digital-flexion in swing, akin to the tarsometatarsus stance-to-swing phase kinematics in running birds [177, 189].

Thus, active knee flexion causes all four joints to rapidly flex towards mid-swing, shortening the leg length for maximum ground clearance (Fig. 3.9C). The shortened swing leg also reduces the hip torque required to accelerate the leg forward during protraction.

The amount of leg flexion depends on the length of the global spring-tendon released by the joint j4 digital-flexion. Suppose the multi-articular tendon is wrapped around the pulley of joint j4 (Fig. 3.9B). In that case, joint j3-j4 digital-flexion creates insufficient tendon slack to substantially shorten the leg. The distal tendons of ratite birds like emus and ostriches are routed in sheaths [135] that permit substantial off-joint motion during digital-flexion, which we also observed in cadaver dissection (Fig. 3.9A). We mimic the bird's sheath morphology with a tendon-catch (Fig. 3.9C and D, Fig. 3.3) for the otherwise loosely mounted multi-articular tendon. The tendon-catch allows for substantial

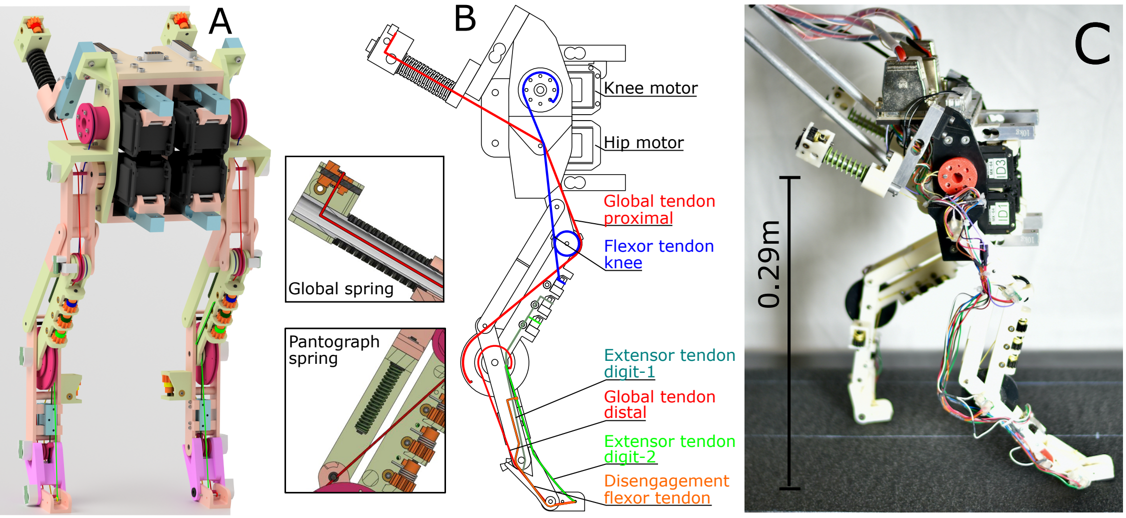

Figure 3.8: **BirdBot leg design and spring-tendon network.** **(A)** Computer-aided design (CAD) drawing of BirdBot. The pantograph spring (spring-12p) is mounted as one-directional elasticity, and the global spring tensions the global multi-articular tendon. Tendon lengths are individually adjusted. **(B)** The global spring-tendon (GST) functionally acts across four joints (j1 to j4), but is also guided over hip joint j0. The GST is implemented as two tendons, proximal and distal, connected in the ankle j2 pulley, with different pulley radii. The knee flexor tendon (blue) connects the knee flexion actuator with the tibiotarsus segment, to elevate and shorten the leg during swing. The digit extensors (dark and light green for digit-1 and digit-2) are coupled to ankle j2 action—extension of the ankle pulls both digits into a digital-extended position. The disengagement flexor tendon (orange) spans joints j3 and j4, and is actuated by the stance rotation of joint j4 to apply a buckling force at the bistable joint j3 at toe-off to disengage the GST. **(C)** Photo of the BirdBot prototype in side-view, overlaid scale bar. BirdBots hip height is 0.29 m.

tendon slack during digital-flexion and guides the tendon back onto its pulley after digital flexion.

An ideal swing-to-stance transition involves a rapid switch from a slack swing leg to an engaged, load-carrying stance leg that supports body weight and cycles elastic energy. In the late swing phase, the leg length actuator stops flexing the knee joint j1, which effectively lengthens the leg as a result of gravity and the leg's angular momentum. Two distal, bi-articular tendons (digit-1 extensor and digit-2 extensor, Fig. 3.8B) couple the ankle j2 extension to the rotation of the distal joints j3 and j4, into their digital-extended position (Fig. 3.10). At the leg's most forward position and while still in-air, all leg joints are extended (Fig. 3.10, still frame $t = 0.08$ s). Next, the hip actuator pulls the leg backward, into touchdown. As soon as the foot contacts the ground, the global spring-tendon propagates back the joint j4 lever-action to all leg joints. The leg

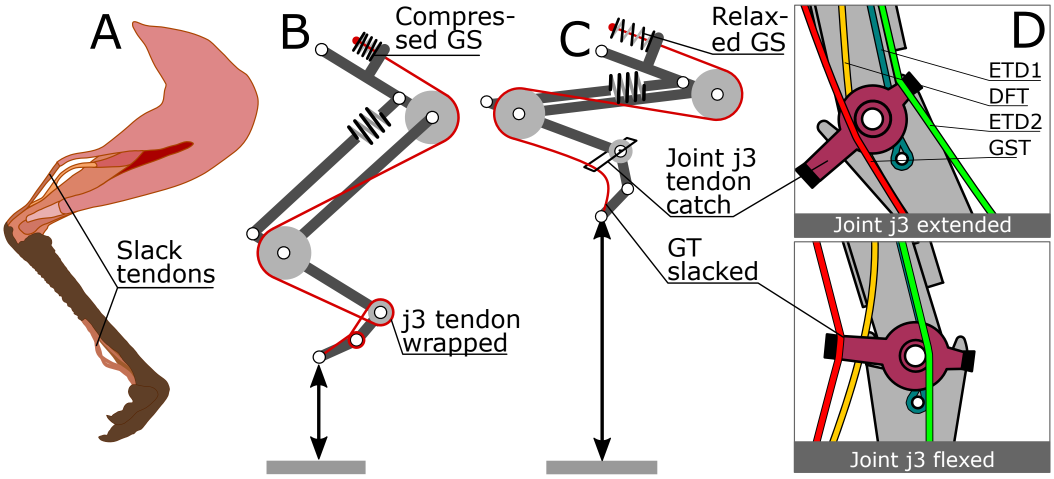

Figure 3.9: **Enabling tendon slack for low resistance flexion in swing.** **(A)** The distal tendons in the emu and ostrich ratites move loosely within their sheaths at the TMP joint during digital-flexion [135]. **(B)** At the transition from stance to swing, j3 and j4 undergo large digital-flexion, which releases the global tendon (GT) length needed to flex the ankle j2 and knee j1. The global tendon can be guided by direct tendon wrapping as shown. However, tight wrapping only releases tendon proportionally to digital flexion angles. Further leg flexion will then load the global spring (GS), which we want to avoid. **(C)** We mimic biological tendon slacking in the robot leg with a detachment and re-alignment 'tendon catch' mechanism at joint j3. This allows full leg flexion without loading the global spring, to achieve low resistance knee flexion without feedback control. **(D)** Mechanism detail: In swing (joint j3 flexed), the global tendon detaches from the j3 pulley. The detachment creates enough tendon slack for full leg shortening.

is again locked as a springy strut and ready to carry high mechanical loads throughout stance phase. An ideal stance-to-swing transition involves a rapid switch from a load-carrying leg to a configuration with all joints slack, allowing rapid leg shortening with low resistance to create ground clearance. In practice, the global spring-tendon clutching mechanism disengages under the following conditions. The global spring reaches its slack length, which occurs when the leg reaches the disengagement angle (Fig. 3.12A), and the foot rotates from a digital-extended position to a digital-flexed position to release the global spring-tendon. Alternatively, disengagement can be forced through actuation of the distal joint j3. At fast speeds, the feedforward actuation patterns cycle the leg length through clutch engagement, mid-stance, and take-off lengths, with the leg lifting off the ground through the robot's momentum. Yet at lower speeds, the momentum is insufficient to drive foot lift-off. Consequently, with a digital-extended foot coupled to the global spring through the global spring-tendon, the foot remains in contact with the global spring-tendon clutching mechanism engaged. Rotating the foot into a vertical ori-

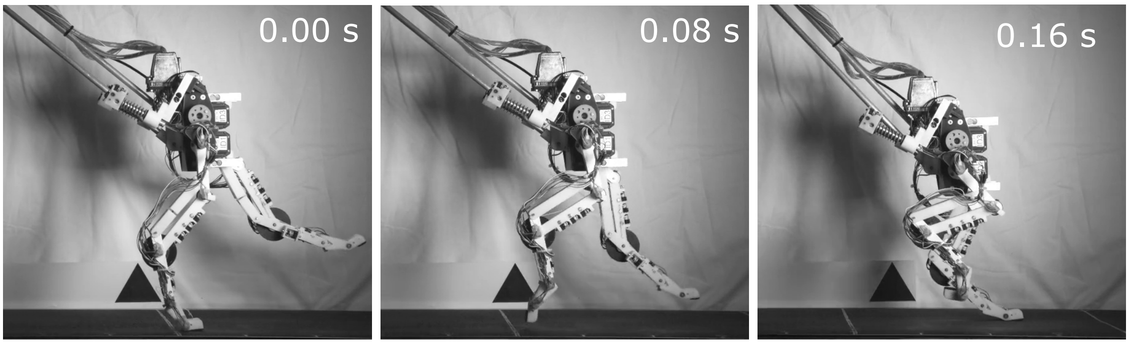

Figure 3.10: **BirdBot running at a stride frequency of** 1.5 Hz**, with a speed of** 0.75 m/s **(Froude number** 0.20**).** Side-view video still frames of BirdBot running on the treadmill, with a four-bar guide to restrict rotation.

entation with $\alpha_{\mathrm{j3}} > 180^\circ$ angle will reliably disengage the clutch, and allow shortening of the slacked leg (Fig. 3.11A). To enable end-stance disengagement with minimal leg work, our aim was to avoid raising the foot to disengage the leg spring. Instead, we added a joint j3 with a disengagement mechanism mediated by a distally mounted, bi-articular tendon ('disengagement flexor tendon', Fig. 3.12C, Fig. 3.11B). The tendon-based disengagement mechanism reduces the work and power required for leg disengagement, and works as follows. During stance phase, a joint j3 hard stop only allows joint angles above 160° close to its snap-through angle (Fig. 3.12C). A bi-articular disengagement flexor tendon wraps around the joints j3 and j4 (Fig. 3.12C, DFT, orange tendon). The joint j4 loads the disengagement flexor tendon increasingly during stance phase with its joint flexing action. In late stance, the disengagement flexor tendon's force pushes the joint j3 over its snap-through angle of 180°. Collapsing joint j3 also slacks the in-parallel global spring-tendon, which then rapidly slacks all remaining joints into the swing leg configuration (Fig. 3.9C, Fig. 3.15B, Fig. 3.13).

Both actuators are feedforward controlled by a Central Pattern Generator with two outputs that are interpreted as commanded hip angle and knee angle over time (Eq. (2.5) to Eq. (2.8)). The hip actuator directly actuates both directions, leg protraction and retraction, while the knee actuator transmits flexion torques but no extension torque. The hip output is a sine-like pattern with amplitude A^{h} oscillating around the femur angle offset O^{h}. A commanded duty factor adjusts the ratio of swing and stance duration; a duty factor of 0.6 commands a stance phase of 60 % of total cycle time. We observe emergent gait patterns with the robot foot already in the air when the femur angle switches from protraction to retraction (end of the commanded swing phase). Consequently, just before touchdown, the hip actuator retracts the leg briefly in air. Similar end-swing characteristics have been shown in underactuated robots with strong natural dynamics [207]. BirdBot's observed duty factor is 0.49 at a stride frequency of 1.5 Hz (Fig. 3.14). In stance, the hip actuator continues to retract the stance leg, propelling the robot forward. As the hip actuator reaches its most posterior angle, leg spring disengagement occurs.

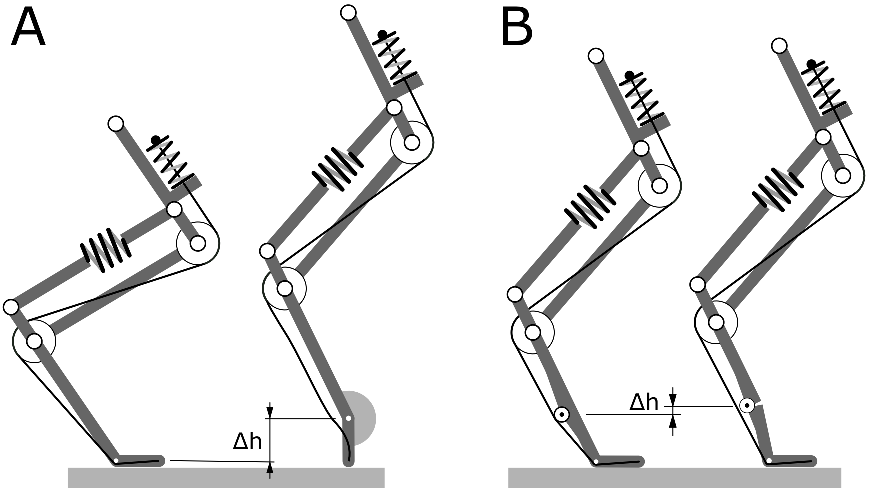

Figure 3.11: Energetic cost of disengagement, for single-digit and two-digit foot designs. **A)** The global spring tendon becomes relaxed after the distal segment reaches a digit-flexed posture, after its joint j3 crosses $\alpha_{\mathrm{j3}} = 180°$. In case of a standing leg, the energetic cost of disengagement is equivalent to $E_{\mathrm{DE}} = disengagementltaE_{\mathrm{pot}} = m \cdot g \cdot disengagementltah$. **B)** In the two-digit configuration, the global spring tendon becomes relaxed when either j3 or j4 cross the parallel orientation with their next proximal segment. The joint j3 shown is designed so that with a minor change in joint angle, the global spring tendon becomes relaxed (snap-through angle). In comparison to configuration **A)**, less vertical work is required to disengage the five-segment leg.

The knee actuator starts flexing the knee at the time of leg spring disengagement, and upon disengagement, rapidly flexes the entire leg into the raised swing-leg configuration. The knee actuator starts to release the knee joint around mid-swing, and the leg re-extends towards the ground. Full leg length is reached at the end of the commanded swing phase, with the leg still in the air and the digital joints extended.

At a 1.5 Hz stride frequency, BirdBot reaches a speed of 0.75 m/s (Froude number $\mathrm{Fr} = 0.20$). In stance phase, a peak retraction torque (leg angle direction) of −1.70(5) Nm (CI) occurred just before mid-stance (Fig. 3.14B). During swing phase, the leg angle torque fluctuated between 0.5 Nm at in-air protraction and −0.5 Nm at in-air leg retraction about one third of the applied leg angle torque during stance (table 3.3). The torque flexing the knee joint during swing phase reached a maximum of 0.31(3) Nm (CI) (Fig. 3.15A, solid line), caused by dynamics of lifting the slack lower leg. This peak torque is comparable in magnitude to the knee flexing torque required during standing (0.09 Nm statically applied torque, Fig. 3.5, table 3.3). In Fig. 3.15A, we also compare the knee flexing torque of BirdBot to that of a modeled robot with the same morphology but a permanently engaged (non-clutching) knee spring, similar to [207]. With the additional torque required by the constantly engaged, in-parallel knee spring, the actuator would require 3.7 Nm of torque, or more than ten times the measured torque of BirdBot's

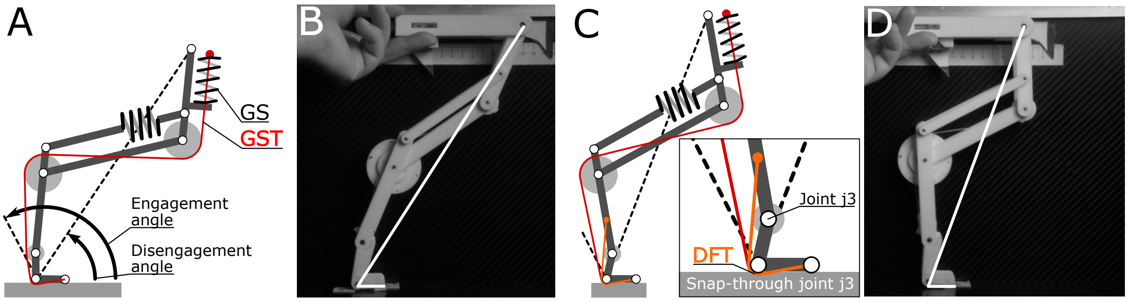

Figure 3.12: **End stance disengagement.** We experimentally measured the disengagement angles with and without the disengagement flexor tendon (DFT), by manually pushing the hip along a horizontal guide at near-constant speed. **(A)** Without the disengagement flexor tendon, leg kinematics unloaded the global spring-tendon (GST) at a virtual leg angle of $59 \pm 0.3°$ ('disengagement angle'). **(B)** Snapshot of disengaged leg, like in **(A)**. **(C)** With the disengagement flexor tendon, the joint j3 snapped through and unloaded the global spring-tendon already at a $69 \pm 1.2°$ angle, showing a 10° difference caused by the disengagement flexor tendon. **(D)** Snapshot of disengaged leg, like in **(C)**. The global spring (GS) in the hardware leg is mounted above the hip joint, the modified GS schematics in **(A)** and **(C)** are shown for simplification.

knee, assuming the same knee joint j1 kinematics (Fig. 3.15C, dashed line, and table 3.3).

Table 3.4: Energy stored, and torques measured, referring to Fig. 3.14. The energy stored and released by the global spring and the disengagement tendon is shown as the change between minimum and maximum cumulative work. Peak torques were measured for the leg angle (hip) actuator, and the leg length flexing actuator. Experimental values shown are mean ± confidence intervals (CI), for a confidence level of 0.95.

	Mean ± CI
Global spring tendon energy, maximum	0.34(2) J
Disengagement tendon energy, maximum	0.037(1) J
Leg angle torque, maximum	−1.71(5) Nm
Knee flexion torque, maximum	−0.31(3) Nm
Knee flexion torque, maximum (modelled)	−3.73 Nm

In Fig. 3.14A, we observe signs of power amplification in the distal tendon work profile, indicated by an asymmetric rate of elastic energy storage and release [159]. Specifically, the bi-articular disengagement flexor tendon stored 0.037(1) J (CI) elastic energy in the first 82 % of the stance phase, and released it in the remaining 18 % of stance phase, corresponding to an asymmetry ratio of 4.6:1. In comparison, the multi-articular global spring-tendon stored and released 0.34(2) J (CI) on average, approximately nine times

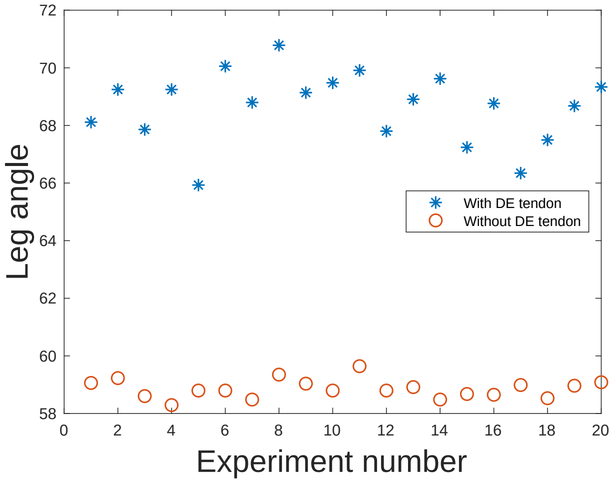

Figure 3.13: Data for experiment shown in Fig. 3.12. We pushed two non-acuated BirdBotlegs (with and without disengagement flexor tendon) each 20 times over the disengagment point. Disengagement angles recorded are plotted here. Round markers show disengagement angles for the leg without disengagement flexor tendon, star markers for the leg with disengagement flexor tendon.

the disengagement flexor tendon energy, with relatively symmetric timing around the peak (Fig. 3.15C, table 3.4). BirdBot's combined actuators drew in average 15.7(4) W and 16.8(4) W of electrical net power at 1.0 Hz and 1.5 Hz locomotion, respectively (table3.5).

Table 3.5: Applied electrical power consumption, for 1.0 Hz and 1.5 Hz stride frequency. The data behind the table is identical to Fig. 3.16A and B. Values are mean ± standard deviation. The net power is the sum of hip motor and leg length (knee flexor) motor power, minus the motors' standby power (four times 1.2 W, in sum 4.8 W).

Frequency	Hip actuator	Leg length actuator	Sum	Standby	Net
1.0 Hz	13.9(4) W	6.5(2) W	20.5(4) W	4.8 W	15.7(4) W
1.5 Hz	15.2(4) W	6.4(2) W	21.6(4) W	4.8 W	16.8(4) W

The instantaneous electrical power consumption of the hip actuator shows one distinct peak at stance-phase leg retraction (Fig. 3.16B). The power consumption of the knee actuator peaked twice, following the step-like knee flexion and extension CPG signal (Fig. 3.16A). According to Eq. (3.3), the cost of transport of a natural runner with BirdBot's weight is 1.45 (table 3.6), and the robot's power consumption at a speed of $v = 0.75$ m/s corresponds to a net cost of transport of 1.32.

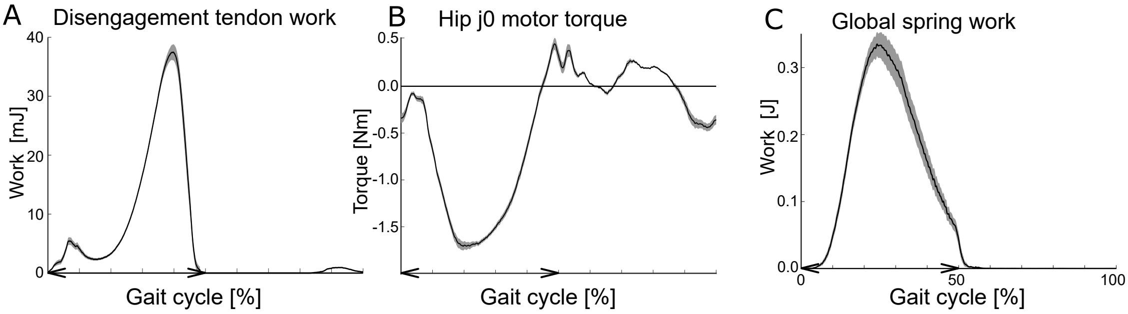

Figure 3.14: Data are averaged from 70 strides, with a 95 % confidence interval shown as a shaded area. The stance period is indicated by '<>' on the x-axes. **(A)** The cumulative work applied at the disengagement flexor tendon. The tendon stores and releases 0.037(1) J (CI) per cycle. The loading and unloading times are asymmetric, indicating power amplification. **(B)** Hip actuator for joint j0 with a peak torque of −1.71(5) Nm (CI) during leg retraction at mid-stance. **(C)** The cumulative work applied at the global spring-tendon, stored and released by the spring as elastic energy. The global spring-tendon stores on average 0.34(2) J (CI) per deflection in this gait.

It is notoriously hard to compare cost of transport among robots—numerous factors can influence COT including use of mechanical guides (planar four bar mechanism, rotating boom), varied walking substrate (laboratory surface, treadmill, outside terrain), power supply (onboard, tethered), control (on-board, remove), the motor type (brushes, brushless), gearing, and robot size. BirdBot' is guided in-plane by a four-bar while walking on a treadmill, with a pitch-locked trunk, actuated by brushed and high-geared motors, and powered and controller by tether. A freely-walking BirdBot would likely consume more power. Nonetheless, BirdBot shows economical locomotion, particularly in comparison to the similarly actuated, freely running robot Cheetah-cub [207]. To allow indirect comparison between robots, we define a relative cost of transport in Eq. (3.4) as the ratio between the robot's cost of transport and that of a natural runner of equal weight, resulting in a relative net cost of transport of 91 % for BirdBot.

3.6 Discussion

Animals vastly outperform current legged robots, achieving agile movement in natural terrain with robust balance and low metabolic cost of transport, compared to legged robots [68, 137, 65, 188, 51, 26, 50, 12, 57]. We used an iterative design process and a physical robot to test the hypothesis that a bird-inspired multi-articular linkage mechanism can replace most of the neural circuitry required for joint coordination and stance-swing transition control. The multi-articular spring-tendon in the five-segment leg creates a whole-leg clutch, which transitions upon loading into a high stiffness configuration for stance, and transitions upon unloading to a slack configuration for swing.

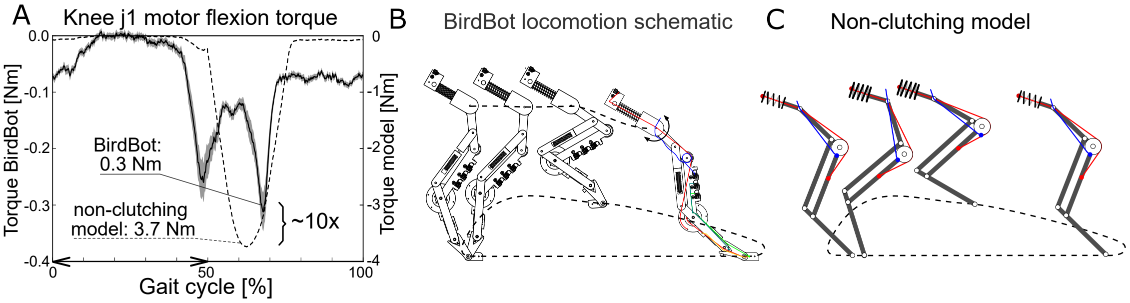

Figure 3.15: Data are averaged from 70 strides, with a 95 % confidence interval shown as a shaded area. The stance period is indicated by '<>' on the x-axes. **(A)** The knee flexing actuator applies a peak torque of 0.31(3) Nm (CI) at mid-swing to lift the lower leg and create foot-ground clearance (solid line). We modeled a non-clutching, parallel leg spring (dashed line, model shown in C) and assumed the same knee joint kinematics as BirdBot (B). The non-clutched knee actuator model would require 3.7 Nm, that is more than ten times higher torque than in BirdBot. **(B)** Schematic of BirdBot's leg and foot trajectory over a gait cycle. **(C)** Schematic of the leg and foot trajectory of the non-clutching model.

The leg design achieves consistent inter-joint coordination of a complex leg trajectory, compliant bodyweight support with elastic energy cycling, and rapid, automatic control of swing/stance transitions. The rapid transition to swing is achieved by action of the spring-tendon network on a bistable joint, which disengages the stance leg spring. These mechanisms enable bipedal gait with just four actuators under simple, model-free feed-forward control. In addition to providing robust mechanics with simple control, the leg design achieves economical cost of transport by reducing knee-flexing torque to one tenth of that of non-clutching leg designs like Cheetah-cub [207].

Research on running ground birds suggested that their remarkable agility and robustness benefit from intrinsic mechanical control [51, 54, 34, 26, 50]. BirdBot's leg clutch relies on a digitigrade posture, in which the toe becomes flat against the ground. To freely shorten its leg in swing, the distal segment rotates from a digital-extended to a digital-flexed posture, which slacks the stance spring. Our analysis suggests a suite of structural features required for the mechanism: elevated, digitigrade posture with a long tarsometatarsus segment, a multi-articular network of ligaments and tendons from femur to toe (Fig. 3.1C), sesamoid bones creating the appropriate cam dimensions, sheaths to guide slack tendons, and a bi-stable configuration in the distal joint.

This analysis helps to identify where similar function is likely to be found among diverse animals. Although BirdBot's leg design is inspired by large ratite birds such as emus and ostriches, the structural elements are present to varying degrees among many birds [195, 196, 2, 39, 50, 227, 78, 177, 189, 241, 13, 27, 190, 101]. BirdBot is an abstracted and simplified model: complex bone surface interactions are approximated as hinge joints, and sesamoid structures are approximated as constant-radius cams. The

Table 3.6: Parameters and cost of transport (COT) of selected legged and hopping robots from the literature. Other abbreviations and explanations: $\mathrm{COT_{et}}$ electrical total, $\mathrm{COT_{me}}$ mechanical, $\mathrm{COT_{ne}}$ net electrical, '*' computer simulation, '–' insufficient data, '$^{\mathrm{R}}$' recuperation of negative power, Bold values indicate data points in Fig. 3.16C.

Robot	m [kg]	v [m/s]	L [m]	Fr $v^2/(gL)$	$\mathrm{COT_{et}}$ [J/N/m]	$\overline{\mathrm{COT_{et}}}$ [%]	$\mathrm{COT_{en}}$ [J/N/m]	$\overline{\mathrm{COT_{en}}}$ [%]	$\mathrm{COT_{me}}$ [J/N/m]	$\overline{\mathrm{COT_{me}}}$ [%]
ARL Monopod II [3]	18.00	1.25	0.70	0.23	–	–	–	–	0.22	32
Spring Flamingo [170]	14.20	0.50	0.88	0.03	2.9	390	–	–	0.07	9
Scout II [205]	25.50	1.30	0.32	0.53	1.7	274	–	–	0.50	80
Cornell Biped [43]	13.00	0.40	0.85	0.02	0.2	26	–	–	0.06	7
FastRunner* [45]	30.00	8.89	1.40	5.75	–	–	–	–	0.50	85
FastRunner* [46]	30.00	9.83	1.40	7.04	–	–	–	–	1.40	237
Cheetah cub [207]	1.10	0.66	0.16	0.28	–	–	6.60	**396**	–	–
MIT Cheetah 1$^{\mathrm{R}}$ [200]	33.00	2.30	–	–	0.51	89	0.48	83	0.13	23
StarlETH [104]	25.00	0.50	0.33	0.08	1.70	**272**	1.10	**176**	–	–
MIT Cheetah 2$^{\mathrm{R}}$ [157]	33.00	4.50	0.70	2.95	0.50	87	–	–	–	–
Titan XIII [120]	5.65	1.38	0.15	1.29	1.76	**177**	–	–	–	–
ATRIAS$^{\mathrm{R}}$ [99]	62.00	0.80	0.90	0.07	–	–	1.13	**240**	–	–
Oncilla robot [210]	4.50	0.63	0.16	0.25	–	–	3.20	**299**	–	–
MIT Cheetah 3$^{\mathrm{R}}$ [28]	45.00	1.32	0.60	0.30	0.45	**87**	–	–	–	–
SPEAR [131]	8.07	0.54	0.56	0.05	–	–	0.86	**96**	0.45	50
BiartLeg [192]	0.90	0.91	0.41	0.21	1.20	68	0.80	**45**	–	–
BirdBot	1.73	0.75	0.29	0.20	1.68	**117**	1.32	**91**	0.13	9

model integrates several features: joint cam radius, distance from the joint center to the virtual leg, segment lengths, and ratios of leg segments. Equation (3.7) and Eq. (3.9) assume a loading of the virtual leg, and establish the required joint moments based on the assumption that all leg joints are mechanically coupled and balanced, resulting in a similar joint velocity for all but the distal joint, which is underdimensioned. Joint coupling propagates loading from proximal and distal, and likewise, distal to proximal. Equation (3.7) and Eq. (3.10) are indifferent to leg postures (erect, or crouched), suggesting that small birds with crouched postures could have a leg clutch. The cam of the distal joint must be under-dimensioned, resulting in larger distal joint deflections compared to the knee and ankle. Rapid deflection of the distal joint upon loading creates a flat 'foot' contact with the ground and engages the stance leg spring. Disengagement of the stance leg spring is triggered by loading a distal, bi-articular tendon, leading to a sudden digital-flexion at toe-off. The distal tendon sheath allows tendon-detachment and slacking in the swing phase, enabling shortening of the swing leg with low resistance.

Across bird species, the degree to which the leg clutch exists as a passive mechanism likely varies. Ostrich legs possess high capacity to support weight and recycle elastic energy in distal tendons [190, 101], and exhibit the distal structures required for the bi-stable mechanism [195, 196]. Running ostriches also have distal joint kinematics consistent with the leg clutch [241]. In large ratites, the elastic tissues in the distal leg might passively support body weight, but in most species, engagement of the leg clutch likely requires active muscle contraction.

The BirdBot model challenges the idea of joint myotatic control, in which antagonistic

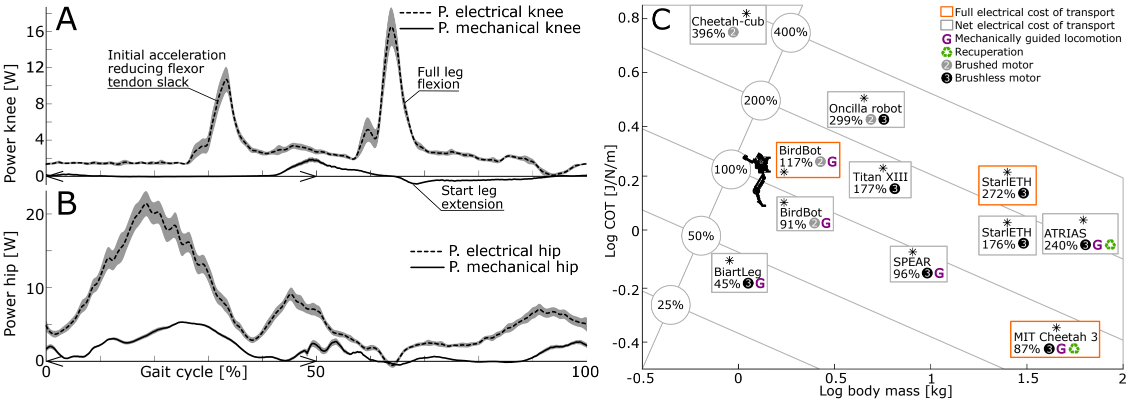

Figure 3.16: **Robot energetic performance and comparative cost of transport (A)** Knee mechanical power (solid line) and instantaneous electrical power of the knee flexing actuator (dashed line). The two electrical power peaks indicate an initial acceleration to reduce tendon slack at the end of stance, and a second burst to fully lift the lower leg in swing. '<>' indicate the observed stance period. **(B)** Hip mechanical power (solid line) and actuator electrical power (dashed line). The highest power consumption occurs during leg retraction in the stance phase. In comparison, swing leg protraction requires considerably less power. **(C)** The electrical cost of transport of selected legged robots, plotted relative to body mass, on a logarithmic scale. As a general reference, the 100 % cost-of-transport-line indicates the metabolic cost of animal runners, according to [217]. Brushless-motor actuated robots that recuperate negative power are indicated with a green recycle symbol. Hopping robots, such as BiartLeg, require no leg shortening for ground clearance in the swing phase, reducing their COT. BirdBot's net cost of transport is slightly below that of a running animal with a similar body mass (1.73 kg). This places BirdBot's net cost of transport in the range of the hopping SPEAR robot and MIT Cheetah 3.

pairs of flexor and extensor muscles control individual joints [154, 204, 35, 154, 167]. A more modern perspective suggests that muscle synergies control functional modules for whole-leg tasks, such as leg stiffness, bodyweight support, propulsion, leg angular cycling, and balance correction [214]. Control via functional modules is consistent with observed muscle activation patterns in guineafowl, a terrestrial bird with size similar to BirdBot [85, 80]. Co-activation of functional modules could actively engage a leg clutch in species where the mechanism is not passive. In terrestrial birds, for example, isometric contraction of ankle extensors might engage the distal tendon network and facilitate proximo-distal energy transfer [178, 54, 52].

The BirdBot leg is a specific implementation of a geometric latch-mediated spring actuation mechanism, as defined by Longo and colleagues [133]. A diverse range of animals use latch-mediated spring actuation to effectively control high-power, spring-mediated movements [133, 128]. In BirdBot, the distal bistable joint supports rapid disengagement of the stance leg spring, actuated by the leg angular rotation in stance. It results in a rapid release of stored energy, similar to the asymmetric joint power profile observed at the tarsometatarso-phalangeal joint in running turkeys [177]. High ground clearance for swing is achieved through rapid, coupled flexion of joints upon clutch disengagement. A similar release of stored elastic energy occurs in horses' legs, triggered by rotation of the ground reaction force vector over leg joint axes, leading to a catapult-like mechanism [231]. A complex but more direct replication of the tendon network in the horse leg has been recently implemented in a robot by [146]. Such engagement and disengagement mechanisms enable automatic release of elastic energy over a range of locomotor frequencies and loading conditions, reducing the demand for actuator work and the need for rapid sensory feedback control.

Current legged robots often use direct joint actuation analogous to myotatic unit control, with extension and flexion by joint torque actuators. Transitions between swing and stance must actively be sensed and controlled, using contact, force or proprioceptive sensors [200, 197, 105]. Although this approach achieves smooth and stable gaits, it relies on precise and high frequency sensor feedback to detect contact and impact events [199, 90]. Paradoxically, existing robots remain clumsy compared to animals, despite using appreciable faster sensing- and information-transfer rates [19]. Sensor data can be noisy, making it hard to reliably detect contact events, particularly in unstructured terrain [30, 90]. To reliably detect contacts and control gait, many robots rely on control architectures that include hybrid feedforward/feedback, model-based prediction and learning strategies [30].

In contrast, BirdBot uses a single feedforward motor command at the proximal joint to coordinate complex leg actuation. BirdBots leg clutch automatically engages and generates ground reaction forces upon loading, and disengages upon unloading, without the need for sensors. BirdBot's stance spring passively deflects under load and rebounds after mid-stance, cycling elastic energy. Similar compliant leg robots can operate with no sensors and even stabilize after step-down perturbations [210, 192]. Thus, spring-leg designs not only minimize actuator work but can also simplify leg control.

As consequence of BirdBot's underactuated design, gaits are not directly commanded. Instead gaits emerge from the interaction between feedforward motor commands and ground reaction forces. This is illustrated by the discrepancy between commanded and observed duty factor. The commanded duty factor of the CPG-driven hip motor is 0.60 at a stride frequency of 1.5 Hz, and the observed gait duty factor is 0.49. This is similar to other robots with elastic legs and CPG-control [207]. Bipeds transition to running gaits at Froude numbers above 0.5 [79]. BirdBot displayed a grounded gait at slower speed (0.50 m/s, Froude 0.09) and brief aerial phases at higher speed, at Froude 0.20 (0.75 m/s). We set the high-level CPG control parameters of amplitude, frequency, and duty factor, and the gait emerged from the robot's elastic leg mechanics.

The structure of Eq. (3.7) indicates no limitations in scaling BirdBot's leg mechanism to very large sizes. In Fig. 3.17, we show a large-scale demonstration with a hip height of 1.75 m that carries a human's weight. Once the foot joint j4 is digital-flexed, the knee joint j1 can be flexed without loading the leg's global spring (Fig. 3.17C). Based on our analysis and physical demonstrations, we suggest that BirdBots leg design can become a blueprint for large legged machines.

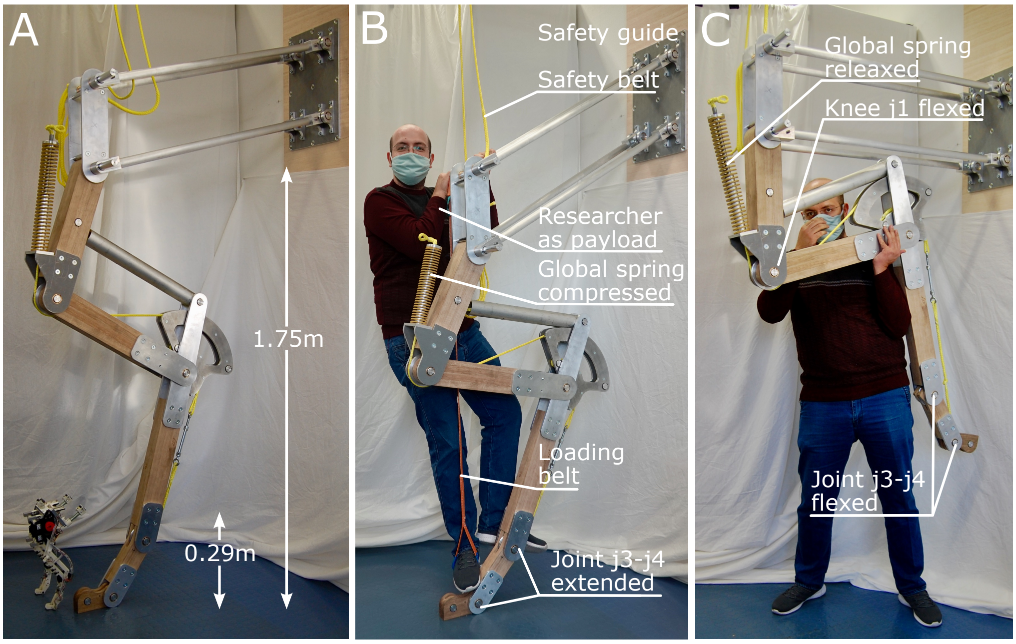

Figure 3.17: **Scalability of the BirtBot leg design.** **(A)** Small- (0.29 m) and large-scale (1.75 m) versions of the BirdBot leg. **(B)** The large BirdBot leg supports the weight of a human, hanging by a belt on the hip joint axis. **(C)** With the distal leg digits flexed, the parallel leg spring is disengaged, and knee and ankle joints can be flexed without resistance from the global spring-tendon.

BirdBot's leg has no direct actuation for leg length extension. Non-steady locomotion can demand net positive or negative work at distal joints [178, 175, 173, 52, 50]. To increase BirdBot's versatility in rough terrain, or to facilitate acceleration, a lightweight leg extension actuator could be placed in parallel with the distal-extensor tendons. Additional actuators would increase versatility and robustness, but also increase the leg mass, draw additional power, and likely require more complex control with sensory feedback.

Clutch mechanisms, similar to that in BirdBot, need to be lightweight, robust, and of minimal complexity for mobile use in prosthetics, exoskeletons, and other legged robots. Loading conditions change rapidly, and clutches in the drive chain connect and disconnect external and internal forces, from zero to multiple body weights within tens of milliseconds [187, 164]. Wiggin et al. designed a clutch for a human ankle joint exoskeleton that loads its spring in stance and releases the stored energy at push-off, freeing the ankle joint for the swing phase [228]. Van den Bogert analyzed whole-leg multi-articular passive exoskeleton designs and found they could substantially reduce joint moments and power; yet, no geometry was found to enable a 'clutch-like' function, with automatic switching from slack (in swing) to stiff (in stance) (page 6 of [220]). Diller et al. designed an active exoskeleton with a lightweight and efficient electrostatic adhesion clutch, which altered ankle joint stiffness by selectively engaging parallel rubber springs [61]. Clutches have been integrated into soft exoskeletons, where they hold and release elastic belts [60]. SPEAR robot's foot features a sprocket-like structure that interlocks with a chain section of a biarticular tendon in stance, and disconnects the robot's knee in swing, allowing efficient forward hopping with slacked joints in swing [131]. The multi-segmented leg of FastRunner featured ankle and/or knee clutch mechanisms. Although the 1.4 m tall FastRunner version did not run in hardware, its simulation reached fast speeds with a single, leg-angle actuator (Froude 5 to 7, see table 3.6) [46, 45, 84]. These findings suggest yet-untapped potential for effectively designed elastic clutches to improve robot performance. For future work, we suggest that a hybrid design with BirdBots clutch mechanism combined with direct actuation and sensory feedback control could merge the benefits of both systems to achieve robust and versatile locomotion. Recently, multiple advances have improved the economy and performance of legged robots. Robots designed with 'quasi-direct' or 'proprioceptive' actuation use strong, brushless motors and low ratio gearboxes [201]. In these robots, inter-joint control is governed by an internal robot model, which matches inter- and intra-joint torque to work against external loads. Joint power is applied directly, with extensor and flexor actuation demanding negative and positive work as the leg compresses and extends. These robots can benefit from power-regeneration during negative power phases and re-distribute recouped power

Figure 3.18: BirdBot can stand with its actuators switched off. Its foot latches and engages the leg mechanism, which in turn carries the robot's bodyweight. The foot provides a viable center of pressure, over which the center of mass can be positioned, see also Fig. 3.2C.

to other actuators or back into the battery [201, 99].

Another approach is to use compliant legs with parallel or serial springs to cycle energy and reduce actuator work [207, 210]. Previous robots with pantograph, spring-loaded legs and in-parallel knee flexing actuation [207, 210] were designed as quadruped robots. Under feedforward control, Cheetah-cub achieved self-stable trot gait patterns with relatively high speeds (Froude 1.3). However, without a disengagement mechanism, the stiff extensor spring requires large and rapid torques to shorten the leg for ground clearance in swing. Consequently, Cheetah-cub demanded high electrical power, resulting in a metabolic cost of transport 6.6 J/N/m, almost four times that of an animal of equal weight (Fig. 3.16C, table 3.6) [207, 192].

BirdBot shares several features with Cheetah-cub, including spring-loaded legs, a proximal pantograph, small-sized, brushed-motor actuators, and a similar weight. BirdBot features an important improvement—its foot-triggered clutch slacks the leg joints during swing. With the stance spring disengaged, the knee torque required to flex the leg for ground clearance decreases, from 3.7 Nm for a Cheetah-cub leg design, to 0.1 Nm with a BirdBot leg (static loading conditions, table 3.3). BirdBots distal tendon also stores energy in stance, and releases it at the end of stance (Fig. 3.14A), similar to the ankle actuation of passive walkers [43]. Both characteristics contribute to BirdBots low COT—low knee flexing torque, and tendon elastic recoil of the distal tendon. As a result, BirdBots cost of transport– one-quarter that of Cheetah-cub—is within the range of an animal of equal weight.

Although comparing robots with different morphology and number of legs is imprecise, it nonetheless provides a general perspective on how energetic performance can be improved by design. BirdBot, MIT Cheetah 3 [28], and SPEAR [131] cluster below the cost of transport of natural runners (Fig. 3.16C). Hence, legged robots with power-regeneration and low-ratio gearing can achieve exceptional energy economy [28, 182] (MIT Cheetah 3, table 3.6). Specialized hopping robots can be especially economical, because they operate with a single leg angle actuator, achieving a relative cost of transport of 45 % [192] (Fig. 3.16C, table 3.6).

BirdBot's guidance system keeps the trunk from translating sideways, and rotating in any direction. Hence, the trunk will not pitch if torque is applied. Immediately before swing-stance transition engagement, the robot's digits require clearance to rotate from digital-flexed to digital-extended. A forward pitching trunk could reduce ground clearance. To compensate for trunk pitching in an unguided version, higher clearance could be achieved by increasing leg angular velocity to reach an earlier maximum forward leg angle with its required posture for clutch-initialization. To implement a fully three-dimensional version of BirdBot will also require dedicated actuation and control for balance correction to move in three-dimensional environments [49, 221, 63]. Generally, pitching moments can be reduced by supporting BirdBot's hip-powered actuation with actuator-powered leg extension, with dedicated designs. Alternatively, the robot's trunk design can be adapted for hip-only actuation [47].

Chapter 4

Disengagement flexor tendon improves BirdBot-2 locomotion efficiency

4.1 Contribution

Major indicates a contribution, without which the paper would probably not have been submitted.
Substantial contribution increase chance of acceptance.
Minor contribution improved the paper, but did not significantly change the form or content.

Author	Author position	Scientific ideas	Data generation	Analysis & interpretation	Paper writing
Alborz Aghamaleki Sarvestani	First	Major	Major	Major	Major
Alexander Badri-Spröwitz	Last	Major	Minor	Substantial	Substantial
Title of paper		Distal disengagement of parallel leg elasticity improves BirdBot-2 locomotion efficiency			
Status in publication process		In preparation for IEEE Transactions on Robotics			

Thesis author contribution based on [1].
Alborz Aghamaleki Sarvestani: conceptualization, methodology, software, validation, formal analysis, data curation, writing - original Draft, visualization.

Content of this chapter is largely based on the below paper:

1. Aghamaleki Sarvestani*, A., Badri-Spröwitz. BirdBot 2: Investigating Parallel Elasticity Disengagement Mechanism Effect on Efficient Legged Locomotion. *In preparation* for **IEEE Transactions on Robotics**

4.2 Abstract

The current trend in legged robotics is to perform locomotion by reducing complexity in leg design and proposing complex controllers, which in the end, have unrealistic locomotion behavior. On the other hand, in nature, we saw animals develop fairy complex and

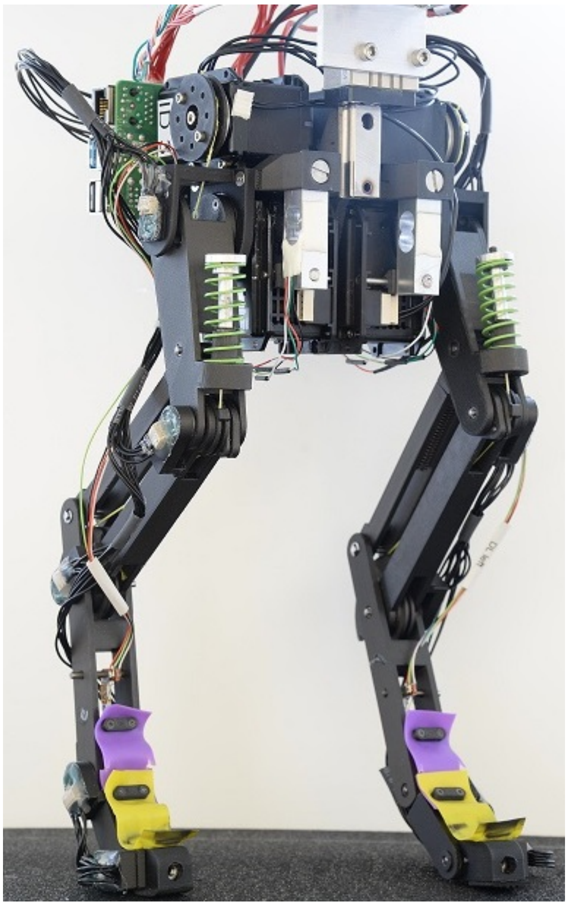

Figure 4.1: BB2 five-segmented leg robot with disengage-able parallel elasticity.

articulate legs that can perform with minimal sensory data. Therefore, we introduced the BirdBot1 (BB1) leg design, a five-segmented, highly coupled with passive spring-tendon system leg. BB1 leg uses a bioinspired disengagement (DE) tendon to disengage parallel elasticity during the swing phase to increase energy efficiency. This chapter studies the robot's disengagement performance over different gait parameters. Robot cost of transport and peak hip torque decreased by 30 % and 40 % respectively, by adding the DE tendon and removing co-contraction during the swing phase. In addition, the DE tendon helps the leg recuperate mechanical energy and works at a higher locomotion energy level. As a result, the robot with the DE tendon achieves a 28 % higher speed.

4.3 Introduction

The primary point that we want to answer in this chapter is to determine the effect of DE tendon on locomotion performance for walking, transition walking to running, and running gaits. BB uses a central pattern generator (CPG) [21, 113, 207] as its motion

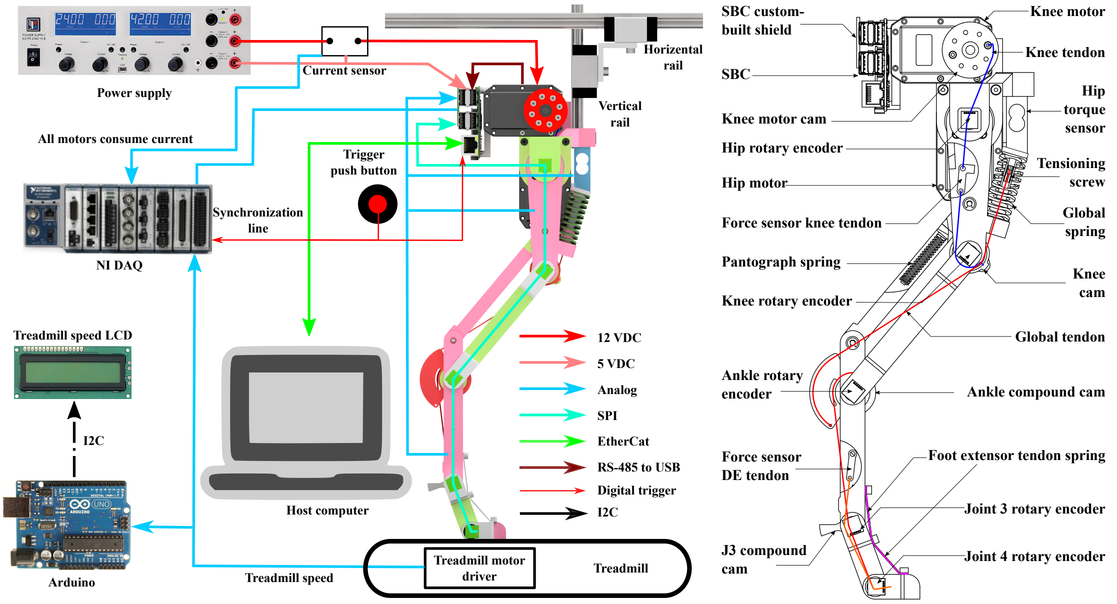

Figure 4.2: BB 2 schematic, sub mechanism, and experimental setup

generator for the hip and knee actuator. CPG trajectory depends on frequency, hip offset, hip amplitude, commanded duty factor, knee amplitude, and knee shifts (Section 2.6). Each of these parameters can change robot locomotion behavior, but the primary parameter affecting the performance of the DE mechanism is speed. In the current study, we compare BB 2 performance during walking, running, and transitioning to running in case of with and without DE tendon.

This chapter consists of three main sections. In the first section, we discuss the method we use for robot design and introduce different components in BB2. Then we discuss robot sub-mechanism and tendon system tasks. The robot instrumentation , measuring robot kinematic and kinetic attributes will be shown after that. We also discuss about different leg phases during locomotion and subsystem tasks in each leg phase. Then, we describe two different sets of experiments to show the robot's performance with and without DE tendon over different speeds. The second set of experiments shows the disengagement performance of BB 2 over the range of gait parameters. In the next section, we show the experiment results. Finally, in the discussion section, we analyze results and discuss finding from experiments and how they can prove our two main hypotheses.

4.4 Methods

Robot design: BB2 is a biped robot. Its legs feature five segments. The robot's body is constrained to move in the sagittal plane by two linear guides (SSVRL24), which also constrain its body rotations (Fig. 4.2). The body holds knee and hip motors and is directly attached to both linear guides. An onboard computer is mounted to the body. Hip motor torques are measured by floating both hip motors' output axes by two bearings and a beam load cell serially connecting motor and body. We calculate hip motor output torque by multiplying load cell force and its effective lever arm.

Leg design: The leg consists of five segments [S1, S2, S3, S4, S5] serially connected by five revolute joints [J0, J1, J2, J3, J4]. Each joint features a cam [cam1, cam2, cam3, cam4GS, cam4DE, cam5], which are part of leg tendon networks. Cam2 and cam3 are compound cams with two radii. Segment S1 and the hip motor output are directly connected.

Knee tendon: The knee motor is connected to segment s2 via a knee flexing tendon. The knee flexing tendon passes over the hip axis. Therefore, joint j2 rotation (flexion) and knee motor output rotation are linearly related.

Global spring tendon: The global spring and its tendon support the leg in the stance phase and passively provide forces to keep the robot standing upright. The global spring and its tendon were developed to replace an active, leg-length extending motor. The global tendon network consists of two connected tendons mounted to a tensioner screw and a spring on the robot's body. The proximal global tendon wraps over the extending side of cam2 and over the larger radius of cam3. The distal part of the global spring tendon begins at the smaller radius of cam3. The remaining part of the distal global tendon passes over cams cam4 and cam5 and is fixed to the end of segment S5.

DE tendon: When mounted into configuration BB2-1DE, the DE tendon supports disengaging the global spring tendon. Specifically, it unloads the leg at the end of the stance phase and readies the leg for the flight phase. The DE tendon connects to a single-axis force sensor, which force sensor connected with a hinge joint to S3. On the other side, the DE tendon is fixed to the S5. The DE tendon functions as a kinematic constraint between joints J3 and J4 by mechanically coupling both joints. In the stance phase, the robot moves over its stance leg, with an increasing joint J4 angle, while the DE tendon wraps around cam5. The DE tendon features high stiffness, and an increasing cam5 tendon wrapping induces a force pushing cam4 over the joint's equilibrium point, eventually slacking the global spring tendon.

Tendon tensioning mechanism: BB2 is built with stiff tendons. These tendons need adjustment, also to counter tendon creep. Therefore all tendons are connected to individual tensioning mechanisms (Fig. 4.2).

Instrumentation, electronic and software We record robot joint angles, motor output torques, and tendon forces. All data is synchronized and recorded onboard Fig. 4.2. The onboard computer also runs the robot's locomotion controller. Our integrated framework allows us to monitor the robot's performance for a given actuator input.

Host and onboard computer: A host computer (Lenovo workstation P 51) runs a custom-written GUI python wrapper. The GUI input receives CPG parameters frequency, duty factor, hip amplitude, hip offset, knee amplitude, phase gains, and phase shifts. The GUI python wrapper generates CPG trajectories from CPG input parameters and sends these via Ethernet to the robot's onboard computer (Raspberry Pi Model 4). The host computer also runs Labview NI MAX, which records and timestamps all remaining incoming sensor data as a TXT file for post-processing. The python GUI visualizes the robot's data as a live graph, and it stores data as a JSON file for post-processing.

The onboard computer receives CPG parameters and sends these to motor controllers. The onboard computer also receives robot joint encoder data through the SSI protocol and sends the data over Ethernet to the host computer's python GUI. Finally, a digital input of the onboard computer connects to the physical trigger and synchronizes all encoder data with the remaining data lines.

Joint encoders: Joint angles are measured by absolute 16-bit magnetic encoders (AEAT 8800-Q24) mounted to a custom-build PCB and are installed on each joint axis on top of a diametrical magnet. Joint encoders send joint angle data via a parallel SSI communication bus at 500 Hz updated frequency to the onboard computer.

Force sensors: We developed two sets of force measuring modules for the robot. The first is a customized beam-type load cell (TAL 220). It measures the motor reaction torque, and data is sampled by a DAQ force sensor module (Fig. 4.2). The second sensor type directly measures forces of global and DE tendons. The sensor is a custom-built, single-axis tension sensor (Fig. 4.2). The force sensor sends data to a DAQ force sensor module like the hip torque sensor.

Motor control: The onboard computer sends motor commands via USB to RS-485 converter (U2D2, Robotis) to servomotors. Motor parameters are accessible for motor calibration from the onboard computer.

Data acquisition (DAQ) system: A DAQ system (compactDAQ-9189, National Instruments) reads all force sensor data from DE tendon, hip and knee force sensors with two integrated strain and bridge modules (NI-9237, National Instruments) at 24-bit resolution, at a sampling frequency of 1 kHz. An analog input module (9205, National Instruments) interfaces a current sensor (ACS723) that reads motor currents and the treadmill speed from its motor driver (DPCANIE-015S400) at 1 kHz sample frequency.

Treadmill speed control. We customized an off-the-shelf treadmill (Christopeit TM500S) with a programmable motor driver (DPCANIE-015S400, Advance motion controller). We set treadmill velocity by a rotary potentiometer interface connected to the motor driver. The analog speed signal of the motor driver is recorded through the DAQ (CompactDAQ). We live-display the treadmill speed on display (LCD-1602) interfaced with a microcontroller board (Arduino Uno).

Physical trigger: All sensor and video data are synchronized with the help of a multi-contact switch distributing trigger signals to devices, either as digital rising or falling edge signals.

Power supplies: The onboard computer and current sensors are supplied with 5 V. 12 V are supplied to the robot's four servomotors.

Experiments We aimed to characterize the influence of the DE tendon mechanism by running BB2 with and without its DE mechanism active, i.e., with and without the

DE tendon mounted. Specifically, we aimed to show robot performance depending on locomotion speed, hip amplitude, and the addition of a DE tendon supporting parallel spring disengagement.

We recorded BB2 energy consumption and speed in all experiments, amongst other gait parameters. The robot runs on a treadmill, held by a guide system in the sagittal plane, with a fixed-pitch trunk posture in all experiments. We implemented robot gaits with four gait frequencies $f = 0.5\,\text{Hz}$, $1.0\,\text{Hz}$, $1.5\,\text{Hz}$, and $2.0\,\text{Hz}$. Each locomotion frequency was tested with a low and a high hip amplitude that provided successful locomotion. In a single experiment, we recorded 20 strides (left and right steps). Each experimental condition was repeated three times leading to in sum 60 strides per experiment for 16 experimental conditions (four frequencies, two tendon configurations, and two hip amplitudes).

Post processing **Cost of transport**: Cost of transport is a non-dimensional value to measure the performance of the system in terms of consumed energy. The CoT is defined as:

$$CoT = \frac{\sum_{i=1}^{n} P_i}{mgv_{CoG}} \tag{4.1}$$

Where n is the number of actuators, P_i is the average power consumption of actuator i, m is the mass of the robot, g is the gravitational acceleration constant, and v_{CoG} is averaged speed of the center of mass which reads from the treadmill.
For calculating input motor power we have:

$$\sum_{i=1}^{n} P_i = \sum_{i=1}^{n} I_i V_i = V \sum_{i=1}^{n} I_i \tag{4.2}$$

Where I_i is the average current of a motor read from the current sensor, and V is the set input voltage of motors.

Robot and leg linear momentum: to calculate motor linear momentum, we use the equation below:

$$L = \sum_{i=1}^{n} m_i \, v_{CoG_i} \tag{4.3}$$

where L is total linear momentum of leg,n is number of segments of robot leg, m_i is mass of segment i and v_{CoG_i} is linear speed of center of mass segment i.

Kinematics and kinetics: In this section, robot kinematics are calculated from the joint angle that is read from the sensor and calculate the ground reaction force and center of pressure of the leg and other kinetic properties of the leg. To simplify the calculation, we have several assumptions. First, the leg segment mass and inertia effect is negligible compared to other forces that act on the system necessary for driving the equation. Second, S5 is on the ground during foot roll-over motion. By this assumption, all leg states are fully defined with a given joint angle. Important parameters that we want to calculate

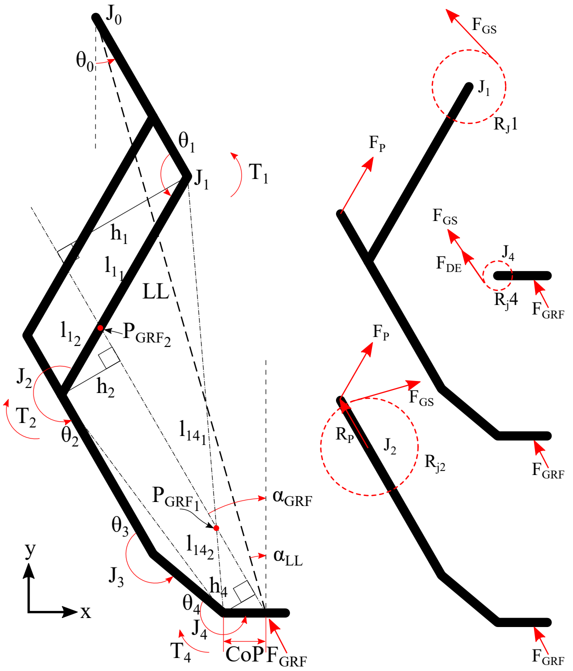

Figure 4.3: Leg schematic for joint angle and other leg entity for defining kinematic and dynamic of the leg.

are 1) α_{GRF}, the angle between GRF and the vertical direction. 2) F_{GRF}, the amplitude of ground reaction force. 3) CoP, the horizontal position of the center of pressure from the J4 joint. We show all the parameters in Fig. 4.3. First, we need to calculate the joint position from encoder data. If we assumes the hip as a reference, we have:

$$P_{J_0} = \begin{bmatrix} 0 \\ 0 \end{bmatrix}, \; P_{J_1} = \begin{bmatrix} l_1 \sin(\theta_0) \\ -l_1 \cos(\theta_0) \end{bmatrix} \tag{4.4}$$

To calculate the rest of the joint position, we have for $i = \{1, ..., 4\}$

$$P_{J_{i+1}} = P_{J_i} + l_i \frac{P_{J_{i-1}} - P_{J_i}}{l_{i-1}} \begin{bmatrix} \cos(\theta_i) & -\sin(\theta_i) \\ \sin(\theta_i) & \cos(\theta_i) \end{bmatrix} \tag{4.5}$$

To calculate pantograph spring force/constrain we can find the length of panto based on kinematic of robot and we have:

$$F_P = \begin{cases} K_P(l_P - l_2 \frac{l_P}{\|l_P\|}) & \|l_P\| > l_2 \\ 0 & \|l_P\| \leq l_2 \end{cases} \tag{4.6}$$

$$T_1 = F_{GRF} h_1 \quad , \quad T_1 = F_{GS} R_{J_1} - R_P \times F_{PS} \tag{4.7}$$

$$T_2 = F_{GRF} h_2 \quad , \quad T_2 = F_{GS} R_{J_2} + R_P \times F_{PS} \tag{4.8}$$

$$T_4 = F_{GRF} h_4 \quad , \quad T_4 = F_{GS} R_{J_4} + F_{DE} R_{J_{4DE}} \tag{4.9}$$

Global spring force is depend on deflection of global spring and we can show it as follow:

$$\begin{aligned} F_{GS} = k_{GS} \Delta x_{GS} = k_{GS}(&R_{j_1}(\theta_{1_0} - \theta_1) + R_{j_2}(\theta_2 - \theta_{2_0}) \\ &+ R_{j_3}(\theta_3 - \theta_{3_0}) + R_{j_4}(\theta_4 - \theta_{4_0})) \end{aligned} \tag{4.10}$$

For DE tendon, we also have

$$\begin{aligned} F_{DE} = k_{DE} \Delta x_{DE} = k_{DE}(&R_{j_{3DE}}(\theta_3 - \theta_{3_0}) \\ &+ R_{j_{4DE}}(\theta_4 - \theta_{4_0})) \end{aligned} \tag{4.11}$$

Also, from triangle similarity we have.

$$\frac{h_1}{h_2} = \frac{l_{1_1}}{l_{1_2}} \tag{4.12}$$

Then from dividing Eq. (4.7) and Eq. (4.8) we have:

$$\frac{T_1}{T_2} = \frac{h_1}{h_2} = \frac{l_{1_1}}{l_{1_2}} \tag{4.13}$$

Using fraction algebra we can add numerator to delimiter and have:

$$\frac{T_1}{T_2 + T_1} = \frac{l_{1_1}}{l_1} \tag{4.14}$$

With same argument we can have:

$$\frac{T_1}{T_4 + T_1} = \frac{l_{14_1}}{l_{14}} \tag{4.15}$$

By replacing Eq. (4.7), Eq. (4.8) and, Eq. (4.9) into Eq. (4.14) and Eq. (4.15) we have

$$\begin{aligned} l_{1_1} &= \frac{l_1 F_{GS}(R_{J_2} + R_{J_1})}{F_{GS} R_{J_1} - R_P \times F_{PS}} \\ l_{14_1} &= \frac{\|P_4 - P_1\| \, F_{GS}(R_{J_2} + R_{J_1}) - R_P \times F_{PS} + F_{DE} R_{J_{4DE}}}{F_{GS} R_{J_1} - R_P \times F_{PS}} \end{aligned} \tag{4.16}$$

with defining l_{1_1} and l_{14_1} length we can calculate direction of F_{GRF} as follow

$$\begin{aligned} P_{GRF_1} &= \frac{P_{J_4} l_{14_1} + P_{J_1}(l_{14} - l_{14_1})}{l_{14}} \\ P_{GRF_2} &= \frac{P_{J_2} l_{1_1} + P_{J_1}(l_1 - l_{1_1})}{l_1} \\ \hat{F_{GRF}} &= \frac{P_{GRF_2} - P_{GRF_1}}{\|P_{GRF_2} - P_{GRF_1}\|} \\ \alpha_{GRF} &= \tan^{-1}\left(\frac{\hat{F_{GRF_y}}}{\hat{F_{GRF_x}}}\right) - \frac{\pi}{2} \end{aligned} \tag{4.17}$$

To calculate $F_{GRF} = \|F_{GRF}\| \, \hat{F_{GRF}}$ we have unit vector,$\hat{F_{GRF}}$ and we need to calculate $\|F_{GRF}\|$ which is:

$$\|F_{GRF}\| = \frac{T_4}{h_4} \tag{4.18}$$

and h_4 can calculate as:

$$h_4 = \hat{F_{GRF}} \cdot (P_{GRF_1} - P_{J_4}) \tag{4.19}$$

The last parameter we need to calculate is CoP

$$CoP = \frac{h_4}{\cos(\alpha_{GRF})} \tag{4.20}$$

For leg length and leg angle we have:

$$\begin{aligned} LL &= sqrt((X_{J_4} + CoP - X_{J_0})^2 + (Y_{J_4} - Y_{J_0})^2) \\ \alpha_{LL} &= \tan^{-1}\left(\frac{Y_{J_0} - Y_{J_1}}{X_{J_0} - CoP - X_{J_1}}\right) - \frac{\pi}{2} \end{aligned} \tag{4.21}$$

Robot property and subsystems Robot component mass are as follow:

Part	Mass [g]	Part	Mass [g]
Robot	1200	S1	32
Trunk	980	S2	39
Leg	110	S3	19
Actuator	165	S4	11
Force sensor	20	S5	9
Tendon force sensor	1		

4.5 Results

In this section, we show the result of experiments to show the performance of the disengagement mechanism.

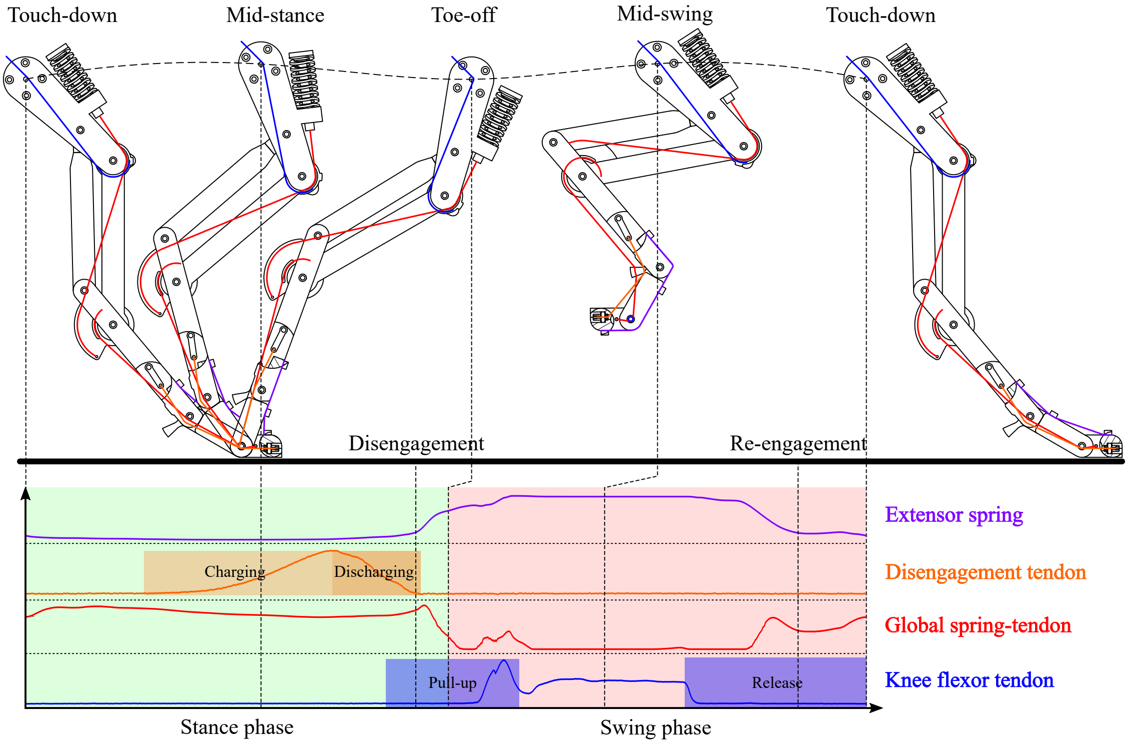

Figure 4.4: Leg phases during the gait cycle and corresponding tendon activation during locomotion. Touch-down) the gait starting point with the leg touching the ground all tendons except the global tendon are slack. Mid-Stance) hip torque moves the leg forward, and the global tendon bears the load of the leg. The DE tendon starts charging. Toe-off) leg start to leave the ground. DE tendon discharge and clutch the global spring, knee motor start flexing the knee joint and lift the leg. Mid-Swing) the knee is at maximum flexion, the global tendon is unloaded, and the knee motor starts to release the leg to start the next touch-down.

leg phases Each robot leg has different phases during locomotion, and due to the CPG parameter necessary for locomotion, the right and left leg have a 50 % phase shift in a gait cycle. In Fig. 4.4 all these phases show, we describe each leg sub mechanisms functionality during each phase.

Stance phase breaking: this phase starts from the moment the leg touches the ground till mid-stance. During this phase, the global spring charges and converts the robot's potential and kinetic energy into spring potential energy. Global spring also passively provides the force in the direction of leg length, so the robot does not need to apply any knee torque via motor. It is a clear advantage of PA leg in comparison to conventional robots. This phase will continue till the mid-stance when the global spring reaches maximum deflection. Therefore, leg loading gets to the maximum.

Stance phase push-off: this phase starts from the mid-stance till the leg loses ground contact. All the energy stored in the global spring will discharge into the system during this phase and provide a push-off for the leg. By matching CPG parameter to the natural dynamic of the robot (e.g., matching the given and observed duty factor), we can use global spring energy to extend the leg and make the leg ready for the flight phase without applying knee torque. Spring discharge will reduce the hip torque required for pushing the robot body forward (Fig. 4.6). This phase will continue till the foot loses ground contact.

Disengagement: DE phase overlaps with the stance phase and the beginning of the flight phase. Disengagement is the most significant phase of these types of leg design. During disengagement, the DE tendon wraps around cam5 while the leg rotates forward. As a result, the tendon will extend and store energy. The source of this stored energy is the forwarding motion of the robot. DE tendon force increases as the leg get to the end of the stance phase due to the lean forward orientation of the leg and reduced GRF. DE tendon force applied on cam4DE will push the J3 out of the locked position. As a result of this snapping of J3 from its hard stop. Global spring-tendon will be disengaged, and the knee motor can lift the leg and start the swing phase without working against global spring.

Knee pull up: At the end of the stance phase, the knee motor via a cam and tendon will flex the knee joint and create enough leg clearance to swing the leg forward and start the next gait cycle. The ideal case for pulling the knee up is after DE happens, then the leg can be lifted and provide enough ground clearance without too much knee motor energy consumption. However, lifting the leg after the DE is complete can cause the robot to fall to the ground, especially if there is no double stance phase. Therefore, we usually pull the knee-tendon before disengagement is complete to avoid this situation. By doing so, it is a trade-off between successful locomotion and consuming more knee motor power.

Swing phase: this phase starts from the moment that leg is losing ground contact till the leg establishes ground contact again. During the swing phase leg need to provide ground clearance to avoid a ground collision before the leg does the full swing forward. In this phase, both the global and the DE tendons are relaxed. The knee motor holds the leg up until the end of the swing phase. Then, the knee releases the leg and establishes ground contact.

Knee release: happens at the end of the swing phase that the knee motor unwraps its tendon, and due to the gravity effect and angular momentum of the leg created during the swing forward, the leg will extend and gets ready for the next gait cycle.

Leg engaging: happens at the end of the swing phase and coincides with passive knee extension. During leg engagement, the knee extends and provides slacking into the global tendon. Soft extensor springs extend J3 and J4. By doing so, the global spring engages, and the robot can start the next stance phase.

Disengagement angle DE tendon is an angular constraint between J3 and J4 and guarantees disengagement at a certain angle of the virtual leg. However, due to loading on leg charging of tendon varies under different gait parameters, we expect different behavior from the tendon at different speeds. In Fig. 4.5 we measure the virtual leg angle at disengagement for three different gait frequencies of 0.5 Hz, 1.0 Hz and 2.0 Hz and two amplitudes of 30 deg and 40 deg, for cases, with and without DE tendon, and plot the result over virtual leg length. We can see by increasing speed, the virtual leg angle at disengagement is reducing. Another observation is that leg length increases at disengagement by increasing hip amplitude for a given gait frequency. Also, disengagement happened in a shorter leg angle range for cases with no DE tendon.

Torque requirement Comparing BB2 robots with and without DE tendons gives us a better understanding of actuator torque requirements and robot performance. Figure 4.6 shows that a robot without a DE tendon required larger hip torque than a robot with a DE tendon. At low speed, none DE tendon version has a peak torque of 1.32 Nm during stance, which is 37 % higher than the version with DE tendon. There is not much difference in hip torque at intermediate speed for cases with and without DE tendon. However, again at high speed, no DE tendon version has a peak hip torque of 2.51 Nm during stance, which is 103 % higher than the version with DE tendon.

In the leg without the DE mechanism, we do not coordinate the disengagement of the global spring. Hence, leg disengagement happens either via leg orientation or force disengagement via knee flexing motion. Combined with speed change, these cases cause a random behavior for knee torque. However, we can observe two main peaks in knee motor torque. The first peak coincides with disengagement (either force or with DE tendon), and the second is for pulling the leg up to the most flex position. The first peak at low and

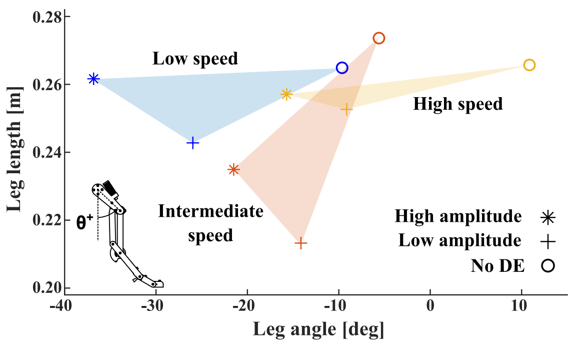

Figure 4.5: leg angle versus leg length at Disengagement point for three sets of low, medium and high speed

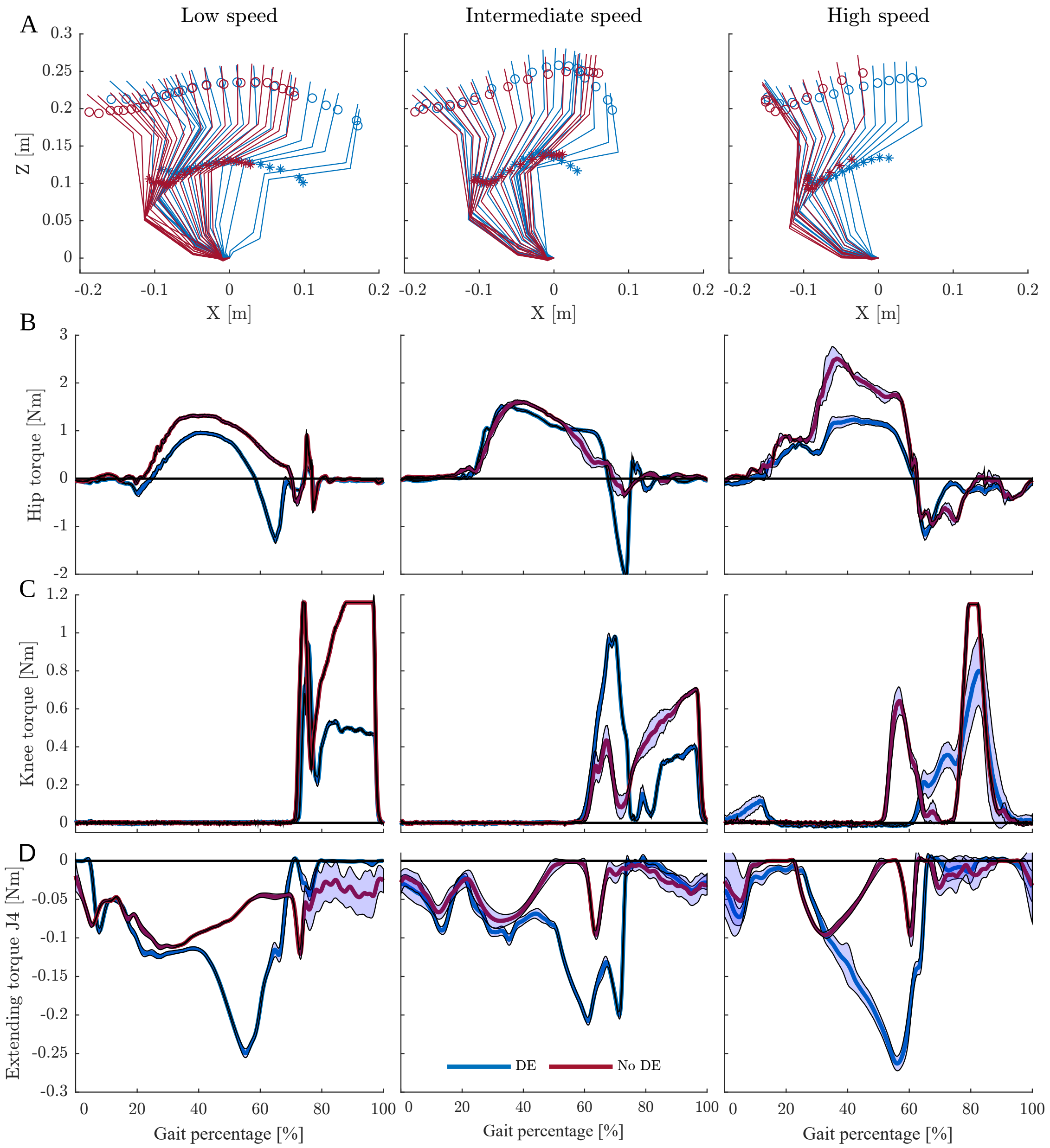

Figure 4.6: **(A)**Leg kinematics and center of mass motion, for cases with and without DE mechanism. **(B)**Comparing hip torque for the case with and without DE tendon at the low and high speeds. Increase in hip torque for the case without DE mechanism at the stance phase. **(C)** knee torque for the case with and without DE tendon at low and high speeds. **(D)** Extending torque at J4 create via Tendons

intermediate speed is visible around 1.0 Nm for the robot with DE tendon. By increasing speed and entering the flight phase, the first knee torque peak decreases to 0.36 Nm and merges into the second peak for the robot with DE tendon. In a robot without DE tendon at the low-speed first knee torque peak is around 1.2 Nm due to force disengagement. At intermediate speed knee peak torque drops to 0.5 Nm due to auto disengagement. Again peak rises to 0.64 Nm for high speed due to force disengagement. Meanwhile, knee torque second peak for the robot with DE tendon at low speed is around 0.53 Nm. This torque is the holding torque of leg mass during the swing. For intermediate speed second peak drop to around 0.5 Nm, the reduction is due to the speed of gait motor cannot flex knee completely, so the holding torque is smaller than low speed. At high-speed gait, the second knee torque peak is around 0.8 Nm, an increase in knee torque caused by fast flexing of the leg. Peak caused by dynamic flexing of the leg is larger than holding leg inertia torque at the lower speed. The second peak for the experiment without a DE tendon is much higher than with a DE tendon. For the low-speed case, the knee torque at the second peak saturated the sensor due to exceeding the limit of knee torque. The reason for that is the knee motor and global spring co-contract the knee joint and cause huge knee torque in comparison with the case with the DE tendon. In intermediate and high-speed gait, the second peak for the case without DE tendon is much higher than the one with DE tendon due to partial co-contraction.

Power amplification One key task of the DE tendon is to store locomotion energy during the stance phase and release that energy at the end of the stance phase. The ratio of the charging time of the flexor tendon (DE tendon) to discharging time of flexor energy is a metric for power amplification.Figure 4.7 shows a DE tendon amplifies power by 1.3, 2.1 and 1.7 for low, intermediate and high speed gaits, respectively. Disengagement tendon power amplification helps reduce hip and knee motors peak torque during stance and maintain total locomotion energy at lower level. Power amplification is the source of energy efficiency in the leg compared to other leg designs without a passive push-off. As shown in Fig. 4.6, more mechanical energy recuperate back into the gait cycle for the case with the DE tendon. Also, this recuperated energy can help achieve a lower cost of transport and higher speed.

Center of mass behavior As shown Fig. 4.6, the robots without DE tendon have more vertical center of mass oscillation. It means we break and accelerate the robot more than if it has DE Tendon. It means, we lose energy during locomotion, and robots need to provide the energy via the hip actuator.

Cost of transport We measure BB2's cost of transport in configurations with and without the disengagement mechanism. Figure 4.8 shows the ratio of BB2's COT versus the COT of a natural runner of the same mass. The resulting relative COT allows us to compare our robot to other, state-of-the-art legged robots.

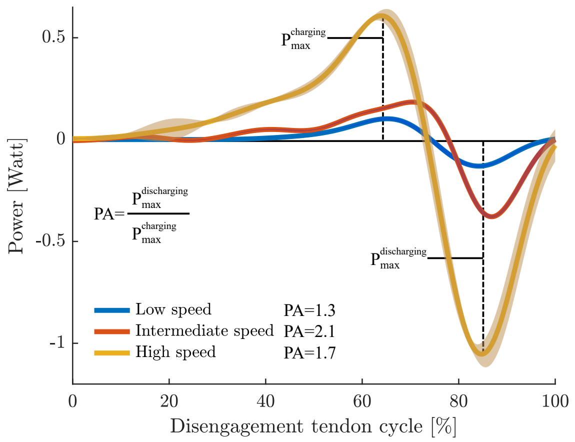

Figure 4.7: Power amplification of leg in case of with DE tendon for three cases of low, intermediate and high speed

Configuration BB2-1DE BB2 shows a relative COT of 86 % and 123 % for configurations with and without the disengagement mechanism. Hence, adding the disengagement mechanism decreases the robot's COT by 30 %. Compared to a robot with a fixed, parallel leg elasticity (Cheetah-cub), BB2 shows an over four times improved relative COT. Figure 4.8 indicates that BB2-1DE's reduced power consumption is caused majorly by a knee power reduction, compared to BB2-0DE.

Configuration BB2-0DE Without the support from the disengagement tendon, the foot segment of BB2-0DE only partially disengages the leg's parallel elasticity into the swing phase. As a result, the knee flexing motor work against the parallel elasticity in swing, which increases the robot's energetic cost (Fig. 4.8). This effect depends on the robot's locomotion speed. At low-speed locomotion, foot segments are insufficiently flexed, and have an incomplete disengagement. At intermediate speeds, self-disengagement is observed. At high-speed locomotion, we observe incomplete disengagement, likely because of the brief contact time, with high leg loading. At high-speed locomotion, early toe-off is observed, where the leg is not yet at its proper self-disengagement angle. Hence, we record a higher COT at low and high locomotion speeds. At intermediate locomotion speeds, self disengagement is observed, resulting in a lower knee flexing torque with lower power consumption (Fig. 4.6).

4.6 Discussion

Disengagement angle To achieve higher speed with lower power consumption, we need to have concise timing between disengagement of parallel elasticity and knee pull-up, but we also need to define a good Disengagement angle. Recuperated energy can not

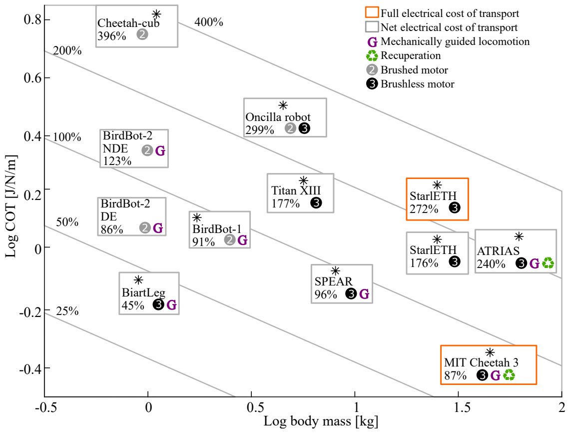

Figure 4.8: Cost of transport (COT) of BB2, for configuration DE-off and DE-on, compared to state-of-the-art legged robots. The diagonal, 100 %-line is Tucker's COT line for natural-runners (animals), which we converted with the following equation $\log_{10} y = -0.3138 \log_{10} x + 0.2346$ into its logarithmic scale. This line presents the ratio of robot COT versus animal COT of the same mass. BB2 in configuration DE-on shows a better performance compared to BB2 without DE-tendon. BB2 shows the most energy-efficient, compared to other bipedal and quadrupedal robots, in terms of normalized COT. References for robots shown: [218, 217, 207, 210, 120, 103, 99, 129, 192, 28].

help the body push-off or knee flexing during the swing phase if the leg is fully unloaded at the disengagement point. So the more we go toward higher leg length on Fig. 4.5 the possibility of passive push-off is reduced. With the same argument, the more we go toward a positive leg angle at disengagement, the leg has more possibility of push-off since the leg is more loaded. Early push-off means an early flight phase and more vertical oscillation than forwarding motion for the high-speed gait. Fig. 4.6(A), shows that center of mass oscillation is higher for the case without DE tendon compare to the case with DE tendon. This is one of the reasons speed was reduced for cases without DE tendon at higher speeds than cases with DE tendon.

Another aspect of the study is to look into the effect of hip amplitude. With increasing hip amplitude, virtual leg angle variation is also increasing. The chance of full disengagement without the help of the motor increases, so the energy required for leg pull-up decreases. As a result, we can achieve higher speed and lower consumption. In addition, we have lower leg angle and higher leg length at disengagement due to geometry for cases with higher hip amplitude, which means the leg is closer to resting length.

Torque requirement Hip torque is a function of joint angle during stance. If we assume zero mass for leg segments. The leg length of the robot is coupled to leg extending mechanisms: 1) global spring and pulley system, which is passively extending the leg. 2) pantograph spring, when it is activated, makes the leg shorter. 3) DE tendon, which

Table 4.1: Result measurement summary table

Parameter	Unit	Value		Improvement in %
		No DE	With DE	
hip torque peak at 2.0 Hz	Nm	2.51	1.23	103
hip torque peak at 0.5 Hz		1.32	0.96	37
knee torque DE peak at 0.5 Hz		1.16	0.94	24
knee torque DE peak at 2.0 Hz		0.64	0.36	80
knee torque swing peak at 0.5 Hz		>1.16	0.53	>117
knee torque swing peak at 2.0 Hz		1.15	0.80	44
DE peak power charging 0.5 Hz	J/s	-	0.10	-
DE peak power charging 1.0 Hz		-	0.18	-
DE peak power charging 2.0 Hz		-	0.61	-
DE peak power discharging 0.5 Hz		-	0.13	-
DE peak power discharging 1.0 Hz		-	0.38	-
DE peak power discharging 2.0 Hz		-	1.05	-
COT (1.5 Hz)	J/J	2.05	1.43	30
speed at 0.5 Hz	m/s	0.24	0.28	17
speed at 1 Hz		0.47	0.46	-2
speed at 2 Hz		0.88	1.13	28

by extending the tendon increases the moment at J3, decreases global spring tension, and then causes leg extension.

Leg equations show that decreasing the leg length for a given leg angle requires less hip torque. When the DE tendon is removed the extension torque at J3 is reduced. Also when we remove the DE tendon, both ground reaction force and angle will change to reduce hip torque. These effects cause the torque required for driving the hip to decrease, and from the result, we can see that we have a reduction between 37% to 103% during the stance phase. Removing the DE tendon introduces co-contraction between the knee motor and global spring during leg pull-up, which causes the knee motor to apply more than double the torque necessary for the leg pull-up compared to the robot with the DE tendon.

To discuss the effect of the knee torque for the case with the DE tendon at the different speeds, we can observe that we generally have two main peaks (Figure 4.6(C)), which, by increasing speed, these two peaks will merge into each other. The first knee peak torque is caused by co-contraction of the knee with global spring during disengagement. The first knee peak torque for low and intermediate speed is roughly around 1 Nm, but for high speed, due to leg disengagement due to flight phase peak is reduced to 0.4 Nm. The knee second peak torque is caused by the leg dynamic, which is required to lift the minimum knee angle and hold it at the position for a portion of the swing phase while the leg is retracting. Figure 4.6(C) shows for the low-speed gait. The second knee peak torque is at 0.53 Nm, which is bigger than 0.36 Nm second knee peak torque for intermediate speed. The reason is at the low-speed motor has enough time to shorten the leg, but at intermediate speed, due to short retraction time motor is not able to flex the knee completely, and the second knee peak torque is lower. However, the duration of the second knee peak torque for high speed gait is even shorter, and since the error in the knee position controller increases, it provides sudden torque to flex the knee, then we have a knee peak torque around 0.8 Nm.

Power amplification as shown in Fig. 4.7, the DE tendon charge slowly during the stance phase and release the energy in a short period of time to snap J3 and clutch the global spring tendon. The power amplification in the DE tendon helps reduce hip torque in steady state locomotion and maintain locomotion energy. As a result, reducing peak hip torque reduces by the hip motor to vault the leg forward and reduces knee torque for lifting the leg. Power amplification depends on stance charging and discharging time and loading. Based on Fig. 4.7 at the low speed, we ham symmetrical loading and unloading. As a result, PA= 1.3 (close to 1) and as speed increases, tendon charging time increases and discharging time decrease as a result for we have PA=2.1 for intermediate speed. As speed increases, we have a flight phase, which means the leg is unloaded via robot dynamic. As a result, DE tendon charging reduces, and the timing between charging and discharging changes. We observed a decrease in power amplification for high speed to PA=1.7. Although DE tendon helps reduce locomotion energy via power amplification in all cases.

Cost of transport BB2 reduces power through passive recuperation through global spring, Pantograph spring, and DE tendon. Global spring reduces the necessity of the knee actuator during the stance phase, and DE tendon and pantograph spring provide push-off at the end of stance and help the hip motor to generate less power for swinging the leg forward and less knee power to pull the leg up. Although DE tendon positively affects locomotion via amplifying power during the stance and releasing it at the end of the stance. The other effect of the DE tendon is to clutch the parallel elasticity and help the leg freely start the next cycle and have more leg retraction angle, and as a result, the robot achieves higher speed. Combining this two behavior gives us a better COT for the robot equipped with a DE tendon. Fig. 4.8 shows a 30 % reduction in the cost of transport with respect to natural-runner data.

Chapter 5

Effect of flexor tendon on the performance of front and hind legs in quadrupeds

5.1 Contribution

Major indicates a contribution, without which the paper would probably not have been submitted.
Substantial contribution increase chance of acceptance.
Minor contribution improved the paper but did not significantly change the form or content.

Author	Author position	Scientific ideas	Data generation	Analysis & interpretation	Paper writing
Alborz Aghamaleki Sarvestani	First	Major	Major	Major	Major
Robin Petereit	Second	Minor	Major	Substantial	Minor
Alexander Badri-Spröwitz	Last	Major	Minor	Substantial	Substantial
Title of paper		Effect of flexor tendon on performance of front and hind legs in quadrupeds			
Status in publication process		In preparation for submitting to Nature Communication			

Thesis author contribution based on [1].

Alborz Aghamaleki Sarvestani: conceptualization, methodology, software, validation, formal analysis, data curation, writing - original Draft, visualization.

Content of this chapter is largely based on the below paper:

1. Aghamaleki Sarvestani*, A., Petereit, R., Badri-Spröwitz, A. RoboManul: Quadrupedal Robot with Passive Disengagement Mechanism for Efficient Locomotion. *In preparation* for **Nature Communication**

5.2 Abstract

Some animals have less mobility in their distal joints for the hind leg compared to the front leg. For example, studies show that the hind leg distal joint can have 50 % less motion during trot gait than the front leg distal joint. This difference is rooted in the development of flexor muscle at distal joints. To show the different functionality of flexor muscles in the front and hind legs, we designed an experiment to measure the performance of a robot with a leg similar to mammalian leg morphology. Then, we simplified all flexor muscles with high stiffness tendon called DE tendon and measured the performance of our quadruped robot, RoboManul, with and without this DE tendon.

We increased robot speed by 56 % under the same gait parameter by adding the DE tendon. At the same time, we also reduced input power by 60 %. The speed and power improvement resulted in the reduction of CoT by 22 % compared to the robot without the DE tendon. However, adding the DE tendon increases the performance of the front leg. The front leg recuperates energy 90% more than the hind leg in walking scenarios. In addition, trunk pitch-down and front leg load more and allows the front leg DE tendon to store more energy compared to the hind legs.

5.3 Introduction

Asymmetric front and hind leg in addition to hip torque cause pitch motion in the trunk during locomotion. Trunk pitch motion is an unwanted source of energy loss [219]. Most of the optimization algorithms for path planning of quadruped robots try to minimize body pitch, narrowing the range of acceptable trajectory and increasing robot speed and efficiency.

Recently, a new robotic leg design was developed [21] that includes a passive distal mechanism similar to what we observe in avians and mammals. With the help of this robotic setup, we can take a deeper look into the functionality of the distal mechanism in quadruped with respect to other parameters during locomotion, such as hip torque, weight distribution, and asymmetric front and hind leg design.

To explain the functionality of the distal leg mechanism in quadrupeds, we simplify the leg and keep the necessary part of the complex leg. In this study, we use a quadruped robot with a newly designed leg mechanism [21](Fig. 5.1). We test the robot under two different scenarios. The first scenario is a leg with a disengagement tendon that acts as a flexor muscle during foot roll-over. The second scenario is a leg without a disengagement tendon. We test the robot in three different gait frequencies for each scenarios. Then we measure the speed and motor consumption of each scenario. Finally, based on the power consumption of the motor and DE tendon activation, we evaluate the performance of the front and hind legs. And the necessity of a disengagement tendon in the leg for the quadrupedal scenario.

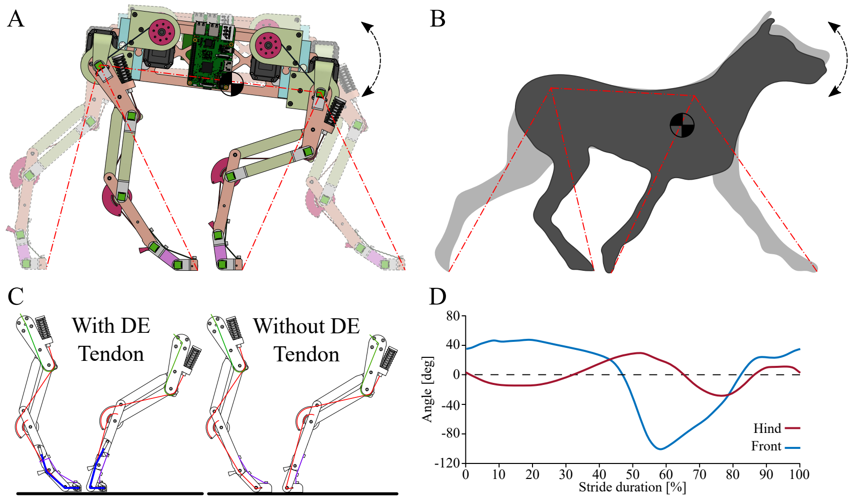

Figure 5.1: **(A)** Quadruped robot in trot has a wider stance angle for the front leg than the hind leg. **(B)** Dog has a wider stance angle for the front leg rather than the hind leg, and foot joint range for front legs is wider than hind legs. [72] **(C)** Leg with and without DE Tendon (blue tendon) **(D)** Foot joint angle for front and hind leg of dog during trot [134]

5.4 Methods

Robot Structure: RoboManul consists of four identical legs and a trunk Fig. 5.2. Each leg has five segments, five revolute joints and one spring-loaded parallel pantograph segment that keep segment one and segment three parallel under no-load scenarios. Each leg connects to the hip motor (Dynamixel, MX-64 AT). The knee joint connects through a fixed pulley and a tendon to the knee motor (Dynamixel, MX-64 AT). The knee motor can flex the knee joint. All robot joints except the hip coordinate passively via the global spring and tendon system. This tendon allows the robot leg to load passively without consuming energy. At the robot foot, we have the flexor disengagement tendon (DE tendon), which connects on one side to segment three and, after wrapping around joints 4 and 5 connects to the set screw at segment 5. This tendon acts as a charging spring which can recuperate locomotion energy back to the leg, especially at the end of the stance phase. The DE tendon also acts as a clutch activation to disengage the global spring and lift the unloaded leg to flight phase Fig. 4.4. Besides the DE tendon at the robot foot, we have two elastic latex band springs that flex joints 4 and 5 at all times. The purpose of this tendon is to passively engage the global spring as knee joint extends.
Instrumentation: RoboManul has several sensors to measure the performance of the leg during the experiment. Each leg has five 16-bit magnetic rotary encoders (AEAT8800-Q24) to measure each joint angle. Each leg has three force sensors, two of them measure the torques of the hip and knee motor, and one tensile force sensor measures tension in the DE tendon. Besides this force and position instrumentation, the robot uses a current sensor (ACS723) to measure the input power of each motor separately and one

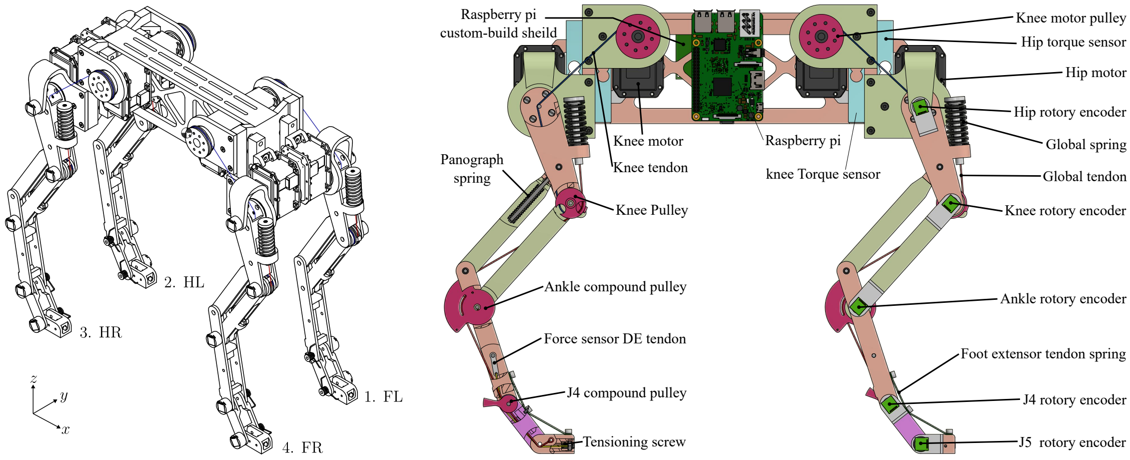

Figure 5.2: Schematic of RoboManul with all components.

rugged IMU (VN-100) to measure trunk movement. All force sensors are read via a custom-built shield for the Itsybitsy microcontroller that communicates all data to the onboard computer (Raspberry Pi 4+). All encoders and the IMU data are read directly via a custom-built Raspberry Pi shield. The onboard computer has the responsibility to communicate with motors via a U2D2 converter.

Software: RoboManul software runs on the host computer and onboard computer. A Python base GUI on the host computer helps the users can set the gait parameters and observe the online data from the sensors. Users can also save experiment results into JSON files for further process in other programs. The onboard computer is a Raspberry Pi 4 B which runs low-level codes for reading from different sensors on the robot and receives actuator trajectory from the host computer to send to motor drivers. The onboard

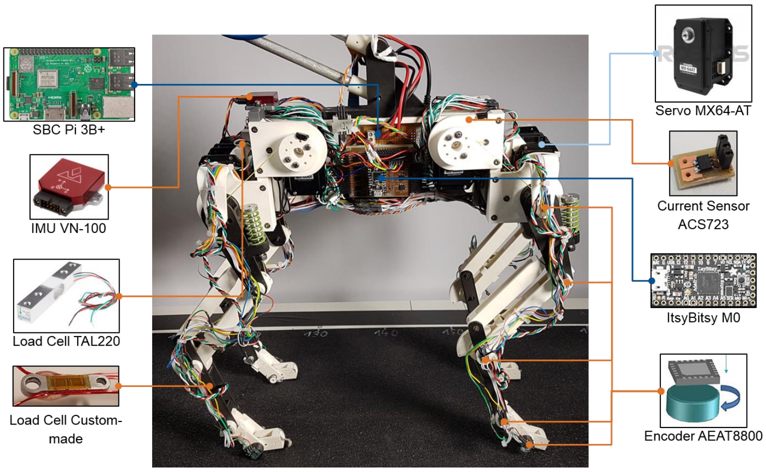

Figure 5.3: RoboManul sensors to measure the performance of robot [160].

computer sends the sensors and motors data back to the host computer for saving and further post-processing.

Gaits and Motion Control: We send a feed-forward position command to the hip and knee motor for the robot to generate trot gait [112, 207]. We can set CPG parameters such as gait frequency, hip amplitude, knee amplitude, knee offset, hip phase shift and knee phase shift via python GUI on the host computer. Later generated patterns are sent to the onboard computer to be applied on the robot actuators. To generate trot gait we use $C = \begin{pmatrix} 0 & 0 & 0 & 0 \\ 1 & 0 & 0 & 0 \\ 1 & 0 & 0 & 0 \\ 1 & 0 & 0 & 0 \end{pmatrix}$ as a coupling matrix and $\varphi = \begin{pmatrix} 1 & 0 & 0 & 0 \\ 0 & 0 & 0 & 0 \\ 1 & 0 & 0 & 0 \\ 0 & 0 & 0 & 0 \end{pmatrix}$ as phase shifts matrix in CPG equation presented in Sec.2.6. A CPG output trajectory for one stride is shown in Sec.2.6.

Experiments: To measure the performance of the DE tendon in the front and hind leg, we design two sets of experiments. The first set robot has a disengagement tendon and in the second set, we remove the disengagement tendon. Then we measure joints angle, tendon forces, motors' torque and power of the robot. To identify the effect of robot dynamic and leg loading on the performance of the passive DE mechanism for each set, we measure 15 strides of the robot at three different gait input frequencies of 1.0 Hz, 1.1 Hz and 1.5 Hz.

In order to perform continuous walking of the robot and record multiple strides of robot data, we put the robot on a treadmill with a linear guide and harness that allows the robot to move and rotate in the sagittal plane. The experiments were recorded with a high-speed camera (Mirolab 110) with 400 fps.

Energetic Energy efficiency is one of the important principles in nature and robotics. One of the governing parameters in the evolution of animals is to evolve in order to have minimal consume food. Also, in robotics in almost all mobile platforms such as wheeled and legged robots having minimum energy consumption is always one of the goals for designers due to limitations for battery size and weight [29]. In legged robotics, over years and years of research, there was a different variation of leg design proposed and used in legged robots. One way to classify these leg designs is by the number of segments and actuators in each leg and the methods of connectivity of these segments and actuators. The simplest leg type is one rigid segment with a hip actuator [38]. Another type of leg is a two-segmented leg with a prismatic [32] or hinge joint [95] for the knee. This configuration has an active hip joint actuator and can have three variations active [201], passive with compliance [95] and one-directional active flexion with passive extension [209, 209] for knee joint actuation. Another type of leg is the three-segmented leg in this leg design three segments connect with hip, knee and ankle joints together. In this design ankle joint angle is coupled to knee joint angle in 3 different methods: first with fix gastrocnemius-like muscle give one-to-one relation between knee and ankle

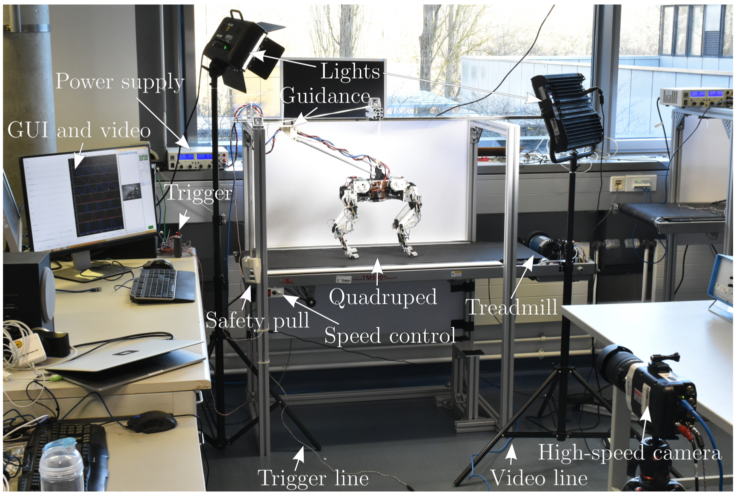

Figure 5.4: RoboManul experimental setup including the instrumented robot, host computer, tradmill and high-speed camera to measure the performance of robot during the experiment [160]

.

angle [191]. Second with gastrocnemius-like linear compliance give a bit more freedom to ankle to recuperates impact energy to the leg [207, 192]. Each of these designs has some shortcomings in energy efficiency. Full actuate systems during the stance phase need to actively apply torque to hold the robot standing, which means when the robot consumes energy in idle mode. On the other hand, leg design with knee compliance is efficient during stance because the spring will hold the whole robot's body weight, but during the swing phase, the same spring work against the knee motor, which wants to provide foot clearance and cause huge power loss. The new proposed leg design [21] combines the advantages of previous leg designs. By introducing a leg length compliance disengagement mechanism to the leg design, it becomes possible to switch off the leg length spring at the end of the stance phase and start the swing phase without having the spring work against the knee motor. This mechanism shows its efficiency in bipedal robots (Chapter 4). In biped robots because of symmetrical gait input and similar locomotion parameters for both legs, Biped has a symmetrical loading for left and right legs, but in quadruped robots weight distribution, gait parameter and trunk pitch cause different loading for front and hind legs [70]. DE mechanism performance depends on the loading of the leg. So there are two questions raised that we need to answer. First, does DE mechanism in front and hind leg quadruped contribute equally, and If so, how much quadruped robot locomotion efficiency improvement is caused by the DE tendon mechanism? One of the ways to show the energy efficiency of the quadrupedal robot is to calculate the cost of transport of the robot[218]. Cost of transport is a non-dimensional value representing the energy consumption of the system as:

$$COT = \frac{W}{mgd} = \frac{P}{mgv} \tag{5.1}$$

Where W is work, P is Power, m is mass of the robot, g is gravitational acceleration, d is displacement of robot and v is speed of robot. This value unit can be: [j/N.m], [cal/cal]. For a quadrupedal robot this equation can be reformulate as:

$$COT_{Mechanical} = \frac{\sum(\mathrm{T}_{Motors}\theta)}{mgd} = \frac{\sum(P_{Motors}\omega)}{mgd} \tag{5.2}$$

Which T_{Motors} is the output torque of the motor, θ is the angular displacement of each motor, P_{Motors} is the output power of the motor and ω is the angular velocity of the motor. COT can also calculate based on robots' consumed electrical energy, which is more similar to metabolic COT for animals. Metabolic or electrical COT can reformulate as:

$$COT_{Electrical} = \frac{\sum(V_{Motors}I_{Motors})}{mgv} \tag{5.3}$$

Which V_{Motors} is supply voltage of motor, I_{Motors} is coil current of each motor.

Tucker calculated metabolic COT for various animals and classified them into several subgroups such as runners, swimmers, and fliers. He also shows a logarithmic linear relation between mass and COT for the natural runners[218]. Seok et al add robot COT to Tucker curve[201]. The percentage of robot COT to the natural runner of the same mass is a meaningful value to compare the efficiency of robots with each other because we completely omit the effect of mass from energy consumption.

Based on the second law of thermodynamics, $COT_{Electrical}$ is always bigger than $COT_{Mechanical}$ because all input energy to the system cannot be less than all output energy in the system.

$$P_{Input\ motor} = P_{Mechanical} + P_{Joule\ heating} = \mathrm{T}\omega + RI^2 \tag{5.4}$$

Where $P_{Input\ motor}$ is the total input electrical power to the motor. $P_{Mechanical}$ is the output mechanical power of the motor. $P_{Joule\ heating}$ is joule heating and power loss in motor coil(s).T is the output torque of the motor. ω is the output angular velocity of the motor. R is coil resistant and I is coil current. Roos shows that we always have mechanical losses in motor gearbox system because of accelerating inertia of motor shaft and gearbox, also we have electrical loss due to joule heating of coil in motor[181]. Roos framework shows that to achieve the optimum energy consumption for the robot motors we need to optimize the combination of the motor parameters (select appropriate motor) and gearbox ratio and effective inertia. To have an optimal system efficiency, we should choose optimal gearbox and motor combination for the desired leg loading.

In this chapter, we first show the mechanical design of the quadruped and explain the DE mechanism of the leg. Then, we describe how the robot works in the different phases of locomotion and the feed-forward CPG network for motor control. We also show the electronic system that we use for sensing, recording joint angles, motor torques, tendon and spring forces and motor input current of the robot. Later we show software communication for sending orders to motors and also receiving all measured data from the robot on the control computer. Then we design experiments and procedures to evaluate robot DE mechanism performance and COT on variate of speed and also a calculation for optimizing motor and gearbox combination to have optimal COT, to full fill goals of this chapter. Next, we have a result and discussion section to show, post-process, analyze and discuss the results of experiments.

5.5 Results

In this section, we present experimental results for the quadruped robot for two cases with and without disengagement tendon to show the performance of the leg distal mechanism. **Hip torque:** according to Fig. 5.5 Average hip torque for front leg reduced by 39 %, 38 % and 56 % when disengagement tendon is active for gait frequencies of 1.0 Hz, 1.1 Hz and 1.5 Hz respectively. Reduction for hind leg average hip torque is 92 %, 98 % and 138 %. It means at the first part of the stance, elastic energy recuperation drives the hind leg forward as a result average hip torque change sign from negative to positive. It means hip torque that protracts the leg forward is higher than the hip torque pushing the body forward.

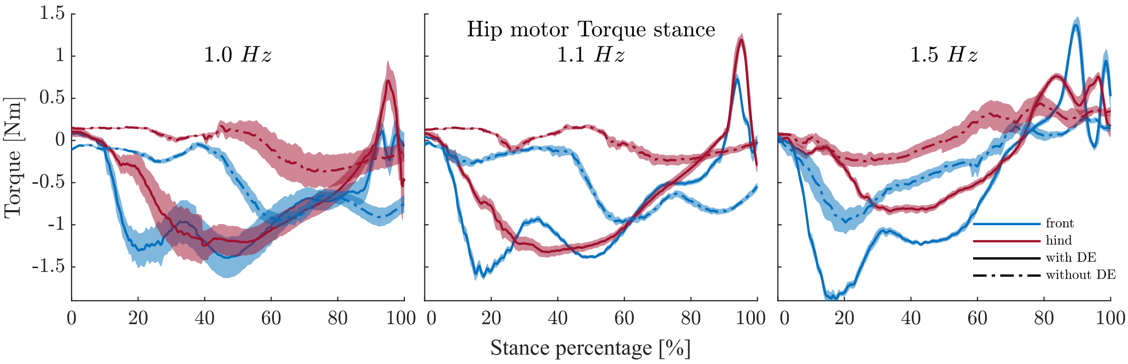

Figure 5.5: Hip motor torque during the stance phase of the robot averaged with confidence 95% for the front (solid blue) and the hind (solid red) leg for two cases with DE tendon (solid) and without DE tendon (dashed-dot).

Hip and knee power: According to Fig. 5.6 we can observe that by increasing speed, we have a reduction of power consumption in the knee motor for all scenarios. For cases with DE tendon, knee power for the front leg reduced by 56 %, 59 % and 91 % compared to the hind leg for gait frequencies of 1.0 Hz,1.1 Hz and 1.5 Hz respectively. Reduction in power for the similar parameters by removing DE tendon is 61 %, 60 % and 87 %. It shows that DE tendon reduces knee power requirement for the leg but does not change the ratio of knee power consumption for the front and hind leg. From Fig. 5.6 we can see that by increasing speed, hip power consumption for the front leg increase, but hind hip power consumption decrease. We can see a portion of hip power consumption between the hind leg and front leg was $56~\%$ to $44~\%$ for 1.0 Hz gait frequency and change to $32~\%$ to $68~\%$ for 1.5 Hz gait frequency. It means robot uses more hind hip power at the low speed for forward locomotion, but at high speed, uses more front hip power for locomotion.

In Fig. 5.6, we can see the front leg almost apply a certain amount of energy into the robot between 1.0 Hz and 1.5 Hz for both with and without DE tendon cases, but, at the same time, we can see a reduction in energy that the hind leg applies into the robot. Interestingly, by increasing speed, motors insert less energy into the system.

General disengagement via foot segmentation helps the front leg more than the hind leg. We can see more energy consume for the hind leg to flex the knee. This energy would be minimal if the DE tendon acts properly and disengages the global spring.

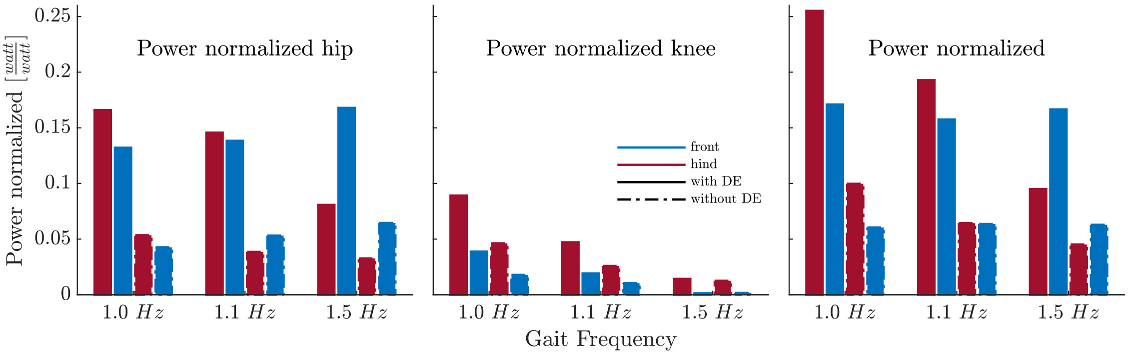

Figure 5.6: Power consumption of hip, knee and total of robot for the front (blue) and the hind (red) leg for the scenario with DE tendon (solid) and without DE tendon (dashed-dot).

DE tendon Work: DE tendon act as a reservoir of locomotion energy that charge during stance and returns that energy to the system at the beginning of the flight phase. We can see that by increasing speed from 1.0 Hz to 1.5 Hz, the ratio of the power of the front leg DE tendon to the hind DE tendon reduces from 90%to10% to 60%to40%. This number shows that the robot rely mostly on front leg disengagement more than hind leg at the lower speed. Therefore, by increasing the speed, dependency of the leg on the DE tendon for disengagement is reduced by 60 %.

Trunk pitch: When the robot applies hip torque in any direction reaction torque will pitch the trunk beside that leg forces for front and hind can also pitch the robot in the positive (upward) or negative (downward) direction. Robots with lesser body oscillation dissipate less locomotion energy. By adding DE tendon, we reduce body oscillation by 19 %, 21 % and 24 % for gait frequencies of 1.0 Hz,1.1 Hz and 1.5 Hz, respectively

(Fig. 5.7). By increasing speed, trunk pitch gets smaller.

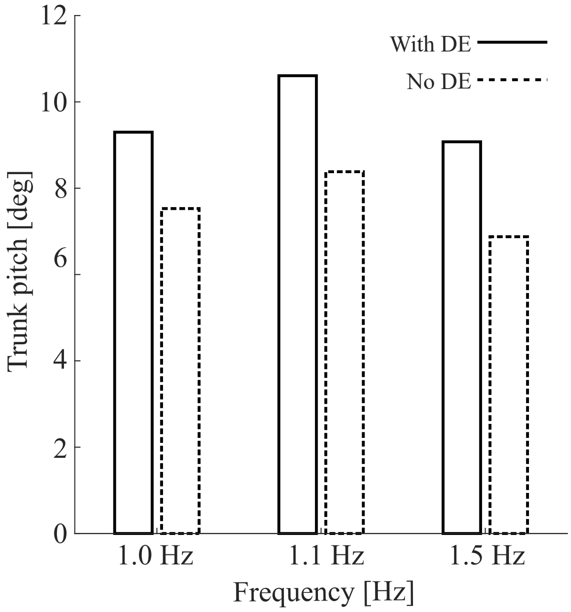

Figure 5.7: Trunk-pitch of quadruped reduces by adding DE tendon up to 24 $\%$.

Speed: As you can see in Fig. 5.8 robot speed increases by 56$\%$, 28$\%$ and 12$\%$ for gait frequencies of 1.0 Hz,1.1 Hz and 1.5 Hz, respectively, by adding DE tendon to the leg. Even though we send the same command to the hip and knee motor, we have a larger angle of contact for the front leg, which means the distal mechanism makes less interference with a knee lift-off and provides more swing push for the front leg.

Cost of transport: Total cost of transport of robot calculate as $CoT = \frac{P_{In}}{m.g.v}$ where P_{in} is input motor power, m is robot mass, v is robot speed. COT is a metric for showing the robot's efficiency. To compare robots to other robots and animal efficiency, we use the natural runner line presented by Tucker [218, 217]. The ratio of the robot's COT to the COT of the natural runner of the same mass would be a metric to compare the energy efficiency of different size robots. This metric shows that adding the DE tendon reduces robot COT by 22$\%$. This efficiency increases by reducing hip and knee input power and achieving higher speed. You can see the COT of RoboManul compared to other state-of-the-art robots.

Optimized motor gearbox selection: In Robomanul, we use a servo drive motor. These motors and gearbox systems are inefficient in energy consumption due to losses because of acceleration and deceleration of gearbox inertia. We know that input electrical energy equals mechanical output energy plus losses.

$$P_{Input\ motor} = P_{Mechanical} + P_{Joule\ heating} = \mathrm{T}\omega + RI^2 \tag{5.5}$$

Roos shows that we always have mechanical losses in the motor gearbox system because

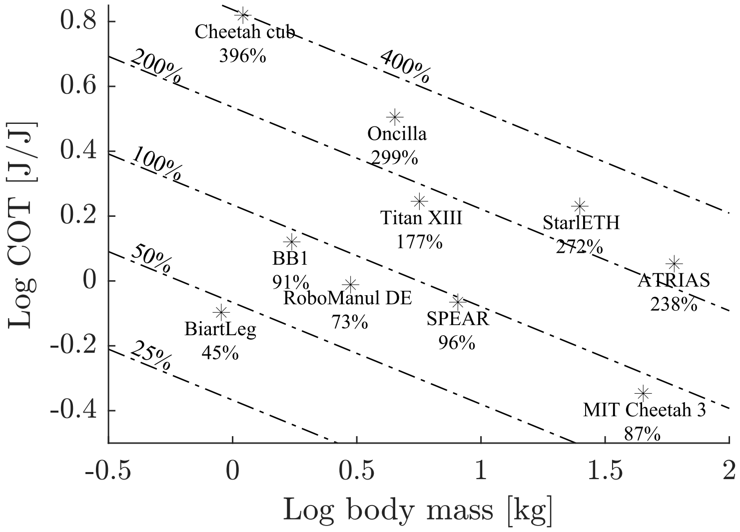

Figure 5.8: CoT of Robomanul in comparison to the state of the art robots [207, 21, 210, 120, 103, 99, 129, 192, 28] on Tucker graph of normalize CoT to natural runners [218, 217].

of the accelerating inertia of the motor shaft and gearbox. We also have electrical losses due to joule heating of coil in motor[181]. Roos framework shows that to achieve the minimum cost of transport for the robot. We need to optimize the combination of the motor parameter (select appropriate motor), gearbox ratio, and effective inertia.

$$P_{Inputmotor} = (J_{Motor} + J_{Gears})\ddot{\theta}_{load}\dot{\theta}_{load}n^2 + \frac{\tau_{load}(t))}{\eta_{gearbox}}\dot{\theta}_{load} + R_{Motor}\frac{T_m^2}{K_T^2} \tag{5.6}$$

By applying this equation to various low inertia gearboxes and off-the-shelf brushless motors, we can get to optimal motor and gearbox to achieve minimum COT for the robot. In our case, if we use brushless motor MN-7005 (T-motor) and gear ratio 8:1, we can get to a normalized COT of 10%.

5.6 Discussion

DE tendon performance is influenced by many front and hind leg parameters. Parameters such as leg loading and angle of roll-over at joint define the amount of the DE tendon mechanical charging and recuperation of locomotion energy during a gait cycle. Trunk oscillation can strongly influence both of these parameters. On the other hand, increasing body oscillation increases locomotion energy costs. By observing the power and torque difference of front and hind leg motors under similar input parameters such as leg design and control and changing DE tendon, we identify DE tendon's role for the front and hind leg during locomotion. The first effect is adding DE tendon was to reduce trunk oscilla-

Table 5.1: Result measurement summary table

Parameter	Unit	Value		Improvement in %
		Without DE	with DE	
Speed at 1.0 Hz	m/s	0.25	0.39	56
Speed at 1 .1 Hz		0.36	0.46	28
Speed at 1.5 Hz		0.60	0.67	12
Pitch maximum 1.0 Hz	deg	9.30	7.53	19
Pitch maximum 1.1 Hz		10.61	8.38	21
Pitch maximum 1.5 Hz		9.08	6.88	24
Hip average torque front at 1.0 Hz	Nm	-0.77	-0.47	39
Hip average torque front at 1.1 Hz		-0.77	-0.48	38
Hip average torque front at 1.5 Hz		-0.61	-0.27	56
Hip average torque hind at 1.0 Hz		-0.62	-0.05	92
Hip average torque hind at 1.1 Hz		-0.63	-0.02	98
Hip average torque hind at 1.5 Hz		-0.20	0.08	139
Hip power front 1.0 Hz	J/s	0.97	0.49	50
Hip power front 1.1 Hz		1.46	0.72	51
Hip power front 1.5 Hz		2.95	1.26	57
Hip power hind 1.0 Hz		1.21	0.6108	50
Hip power hind 1.1 Hz		1.54	0.52	66
Hip power hind 1.5 Hz		1.42	0.64	55
DE tendon recuperate work front 1.0 Hz	J	-	0.015	-
DE tendon recuperate work front 1.1 Hz		-	0.015	-
DE tendon recuperate work front 1.5 Hz		-	0.004	-
DE tendon recuperate work hind 1.0 Hz		-	0.003	-
DE tendon recuperate work hind 1.1 Hz		-	0.002	-
DE tendon recuperate work hind 1.5 Hz		-	0.003	-
Input mechanical power 1.0 Hz	J/s	0.11	0.06	41
Input mechanical power 1.1 Hz		0.13	0.06	53
Input mechanical power 1.5 Hz		0.16	0.07	53
COT (1.5 Hz)	J/J	1.25	0.97	22
Knee power ratio front to hind 1.0 Hz	%	56	61	-
Knee power ratio front to hind 1.1 Hz		59	60	-
Knee power ratio front to hind 1.5 Hz		91	87	-
DE tendon work ratio front to hind 1.0 Hz		-	78	-
DE tendon work ratio front to hind 1.1 Hz		-	87	-
DE tendon work ratio front to hind 1.5 Hz		-	21	-

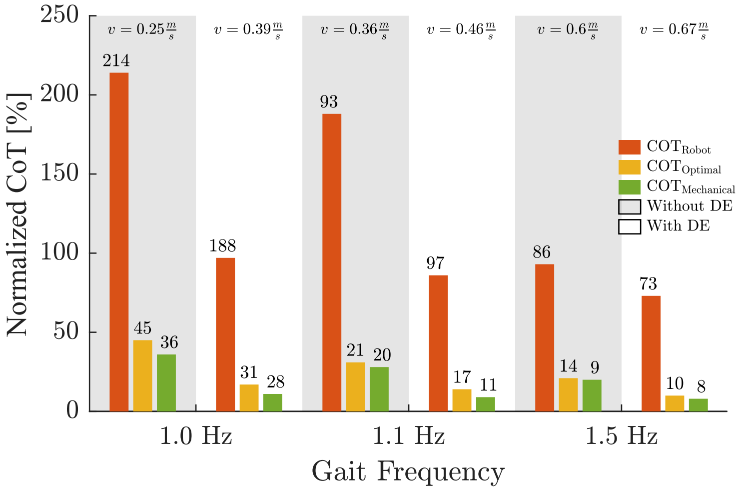

Figure 5.9: Cost of transport mechanical (orange), electrical (green) and optimized (yellow) one base on roos framework [181] for six experiments with DE tendon (white shadow) and without DE tendon (gray shadow) and robot achieve speed.

tion by 24%. Also, by adding the DE tendon, we introduce a third elastic element that allows us to compensate for one source of energy loss. The task of the global tendon is to recuperate mechanical energy in leg length direction [8]. The task of the pantograph spring is to recuperate energy in the leg angle direction [192]. And the DE tendon task is to act as some form of memory elasticity that depends on ground contact to store energy during the stance phase and release that energy as push at the stance phase and knee flexing at the beginning of the swing phase.

From the data, we can see the front leg DE tendon recuperate nine times higher than the hind leg, and also hind leg uses more knee energy to lift off from the ground, which means clutch behavior did not happen properly in the hind leg foot joint. One of the conclusion is that DE tendon at the hind leg in quadruped is not functioning as it should do it could be a source why hind leg foot segment in quadruped (segment 3-4) are more fixed during stance phase. The other reason that a quadruped robot does not need clutching parallel elasticity via DE tendon is the main purpose of disengagement is to lift the leg and create leg clearance during the swing phase. If we can clear that clearance via another source, the robot or animal does not knee to flex its knee during the swing. As we can see this clearance can provide at a higher speed when the robot has a flight phase means the center of mass push into the air during leg push off and create leg clearance or it can create for low speed via trunk oscillation and specifically head down motion of trunk at hind leg toe-off. On the other hand, we can observe DE tendon in the front leg due to higher leg loading and wider roll-over angle, charge more and release more energy to extend proximal underactuated part of the leg to sweep higher angle during stance and as a result during swing phase. Again, this effect can amplify by the head-up motion of the trunk on the front leg at the point of toe-off.

Besides these differences between the front and hind leg, adding DE tendon and mechanism into the leg design change the natural dynamic of the system. Specifically by introducing more serial springs into the system and reducing the system's natural frequency. This reduction in natural frequency helps us to walk and run at higher locomotion energy at lower gait frequency for given input energy.
Result shows that by adding DE tendon despite increase speed of the robot by 56%, 28% and 12% for gait frequencies of 1.0 Hz,1.1 Hz and 1.5 Hz, respectively, we reduce input energy by 53% for maximum speed.

Chapter 6

Hybrid parallel compliance allows robots to operate with sensorimotor delays

6.1 Contribution

Major indicates a contribution, without which the paper would probably not have been submitted.
Substantial contribution increase chance of acceptance.
Minor contribution improved the paper, but did not significantly change the form or content.

Author	Author position	Scientific ideas	Data generation	Analysis & interpretation	Paper writing
Milad Shafiee Ashtiani	First	Major	Major	Major	Major
Alborz Aghamaleki Sarvestani	First	Major	Major	Major	Major
Alexander Badri-Spröwitz	Last	Major	Minor	Substantial	Major
Title of paper		Hybrid parallel compliance allows robots to operate with sensorimotor delays and low control frequencies			
Status in publication process		Published at Frontiers in Robotics and AI			

Thesis author contribution based on [1].

Alborz Aghamaleki Sarvestani: conceptualization, methodology, software, validation, formal analysis, data curation, writing - original Draft, visualization.

Content of this chapter is largely base on the below paper:

1. Shafiee Ashtiani*, M., Sarvestani*, A.A. and Badri-Spröwitz, A., 2021. Hybrid parallel compliance allows robots to operate with sensorimotor delays and low control frequencies. **Frontiers in Robotics and AI**, 8, p.170.

6.2 Abstract

Animals locomote robustly and agile, albeit significant sensorimotor delays of their nervous system and the harsh loading conditions resulting from repeated, high-frequent impacts. The engineered sensorimotor control in legged robots is implemented with high control frequencies, often in the kilohertz range. Consequently, robot sensors and actuators can be polled within a few milliseconds. However, especially at harsh impacts with unknown touch-down timing, controllers of legged robots can become unstable, while animals are seemingly not affected. We examine this discrepancy and suggest and implement a hybrid system consisting of a parallel compliant leg joint with varying amounts of passive stiffness and a virtual leg length controller. We present systematic experiments both in computer simulation and robot hardware. Our system shows previously unseen robustness, in the presence of sensorimotor delays up to 60 ms, or control frequencies as low as 20 Hz, for a drop landing task from 1.3 leg lengths high and with a compliance ratio (fraction of physical stiffness of the sum of virtual and physical stiffness) of 0.7. In computer simulations, we report successful drop-landings from 3.8 leg lengths (1.2 m) for a 2 kg quadruped robot with 100 Hz control frequency and a sensorimotor delay of 35 ms.

6.3 Introduction

In this work, we aim to merge two diametrical principles while maintaining their best properties; a) Passive leg joint compliance that works without feedback and at low control frequency, and b) active joint compliance providing control authority. We hypothesize that, for a given robot design and locomotion task, there exists a range of compliance ratios—a hybrid range—that works best despite significant feedback delays and low control frequencies.

This work uniquely contributes as follows; We systematically characterize the full range of active-to-passive parallel compliance ratios for a given total leg joint compliance. We simulate adverse controller conditions in simulated and hardware drop landings, including significant feedback delays, low control frequencies, and varying duty cycles. Previous work in parallel-elastic legged robotics typically investigated parallel compliance with high-frequency and low delay actuation [140].

In Section 6.4, we present a stability analysis of a simplified model in the presence of sensorimotor delays for two ratios of parallel compliance. We then present computer simulations and hardware experiments and investigate the effect of control frequencies, sensorimotor delays, and duty cycles on a robot leg with varying ratios of parallel compliance for drop-landings (Section 6.5). We also characterize a simulated quadruped robot made of four of these legs for multiple drop-landing heights. We discuss and conclude the work in Section 6.6.

6.4 Materials and methods

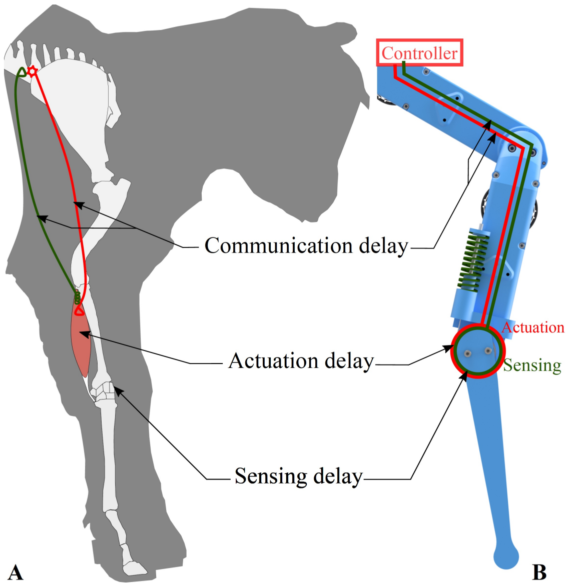

Figure 6.1: A) Animal locomotion control is subject to sensorimotor delays from sensing, communication, and actuation. The drawing is loosely inspired by Figure 1 of [149]. B) Robots typically have lower intrinsic delays from electronic sensing and communication. Instead, delays are caused, for example, by filtering noisy data. We systematically tested robot controllers with varying sensorimotor delay and control frequency. We hypothesized that a hybrid system comprised of passive joint elasticity and parallel active joint stiffness can reject sensorimotor delays robustly for appropriate compliance ratios.

We quantify the total (sum of) system compliance as active compliance in parallel to passive (spring-based) compliance, acting at the knee joint (Fig. 6.1B):

$$K_{\text{total}} = K_{\text{active}} + K_{\text{passive}} \tag{6.1}$$

Where K_{passive} [Nm/rad] is the joint's passive rotational stiffness, K_{active} [Nm/rad] is the joint's active, virtual, rotational stiffness produced by the actuator. K_{total} [Nm/rad] is the summed up rotational joint stiffness. We define a 'compliance ratio' λ_{passive} as the ratio of passive stiffness and total stiffness:

$$\lambda_{\text{passive}} = K_{\text{passive}}/K_{\text{total}}$$

Hence, for a compliance ratio $\lambda_{\text{passive}} = 0.1$, the knee spring supplies 10 % of the knee torque to carry the robot, and the knee actuator supplies the remaining 90 %. A λ_{passive} of 1.0 indicates a knee joint with a physical spring and no motor.

6.4.1 Theoretical analysis of a simplified model

We analyzed a simplified system with parallel compliance to analytically quantify the effects of sensorimotor delays. The reduced-order model consists of a strut-like leg mounted as a single degree-of-freedom pendulum and represents a simplified robot lower leg (Fig. 6.4A). The equations governing the pendulum motion are:

$$I\ddot{\theta} + mgL \cdot sin(\theta - \theta_0) + K_{\text{passive}}(\theta - \theta_0) + D\dot{\theta} = \tau_{\text{m}}$$

where $D = 0.14$ Nms/rad is the system damping, K_{passive} is the stiffness of the parallel compliant element, $L = 0.16$ m is the center of mass distance to the pivot point, $m = 0.5$ kg is the mass, $I = mL^2$ is the moment of inertia, g is the standard gravity, and θ_0 is the equilibrium joint angle of the relaxed spring. We set a total stiffness of $K_{\text{total}} = 1.15$ Nm/rad. The instantaneous joint angle is θ, and τ_{knee} is the knee joint control torque input, implemented as active compliance:

$$I\ddot{\theta} + mgL \cdot sin(\theta - \theta_0) + K_{\text{passive}}(\theta - \theta_0) + D\dot{\theta} = -K_{\text{active}}(\theta_{\text{feedback}} - \theta_0) \qquad (6.2)$$

where K_{active} is the active motor compliance. The sensor reads the joint angle θ_{feedback}. We assume a small enough angular deviation of the pendulum around the equilibrium point: $sin(\theta - \theta_0) \simeq (\theta - \theta_0)$, which allows to write Eq. (6.2) as a linear differential equation. We converted Eq. (6.2) to the Laplace domain and incorporated a fixed feedback time delay t_{d} of the control input (active compliance). The resulting closed-loop system transfer function can be presented in the frequency domain as:

$$\frac{\Theta_{\text{s}}}{\Theta_{\text{ds}}} = \frac{K_{\text{active}}e^{-t_d s} + mgL + K_{\text{passive}}}{s^2 I + Ds + K_{\text{active}}e^{-t_d s} + K_{\text{passive}} + mgL} \qquad (6.3)$$

We linearised the system's exponential time delay term with a third-order Padé approximation. A system pole analysis of this simple system provides an intuitive understanding of the effects of two compliance ratios for the given total joint stiffness on closed-loop stability and for the given sensorimotor delays.

6.4.2 Computer simulation of articulated robot legs

We characterized a single, articulated robot leg with hybrid joint compliance. Drop landings are one of the most challenging tasks due to high, impulse-like ground reaction forces and nonlinear and hybrid leg loading. Drop landing is similar to a step response perturbation, which is a conventional control theory tool to characterize black box systems. We computer simulated the robot leg in PyBullet [48], and performed extensive drop-landing simulations for a broad range of sensorimotor delays, duty cycle frequencies, and λ_{passive}. We simulated a single leg and a quadruped robot, both modified from the open-source quadruped robot Solo [91]. In Fig. 6.2, we show the control and sensorimotor strategies tested. The black curve is the schematic, desired knee motor torque trajectory. The control frequency (step-like, brown line) is measured in commands per second. For reference, the control frequency of proprioceptive actuation in legged robots is often around 1 kHz, i.e., a cycle period takes $dt_{\text{control}} = \frac{1}{f} = 1$ ms. We are especially interested in investigating scenarios with control frequencies well below 1 kHz. Torque is applied with three strategies; First, the activation duration $dt_{\text{activation}}$ is defined as the time period between control commands, i.e., $dt_{\text{activation}} = DC \times dt_{\text{control}}$. The activation duration lasts at least 1 ms and at most $\frac{1}{f}$. For $dt_{\text{activation,min}}$, the control command is applied for a period of 1 ms and then reset to zero. For $dt_{\text{activation,max}}$, the actuator will maintain its value until the control command is updated (Fig. 6.2A, brown line). Second, we applied a sensorimotor delay to the control command (Fig. 6.2B). Third, the force-activity relationship of muscles is not fully understood [176], and we included tests with varying duty cycles, defined as the fraction of dt_{control} with a non-zero actuator torque (Fig. 6.2C). The active compliance controller knee joint input is:

$$\tau_{\text{knee,motor}} = K_{\text{total}}(1 - \lambda_{\text{passive}})(\theta_{\text{feedback,knee}} - \theta_{0,\text{knee}}) \tag{6.4}$$

To simulate the spring in PyBullet, we implemented a knee joint spring torque:

$$\tau_{\text{knee,spring}} = K_{\text{total}}(\lambda_{\text{passive}})(\theta_{\text{knee}} - \theta_{0,\text{knee}}) \tag{6.5}$$

6.4.3 Setup hardware experiments

We modified a single leg of the eight degree-of-freedom (8-DOF), open-source, quadruped robot 'Solo' [91]. The leg has two active degrees of freedom, one at the hip and one at the knee. Both leg segments are 0.16 m long, the lower leg mounts a semi-circular foot of 15 mm radius. A brushless motor (Antigravity MN4004-kv380, T-Motor) drives a two-stage belt transmission with an overall $9 : 1$ gear ratio for each active joint. An optical encoder (AEDT-9810-T00, Avago) measures the motor's rotor position, which is recalculated into joint angles. We mounted physical springs in parallel to the knee joint (SWY 16.5-30 for $\lambda_{\text{passive}} = 1.0$, SWY 16.5-45 for $\lambda_{\text{passive}} = 0.67$, SWY 16.5-80 for $\lambda_{\text{passive}} = 0.37$, Misumi). The spring's tendon inserts into a knee joint pulley with radius 18.9 mm (Fig. 6.3B). The spring mount allows rapid exchange of springs between experiments.

To simplify the touch-down scenario, the robot leg was dropped, guided by a vertical rail (Fig. 6.3A). The hip joint was constrained to follow half of the knee joint angle at all times, controlled by a position controller creating foot contact vertically below the hip joint. We recorded the vertical hip position with two draw-wire sensors (LX-PA-40, WayCon) mounted above and below the robot, to cancel out single sensor force bias. The hip position allows quantifying the robot's landing behavior and characterizing hybrid compliance. The hip position was sampled by an analog-to-digital (A/D) converter on

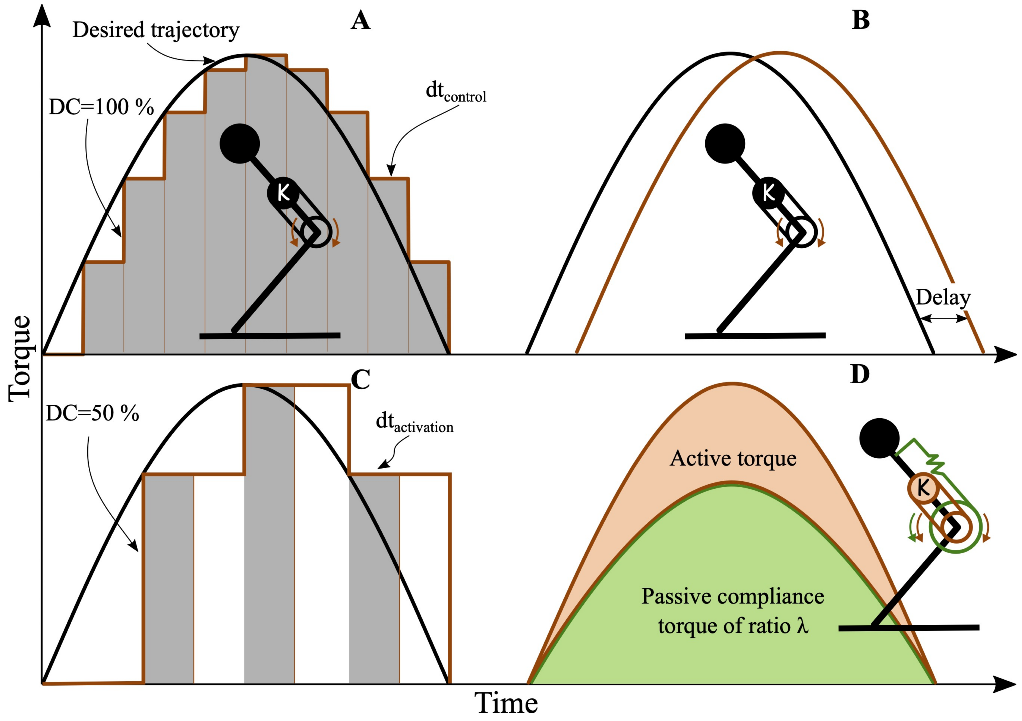

Figure 6.2: Knee motor command for the different combinations of control frequency, duty cycle, and sensorimotor delay. A) A 100 % duty cycle at low control frequency. B) A set sensorimotor delay between the desired knee output torque and the commanded output torque. C) A 50 % duty cycle. D) An example for a compliance ratio of $\lambda_{\text{passive}} \approx 0.75$ is shown. The mechanical knee spring produces three quarters of the total knee torque (green). The knee actuator is programmed as a virtual spring producing the remaining torque (brown).

the brushless motor driver board. The motor board sends motor position and vertical position data via a serial peripheral interface (SPI) to the PC communication board. The PC communication board connects the motor driver board via EtherCAT to a PC (Intel Xeon(R) W-2145 CPU, 3.7 GHz, 16 cores, 64 bit, 62.5 GB Ram, Ubuntu 18.04). We wrote a Python wrapper to control the robot. The Python wrapper timestamps and saves joint angles, motor currents, and hip height into a text file. We analyzed and plotted data in Matlab.

6.5 Results

This section initially presents results from the pendulum task. We then show computer simulation results with a single robot leg and hybrid joint compliance. We simulated quadruped-robot drops from multiple heights, and we present hardware experiment re-

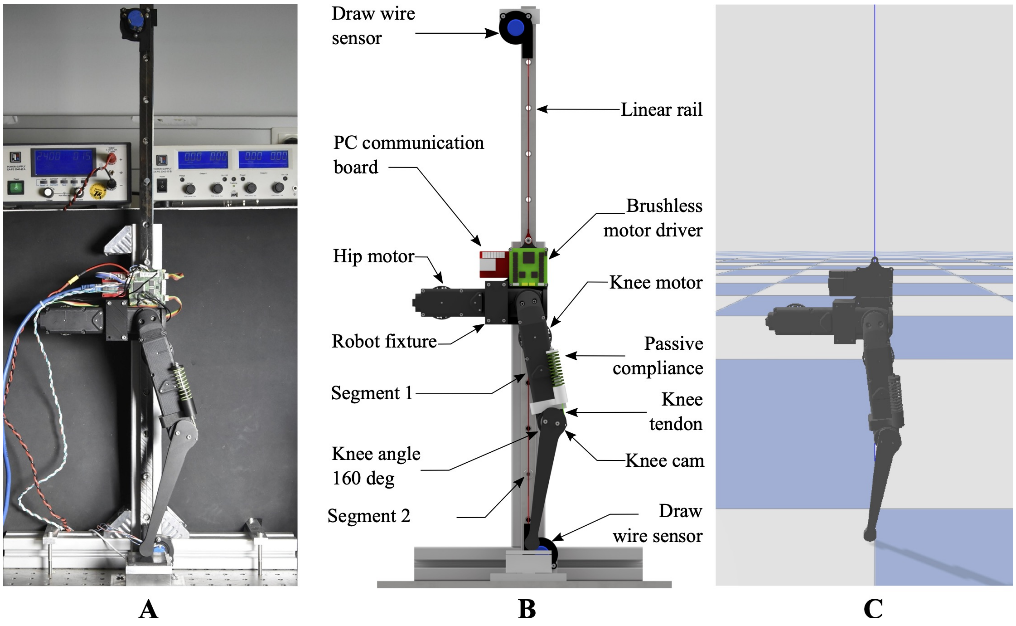

Figure 6.3: Experimental setup. A) The 2-DOF hybrid compliant leg. The one-directional spring (passive compliance) extends the knee joint via a knee tendon and a knee pulley. Knee springs with varying stiffness were mounted during the experiments, supporting between 0 % to 100 % robot's weight. A rail guides the robot's vertical drop, and a pair of potentiometers measure the robot's height. The knee motor produces torques in parallel to the mounted knee spring. B) Setup details, computer-aided drawing. C) The Unified Robot Description Format (URDF)-based model of the hybrid compliant robot leg, simulated in PyBullet.

sults with a single leg mounted to a vertical slider.

6.5.1 Hanging pendulum analysis, simplified model

The pendulum pole analysis shows that for $\lambda_{\text{passive}} = 0$ and with increasing feedback delay, the dominant system poles move from their stable region towards the unstable region at the imaginary axis (Fig. 6.4B). For medium compliance ratios, the rate of divergence is lower. The step response indicates that increasing the sensorimotor delay with active control ($\lambda_{\text{passive}} = 0.0$) leads to continuous oscillations, and resonance eventually destabilizes the system (Fig. 6.4C). For hybrid passive compliance and a feedback delay of 20 ms, the closed-loop response is stable and smooth (Fig. 6.4D).

The pendulum example is a simplification allowing a pole analysis with few parameters, but with an intuitive interpretation; Fig. 6.4B shows when parameters lead to destabilization, with a clear cross-over into the unstable regime. The robot leg computer simulations in the following sections require more elaborate interpretation, but are more precise in terms of mechanics and less simplified. Instead of continuous time analyses, time-discrete analyses are also applied for simplified systems. We briefly provide the results of a time-discrete analysis of the pendulum example in the supplemental section for the interested reader.

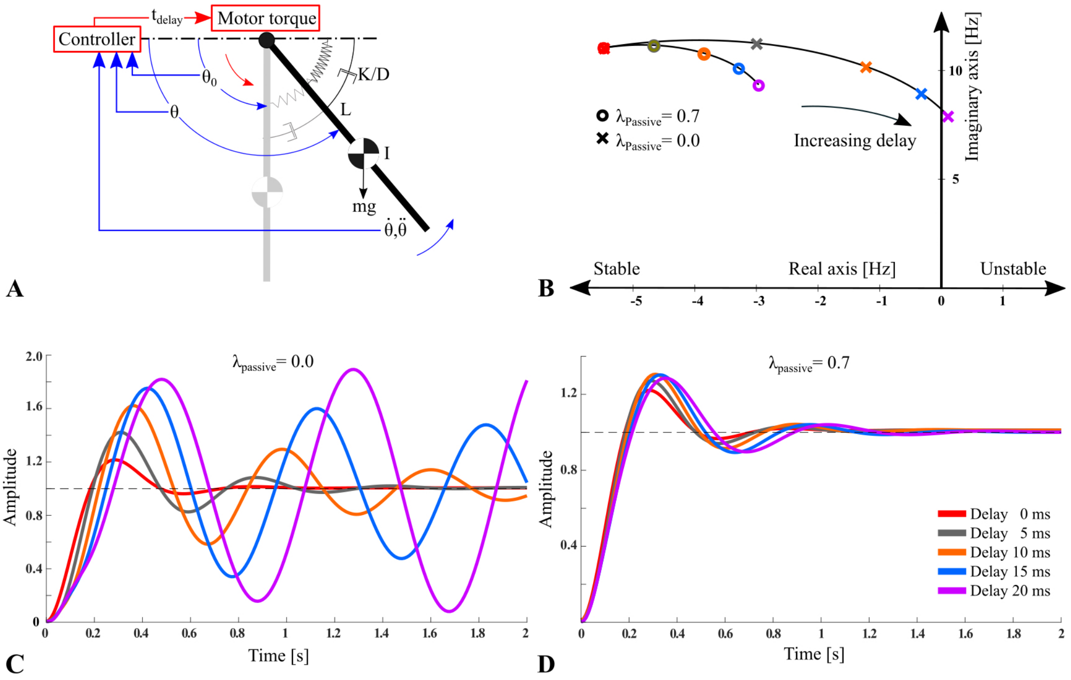

Figure 6.4: Simulation results of a simplified, single-link pendulum mounted to a parallel motor-spring combination (A). Parameters are provided in Section 6.4.1. B) Graphical pole analysis of the actuated pendulum. The effects of varying delay and compliance ratios on the system stability are shown. C) The system's step response for varying delays with $\lambda_{\text{passive}} = 0.0$, and D) $\lambda_{\text{passive}} = 0.7$. The hybrid parallel compliance controller ($\lambda_{\text{passive}} = 0.7$) is stable for all tested delays, and performs better compared to fully active actuation ($\lambda_{\text{passive}} = 0.0$).

6.5.2 Single-leg computer simulation

We studied the effects of varying combinations of sensorimotor delay, control frequency, and compliance ratio λ_{passive} on controller performance during landing. We initially recorded a reference hip height trajectory dropping the robot leg with $\lambda_{\text{passive}} = 1.0$, which settled after 0.35 s at a hip height of 33 cm (Fig. 6.5).

We then performed computer simulations to quantify the viability of the landing task, varying λ_{passive} from 0.0 to 1.0 in steps of 0.05, the sensorimotor delay from 0 ms to

60 ms in steps of 5 ms, and sensorimotor control frequencies of 20, 50, 100, 250, and 1000 Hz. We tested duty cycles of 25%, 50%, and 100%.

In PyBullet, we set joint damping values of 0.01 Nms/rad and 0.05 Nms/rad for hip and knee, respectively. A single leg weighs 0.6 kg, and the quadruped robot 2.0 kg. We chose the total knee joint stiffness so that leg length changed by 10 % during the first mid-stance, after dropping it from 42.5 cm. We implemented a $\lambda_{\text{passive}} = 1.0$ with a spring of stiffness $K = 4680$ N/m acting on the knee pulley of radius $r = 18.9$ mm, leading to a rotational stiffness of $Kr^2 = 1.67$ Nm/rad. We defined settling time as the difference between the initiated drop time and the hip position stabilizing within a ±1 % margin of the settling hip height after 3 s simulation time. We applied the Matlab function stepinfo for this analysis. We used twice the $\lambda_{\text{passive}} = 1.0$ value as the global settling time (0.7 s) and defined 90 % of the passive compliant $\lambda_{\text{passive}} = 1.0$ settling hip height as minimum final hip height (30 cm).

In Fig. 6.5, the results of 273 drop-landing simulations are shown, with varying sensorimotor delays and λ_{passive} settings, a 100 % duty cycle, and a control frequency of 1 kHz. Grey data points represent failed landings with a settling time higher than 0.7 s or too low settling hip heights. For full active actuation ($\lambda_{\text{passive}} = 0.0$), and when increasing the sensorimotor delay above 25 ms, all landings fail. For $\lambda_{\text{passive}} > 0.4$, the leg lands successfully in the presence of 40 ms delays. Results show that the hybrid compliant leg has successful intermediate regimes allowing for relatively large sensorimotor delays, with an appropriate combination of passive and active compliance.

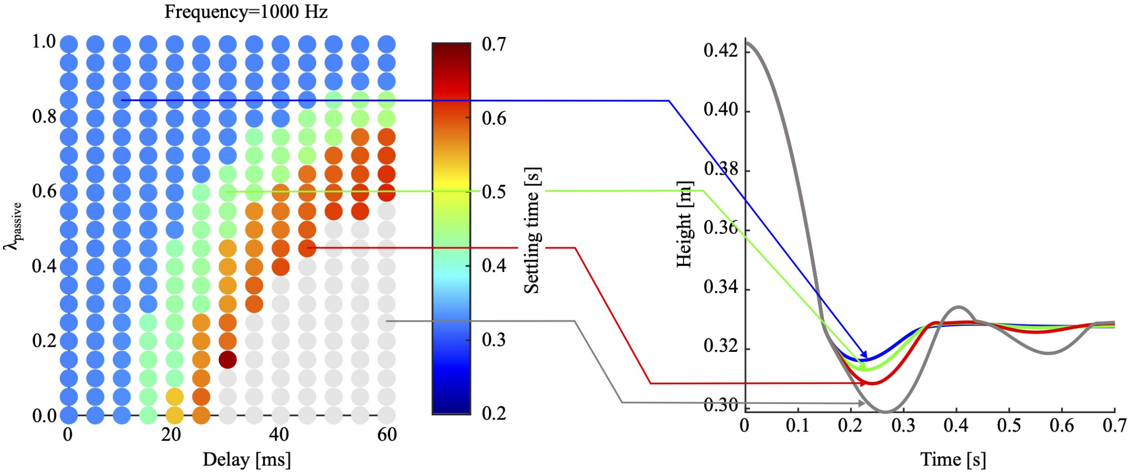

Figure 6.5: Computer simulation results: 273 drops were simulated for the robot leg controlled with a control frequency of 1000 Hz and a duty cycle of 100 %. The compliance ratio λ_{passive} was varied between 0 to 1 in steps of 0.05, and the sensorimotor delay between 0 ms to 60 ms in steps of 5 ms. The grey data points and the grey hip height trajectory show failed landings with too large settling times. All colored data points and trajectories show successful landings. Successful landings are visible for sensorimotor delays up to 60 ms, in combination with compliance ratios of $\lambda_{\text{passive}} = 0.6$ and above.

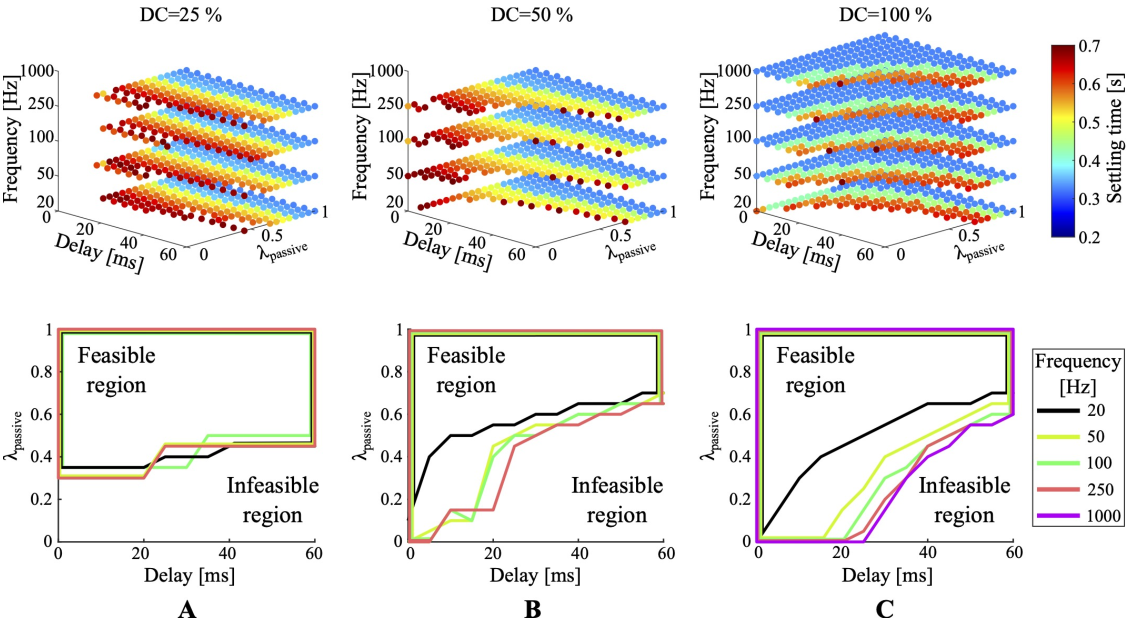

Figure 6.6: Simulation results: Dropping the hybrid actuated robot leg from a height of 42.5 cm. Parameters varied are duty cycle (DC), control frequency, system delay, and compliance ratio (λ_{passive}). The reference landing performance is the top-left data point in each plot. It presents the behavior of the fully passive leg ($\lambda_{\text{passive}} = 1.0$). Plots for DC=25 % and DC=50 % show no data for 1000 Hz; with a step time of 1 ms partial duty cycles are not possible.

We then investigated the effect of varying control frequency (20, 50, 100, 250, and 1000 Hz) and duty cycle (25, 50, and 100 %, Fig. 6.6). Most visible is a decreasing feasible area for all three duty cycles at reduced control frequencies. Comparing duty cycles of 25 % and 100 % (Fig. 6.6A, Fig. 6.6C) shows that the feasible area did change with reduced duty cycles. Low compliance ratios ($\lambda_{\text{passive}} \approx 0.2$) lead to successful landings combined with a duty cycle of 50 % or the highest control frequency (1 kHz). Fig. 6.6C shows that duty cycles of 100 % at control frequencies of 100, 250, and 1000 Hz have a similar-sized feasible region. When switching to a low control frequency (20 Hz, black line) the feasible area reduces much. For a 50 % duty cycle, the feasible area changes slightly when switching between 50 and 250 Hz control frequency (Fig. 6.6B). The biggest changes are visible when changing from 1000 Hz to 250 Hz, and from 50 to 20 Hz.

Typically, higher duty cycle values led to better results for otherwise identical parameters. An exception is found when comparing duty cycles of 25 and 100 %. The hatched area in Fig. 6.7A indicates successful landings at low duty cycles, where high duty cycle landings failed because of hip height oscillations beyond the settling time limit (Fig. 6.7B).

For most compliance ratios above 0.6, we observe successful landings, including crit-

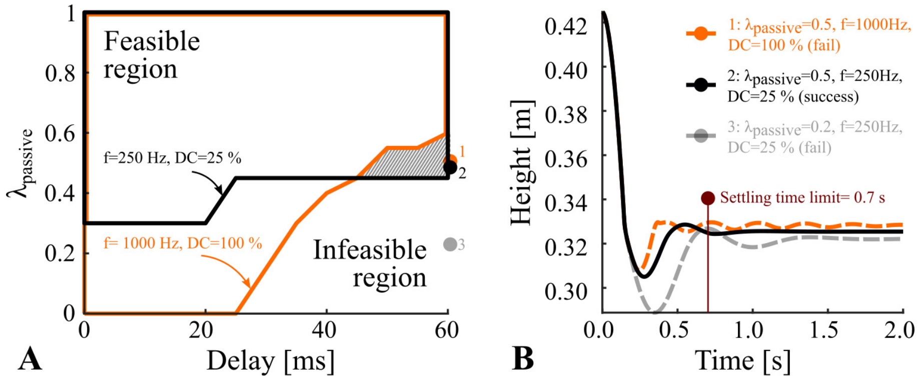

Figure 6.7: For simulations with a 25 % duty cycle and 60 ms feedback delay feasible solutions are visible for compliance ratios of $\lambda = 0.5$ (B, solid black). In the indicated overlapping parameter area (A), 25 % duty cycle simulations fail with insufficient settling time (B, dashed orange).

ical combinations of 60 ms delay and 20 Hz control frequency. All results indicate successful landing for compliance ratios equal to and higher than 0.7.

6.5.3 Quadruped computer simulation

The previous single-leg simulation results indicate that robot performance becomes largely independent of sensorimotor delay and control frequency with a high compliance ratio. But fully passive compliance reduces control authority. In seven drop-landing scenarios, we altered the drop height and passive and active stiffness of a quadruped robot to characterize system and controller performance, but also to emphasize the importance of control authority (Fig. 6.8). The duty cycle was set to 100 % in all quadruped robot simulations. The simulation parameters are provided in Table 6.1.

Table 6.1: Simulation parameters of the quadrupedal robot, with a duty cycle of 100 %.

Case	Total compliance [Nm/rad]	λ_{passive} [%]	Control frequency [Hz]	Delay [ms]
1	1.6717	100	1000	0
2	1.6717	100	1000	0
3	1.6717	0	1000	0
4	1.6717	0	1000	17
5	2.5076	67	200	27
6	2.5076	67	100	27
7	2.8419	59	100	35

The case-1 robot simulated a compliance ratio of 1.0, i.e., fully passive elastic knee joints. The robot was dropped from a height of 0.7 m and landed successfully. The case-2 robot used identical control parameters, was dropped from 1.0 m height, and failed to land successfully. At close observation, it becomes visible that its knee joints inverted after the first landing rebound, and the robot landed with inverted knee angles and without spring support. Case-2 emphasizes the drawback of passive compliance; without control, the knee joint orientation cannot be adjusted prior to rebounding. The case-3 configuration featured a controller with full, bi-directionally active compliance (no passive compliance), and without sensorimotor delay. The controller ran at 1 kHz and successfully guided the landing. In case-4, a fully active compliant robot with 17 ms sensorimotor delay failed to land properly, which shows the vulnerability of active compliance in the presence of sensorimotor delay. Case-5 shows a successful landing scenario by combining passive and active compliance ($\lambda_{\text{passive}} = 0.67$), with 27 ms sensorimotor delay, and reduced control frequency (200 Hz). Case-6 was also configured with a $\lambda_{\text{passive}} = 0.67$, a control frequency of 100 Hz, and failed landing the robot. For case-7, we decreased the compliance ratio to $\lambda_{\text{passive}} = 0.59$, and the robot landed successfully from a height of 1.2 m, and with a sensorimotor delay of 35 ms at a control frequency of 100 Hz. Case-7 shows how an appropriate combination of active and passive compliance at a low control frequency maintains good control authority and robustness in the presence of sensorimotor delay.

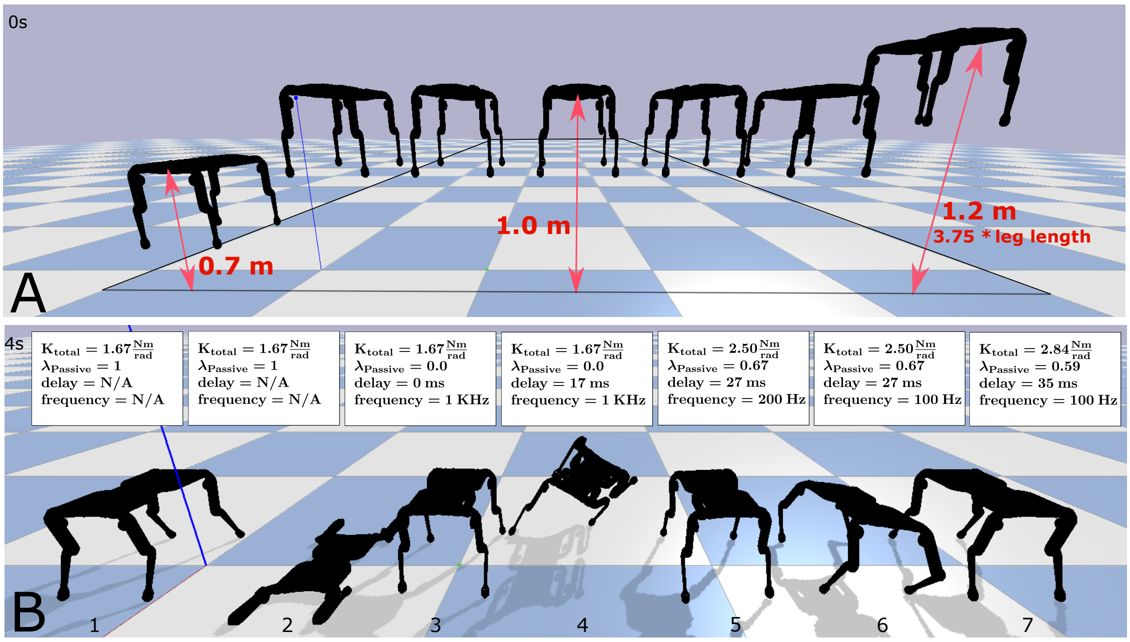

Figure 6.8: Computer simulated quadruped robots landing, in seven different scenarios, controlled with a duty cycle of 100 %. A) The robot's initial drop heights are indicated with red arrows. B) Converged robot state after 10 s. Cases 1, 3, 5, and 7 landed successfully. The panels also provide controller parameters.

6.5.4 Hardware experiments

We validated the previous single-leg simulations with hardware experiments. We chose compliance ratios of $\lambda_{\text{passive}} = [0\ , 0.37\ , 0.67\ , 1]$ and a total rotational knee stiffness of $K_{\text{total}} = 1.67$ Nm/rad. We then varied control frequencies ($[1000,\ 100,\ 10]$Hz) and sensorimotor delays ($[0,\ 10,\ 20,\ 30,\ 50]$ms). The duty cycle was set to 50 % for 10 and 100 Hz control frequency, and 100 % for 1000 Hz control frequency.

In Fig. 6.9, we assess the difference e_{sim2real} between computer simulations and hardware experiments, as the root-mean-square error (RMSE) between two resulting hip trajectories, normalized by the maximum leg length, measured during the settling duration of 0.7 s. The criteria for successful drop landings in hardware and computer simulation are identical (Section 6.5.2). Grey-colored data shows failure cases in both experiments and simulations. Viable cases with an RMSE of less than 6 % (Fig. 6.9) indicate good consistency between hardware experiment and computer simulation. We show four exemplary hip trajectories for varying compliance ratios (Fig. 6.9, I-IV). The first two cases are feasible landings with good consistency between simulation and experiments. In case III, the hardware experiment stabilized at a lower-than-simulation hip height but still within the required margin. Case IV is a failed drop, and neither the hardware experiment nor the simulated robot leg showed the necessary settling behavior.

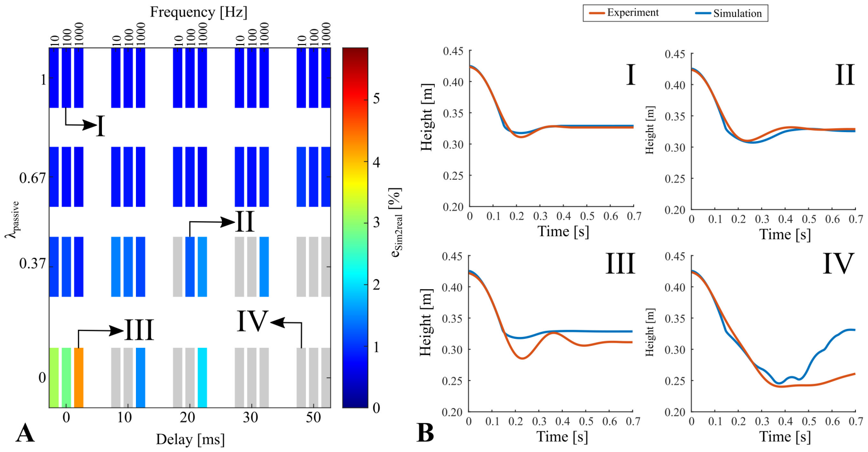

Figure 6.9: Results comparing computer simulations and hardware experiments, as root-mean-square error of the instantaneous hip height normalized by the initial leg length. A) Good similarities are shown as colored data patches. Grey data patches indicate unsuccessful drop experiments, violating settling time or final height criteria. B) Hip trajectories. I-III) Successful landings with short settling times and sufficient settling hip heights. IV) An example of an unsuccessful landing in simulation and hardware.

6.6 Discussion

The single-leg drop results in Fig. 6.5 show a continuous and gentle decrease of system robustness with increasing feedback delay when transitioning from a fully physically springy leg towards a fully actuated leg controlled by a virtual-spring controller. Hence, parallel structures of active compliance with the correct amount of passive compliance offer one possible answer to the question of how animals counteract perturbations in the presence of large sensorimotor delays. The ratio of passive to active compliance could be permanently set genetically, formed over a lifetime by training [75], or set when required by partial or full recruitment of slacked muscle-tendon structures [98]. Legged robots equally benefit from intrinsic robustness against feedback delay. We believe that compliance ratios for other designs will depend on the specific leg and controller design parameters, the locomotion task, and the required controllability. A higher compliance ratio can be used if the available control frequency is limited or high delays are expected. In the future, we are especially interested in exploring compliance rations of $\lambda_{\text{passive}} > 0.5$. One early design choice to consider is the effective spring deflection. Typically, stiffer springs feature a smaller deflection range, possibly leading to limited joint movement range, compared to softer springs. We used springs designed for large deflections. One can also balance the knee cam radius with the spring's movement range and stiffness. We suggest the following general procedure to establish a compliance ratio for a given task and robot:

1. Select a total joint stiffness based on the required steady-state leg length, the maximum leg deflection, and the leg geometry (segment lengths, robot mass, cam radius). This step can be executed by test-mounting a $\lambda = 1$ spring (no actuator) with given stiffness and spring slack position, dropping the robot leg, and observing its joint angles.

2. Alternatively, a simplified kinematic model can provide an estimate of the steady-state leg length (supplemental Section 3).

3. Select the desired compliance ratio. In the examples shown, compliance ratios between 0.5 and 0.7 worked well. Low compliance ratios provide higher controllability, as long as control frequencies are high and feedback delays are low, and vice versa. Duty cycles should be set to maximum (100 %), unless they are specifically exploited.

4. Check that the parallel mounted actuator has the capacity to supply the required torque and speed. Low compliance ratios (≈ 0.5) require an actuator to provide a higher work and power output throughout the task. With higher compliance ratios (> 0.7) the parallel spring carries more base load. When spring dynamics must be overwritten, high actuator torques are required but typically for a shorter time. For a motor-gearbox design methodology, we refer to [182].

This work centers around adjusting the ratio of physical and passive compliance for a given total joint compliance. Online-adjustable spring stiffness mechanisms have been proposed, but many are still bulky and heavy [236, 224, 235]. If a locomotion task requires large changes of total joint stiffness with a constant ratio of passive compliance [69], robust and light-weight adjustable stiffness designs will be needed. For versatile locomotion sequences like jumping, landing and fast running, learning-based methods could extract a 'best' range of compliance ratios from large locomotion data sets.

We see at least three applications for hybrid compliance ratios in legged robots; a) For legged robots which exploit natural dynamics of mechanical springs but require intermittent, high controllability for tasks like jumping or acceleration [208, 124]. b) For legged robots without access to high-frequency control or low-noise and low-latency sensors, which are expensive and time-consuming to develop [151]. c) For motion planners featuring update frequencies in the low sub-kilohertz range, in need of a legged robot with intrinsic robustness when controlled at these frequencies [166].

Chapter 7

Conclusion

Legged robot designers tend to neglect typologies and mechanisms observed in animal legs and often prefer high-powered actuation and relatively simple leg structures. Despite the limitations of biological tissues, the agile and robust performance of animals suggests that robot designs can benefit from a rigorous understanding of more complex multi-articular, strategically geared spring mechanisms to achieve simple, fast, and economic leg control. An additional benefit of the mechanism demonstrated here is the potential for more effective foot-substrate interactions. Many robots still use point-foot designs, which simplifies internal model computation. A clear advantage of the mechanism proposed here is its ability to stand upright with all actuators switched off. The torque-loaded foot segment creates a range of center of pressure points, where the robot can be balanced above, reminiscent of a flamingo standing while sleeping (Fig. 3.17A, Fig. 3.18) [39]. The functional implications of a foot acting as an effective leg-clutching mechanism in a multi-segment elastic leg remain unexplored. The proposed mechanism allows rapid mechanical control of swing-stance transitions, which can be particularly beneficial for navigating uneven, unpredictable, or soft terrains. The leg clutch and foot segment enable rapid spring engagement and adjustment of the center of pressure in direct response to altered loading.[1]

Disengagement tendon plays an important role in bipedal locomotion. Not only does it provide robust parallel elasticity clutching, but also it helps to amplify power during leg roll-over motion and uses the recuperated energy to have faster leg retraction with large ground clearance. As a result, the robot achieves 28 % faster speed at 2 Hz gait frequency. Furthermore, the leg with the DE tendon has a robust PE disengagement at the end of stance independent of the gait parameter as long as the virtual leg angle reaches to set disengagement angle. This behavior lets the leg to avoid co-contraction during leg pull-up and reduce the robot's consumption of energy by 10 %. Furthermore, the improvement in energy consumption and increasing speed for a given input parameter improve the robot's COT by 50 % compared to natural-runner data.[1]

The other important aspect of the disengagement mechanism in the leg is the necessity of the DE tendon for different gait speeds. We observe that DE tendons for walking and running have two different functions. At low speed, the co-contraction torque reduction

---

[1] This paragraph uses original or modified text from [21, 20]

during leg flexion caused by the disengagement is a more significant characteristic of having the DE tendon. We have a reduction of up to 40 % in hip peak torque and a reduction of more than 60 % in knee peak torque. However, for high-speed gait, the important characteristic of the DE tendon besides the reducing peak torque for hip and knee motors, is to increase robot speed by lengthening the robot's push-off time before entering the swing phase. Also, provide rapid leg retraction in the short time window of the flight phase for high-speed gait.[1]

Combined effects of clutching and mechanical recuperation of energy are vital for efficient bipedal legged locomotion. New leg designs need to exploit this disengagement mechanism in their future leg design to reduce and simplify locomotion controllers and make a robot that can walk on uneven terrain with minimum computational cost and minimum sensory data.[1]

The DE tendon performance is influenced by many front and hind leg parameters during quadrupedal trotting. Parameters such as the leg loading and the roll-over angle at the foot joint define the amount of the DE tendon mechanical charging and recuperation of locomotion energy during a gait cycle. Trunk oscillation can strongly influence both of these parameters. On the other hand, increasing body oscillation increases locomotion energy costs. We identify DE tendon's role for the front and hind leg during locomotion by observing the power and torque difference of front and hind leg motors under similar input parameters such as leg design and control and changing DE tendon. The first effect of adding the DE tendon was to reduce trunk oscillation by 24%. Also, by adding the DE tendon, we introduce a third elastic element that allows us to compensate for one source of energy loss. The task of the global tendon is to recuperate mechanical energy in leg length direction [8]. The task of the pantograph spring is to recuperate energy in the leg angle direction [192]. The DE tendon task is to act as a memory elasticity that depends on ground contact to store energy during the stance phase and release that energy as push at the end of the stance phase and knee flexing at the beginning of the swing phase.
From data, we can see the front leg DE tendon recuperate nine times higher than the hind leg and the hind leg uses more knee energy to lift off from the ground, which means clutching PE did not happen properly in the hind leg foot joints. The DE tendon at the hind was not charged, although it was mounted in the same way as the front leg. This observation implies that the hind leg foot segments in the quadruped (segment 3-4) are more fixed during the stance phase. The other reason that the quadruped robot does not need clutching parallel elasticity via the DE tendon is that the leg can create clearance via other sources. The robot or the animal does not need a knee motor to flex the knee completely during the swing. As we can see, this clearance can be created at a higher speed via the robot flight phase. The clearance at low speed is created via the trunk oscillation and specifically the head down motion of the trunk at the hind leg toe-off. On the other hand, the DE tendon in the front leg charges more due to the higher leg loading and

---

[1] This paragraph uses original or modified text from [21, 20]

wider roll-over angle. The DE tendon releases more energy and extends the leg before the toe-off. The leg loading of the front leg is amplified by the head-up motion of the trunk on the front leg.[1]

Besides these differences between the front and the hind leg, adding the DE tendon changes the natural dynamic of the system by introducing more serial springs into the system. This reduction in natural frequency helps us to locomote at higher locomotion energy at lower gait frequency for given motor input energy.[1]

Results show that by adding DE tendon despite increasing the total mechanic energy of the robot by 56%, 28% and 12% for gait frequencies of 1.0 Hz,1.1 Hz and 1.5 Hz, respectively, we reduce input energy by almost 60% for all speeds.[1]

Parallel elasticity helps reduce system energy during the stance phase for both animals and robots. Besides this power reduction effect, adding parallel compliance helps animals and robots respond to sensorimotor delays. In order to specifically study this property of parallel elasticity, we systematically characterized the combinations of parallel mounted passive and active joint compliance for their ability to control the robot's leg length after landing. In addition, we tested against the detrimental effects of significant feedback delays, low control frequencies, and low duty cycles in the full range of compliance ratios. Our goal was to find a compliance ratio for one given total knee compliance that works well with the above controller limitations. In comparison, previous work in parallel-elastic legged robotics typically investigated parallel compliance with high-frequency and low delay actuation [140, 23].[1]

Our computer simulations show successful single-leg drop-landings for sensorimotor delays up to 60 ms, and control frequencies as low as 20 Hz in combination with a compliance ratio of $\lambda_{\mathrm{passive}} = 0.7$. For a 'hybrid' setting between $\lambda_{\mathrm{passive}}$ 0.4 and 0.7, the partially active compliance ensures good control authority, and the remaining passive, spring-based compliance reacts immediately and independently from the controller. We verified single-leg computer simulations with hardware experiments for various parameters and showed good agreement between both. We ran computer simulations of quadruped robots with varying total leg stiffness values when landing from multiple drop heights. Compliance ratios in the hybrid range (around 0.5) worked better in the presence of adverse controller settings (delays, control frequency) than active compliance, and allowed for the necessary amount of controllability compared to pure passive compliance. We finally note that the engineered compliance ratios were robustly handling feedback delays similar to the neuromuscular sensorimotor delays reported of running animals of equal size to the presented hybrid robot leg.[1]

To sum up, in this dissertation, we first introduced a novel bioinspired clutchable parallel elastic leg. We showed the merit of this leg in terms of energy efficiency and increasing robot speed. Then we showed power amplification of the DE tendon system during walking and running. Then we showed the contribution of the DE tendon to in-

---

[1] This paragraph uses original or modified text from [21, 20]

creasing speed and reducing system energy besides the DE tendon clutching function. After improving the leg physical model, we investigated the different roles of the DE tendon for the front and the hind leg in the quadrupedal animal. We showed that the front leg benefits from DE tendon and the hind leg does not need the DE tendon to clutch parallel elasticity. We also showed that the parallel elasticity reduces energy during the stance phase and allows the controller to reject sensorimotor delays in the system and provides stable locomotion at high delays and low control update rate frequencies.

Bibliography

[1] `https://www.elsevier.com/authors/policies-and-guidelines/credit-author-statement`.

[2] A. Abourachid and E. Höfling. The legs: a key to bird evolutionary success. *Journal of Ornithology*, 153(1):193–198, 2012.

[3] M. Ahmadi and M. Buehler. The ARL monopod II running robot: control and energetics. In *1999 IEEE International Conference on Robotics and Automation, 1999. Proceedings*, volume 3, pages 1689–1694, 1999. doi: 10.1109/ROBOT.1999.770352.

[4] M. AhmadSharbafi, M. J. Yazdanpanah, M. N. Ahmadabadi, and A. Seyfarth. Parallel compliance design for increasing robustness and efficiency in legged locomotion-theoretical background and applications. *IEEE/ASME Transactions on Mechatronics*, 2020. doi: 10.1109/TMECH.2020.3019686.

[5] R. Alexander. Optimization and gaits in the locomotion of vertebrates. *Physiological reviews*, 69(4):1199–1227, 1989.

[6] R. Alexander. Three uses for springs in legged locomotion. *International Journal of Robotics Research*, 9(2):53–61, 1990. doi: 10.1177/027836499000900205. URL `https://www.frontiersin.org/articles/10.3389/fnbot.2019.00064/full#supplementary-material`.

[7] R. M. Alexander. Storage of elastic strain energy in muscle and other tissues. *Nature*, 265:114–117, Jan. 1977. URL `http://adsabs.harvard.edu/abs/1977Natur.265..114A`.

[8] R. M. Alexander. Elastic energy stores in running vertebrates. *American Zoologist*, 24(1):85–94, 1984.

[9] R. M. Alexander. Elastic Energy Stores in Running Vertebrates. *American Zoologist*, 24(1):85 –94, Jan. 1984. doi: 10.1093/icb/24.1.85. URL `http://icb.oxfordjournals.org/content/24/1/85.abstract`.

[10] R. M. Alexander. Walking and Running: Legs and leg movements are subtly adapted to minimize the energy costs of locomotion. *American Scientist*, 72

(4):348–354, July 1984. ISSN 0003-0996. URL `http://www.jstor.org/stable/27852758`.

[11] R. M. Alexander. Three Uses for Springs in Legged Locomotion. *The International Journal of Robotics Research*, 9(2):53–61, Apr. 1990. ISSN 0278-3649, 1741-3176. doi: 10.1177/027836499000900205. URL `http://ijr.sagepub.com/content/9/2/53`.

[12] R. M. Alexander, G. Maloiy, R. Njau, and A. Jayes. Mechanics of running of the ostrich (struthio camelus). *Journal of Zoology*, 187(2):169–178, 1979.

[13] V. R. Allen, R. E. Kambic, S. M. Gatesy, and J. R. Hutchinson. Gearing effects of the patella (knee extensor muscle sesamoid) of the helmeted guineafowl during terrestrial locomotion. *Journal of Zoology*, pages 178–187, 2017. ISSN 1469-7998. doi: 10.1111/jzo.12485. URL `http://onlinelibrary.wiley.com/doi/10.1111/jzo.12485/abstract`.

[14] E. Ambrose and A. D. Ames. Improved performance on moving-mass hopping robots with parallel elasticity. In *2020 IEEE International Conference on Robotics and Automation (ICRA)*, pages 2457–2463. IEEE, 2020. doi: 10.1109/ICRA40945.2020.9197070.

[15] A. Ananthanarayanan, M. Azadi, and S. Kim. Towards a bio-inspired leg design for high-speed running. *Bioinspiration & Biomimetics*, 7(4):046005, Dec. 2012. ISSN 1748-3182, 1748-3190. doi: 10.1088/1748-3182/7/4/046005. URL `http://iopscience.iop.org/1748-3182/7/4/046005`.

[16] A. Ananthanarayanan, S. Foong, and S. Kim. A compact two DOF magneto-elastomeric force sensor for a running quadruped. In *2012 IEEE International Conference on Robotics and Automation (ICRA)*, pages 1398 –1403, May 2012. doi: 10.1109/ICRA.2012.6225201.

[17] S. Aoi, T. Ohashi, R. Bamba, S. Fujiki, D. Tamura, T. Funato, K. Senda, Y. Ivanenko, and K. Tsuchiya. Neuromusculoskeletal model that walks and runs across a speed range with a few motor control parameter changes based on the muscle synergy hypothesis. *Scientific Reports*, 9(1):369, Dec. 2019. ISSN 2045-2322. doi: 10.1038/s41598-018-37460-3. URL `http://www.nature.com/articles/s41598-018-37460-3`.

[18] K. Arikawa and S. Hirose. Development of quadruped walking robot TITAN-VIII. In *Proceedings of the 1996 IEEE/RSJ International Conference on Intelligent Robots and Systems '96, IROS 96*, volume 1, pages 208–214. IEEE, Nov. 1996. ISBN 0-7803-3213-X. doi: 10.1109/IROS.1996.570670.

[19] M. S. Ashtiani, A. Aghamaleki Sarvestani, and A. Badri-Sprwitz. Hybrid Parallel Compliance Allows Robots to Operate With Sensorimotor Delays and Low Control Frequencies. *Frontiers in Robotics and AI*, 8, 2021. ISSN 2296-9144. doi: 10.3389/frobt.2021.645748. URL `https://www.frontiersin.org/articles/10.3389/frobt.2021.645748/full`.

[20] M. S. Ashtiani, A. A. Sarvestani, and A. T. Badri-Spröwitz. Hybrid parallel compliance allows robots to operate with sensorimotor delays and low control frequencies. *Frontiers in Robotics and AI*, 8:170, 2021.

[21] A. Badri-Spröwitz, A. Aghamaleki Sarvestani, M. Sitti, and M. A. Daley. Birdbot achieves energy-efficient gait with minimal control using avian-inspired leg clutching. *Science Robotics*, 7(64):eabg4055, 2022.

[22] H. Barazesh and M. Ahmad Sharbafi. A biarticular passive exosuit to support balance control can reduce metabolic cost of walking. *Bioinspiration & Biomimetics*, 15(3):036009, Mar. 2020. ISSN 1748-3190. doi: 10.1088/1748-3190/ab70ed. URL `https://iopscience.iop.org/article/10.1088/1748-3190/ab70ed`.

[23] Z. Batts, J. Kim, and K. Yamane. Design of a hopping mechanism using a voice coil actuator: Linear elastic actuator in parallel (LEAP). In *2016 IEEE International Conference on Robotics and Automation (ICRA)*, pages 655–660, May 2016. doi: 10.1109/ICRA.2016.7487191.

[24] J. E. A. Bertram, A. Gutmann, J. Randev, and M. Hulliger. Domestic cat walking parallels human constrained optimization: Optimization strategies and the comparison of normal and sensory deficient individuals. *Human Movement Science*, 36:154–166, Aug. 2014. ISSN 0167-9457. doi: 10.1016/j.humov.2014.05.008. URL `http://www.sciencedirect.com/science/article/pii/S0167945714000876`.

[25] A. A. Biewener. Scaling Body Support in Mammals: Limb Posture and Muscle Mechanics. *Science*, 245(4913):45–48, July 1989. ISSN 0036-8075, 1095-9203. doi: 10.1126/science.2740914. URL `http://www.sciencemag.org/content/245/4913/45`.

[26] A. V. Birn-Jeffery, C. M. Hubicki, Y. Blum, D. Renjewski, J. W. Hurst, and M. A. Daley. Don't break a leg: running birds from quail to ostrich prioritise leg safety and economy on uneven terrain. *Journal of Experimental Biology*, 217(21):3786–3796, 2014.

[27] P. J. Bishop, K. B. Michel, A. Falisse, A. R. Cuff, V. R. Allen, F. D. Groote, and J. R. Hutchinson. Computational modelling of muscle fibre operating ranges in

the hindlimb of a small ground bird (Eudromia elegans), with implications for modelling locomotion in extinct species. *PLOS Computational Biology*, 17(4): e1008843, Apr. 2021. ISSN 1553-7358. doi: 10.1371/journal.pcbi.1008843. URL `https://journals.plos.org/ploscompbiol/article?id=10.1371/journal.pcbi.1008843`. Publisher: Public Library of Science.

[28] G. Bledt, M. J. Powell, B. Katz, J. D. Carlo, P. M. Wensing, and S. Kim. MIT Cheetah 3: Design and Control of a Robust, Dynamic Quadruped Robot. In *2018 IEEE/RSJ International Conference on Intelligent Robots and Systems (IROS)*, pages 2245–2252, Oct. 2018. doi: 10.1109/IROS.2018.8593885. ISSN: 2153-0866.

[29] G. Bledt, M. J. Powell, B. Katz, J. Di Carlo, P. M. Wensing, and S. Kim. Mit cheetah 3: Design and control of a robust, dynamic quadruped robot. In *2018 IEEE/RSJ International Conference on Intelligent Robots and Systems (IROS)*, pages 2245–2252. IEEE, 2018.

[30] G. Bledt, P. M. Wensing, S. Ingersoll, and S. Kim. Contact Model Fusion for Event-Based Locomotion in Unstructured Terrains. In *2018 IEEE International Conference on Robotics and Automation (ICRA)*, pages 4399–4406, May 2018. doi: 10.1109/ICRA.2018.8460904. ISSN: 2577-087X.

[31] R. Blickhan. The spring-mass model for running and hopping. *Journal of biomechanics*, 22(11-12):1217–1227, 1989.

[32] R. Blickhan. The spring-mass model for running and hopping. *Journal of Biomechanics*, 22(11-12):1217–1227, 1989. ISSN 0021-9290. doi: 10.1016/0021-9290(89)90224-8. URL `http://www.sciencedirect.com/science/article/B6T82-4C4FF6M-P/2/ffc4c332ada4ee147e9aabf0f8b6b89d`.

[33] R. Blickhan, A. Seyfarth, H. Geyer, S. Grimmer, H. Wagner, and M. Günther. Intelligence by mechanics. *Philosophical Transactions of the Royal Society A: Mathematical, Physical and Engineering Sciences*, 365(1850):199–220, 2007. doi: 10.1098/rsta.2006.1911.

[34] Y. Blum, H. R. Vejdani, A. V. Birn-Jeffery, C. M. Hubicki, J. W. Hurst, and M. A. Daley. Swing-leg trajectory of running guinea fowl suggests task-level priority of force regulation rather than disturbance rejection. *PloS one*, 9(6):e100399, 2014.

[35] N. S. Bradley and A. Bekoff. Development of coordinated movement in chicks: I. temporal analysis of hindlimb muscle synergies at embryonic days 9 and 10. *Developmental Psychobiology: The Journal of the International Society for Developmental Psychobiology*, 23(8):763–782, 1990.

[36] D. J. Braun, S. Apte, O. Adiyatov, A. Dahiya, and N. Hogan. Compliant actuation for energy efficient impedance modulation. In *2016 IEEE International Conference on Robotics and Automation (ICRA)*, pages 636–641, May 2016. doi: 10.1109/ICRA.2016.7487188.

[37] A. Calanca, R. Muradore, and P. Fiorini. A review of algorithms for compliant control of stiff and fixed-compliance robots. *IEEE/ASME Transactions on Mechatronics*, 21(2):613–624, 2015. doi: 10.1109/TMECH.2015.2465849.

[38] G. A. Cavagna, H. Thys, and A. J. Zamboni. The sources of external work in level walking and running. *The Journal of physiology*, 262(3):639–657, 1976.

[39] Y.-H. Chang and L. H. Ting. Mechanical evidence that flamingos can support their body on one leg with little active muscular force. *Biology letters*, 13(5):20160948, 2017.

[40] Y.-H. Chang and L. H. Ting. Mechanical evidence that flamingos can support their body on one leg with little active muscular force. *Biology letters*, 13(5):20160948, 2017.

[41] J. Choi, S. Hong, W. Lee, S. Kang, and M. Kim. A Robot Joint With Variable Stiffness Using Leaf Springs. *IEEE Transactions on Robotics*, 27(2):229–238, Apr. 2011. ISSN 1552-3098. doi: 10.1109/TRO.2010.2100450.

[42] S. Collins and A. Ruina. A Bipedal Walking Robot with Efficient and Human-Like Gait. In *Proceedings of the 2005 IEEE International Conference on Robotics and Automation, 2005. ICRA 2005*, pages 1983–1988, 2005. doi: 10.1109/ROBOT.2005.1570404.

[43] S. Collins, A. Ruina, R. Tedrake, and M. Wisse. Efficient Bipedal Robots Based on Passive-Dynamic Walkers. *Science*, 307(5712):1082–1085, Feb. 2005. doi: 10.1126/science.1107799. URL `http://www.sciencemag.org/cgi/content/abstract/307/5712/1082`.

[44] S. H. Collins, M. Wisse, and A. Ruina. A Three-Dimensional Passive-Dynamic Walking Robot with Two Legs and Knees. *The International Journal of Robotics Research*, 20(7):607–615, July 2001. ISSN 0278-3649, 1741-3176. doi: 10.1177/02783640122067561. URL `http://ijr.sagepub.com/content/20/7/607`.

[45] S. Cotton, J. Godowski, C. Schmidt-Wetekam, N. Payton, I. M. C. Olaru, and J. Pratt. Bipedal Running: When Leg Architecture Inuences Speed, Efciency and Robustness. In *Dynamic Walking Proceedings, 7th Annual Dynamic Walking Conference*, pages 216–217, 2012. URL `https://www.ihmc.us/dwc2012files/2012_DynamicWalking_Proceedings.pdf`.

[46] S. Cotton, I. Olaru, M. Bellman, T. van der Ven, J. Godowski, and J. Pratt. FastRunner: A fast, efficient and robust bipedal robot. Concept and planar simulation. In *2012 IEEE International Conference on Robotics and Automation (ICRA)*, pages 2358–2364, 2012. doi: 10.1109/ICRA.2012.6225250.

[47] S. Cotton, J. C. Godowski, N. R. Payton, M. Vignati, l. Olaru, C. Schmidt-Wetekam, and C. Black. Multi-Legged Running Robot, Jan. 2016. URL `https://patents.google.com/patent/US20160001831A1/en`.

[48] E. Coumans and Y. Bai. Pybullet, a python module for physics simulation for games, robotics and machine learning. `http://pybullet.org`, 2016–2019.

[49] X. Da, R. Hartley, and J. W. Grizzle. Supervised learning for stabilizing underactuated bipedal robot locomotion, with outdoor experiments on the wave field. In *2017 IEEE International Conference on Robotics and Automation (ICRA)*, pages 3476–3483, May 2017. doi: 10.1109/ICRA.2017.7989397.

[50] M. A. Daley. Understanding the agility of running birds: sensorimotor and mechanical factors in avian bipedal locomotion. *Integrative and comparative biology*, 58(5):884–893, 2018.

[51] M. A. Daley and A. A. Biewener. Running over rough terrain reveals limb control for intrinsic stability. *Proceedings of the National Academy of Sciences*, 103(42): 15681–15686, 2006.

[52] M. A. Daley and A. A. Biewener. Leg muscles that mediate stability: mechanics and control of two distal extensor muscles during obstacle negotiation in the guinea fowl. *Philosophical Transactions of the Royal Society B: Biological Sciences*, 366(1570):1580–1591, 2011.

[53] M. A. Daley, J. R. Usherwood, G. Felix, and A. A. Biewener. Running over rough terrain: guinea fowl maintain dynamic stability despite a large unexpected change in substrate height. *J Exp Biol*, 209(1):171–187, Jan. 2006. doi: 10.1242/jeb.01986. URL `http://jeb.biologists.org/cgi/content/abstract/209/1/171`.

[54] M. A. Daley, G. Felix, and A. A. Biewener. Running stability is enhanced by a proximo-distal gradient in joint neuromechanical control. *Journal of Experimental Biology*, 210(3):383–394, 2007.

[55] M. A. Daley, G. Felix, and A. A. Biewener. Running stability is enhanced by a proximo-distal gradient in joint neuromechanical control. *Journal of Experimental Biology*, 210(3):383–394, 2007.

[56] M. A. Daley, A. Voloshina, and A. A. Biewener. The role of intrinsic muscle mechanics in the neuromuscular control of stable running in the guinea fowl. *The Journal of physiology*, 587(11):2693–2707, 2009.

[57] M. A. Daley, A. J. Channon, G. S. Nolan, and J. Hall. Preferred gait and walk–run transition speeds in ostriches measured using gps-imu sensors. *Journal of Experimental Biology*, 219(20):3301–3308, 2016.

[58] J. Delmerico, S. Mintchev, A. Giusti, B. Gromov, K. Melo, T. Horvat, C. Cadena, M. Hutter, A. Ijspeert, D. Floreano, et al. The current state and future outlook of rescue robotics. *Journal of Field Robotics*, 36(7):1171–1191, 2019.

[59] J.-M. Denoix and J.-P. Pailloux. Physiotherapie und Massage bei Pferden. *Stuttgart: Ulmer*, 2000.

[60] C. Di Natali, A. Sadeghi, A. Mondini, E. Bottenberg, B. Hartigan, A. De Eyto, L. O'Sullivan, E. Rocon, K. Stadler, B. Mazzolai, D. G. Caldwell, and J. Ortiz. Pneumatic Quasi-Passive Actuation for Soft Assistive Lower Limbs Exoskeleton. *Frontiers in Neurorobotics*, 14, 2020. ISSN 1662-5218. doi: 10.3389/fnbot.2020.00031.

[61] S. Diller, C. Majidi, and S. H. Collins. A lightweight, low-power electroadhesive clutch and spring for exoskeleton actuation. In *2016 IEEE International Conference on Robotics and Automation (ICRA)*, pages 682–689. IEEE, 2016.

[62] Y. Ding and H.-W. Park. Design and Experimental Implementation of a Quasi-Direct-Drive Leg for Optimized Jumping. In *2017 IEEE/RSJ International Conference on Intelligent Robots and Systems (IROS)*, pages 300–305, 2017.

[63] z. Drama and A. Sprwitz. Trunk pitch oscillations for energy trade-offs in bipedal running birds and robots. *Bioinspiration & Biomimetics*, 15(3):036013, 2020. ISSN 1748-3190. doi: 10.1088/1748-3190/ab7570. URL `http://iopscience.iop.org/10.1088/1748-3190/ab7570`.

[64] H. Elftman. The function of muscles in locomotion. *American Journal of Physiology-Legacy Content*, 125(2):357–366, Jan. 1939. ISSN 0002-9513. doi: 10.1152/ajplegacy.1939.125.2.357. URL `https://www.physiology.org/doi/10.1152/ajplegacy.1939.125.2.357`.

[65] D. J. Ellerby, M. Cleary, R. L. Marsh, and C. I. Buchanan. Measurement of maximum oxygen consumption in guinea fowl numida meleagris indicates that birds and mammals display a similar diversity of aerobic scopes during running. *Physiological and Biochemical Zoology*, 76(5):695–703, 2003.

[66] M. Ernst, M. Gtze, R. Blickhan, and R. Mller. Humans adjust the height of their center of mass within one step when running across camouflaged changes in ground level. *Journal of Biomechanics*, Dec. 2018. ISSN 0021-9290. doi: 10.1016/j.jbiomech.2018.12.036. URL `http://www.sciencedirect.com/science/article/pii/S0021929018309357`.

[67] C. Farley, J. Glasheen, and T. McMahon. Running springs: speed and animal size. *J Exp Biol*, 185(1):71–86, Dec. 1993. URL `http://jeb.biologists.org/cgi/content/abstract/185/1/71`.

[68] M. A. Fedak and H. J. Seeherman. Reappraisal of energetics of locomotion shows identical cost in bipeds and quadrupeds including ostrich and horse. *Nature*, 282 (5740):713–716, 1979.

[69] D. P. Ferris, M. Louie, and C. T. Farley. Running in the real world: adjusting leg stiffness for different surfaces. *Proceedings of the Royal Society of London. Series B: Biological Sciences*, 265(1400):989–994, June 1998. ISSN 0962-8452, 1471-2954. doi: 10.1098/rspb.1998.0388. URL `http://rspb.royalsocietypublishing.org/content/265/1400/989`.

[70] M. S. Fischer and R. Blickhan. The tri-segmented limbs of therian mammals: kinematics, dynamics, and self-stabilizationa review. *Journal of Experimental Zoology Part A: Comparative Experimental Biology*, 305(11):935–952, 2006.

[71] M. S. Fischer, N. Schilling, M. Schmidt, D. Haarhaus, and H. Witte. Basic limb kinematics of small therian mammals. *J Exp Biol*, 205(9):1315–1338, May 2002. URL `http://jeb.biologists.org/cgi/content/abstract/205/9/1315`.

[72] M. S. Fischer, K. Lilje, J. Laustrer, and A. Andikfar. *Dogs in motion*. VDH Service, 2011.

[73] F. Flacco, A. D. Luca, I. Sardellitti, and N. G. Tsagarakis. On-line estimation of variable stiffness in flexible robot joints. *The International Journal of Robotics Research*, 31(13):1556–1577, Nov. 2012. ISSN 0278-3649, 1741-3176. doi: 10.1177/0278364912461813. URL `http://ijr.sagepub.com/content/31/13/1556`.

[74] H. Forssberg, S. Grillner, and S. Rossignol. Phasic gain control of reflexes from the dorsum of the paw during spinal locomotion. *Brain Research*, 132(1): 121–139, Aug. 1977. ISSN 0006-8993. doi: 10.1016/0006-8993(77)90710-7. URL `https://www.sciencedirect.com/science/article/pii/0006899377907107`.

[75] A. Four, A. Nordez, and C. Cornu. Effects of eccentric training on mechanical properties of the plantar flexor muscle-tendon complex. *Journal of Applied Physiology*, 114(5):523–537, Dec. 2012. ISSN 8750-7587. doi: 10.1152/japplphysiol.01313.2011. URL `https://journals.physiology.org/doi/full/10.1152/japplphysiol.01313.2011`. Publisher: American Physiological Society.

[76] D. W. Franklin and D. M. Wolpert. Computational Mechanisms of Sensorimotor Control. *Neuron*, 72(3):425–442, Nov. 2011. ISSN 0896-6273. doi: 10.1016/j.neuron.2011.10.006. URL `https://www.cell.com/neuron/abstract/S0896-6273(11)00891-9`. Publisher: Elsevier.

[77] Y. Fukuoka, H. Kimura, and A. H. Cohen. Adaptive dynamic walking of a quadruped robot on irregular terrain based on biological concepts. *The International Journal of Robotics Research*, 22(3-4):187–202, 2003.

[78] D. Gangl, G. E. Weissengruber, M. Egerbacher, and G. Forstenpointner. Anatomical Description of the Muscles of the Pelvic Limb in the Ostrich (Struthio camelus). *Anatomia, Histologia, Embryologia*, 33(2):100–114, Apr. 2004. ISSN 1439-0264. doi: 10.1111/j.1439-0264.2003.00522.x. URL `http://onlinelibrary.wiley.com/doi/10.1111/j.1439-0264.2003.00522.x/abstract`.

[79] S. Gatesy and A. Biewener. Bipedal locomotion: effects of speed, size and limb posture in birds and humans. *Journal of Zoology*, 224(1):127–147, 1991.

[80] S. M. Gatesy. Guineafowl hind limb function. ii: Electromyographic analysis and motor pattern evolution. *Journal of Morphology*, 240(2):127–142, 1999.

[81] H. Geyer and H. Herr. A muscle-reflex model that encodes principles of legged mechanics produces human walking dynamics and muscle activities. *IEEE Transactions on neural systems and rehabilitation engineering*, 18(3):263–273, 2010.

[82] H. Geyer, A. Seyfarth, and R. Blickhan. Compliant leg behaviour explains basic dynamics of walking and running. *Proceedings of the Royal Society of London B: Biological Sciences*, 273(1603):2861–2867, 2006.

[83] M. Gnther, V. A. Sholukha, D. Kessler, V. Wank, and R. Blickhan. Dealing with skin motion and wobbling masses in inverse dynamics. *Journal of Mechanics in Medicine and Biology*, 3(03n04):309–335, 2003.

[84] J. Godowski. Fast Runner Limb Articulation System, Aug. 2013. URL `http://www.google.com/patents/US20130192406`.

[85] J. C. Gordon, J. W. Rankin, and M. A. Daley. How do treadmill speed and terrain visibility influence neuromuscular control of guinea fowl locomotion? *Journal of Experimental Biology*, 218(19):3010–3022, 2015.

[86] J. C. Gordon, N. C. Holt, A. Biewener, and M. A. Daley. Tuning of feedforward control enables stable muscle force-length dynamics after loss of autogenic proprioceptive feedback. *Elife*, 9:e53908, 2020.

[87] J. Gray. Studies in the Mechanics of the Tetrapod Skeleton. *J Exp Biol*, 20(2):88–116, June 1944. URL `http://jeb.biologists.org/cgi/content/abstract/20/2/88`.

[88] S. Grillner and P. Wallen. Central Pattern Generators for Locomotion, with Special Reference to Vertebrates. *Annual Review of Neuroscience*, 8(1):233–261, 1985. doi: 10.1146/annurev.ne.08.030185.001313.

[89] M. Grimmer, M. Eslamy, S. Gliech, and A. Seyfarth. A comparison of parallel-and series elastic elements in an actuator for mimicking human ankle joint in walking and running. In *Robotics and Automation (ICRA), 2012 IEEE International Conference on*, pages 2463–2470. IEEE, 2012. URL `http://ieeexplore.ieee.org/xpls/abs_all.jsp?arnumber=6224967`.

[90] F. Grimminger, A. Meduri, M. Khadiv, J. Viereck, M. Wüthrich, M. Naveau, V. Berenz, S. Heim, F. Widmaier, T. Flayols, J. Fiene, A. Badri-Spröwitz, and L. Righetti. An Open Torque-Controlled Modular Robot Architecture for Legged Locomotion Research. *IEEE Robotics and Automation Letters*, 5(2):3650–3657, Apr. 2020. ISSN 2377-3766. doi: 10.1109/LRA.2020.2976639.

[91] F. Grimminger, A. Meduri, M. Khadiv, J. Viereck, M. Wüthrich, M. Naveau, V. Berenz, S. Heim, F. Widmaier, T. Flayols, et al. An open torque-controlled modular robot architecture for legged locomotion research. *IEEE Robotics and Automation Letters*, 5(2):3650–3657, 2020. doi: 10.1109/LRA.2020.2976639.

[92] F. Gunther, Y. Shu, and F. Iida. Parallel elastic actuation for efficient large payload locomotion. In *2015 IEEE International Conference on Robotics and Automation (ICRA)*, pages 823–828, May 2015. doi: 10.1109/ICRA.2015.7139273.

[93] B. Hammoud, M. Khadiv, and L. Righetti. Impedance Optimization for Uncertain Contact Interactions Through Risk Sensitive Optimal Control. *arXiv:2011.04684 [cs, eess]*, Nov. 2020. URL `http://arxiv.org/abs/2011.04684`.

[94] D. F. Häufle, M. Taylor, S. Schmitt, and H. Geyer. A clutched parallel elastic actuator concept: Towards energy efficient powered legs in prosthetics and robotics. In *2012 4th IEEE RAS & EMBS International Conference on Biomedical Robotics and Biomechatronics (BioRob)*, pages 1614–1619. IEEE, 2012.

[95] S. Heim, F. Ruppert, A. A. Sarvestani, and A. Spröwitz. Shaping in practice: training wheels to learn fast hopping directly in hardware. In *2018 IEEE International Conference on Robotics and Automation (ICRA)*, pages 5076–5081. IEEE, 2018.

[96] M. Hildebrand. The mechanics of horse legs. *American Scientist*, pages 594–601, 1987. URL `http://www.jstor.org/stable/27854888`.

[97] A. Hof, B. Geelen, and J. Van den Berg. Calf muscle moment, work and efficiency in level walking; role of series elasticity. *Journal of biomechanics*, 16(7):523–537, 1983.

[98] N. Hogan. Adaptive control of mechanical impedance by coactivation of antagonist muscles. *IEEE Transactions on automatic control*, 29(8):681–690, 1984. Publisher: IEEE.

[99] C. Hubicki, J. Grimes, M. Jones, D. Renjewski, A. Spröwitz, A. Abate, and J. Hurst. ATRIAS: Design and validation of a tether-free 3D-capable spring-mass bipedal robot. *The International Journal of Robotics Research*, 35(12):1497–1521, Oct. 2016. ISSN 0278-3649, 1741-3176. doi: 10.1177/0278364916648388. URL `http://ijr.sagepub.com/content/35/12/1497`.

[100] J. R. Hutchinson, F. C. Anderson, S. S. Blemker, and S. L. Delp. Analysis of hindlimb muscle moment arms in Tyrannosaurus rex using a three-dimensional musculoskeletal computer model: implications for stance, gait, and speed. *Paleobiology*, 31(4):676–701, Dec. 2005. ISSN 0094-8373. doi: 10.1666/04044.1. URL `http://www.psjournals.org/doi/abs/10.1666/04044.1`.

[101] J. R. Hutchinson, J. W. Rankin, J. Rubenson, K. H. Rosenbluth, R. A. Siston, and S. L. Delp. Musculoskeletal modelling of an ostrich (*Struthio camelus*) pelvic limb: influence of limb orientation on muscular capacity during locomotion. *PeerJ*, 3:e1001, 2015. ISSN 2167-8359. doi: 10.7717/peerj.1001. URL `https://dx.doi.org/10.7717/peerj.1001`.

[102] M. Hutter, C. D. Remy, M. A. Hoepflinger, and R. Siegwart. Scarleth: Design and control of a planar running robot. In *2011 IEEE/RSJ International Conference on Intelligent Robots and Systems*, pages 562–567. IEEE, 2011. doi: 10.1142/9789814415958_0062.

[103] M. Hutter, C. Gehring, M. Bloesch, M. A. Hoepflinger, C. D. Remy, and R. Siegwart. Starleth: A compliant quadruped robot for fast, efficient, and versatile locomotion. In *Adaptive Mobile Robotics*, pages 483–490. WORLD SCIENTIFIC, 7 2012. doi: 10.1142/9789814415958_0062.

[104] M. Hutter, C. Gehring, M. Hopflinger, M. Blosch, and R. Siegwart. Toward Combining Speed, Efficiency, Versatility, and Robustness in an Autonomous

Quadruped. *IEEE Transactions on Robotics*, PP(99):1–14, 2014. ISSN 1552-3098. doi: 10.1109/TRO.2014.2360493.

[105] M. Hutter, C. Gehring, D. Jud, A. Lauber, C. D. Bellicoso, V. Tsounis, J. Hwangbo, K. Bodie, P. Fankhauser, M. Bloesch, et al. Anymal-a highly mobile and dynamic quadrupedal robot. In *2016 IEEE/RSJ International Conference on Intelligent Robots and Systems (IROS)*, pages 38–44. IEEE, 2016.

[106] D. J. Hyun, S. Seok, J. Lee, and S. Kim. High speed trot-running: Implementation of a hierarchical controller using proprioceptive impedance control on the MIT Cheetah. *The International Journal of Robotics Research*, 33(11):1417–1445, Aug. 2014. ISSN 0278-3649, 1741-3176. doi: 10.1177/0278364914532150. URL `http://ijr.sagepub.com/content/early/2014/08/21/0278364914532150`.

[107] F. Iida and A. J. Ijspeert. Biologically inspired robotics. In *Springer Handbook of Robotics*, pages 2015–2034. Springer, 2016.

[108] F. Iida and R. Pfeifer. Cheap rapid locomotion of a quadruped robot: Self-stabilization of bounding gait. *Intelligent Autonomous Systems*, 8:642–649, 2004.

[109] A. J. Ijspeert. Central pattern generators for locomotion control in animals and robots: A review. *Neural Networks*, 21(4):642–653, May 2008. ISSN 0893-6080. doi: 10.1016/j.neunet.2008.03.014. URL `http://www.sciencedirect.com/science/article/B6T08-4SH6B9F-2/2/2e0a2fdad02d315becc218a6602f054d`.

[110] A. J. Ijspeert. Biorobotics: Using robots to emulate and investigate agile locomotion. *science*, 346(6206):196–203, 2014.

[111] A. J. Ijspeert. Biorobotics: Using robots to emulate and investigate agile locomotion. *Science*, 346(6206):196–203, Oct. 2014. ISSN 0036-8075, 1095-9203. doi: 10.1126/science.1254486. URL `http://www.sciencemag.org/content/346/6206/196`.

[112] A. J. Ijspeert, A. Crespi, D. Ryczko, and J.-M. Cabelguen. From swimming to walking with a salamander robot driven by a spinal cord model. *science*, 315 (5817):1416–1420, 2007.

[113] A. J. Ijspeert, A. Crespi, D. Ryczko, and J.-M. Cabelguen. From Swimming to Walking with a Salamander Robot Driven by a Spinal Cord Model. *Science*, 315 (5817):1416–1420, Mar. 2007. doi: 10.1126/science.1138353. URL `http://www.sciencemag.org/cgi/content/abstract/315/5817/1416`.

[114] Y. P. Ivanenko, R. E. Poppele, and F. Lacquaniti. Five basic muscle activation patterns account for muscle activity during human locomotion. *The Journal of Physiology*, 556(1):267–282, 2004. ISSN 1469-7793. doi: 10.1113/jphysiol.2003.057174. URL `http://onlinelibrary.wiley.com/doi/10.1113/jphysiol.2003.057174/abstract`.

[115] G. Jan Van Ingen Schenau. On the Action of Bi-Articular Muscles, a Review. *Netherlands Journal of Zoology*, 40(3):521–543, 1989. ISSN 0028-2960, 1568-542X. doi: 10.1163/156854290X00073. URL `https://brill.com/view/journals/njz/40/3/article-p521_7.xml`.

[116] K. E. Jones, K. D. Angielczyk, and S. E. Pierce. Stepwise shifts underlie evolutionary trends in morphological complexity of the mammalian vertebral column. *Nature communications*, 10(1):1–13, 2019.

[117] D. C. Kar. Design of Statically Stable Walking Robot: A Review. *Journal of Robotic Systems*, 20(11):671–686, Nov. 2003. ISSN 1097-4563. doi: 10.1002/rob.10118. URL `http://onlinelibrary.wiley.com/doi/10.1002/rob.10118/abstract`.

[118] N. Kashiri, A. Abate, S. J. Abram, A. Albu-Schaffer, P. J. Clary, M. Daley, S. Faraji, R. Furnemont, M. Garabini, H. Geyer, A. M. Grabowski, J. Hurst, J. Malzahn, G. Mathijssen, D. Remy, W. Roozing, M. Shahbazi, S. N. Simha, J.-B. Song, N. Smit-Anseeuw, S. Stramigioli, B. Vanderborght, Y. Yesilevskiy, and N. Tsagarakis. An overview on principles for energy efficient robot locomotion. *Frontiers Robotics AI*, 5(DEC):129, Dec. 2018. doi: 10.3389/frobt.2018.00129. URL `https://koreauniv.pure.elsevier.com/en/publications/an-overview-on-principles-for-energy-efficient-robot-locomotion`.

[119] B. Katz, J. Di Carlo, and S. Kim. Mini cheetah: A platform for pushing the limits of dynamic quadruped control. In *2019 International Conference on Robotics and Automation (ICRA)*, pages 6295–6301. IEEE, 2019.

[120] S. Kitano, S. Hirose, A. Horigome, and G. Endo. TITAN-XIII: sprawling-type quadruped robot with ability of fast and energy-efficient walking. *ROBOMECH Journal*, 3(1):1–16, Mar. 2016. ISSN 2197-4225. doi: 10.1186/s40648-016-0047-1. URL `http://link.springer.com/article/10.1186/s40648-016-0047-1`.

[121] T. Kubo, M. Sakamoto, A. Meade, and C. Venditti. Transitions between foot postures are associated with elevated rates of body size evolution in mammals. *Proceedings of the National Academy of Sciences*, 116(7):2618–2623, 2019.

[122] A. D. Kuo. The action of two-joint muscles: the legacy of WP Lombard. *Classics in movement science*, pages 289–316, 2001. Publisher: Human Kinetics: Champaign, IL.

[123] K. Kurokawa, R. Sato, S. Hiasa, A. Ming, F. Meng, H. Liu, X. Fan, X. Chen, Z. Yu, and Q. Huang. Introduction of Toe Mechanism with Bi-articular Tendon into Legged Robot. In *2018 IEEE International Conference on Mechatronics and Automation (ICMA)*, pages 1597–1602, Aug. 2018. doi: 10.1109/ICMA.2018.8484678.

[124] D. Lakatos, W. Friedl, and A. Albu-Schaffer. Eigenmodes of Nonlinear Dynamics: Definition, Existence, and Embodiment into Legged Robots with Elastic Elements. *IEEE Robotics and Automation Letters*, PP(99):1–1, 2017. ISSN 2377-3766. doi: 10.1109/LRA.2017.2658018.

[125] L. P. Lamas, R. P. Main, and J. R. Hutchinson. Ontogenetic scaling patterns and functional anatomy of the pelvic limb musculature in emus (dromaius novaehollandiae). *PeerJ*, 2:e716, 2014.

[126] D. Lee and M. W. Spong. Passive bilateral teleoperation with constant time delay. *IEEE transactions on robotics*, 22(2):269–281, 2006. Publisher: IEEE.

[127] C. Li, Y. Ding, and H.-W. Park. Centroidal-momentum-based trajectory generation for legged locomotion. *Mechatronics*, 68:102364, 2020. doi: 10.1016/j.mechatronics.2020.102364.

[128] S. W. Lipfert, M. Günther, D. Renjewski, and A. Seyfarth. Impulsive ankle push-off powers leg swing in human walking. *Journal of experimental biology*, 217(8): 1218–1228, 2014.

[129] X. Liu, A. Rossi, and I. Poulakakis. SPEAR: A monopedal robot with Switchable Parallel Elastic actuation. In *2015 IEEE/RSJ International Conference on Intelligent Robots and Systems (IROS)*, pages 5142–5147, Sept. 2015. doi: 10.1109/IROS.2015.7354101.

[130] X. Liu, A. Rossi, and I. Poulakakis. A switchable parallel elastic actuator and its application to leg design for running robots. *IEEE/ASME Transactions on Mechatronics*, 23(6):2681–2692, 2018. doi: 10.1109/TMECH.2018.2871670.

[131] X. Liu, A. Rossi, and I. Poulakakis. A Switchable Parallel Elastic Actuator and its Application to Leg Design for Running Robots. *IEEE/ASME Transactions on Mechatronics*, pages 1–1, 2018. ISSN 1083-4435. doi: 10.1109/TMECH.2018.2871670.

[132] W. P. Lombard. The tendon action and leverage of two-joint muscles of the hind leg of the frog, with special reference to the spring movement. *Contributions to medical research. Wahr, Ann Arbor*, pages 280–301, 1903.

[133] S. Longo, S. Cox, E. Azizi, M. Ilton, J. Olberding, R. St Pierre, and S. Patek. Beyond power amplification: latch-mediated spring actuation is an emerging framework for the study of diverse elastic systems. *Journal of Experimental Biology*, 222(15):jeb197889, 2019.

[134] M. Lorke, M. Willen, K. Lucas, M. Beyerbach, P. Wefstaedt, H. M. Escobar, and I. Nolte. Comparative kinematic gait analysis in young and old beagle dogs. *Journal of Veterinary Science*, 18(4):521–530, 2017. doi: https://doi.org/10.4142/jvs.2017.18.4.521.

[135] E. Mahdy and M. Raouf. Normal anatomical and diagnostic imaging techniques of the musculotendinous structures of the ostrich (Struthio camelus) foot. *Journal of Advanced Veterinary and Animal Research*, 7(2):242, 2020. ISSN 2311-7710. doi: 10.5455/javar.2020.g416. URL `https://www.ejmanager.com/fulltextpdf.php?mno=81080`.

[136] R. L. Marsh, D. J. Ellerby, J. A. Carr, H. T. Henry, and C. I. Buchanan. Partitioning the Energetics of Walking and Running: Swinging the Limbs Is Expensive. *Science*, 303(5654):80 –83, Jan. 2004. doi: 10.1126/science.1090704. URL `http://www.sciencemag.org/content/303/5654/80.abstract`.

[137] R. L. Marsh, D. J. Ellerby, H. T. Henry, and J. Rubenson. The energetic costs of trunk and distal-limb loading during walking and running in guinea fowl numida meleagris: I. organismal metabolism and biomechanics. *Journal of Experimental Biology*, 209(11):2050–2063, 2006.

[138] C. Mastalli, R. Budhiraja, W. Merkt, G. Saurel, B. Hammoud, M. Naveau, J. Carpentier, L. Righetti, S. Vijayakumar, and N. Mansard. Crocoddyl: An Efficient and Versatile Framework for Multi-Contact Optimal Control. In *2020 IEEE International Conference on Robotics and Automation (ICRA)*, pages 2536–2542, May 2020. doi: 10.1109/ICRA40945.2020.9196673. ISSN: 2577-087X.

[139] G. Mathijssen, R. Furnemont, B. Brackx, R. Van Ham, D. Lefeber, and B. Vanderborght. Design of a novel intermittent self-closing mechanism for a MACCEPA-based Series-Parallel Elastic Actuator (SPEA). In *2014 IEEE/RSJ International Conference on Intelligent Robots and Systems (IROS 2014)*, pages 2809–2814, Sept. 2014. doi: 10.1109/IROS.2014.6942947.

[140] A. Mazumdar, S. J. Spencer, C. Hobart, J. Salton, M. Quigley, T. Wu, S. Bertrand, J. Pratt, and S. P. Buerger. Parallel Elastic Elements Improve Energy Efficiency on

the STEPPR Bipedal Walking Robot. *IEEE/ASME Transactions on Mechatronics*, PP(99):1–1, 2016. ISSN 1083-4435. doi: 10.1109/TMECH.2016.2631170.

[141] T. McGeer. Passive Dynamic Walking. *The International Journal of Robotics Research*, 9(2):62–82, Apr. 1990. doi: 10.1177/027836499000900206. URL `http://ijr.sagepub.com/cgi/content/abstract/9/2/62`.

[142] C. P. McGowan, H. A. Duarte, J. B. Main, and A. A. Biewener. Effects of load carrying on metabolic cost and hindlimb muscle dynamics in guinea fowl (Numida meleagris). *Journal of Applied Physiology*, 101(4):1060–1069, Oct. 2006. ISSN 8750-7587, 1522-1601. doi: 10.1152/japplphysiol.01538.2005. URL `http://jap.physiology.org/content/101/4/1060`.

[143] M. P. McGuigan and A. M. Wilson. The effect of gait and digital flexor muscle activation on limb compliance in the forelimb of the horse equus caballus. *Journal of Experimental Biology*, 206(8):1325–1336, 2003.

[144] T. A. McMahon. The role of compliance in mammalian running gaits. *Journal of Experimental Biology*, 115(1):263–282, Mar. 1985. ISSN 0022-0949, 1477-9145. URL `http://jeb.biologists.org/content/115/1/263`.

[145] T. A. McMahon and G. C. Cheng. The mechanics of running: how does stiffness couple with speed? *Journal of Biomechanics*, 23:65–78, 1990. ISSN 0021-9290. URL `http://www.ncbi.nlm.nih.gov/pubmed/2081746`.

[146] K. Miyashita, Y. Masuda, M. Gunji, A. Fukuhara, K. Tadakuma, and M. Ishikawa. Emergence of Swing-to-Stance Transition from Interlocking Mechanism in Horse Hindlimb. In *2020 IEEE/RSJ International Conference on Intelligent Robots and Systems (IROS)*, pages 7860–7865, Las Vegas, NV, USA, Oct. 2020. IEEE. ISBN 978-1-72816-212-6. doi: 10.1109/IROS45743.2020.9341026. URL `https://ieeexplore.ieee.org/document/9341026/`.

[147] A. Mo, F. Izzi, D. F. Haeufle, and A. Badri-Spröwitz. Effective viscous damping enables morphological computation in legged locomotion. *arXiv preprint arXiv:2005.05725*, 2020.

[148] A. Mo, F. Izzi, D. F. B. Haeufle, and A. Badri-Sprwitz. Effective Viscous Damping Enables Morphological Computation in Legged Locomotion. *Frontiers in Robotics and AI*, 7, 2020. ISSN 2296-9144. doi: 10.3389/frobt.2020.00110. URL `https://www.frontiersin.org/articles/10.3389/frobt.2020.00110/full`.

[149] H. L. More and J. M. Donelan. Scaling of sensorimotor delays in terrestrial mammals. *Proceedings of the Royal Society B: Biological Sciences*, 285(1885): 20180613, 2018. doi: 10.1098/rspb.2018.0613.

[150] H. L. More, J. R. Hutchinson, D. F. Collins, D. J. Weber, S. K. H. Aung, and J. M. Donelan. Scaling of Sensorimotor Control in Terrestrial Mammals. *Proceedings of the Royal Society B: Biological Sciences*, 277(1700):3563–3568, Dec. 2010. ISSN 0962-8452, 1471-2954. doi: 10.1098/rspb.2010.0898. URL `http://rspb.royalsocietypublishing.org/content/277/1700/3563`.

[151] H. Nam, Q. Xu, and D. Hong. A Reliable Low-Cost Foot Contact Sensor for Legged Robots. In *2020 17th International Conference on Ubiquitous Robots (UR)*, pages 219–224, June 2020. doi: 10.1109/UR49135.2020.9144878. ISSN: 2325-033X.

[152] K. Narioka, A. Rosendo, A. Sprwitz, and K. Hosoda. Development of a Minimalistic Pneumatic Quadruped Robot for Fast Locomotion. In *Proceedings of IEEE International Conference on Robotics and Biomimetics (ROBIO)*, pages 307–311, Guangzhou, China, 2012. doi: 10.1109/ROBIO.2012.6490984.

[153] R. Nasiri, M. Khoramshahi, M. Shushtari, and M. N. Ahmadabadi. Adaptation in variable parallel compliance: Towards energy efficiency in cyclic tasks. *IEEE/ASME Transactions on Mechatronics*, 22(2):1059–1070, 2016. doi: 10.1109/TMECH.2016.2637826.

[154] T. R. Nichols, T. C. Cope, and T. A. Abelew. 8 rapid spinal mechanisms of motor coordination. *Exercise and sport sciences reviews*, 27(1):255–284, 1999.

[155] T. D. Niehues, P. Rao, and A. D. Deshpande. Compliance in parallel to actuators for improving stability of robotic hands during grasping and manipulation. *The International Journal of Robotics Research*, 34(3):256–269, 2015. doi: 10.1177/0278364914558016.

[156] K. Nishikawa, A. A. Biewener, P. Aerts, A. N. Ahn, H. J. Chiel, M. A. Daley, T. L. Daniel, R. J. Full, M. E. Hale, T. L. Hedrick, et al. Neuromechanics: an integrative approach for understanding motor control. *Integrative and Comparative Biology*, 47(1):16–54, 2007.

[157] H.-W. Park, S. Park, and S. Kim. Variable-speed quadrupedal bounding using impulse planning: Untethered high-speed 3D Running of MIT Cheetah 2. In *2015 IEEE International Conference on Robotics and Automation (ICRA)*, pages 5163–5170, May 2015. doi: 10.1109/ICRA.2015.7139918.

[158] H.-W. Park, P. M. Wensing, and S. Kim. High-speed bounding with the MIT Cheetah 2: Control design and experiments. *The International Journal of Robotics Research*, page 0278364917694244, Mar. 2017. ISSN 0278-3649. doi: 10.1177/0278364917694244. URL `http://dx.doi.org/10.1177/0278364917694244`.

[159] S. N. Patek, B. N. Nowroozi, J. E. Baio, R. L. Caldwell, and A. P. Summers. Linkage mechanics and power amplification of the mantis shrimp's strike. *Journal of Experimental Biology*, 210(20):3677–3688, Oct. 2007. ISSN 0022-0949, 1477-9145. doi: 10.1242/jeb.006486. URL `http://jeb.biologists.org/content/210/20/3677`.

[160] R. Petereit. Electronics, software and analysis of a bioinspired sensorized quadrupedal robot. Master's thesis, Technische Universitt Mnchen, 2019.

[161] R. Pfeifer, M. Lungarella, and F. Iida. Self-Organization, Embodiment, and Biologically Inspired Robotics. *Science*, 318(5853):1088–1093, Nov. 2007. doi: 10.1126/science.1145803. URL `http://www.sciencemag.org/cgi/content/abstract/318/5853/1088`.

[162] M. Plooij, G. Mathijssen, P. Cherelle, D. Lefeber, and B. Vanderborght. Lock Your Robot: A Review of Locking Devices in Robotics. *IEEE Robotics Automation Magazine*, 22(1):106–117, Mar. 2015. ISSN 1070-9932. doi: 10.1109/MRA.2014.2381368.

[163] M. Plooij, M. Wisse, and H. Vallery. Reducing the energy consumption of robots using the bidirectional clutched parallel elastic actuator. *IEEE Transactions on Robotics*, 32(6):1512–1523, 2016. doi: 10.1109/TRO.2016.2604496.

[164] M. Plooij, M. Wisse, and H. Vallery. Reducing the Energy Consumption of Robots Using the Bidirectional Clutched Parallel Elastic Actuator. *IEEE Transactions on Robotics*, 32(6):1512–1523, Dec. 2016. ISSN 1941-0468. doi: 10.1109/TRO.2016.2604496.

[165] M. Plooij, W. Wolfslag, and M. Wisse. Clutched elastic actuators. *IEEE/ASME Transactions on Mechatronics*, 22(2):739–750, 2017.

[166] B. Ponton, A. Herzog, A. Del Prete, S. Schaal, and L. Righetti. On time optimization of centroidal momentum dynamics. In *2018 IEEE International Conference on Robotics and Automation (ICRA)*, pages 5776–5782. IEEE, 2018.

[167] R. Poppele and C. Terzuolo. Myotatic reflex: its input-output relation. *Science*, 159(3816):743–745, 1968.

[168] J. Pratt and G. Pratt. Intuitive control of a planar bipedal walking robot. In *1998 IEEE International Conference on Robotics and Automation, 1998. Proceedings*, volume 3, pages 2014–2021, 1998. doi: 10.1109/ROBOT.1998.680611.

[169] J. Pratt, P. Dilworth, and G. Pratt. Virtual model control of a bipedal walking robot. In *, 1997 IEEE International Conference on Robotics and Automation, 1997. Proceedings*, volume 1, pages 193–198, Apr. 1997. doi: 10.1109/ROBOT.1997.620037.

[170] J. E. Pratt. *Exploiting Inherent Robustness and Natural Dynamics in the Control of Bipedal Walking Robots*. Ph.D., Massachusetts Institute of Technology, Cambridge, June 2000.

[171] J. E. Pratt and B. T. Krupp. Series elastic actuators for legged robots. In *Unmanned Ground Vehicle Technology Vi*, volume 5422, pages 135–144. International Society for Optics and Photonics, 2004.

[172] M. H. Raibert, H. B. Brown Jr, and S. S. Murthy. Machines that walk. In *Robotics and Artificial Intelligence*, pages 345–364. Springer, 1984.

[173] J. W. Rankin, J. Rubenson, and J. R. Hutchinson. Inferring muscle functional roles of the ostrich pelvic limb during walking and running using computer optimization. *Journal of The Royal Society Interface*, 13(118):20160035, May 2016. ISSN 1742-5689, 1742-5662. doi: 10.1098/rsif.2016.0035. URL `http://rsif.royalsocietypublishing.org/content/13/118/20160035`.

[174] L. Righetti, J. Buchli, M. Mistry, M. Kalakrishnan, and S. Schaal. Optimal distribution of contact forces with inverse-dynamics control. *The International Journal of Robotics Research*, 32(3):280–298, Mar. 2013. ISSN 0278-3649, 1741-3176. doi: 10.1177/0278364912469821. URL `http://ijr.sagepub.com/content/32/3/280`.

[175] T. J. Roberts and E. Azizi. Flexible mechanisms: the diverse roles of biological springs in vertebrate movement. *Journal of experimental biology*, 214(3):353–361, 2011.

[176] T. J. Roberts and A. M. Gabaldn. Interpreting muscle function from EMG: lessons learned from direct measurements of muscle force. *Integrative and Comparative Biology*, 48(2):312–320, Aug. 2008. ISSN 1540-7063, 1557-7023. doi: 10.1093/icb/icn056. URL `http://icb.oxfordjournals.org/content/48/2/312`.

[177] T. J. Roberts and J. A. Scales. Adjusting muscle function to demand: joint work during acceleration in wild turkeys. *Journal of Experimental Biology*, 207(23): 4165–4174, Nov. 2004. ISSN 0022-0949, 1477-9145. doi: 10.1242/jeb.01253. URL `http://jeb.biologists.org/content/207/23/4165`.

[178] T. J. Roberts, R. L. Marsh, P. G. Weyand, and C. R. Taylor. Muscular force in running turkeys: the economy of minimizing work. *Science*, 275(5303):1113–1115, 1997.

[179] T. J. Roberts, M. S. Chen, and C. R. Taylor. Energetics of bipedal running. II. Limb design and running mechanics. *Journal of Experimental Biology*, 201

(19):2753–2762, Oct. 1998. ISSN 0022-0949, 1477-9145. URL `http://jeb.biologists.org/content/201/19/2753`.

[180] D. W. Robinson, J. E. Pratt, D. J. Paluska, and G. A. Pratt. Series elastic actuator development for a biomimetic walking robot. In *1999 IEEE/ASME International Conference on Advanced Intelligent Mechatronics (Cat. No. 99TH8399)*, pages 561–568. IEEE, 1999.

[181] F. Roos, H. Johansson, and J. Wikander. Optimal selection of motor and gearhead in mechatronic applications. *Mechatronics*, 16(1):63–72, 2006.

[182] F. Roos, H. Johansson, and J. Wikander. Optimal selection of motor and gearhead in mechatronic applications. *Mechatronics*, 16(1):63–72, Feb. 2006. ISSN 0957-4158. doi: 10.1016/j.mechatronics.2005.08.001. URL `http://www.sciencedirect.com/science/article/B6V43-4HC0PY9-1/2/5cfd133b35a4be3952050fa55bee7d2f`.

[183] W. Roozing, Z. Li, D. Caldwell, and N. Tsagarakis. Design Optimisation and Control of Compliant Actuation Arrangements in Articulated Robots for Improved Energy Efficiency. *IEEE Robotics and Automation Letters*, PP(99):1–1, 2016. ISSN 2377-3766. doi: 10.1109/LRA.2016.2521926.

[184] W. Roozing, Z. Ren, and N. G. Tsagarakis. An efficient leg with series–parallel and biarticular compliant actuation: design optimization, modeling, and control of the eleg. *The International Journal of Robotics Research*, page 0278364919893762, 2019. doi: 10.1177/0278364919893762.

[185] K. A. Rose, R. L. Nudds, and J. R. Codd. Intraspecific scaling of the minimum metabolic cost of transport in leghorn chickens (Gallus gallus domesticus): links with limb kinematics, morphometrics and posture. *Journal of Experimental Biology*, 218(7):1028–1034, Apr. 2015. ISSN 0022-0949. doi: 10.1242/jeb.111393. URL `https://doi.org/10.1242/jeb.111393`.

[186] E. J. Rouse, L. M. Mooney, and H. M. Herr. Clutchable series-elastic actuator: Implications for prosthetic knee design. *The International Journal of Robotics Research*, 33(13):1611–1625, 2014.

[187] E. J. Rouse, L. M. Mooney, and H. M. Herr. Clutchable series-elastic actuator: Implications for prosthetic knee design. *The International Journal of Robotics Research*, page 0278364914545673, Oct. 2014. ISSN 0278-3649, 1741-3176. doi: 10.1177/0278364914545673. URL `http://ijr.sagepub.com/content/early/2014/10/07/0278364914545673`.

[188] J. Rubenson, D. B. Heliams, D. G. Lloyd, and P. A. Fournier. Gait selection in the ostrich: mechanical and metabolic characteristics of walking and running with

and without an aerial phase. *Proceedings of the Royal Society of London. Series B: Biological Sciences*, 271(1543):1091–1099, 2004.

[189] J. Rubenson, D. G. Lloyd, T. F. Besier, D. B. Heliams, and P. A. Fournier. Running in ostriches (Struthio camelus): three-dimensional joint axes alignment and joint kinematics. *Journal of Experimental Biology*, 210(14):2548–2562, July 2007. ISSN 0022-0949, 1477-9145. doi: 10.1242/jeb.02792. URL `http://jeb.biologists.org/content/210/14/2548`.

[190] J. Rubenson, D. G. Lloyd, D. B. Heliams, T. F. Besier, and P. A. Fournier. Adaptations for economical bipedal running: the effect of limb structure on three-dimensional joint mechanics. *Journal of The Royal Society Interface*, 8(58):740–755, May 2011. ISSN 1742-5689, 1742-5662. doi: 10.1098/rsif.2010.0466. URL `http://rsif.royalsocietypublishing.org/content/8/58/740`.

[191] F. Ruppert and A. Badri-Spröwitz. Series elastic behavior of biarticular muscle-tendon structure in a robotic leg. *Frontiers in Neurorobotics*, 13:64, 2019.

[192] F. Ruppert and A. Badri-Spröwitz. Series Elastic Behavior of Biarticular Muscle-Tendon Structure in a Robotic Leg. *Frontiers in Neurorobotics*, 13:64, Aug. 2019. doi: 10.3389/fnbot.2019.00064.

[193] F. Ruppert and A. Badri-Sprwitz. FootTile: a Rugged Foot Sensor for Force and Center of Pressure Sensing in Soft Terrain. In *2020 IEEE International Conference on Robotics and Automation (ICRA)*, pages 4810–4816. IEEE, 2020. doi: 10.1109/ICRA40945.2020.9197466. URL `https://arxiv.org/abs/2005.09025`.

[194] T. Ryschon, M. Fowler, R. Wysong, A.-R. Anthony, and R. Balaban. Efficiency of human skeletal muscle in vivo: comparison of isometric, concentric, and eccentric muscle action. *Journal of applied physiology*, 83(3):867–874, 1997.

[195] N. U. Schaller. *Structural attributes contributing to locomotor performance in the ostrich*. PhD, University of Heidelberg, Heidelberg, Germany, 2008.

[196] N. U. Schaller, B. Herkner, R. Villa, and P. Aerts. The intertarsal joint of the ostrich (struthio camelus): anatomical examination and function of passive structures in locomotion. *Journal of anatomy*, 214(6):830–847, 2009.

[197] C. Semini, N. G. Tsagarakis, E. Guglielmino, M. Focchi, F. Cannella, and D. G. Caldwell. Design of hyq–a hydraulically and electrically actuated quadruped robot. *Proceedings of the Institution of Mechanical Engineers, Part I: Journal of Systems and Control Engineering*, 225(6):831–849, 2011.

[198] S. Seok, A. Wang, D. Otten, and S. Kim. Actuator design for high force proprioceptive control in fast legged locomotion. In *2012 IEEE/RSJ International Conference on Intelligent Robots and Systems*, pages 1970–1975. IEEE, 2012.

[199] S. Seok, A. Wang, D. Otten, and S. Kim. Actuator design for high force proprioceptive control in fast legged locomotion. In *2012 IEEE/RSJ International Conference on Intelligent Robots and Systems (IROS)*, pages 1970–1975, 2012. doi: 10.1109/IROS.2012.6386252.

[200] S. Seok, A. Wang, M. Y. Chuah, D. Otten, J. Lang, and S. Kim. Design principles for highly efficient quadrupeds and implementation on the mit cheetah robot. In *2013 IEEE International Conference on Robotics and Automation*, pages 3307–3312. IEEE, 2013.

[201] S. Seok, A. Wang, M. Y. Chuah, D. J. Hyun, J. Lee, D. M. Otten, J. H. Lang, and S. Kim. Design Principles for Energy-Efficient Legged Locomotion and Implementation on the MIT Cheetah Robot. *IEEE/ASME Transactions on Mechatronics*, 20(3):1117–1129, June 2015. ISSN 1941-014X. doi: 10.1109/TMECH.2014.2339013.

[202] M. Shafiee, G. Romualdi, S. Dafarra, F. J. A. Chavez, and D. Pucci. Online dcm trajectory generation for push recovery of torque-controlled humanoid robots. In *2019 IEEE-RAS 19th International Conference on Humanoid Robots (Humanoids)*, pages 671–678. IEEE, 2019. doi: 10.1109/Humanoids43949.2019.9034996.

[203] M. Shafiee-Ashtiani, A. Yousefi-Koma, and M. Shariat-Panahi. Robust bipedal locomotion control based on model predictive control and divergent component of motion. In *2017 IEEE International Conference on Robotics and Automation (ICRA)*, pages 3505–3510. IEEE, 2017. doi: 10.1109/ICRA.2017.7989401.

[204] A. A. Sharp, E. Ma, and A. Bekoff. Developmental changes in leg coordination of the chick at embryonic days 9, 11, and 13: uncoupling of ankle movements. *Journal of neurophysiology*, 82(5):2406–2414, 1999.

[205] J. A. Smith and I. Poulakakis. Rotary gallop in the untethered quadrupedal robot scout II. In *2004 IEEE/RSJ International Conference on Intelligent Robots and Systems, 2004. (IROS 2004). Proceedings*, volume 3, pages 2556– 2561. IEEE, Oct. 2004. ISBN 0-7803-8463-6. doi: 10.1109/IROS.2004.1389793.

[206] N. Smith, A. Wilson, K. Jespers, and R. Payne. Muscle architecture and functional anatomy of the pelvic limb of the ostrich (struthio camelus). *Journal of Anatomy*, 209(6):765–779, 2006.

[207] A. Spröwitz, A. Tuleu, M. Vespignani, M. Ajallooeian, E. Badri, and A. Ijspeert. Towards Dynamic Trot Gait Locomotion: Design, Control and Experiments with Cheetah-cub, a Compliant Quadruped Robot. *International Journal of Robotics Research*, 32(8):932 – 950, 2013. ISSN 0278-3649. doi: 10.1177/0278364913489205.

[208] A. Spröwitz, A. Tuleu, M. Vespignani, M. Ajallooeian, E. Badri, and A. J. Ijspeert. Towards dynamic trot gait locomotion: Design, control, and experiments with cheetah-cub, a compliant quadruped robot. *The International Journal of Robotics Research*, 32(8):932–950, 2013.

[209] A. Spröwitz, A. Tuleu, M. Ajallooeian, M. Vespignani, R. Möckel, P. Eckert, M. D'Haene, J. Degrave, A. Nordmann, B. Schrauwen, J. Steil, and A. J. Ijspeert. Oncilla robot: A versatile open-source quadruped research robot with compliant pantograph legs. *Frontiers in Robotics and AI*, 5, 2018. doi: 10.3389/frobt.2018.00067.

[210] A. Spröwitz, A. Tuleu, M. Ajallooeian, M. Vespignani, R. Möckel, P. Eckert, M. D'Haene, J. Degrave, A. Nordmann, B. Schrauwen, J. Steil, and A. J. Ijspeert. Oncilla Robot: A Versatile Open-Source Quadruped Research Robot With Compliant Pantograph Legs. *Frontiers in Robotics and AI*, 5, 2018. ISSN 2296-9144. doi: 10.3389/frobt.2018.00067.

[211] P. Stratmann, A. Albu-Schffer, and H. Jrntell. Scaling Our World View: How Monoamines Can Put Context Into Brain Circuitry. *Frontiers in Cellular Neuroscience*, 12, 2018. ISSN 1662-5102. doi: 10.3389/fncel.2018.00506. URL `https://www.frontiersin.org/articles/10.3389/fncel.2018.00506/full`.

[212] K. Takakusaki, R. Chiba, T. Nozu, and T. Okumura. Brainstem control of locomotion and muscle tone with special reference to the role of the mesopontine tegmentum and medullary reticulospinal systems. *Journal of Neural Transmission*, 123 (7):695–729, July 2016. ISSN 1435-1463. doi: 10.1007/s00702-015-1475-4. URL `https://doi.org/10.1007/s00702-015-1475-4`.

[213] R. Tedrake, T. W. Zhang, M.-f. Fong, and H. S. Seung. Actuating a simple 3D passive dynamic walker. In *Robotics and Automation, 2004. Proceedings. ICRA'04. 2004 IEEE International Conference on*, volume 5, pages 4656–4661. IEEE, 2004. URL `http://ieeexplore.ieee.org/abstract/document/1302452/`.

[214] L. H. Ting and H. J. Chiel. Muscle, biomechanics, and implications for neural control. *Neurobiology of Motor Control: Fundamental Concepts and New Directions*, pages 365–416, 2017.

[215] L. H. Ting, H. J. Chiel, R. D. Trumbower, J. L. Allen, J. L. McKay, M. E. Hackney, and T. M. Kesar. Neuromechanical principles underlying movement modularity and their implications for rehabilitation. *Neuron*, 86(1):38–54, 2015.

[216] S. Toxiri, A. Calanca, J. Ortiz, P. Fiorini, and D. G. Caldwell. A Parallel-Elastic Actuator for a Torque-Controlled Back-Support Exoskeleton. *IEEE Robotics and Automation Letters*, 3(1):492–499, Jan. 2018. ISSN 2377-3766. doi: 10.1109/LRA.2017.2768120.

[217] V. A. Tucker. The Energetic Cost of Moving About: Walking and running are extremely inefficient forms of locomotion. Much greater efficiency is achieved by birds, fishand bicyclists. *American Scientist*, 63(4):413–419, July 1975. ISSN 0003-0996. URL `http://www.jstor.org/stable/27845576`.

[218] V. A. Tucker et al. Energetic cost of locomotion in animals. *Comparative Biochemistry and Physiology*, 34:841–846, 1970.

[219] J. R. Usherwood and M. C. Granatosky. Limb work and joint work minimization reveal an energetic benefit to the elbows-back, knees-forward limb design in parasagittal quadrupeds. *Proceedings of the Royal Society B*, 287(1940): 20201517, 2020.

[220] A. J. Van den Bogert. Exotendons for assistance of human locomotion. *Biomedical engineering online*, 2(1):1–8, 2003.

[221] M. van den Broek. Fast Self-Stable Planar Bipedal Running. Master's thesis, Delft University of Technology, 2019.

[222] R. Van Ham, T. G. Sugar, B. Vanderborght, K. W. Hollander, and D. Lefeber. Compliant actuator designs. *IEEE Robotics & Automation Magazine*, 16(3):81–94, 2009.

[223] G. J. van Ingen Schenau, M. F. Bobbert, and R. H. Rozendal. The unique action of bi-articular muscles in complex movements. *Journal of Anatomy*, 155:1–5, Dec. 1987. ISSN 0021-8782. URL `https://www.ncbi.nlm.nih.gov/pmc/articles/PMC1261869/`.

[224] B. Vanderborght, A. Albu-Schaeffer, A. Bicchi, E. Burdet, D. G. Caldwell, R. Carloni, M. Catalano, O. Eiberger, W. Friedl, G. Ganesh, M. Garabini, M. Grebenstein, G. Grioli, S. Haddadin, H. Hoppner, A. Jafari, M. Laffranchi, D. Lefeber, F. Petit, S. Stramigioli, N. Tsagarakis, M. Van Damme, R. Van Ham, L. C. Visser, and S. Wolf. Variable impedance actuators: A review. *Robotics and Autonomous Systems*, 61(12):1601–1614, Dec. 2013. ISSN 0921-8890. doi: 10.1016/j.robot.2013.06.009. URL `http://www.sciencedirect.com/science/article/pii/S0921889013001188`.

[225] T. A. Varkonyi, I. J. Rudas, P. Pausits, and T. Haidegger. Survey on the control of time delay teleoperation systems. In *IEEE 18th International Conference on Intelligent Engineering Systems INES 2014*, pages 89–94. IEEE, 2014. doi: 10.1109/INES.2014.6909347.

[226] T. Verstraten, P. Beckerle, R. Furnmont, G. Mathijssen, B. Vanderborght, and D. Lefeber. Series and Parallel Elastic Actuation: Impact of natural dynamics on power and energy consumption. *Mechanism and Machine Theory*, 102:232–246, 2016. URL `http://www.sciencedirect.com/science/article/pii/S0094114X16300301`.

[227] G. E. Weissengruber, G. Forstenpointner, and D. Gangl. Gut zu Fu - funktionell-anatomische Aspekte des bipeden Laufens beim Afrikanischen Strau (Struthio camelus Linn, 1758). *Vet. Med. Austria*, 90:67–78, 2003.

[228] M. Wiggin, G. Sawicki, and S. Collins. An exoskeleton using controlled energy storage and release to aid ankle propulsion. In *2011 IEEE International Conference on Rehabilitation Robotics (ICORR)*, pages 1–5, June 2011. doi: 10.1109/ICORR.2011.5975342.

[229] A. Wilson and G. Lichtwark. The anatomical arrangement of muscle and tendon enhances limb versatility and locomotor performance. *Philosophical Transactions of the Royal Society B: Biological Sciences*, 366(1570):1540–1553, 2011.

[230] A. M. Wilson, J. C. Watson, and G. A. Lichtwark. A catapult action for rapid limb protraction. *Nature*, 421(6918):35–36, 2003. doi: https://doi.org/10.1038/421035a.

[231] A. M. Wilson, J. C. Watson, and G. A. Lichtwark. A catapult action for rapid limb protraction. *Nature*, 421(6918):35–36, Jan. 2003. ISSN 0028-0836. doi: 10.1038/421035a. URL `http://dx.doi.org/10.1038/421035a`.

[232] H. Witte, R. Hackert, K. Lilje, N. Schilling, D. Voges, G. Klauer, W. Ilg, J. Albiez, A. Seyfarth, D. Germann, M. Hiller, R. Dillmann, and M. Fischer. Transfer of biological principles into the construction of quadruped walking machines. In *Proceedings of the Second International Workshop on Robot Motion and Control. RoMoCo'01 (IEEE Cat. No.01EX535)*, pages 245–249, Oct 2001.

[233] H. Witte, R. Hackert, K. Lilje, N. Schilling, D. Voges, G. Klauer, W. Ilg, J. Albiez, A. Seyfarth, D. Germann, M. Hiller, R. Dillmann, and M. Fischer. Transfer of biological principles into the construction of quadruped walking machines. In *Robot Motion and Control, 2001 Proceedings of the Second International Workshop on*, pages 245 –249, 2001. doi: 10.1109/ROMOCO.2001.973462.

[234] H. Witte, J. Biltzinger, R. Hackert, N. Schilling, M. Schmidt, C. Reich, and M. S. Fischer. Torque patterns of the limbs of small therian mammals during locomotion on flat ground. *J Exp Biol*, 205(9):1339–1353, May 2002. URL `http://jeb.biologists.org/cgi/content/abstract/205/9/1339`.

[235] S. Wolf, G. Grioli, W. Friedl, M. Grebenstein, H. Hoeppner, E. Burdet, D. Caldwell, A. Bicchi, S. Stramigioli, and B. Vanderborght. Variable Stiffness Actuators: Review on Design and Components. *IEEE/ASME Transactions on Mechatronics*, PP(99):1–1, 2015. ISSN 1083-4435. doi: 10.1109/TMECH.2015.2501019.

[236] J. Yamaguchi and A. Takanishi. Design of biped walking robots having antagonistic driven joints using nonlinear spring mechanism. In , *Proceedings of the 1997 IEEE/RSJ International Conference on Intelligent Robots and Systems, 1997. IROS '97*, volume 1, pages 251–259 vol.1, 1997. doi: 10.1109/IROS.1997.649062.

[237] G.-Z. Yang, J. Bellingham, P. E. Dupont, P. Fischer, L. Floridi, R. Full, N. Jacobstein, V. Kumar, M. McNutt, R. Merrifield, B. J. Nelson, B. Scassellati, M. Taddeo, R. Taylor, M. Veloso, Z. L. Wang, and R. Wood. The grand challenges of Science Robotics. *Science Robotics*, 3(14):eaar7650, Jan. 2018. ISSN 2470-9476. doi: 10.1126/scirobotics.aar7650. URL `http://robotics.sciencemag.org/content/3/14/eaar7650`.

[238] Y. Yesilevskiy, Z. Gan, and C. D. Remy. Optimal configuration of series and parallel elasticity in a 2D Monoped. In *2016 IEEE International Conference on Robotics and Automation (ICRA)*, pages 1360–1365, May 2016. doi: 10.1109/ICRA.2016.7487269.

[239] Y. Yesilevskiy, Z. Gan, and C. David Remy. Energy-optimal hopping in parallel and series elastic one-dimensional monopeds. *Journal of Mechanisms and Robotics*, 10(3), 2018. doi: 10.1115/1.4039496.

[240] N. M. Young and B. HallgrÍmsson. Serial homology and the evolution of mammalian limb covariation structure. *Evolution*, 59(12):2691–2704, 2005.

[241] R. Zhang, Q. Ji, G. Luo, S. Xue, S. Ma, J. Li, and L. Ren. Phalangeal joints kinematics during Ostrich (Struthio Camelus) locomotion. *PeerJ*, 4:e2324v1, 2016. URL `https://peerj.com/preprints/2324`.

1 BirdBot achieves energy-efficient gait with minimal control using avian-inspired leg clutching

SCIENCE ROBOTICS | RESEARCH ARTICLE

ANIMAL ROBOTS

BirdBot achieves energy-efficient gait with minimal control using avian-inspired leg clutching

Alexander Badri-Spröwitz[1]*†, Alborz Aghamaleki Sarvestani[1]†, Metin Sitti[2,3,4], Monica A. Daley[5,6]

Designers of legged robots are challenged with creating mechanisms that allow energy-efficient locomotion with robust and minimalistic control. Sources of high energy costs in legged robots include the rapid loading and high forces required to support the robot's mass during stance and the rapid cycling of the leg's state between stance and swing phases. Here, we demonstrate an avian-inspired robot leg design, BirdBot, that challenges the reliance on rapid feedback control for joint coordination and replaces active control with intrinsic, mechanical coupling, reminiscent of a self-engaging and disengaging clutch. A spring tendon network rapidly switches the leg's slack segments into a loadable state at touchdown, distributes load among joints, enables rapid disengagement at toe-off through elastically stored energy, and coordinates swing leg flexion. A bistable joint mediates the spring tendon network's disengagement at the end of stance, powered by stance phase leg angle progression. We show reduced knee-flexing torque to a 10th of what is required for a nonclutching, parallel-elastic leg design with the same kinematics, whereas spring-based compliance extends the leg in stance phase. These mechanisms enable bipedal locomotion with four robot actuators under feedforward control, with high energy efficiency. The robot offers a physical model demonstration of an avian-inspired, multiarticular elastic coupling mechanism that can achieve self-stable, robust, and economic legged locomotion with simple control and no sensory feedback. The proposed design is scalable, allowing the design of large legged robots. BirdBot demonstrates a mechanism for self-engaging and disengaging parallel elastic legs that are contact-triggered by the foot's own lever-arm action.

INTRODUCTION

Agile legged locomotion in robots remains a challenge at the frontiers of science (*1*–*4*). No current bipedal robot can run quickly, untethered, in natural environments over long distances. However, these activities are commonplace for terrestrial animals. Despite the apparent agility of running animals, legged locomotion is complex and requires robust control of leg-substrate interaction forces in the face of terrain variation and sensorimotor noise (*5*–*8*). Innovation is needed to design legged robots that achieve low energy consumption locomotion (*9*) with robust mechanics and simple control. For operational robustness, the system should be able to deal with external perturbations that occur faster than communication delays and actuator response times (*10*). Hence, systems should minimize dependence on communication speed and sensor quality.

In biological systems, the prevailing theory suggests that legged animals coordinate joint actuation through antagonistic pairs of muscles controlled by spinal sensorimotor circuits, functioning as "myotatic units" (Fig. 1B) (*11*–*15*). The myotatic unit concept is mimicked in robotics through the control of joint extension and flexion by separate actuators at each joint. Joint actuation is typically controlled through complex, optimized algorithms that rely on internal robot models and rapid sensory feedback loops (*16*). Phase transitions are controlled through contact and load sensors at the feet or within the leg structure (*17*), or as "proprioceptive" sensing within the actuator's electrical circuits (*18*). With fast sensory feedback and communication, robots can smoothly transition through the gait cycle and react to unforeseen perturbations (*19*, *20*). However, the robustness and agility of legged robots remain limited. Paradoxically, animals vastly outperform current robots despite considerably slower sensing and information transfer rates (*10*, *21*, *22*).

Previous evidence suggests the potential for embodied, intrinsic mechanics and interjoint mechanical coupling in vertebrates' legs

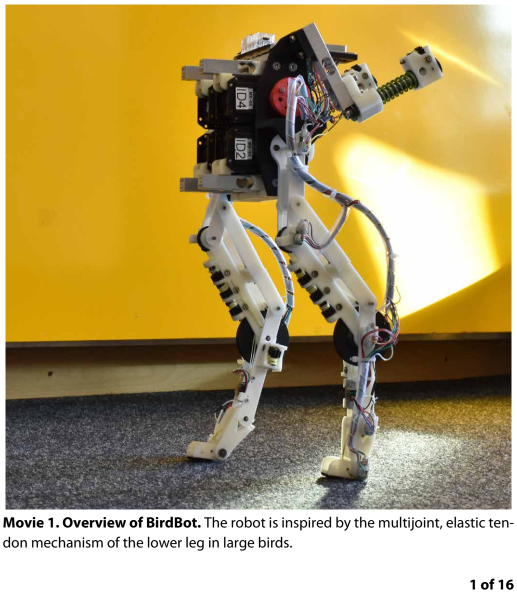

Movie 1. Overview of BirdBot. The robot is inspired by the multijoint, elastic tendon mechanism of the lower leg in large birds.

---

[1]Dynamic Locomotion Group, Max Planck Institute for Intelligent Systems, Stuttgart, Germany. [2]Physical Intelligence Department, Max Planck Institute for Intelligent Systems, Stuttgart, Germany. [3]Institute for Biomedical Engineering, ETH-Zürich, Zürich, Switzerland. [4]School of Medicine and College of Engineering, Koç University, Istanbul, Turkey. [5]Department of Ecology and Evolutionary Biology, University of California, Irvine, CA, USA. [6]Royal Veterinary College, London, UK.
*Corresponding author. Email: sprowitz@is.mpg.de
†These authors contributed equally to this work.

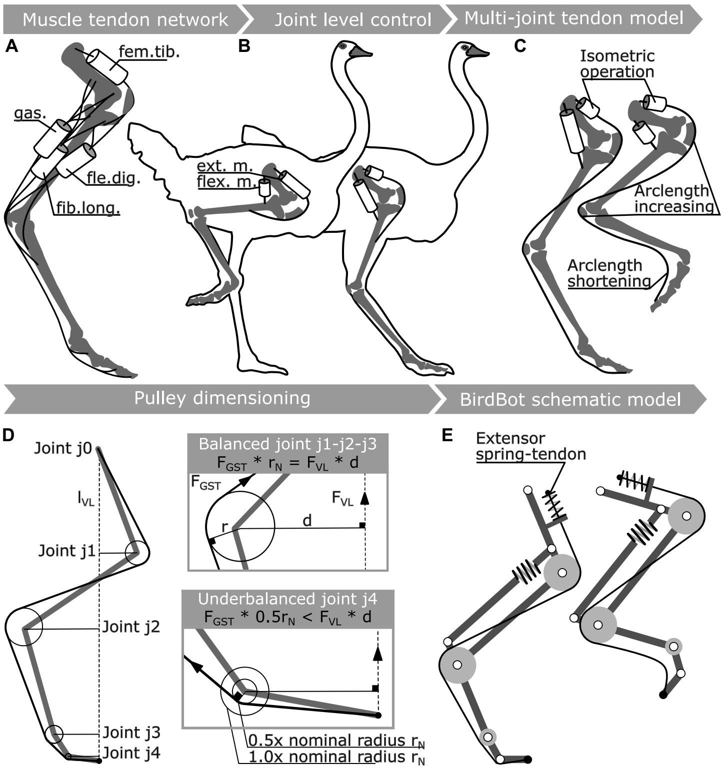

Fig. 1. Biologically inspired design of BirdBot's leg. (**A**) Major muscle-tendon networks that contribute to coordinated stance leg extension and weight support in large ratite birds such as emus and ostriches. Figure inspired from (*61*). (**B**) Classic theory suggests that joints are coordinated by flexor-extensor pairs at each joint, acting as myotatic units. However, in birds, distal joints are actuated by a multiarticular musculotendon network. Figure modified from (*126*). (**C**) Mechanical analysis demonstrates that a solution exists for a single, multiarticular tendon to support stance loads and allow the leg to be fully flexed for swing. The increase in arclength from knee and ankle flexion is balanced by the shortened arclength at the distal distal joints, with tendon slack at the distal joints. The change from stance to swing configuration requires no net change in length, so it is feasible for a muscle acting in series to contract isometrically. (**D**) In BirdBot's leg design, we dimensioned all but the most distal pulleys to balance the external joint moment ($F_{VL}\, d$) against internal joint moment ($F_{GST}\, r_N$). All joints share an equal global tendon force F_{GST}. The distal pulley radius is 0.5 times of the nominal pulley radius r_N. The underbalanced distal joint results in rapid digital extension into a flat-foot position under load. (**E**) Together, the multiarticular tendon and pulley design create a self-engaging clutch for the stance leg, which provides bodyweight support and distributes force and power among the joints. The foot's leveraction mechanically releases and slacks the multiarticular tendon in swing phase. BirdBot's leg design enables bipedal locomotion with minimalistic feedforward control.

to simplify control (*6*, *23*–*32*). Multiarticular muscle-tendon coupling can facilitate energy transfer between joints and improve efficiency by allowing muscles to work closer to optimal length and velocity (*33*–*36*). Nonetheless, the role of multiarticular mechanisms in the control of animal locomotion remains poorly understood. A challenge for demonstrating the role of embodied, intrinsic mechanics in animal locomotion is that both active neural and intrinsic mechanical control occur simultaneously (*5*, *7*, *37*, *38*). This makes it nearly impossible to disentangle the contributions of each. Robot experiments provide an opportunity to directly demonstrate the function of intrinsic mechanical coupling, using a physical model of the salient musculoskeletal features to test hypotheses about biological function while also inspiring innovations in robot leg design (*2*, *39*).

BirdBot showcases a foot contact-based, self-engaging leg spring clutch mechanism (Movie 1). It is minimally actuated with two actuators per leg—hip joint protraction and retraction and knee flexion actuators—controlled in feedforward mode. BirdBot builds upon established mechanisms and principles including cable-and-pulley–driven actuation, tendons routed over multiple joints ("multiarticular" tendons), clutching of leg forces, parallel and series leg elasticity during stance, and slack leg joints during swing. BirdBot's clutching mechanism engages and disengages robustly with no feedback control. Our design framework demonstrates how intrinsic leg mechanics can enable self-stable and economical gait with consistent phase transitions that are robust to variation under initial conditions.

Many legged animals show coupled joint kinematics, mediated by multiarticular muscle-tendon units, suggesting that such mechanisms are an essential feature of leg design and control in terrestrial animals (*31*, *36*, *40*, *41*). Passive mechanical coupling of joints through multiarticular muscle-tendons without active central nervous system control has been directly observed in frogs, horses, and ratites (*23*, *24*, *31*, *40*). Bioinspired robots and exoskeletons have demonstrated functional benefits of coupled joints by creating analogous structures using spring-loaded four-bar, pantograph, and multiarticular cable mechanisms (*42*–*47*). Multiarticular mechanisms enable lightweight leg designs, with the heavy actuators mounted proximally. For example, the Spring Flamingo robot has series elastic actuators in its trunk, with leg joints actuated by long tendons routed over pulleys (*48*). Such mechanically elastic legs also mimic the spring-like function observed in animal gaits (*45*, *48*–*51*). The MIT Cheetah robot's leg mounts a stiff belt as an Achilles tendon spanning multiple joints in a tensegrity structure, which maximizes the leg's strength to weight ratio (*52*). Kurokawa *et al.* (*53*) designed a biarticular mechanism that couples ankle and toe movement, enabling transfer of energy between leg joints for jumping. Mechanically coupled actuators can reduce overall work and force demands and thereby improve energy efficiency in robots, exoskeletons, and prosthetic devices (*54*, *55*).

Our approach also draws inspiration from research in passive mechanical walking robots that demonstrate locomotion principles with either no actuation or minimal actuation under open loop control. Purely mechanical walkers convert potential energy from a slope into center of mass and swing leg motion (*56*). Related minimally actuated walkers achieve the lowest cost of transport (COT) among legged walking machines (*57*). Mechanical walkers and their models illustrate principles for economic walking by identifying sources of energy loss and fluctuation, including inelastic collisions between the foot and the ground, redirecting the center of mass velocity at foot impact, achieving ground clearance during forward leg swing, carrying the robot's weight during stance, and joint friction (*56*–*60*). Although exceptionally energy efficient, passive mechanical walking robots remain limited to flat, smooth terrain, and their stability is sensitive to initial conditions and small perturbations. They have low foot-ground clearance, and even small perturbations such as bouncing joint locks can be destabilizing (*59*).

In this study, we test the hypothesis that an avian-inspired linkage mechanism can replace most of the neural circuitry required to control leg trajectory and transitions between stance and swing phases (Fig. 1). In an iterative design process, we developed a multijoint linkage mechanism fully integrated into a bipedal robot's legs that achieves consistent interjoint coordination and rapid, automatic phase transitions between stance and swing. The leg design was inspired by the muscle-tendon units of large ratite birds, such as the emu (*Dromaius novaehollandiae*) and ostriches (*Struthio* species), but the abstracted structural elements are common among ground-moving birds (*6*, *23*, *24*, *30*, *61*–*67*). A multiarticular spring network guides the leg trajectory and provides a rapid transition between stance and swing using a mechanism reminiscent of a self-engaging and disengaging clutch. We demonstrated the leg mechanism on a treadmill, held by a four-bar guide that allows free vertical and fore-aft horizontal translations but limits sideways translation, pitch, yaw, and roll. We documented the design process, mechanical features, and locomotor dynamics of BirdBot, which embodies mechanics and control elements conceived according to anatomical and functional features of avian locomotion (*6*, *24*, *67*).

RESULTS

We used a robot leg design as a physical model to test the hypothesis that a rigorously designed multiarticular spring tendon network can fully support locomotor loads during stance, coordinate the transfer of mechanical load among the joints, and enable automatic stance/swing phase transitions (Fig. 1). The distal segment's (foot) lever action and a global spring tendon (GST) automatically switch the leg's joints into a loadable state during touchdown and mechanically distribute torques among joints during stance (Fig. 1D). A dedicated tendon disengagement mechanism supports stance-to-swing transition during toe-off by actuating a snap-through (bistable) joint using elastically stored energy. The GST and the compliant four-bar linkage couple leg joints into coordinated leg flexion during swing and rapidly create foot ground clearance for swift leg protraction. BirdBot was designed as a proof-of-concept planarized bipedal robot, with high-geared (200:1 ratio), brushed-motor actuators that enable moderate frequencies and speeds [Froude number $Fr = v^2/(gl) = (0.75\ \mathrm{m/s})^2/(9.81\ \mathrm{m/s^2} \cdot 0.29\ \mathrm{m}) = 0.20$], but not fast running. The bioinspired features, design process, and resulting gait mechanics are detailed below.

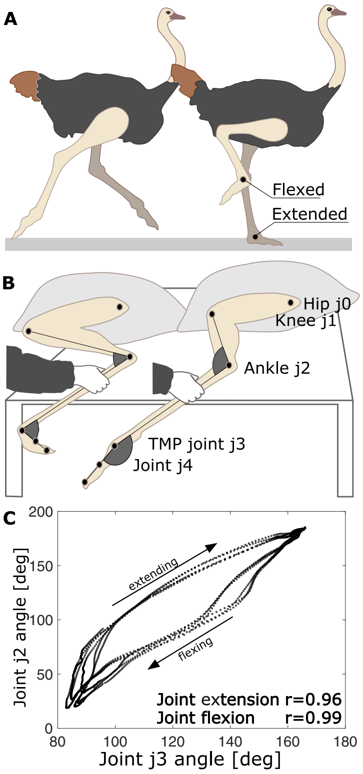

Fig. 2. Mechanical coupling of distal joints in the ratite leg. (**A**) In the running ratite birds, the digits are digital-flexed in swing and digital-extended upon knee extension in preparation for stance. (**B**) The distal avian hindlimb exhibits passive mechanical joint coupling, which can be determined by manually flexing and extending the ankle joint, j2, and measuring coupled motions at the TMP joint, j3. (**C**) Strong coupling exists between the two joints in both flexion and extension, demonstrated by correlation coefficients of $r = 0.99$ and $r = 0.96$, respectively.

We measured the joint angular coupling in an emu cadaver leg by manually moving the tibiotarsus in an unloaded leg while observing the coupled flexion and extension of the ankle and tarsometatarso-phalangeal (TMP) joints (Fig. 2, A to C). Upon manually flexing and extending the ankle joint j2, we measured coupled motions at the TMP joint j3. Strong coupled motion between the ankle and TMP is evidence based on an observed correlation coefficient of 0.96 for extension and 0.99 for flexion (Fig. 2C). In our measurements, the mechanical coupling arose only from passive tissue elasticity because the central nervous system was inactive. Sources of passive tissue connectivity in the avian limb include the proximal origins of major ankle extensors and digital flexors from the patellar tendofascial sheet at the knee (*68*), and ligament connectivity between distal joints including the intertarsal joint (Fig. 1A) (*23*, *24*). In particular, Schaller *et al.* (*24*) observed an ankle-locking mechanism based on ligament interactions in ostrich legs, although it remains unclear whether these passive structures alone can fully support body weight in these animals.

To enable a rigorous approach for designing a ratite-inspired tendon network, we initially "linearized" many of the biologically relevant structures. That is, we assumed constant pulley radii and simple hinge joints (Fig. 1, D and E), in place of nonlinear curved sesamoid surfaces and bone surface interactions that lead to a complex, translating center of rotation. Nonetheless, the robot tendon network retains the essential connectivity features of the avian limb. The spring tendon network is designed to establish coupled joint kinematics in swing phase, to flex all joints to provide ground clearance, to engage the global leg spring upon loading into stance phase, to support body weight and distribute torque and power among joints during stance, and to disengage at the end of stance and rapidly transition the leg into the swing phase. The joint coupling during stance distributes the load among the individual joints, without the danger of catastrophic collapse at any single joint, and supports compliant leg compression under load for elastic energy cycling (*49*).

To achieve these mechanical features, we first introduced a single multiarticular spring tendon structure connecting all leg joints (Fig. 1C). We designed a z-like leg structure (Fig. 1, D and E) commonly observed in vertebrates (*69*–*71*). We further assumed a planar configuration, without off-plane influence. Pulley radii r_{jx} of joint j_x were calculated to establish an equal effective mechanical advantage (EMA) (*72*) for all joints sharing the same multiarticular spring tendon ("GST"), with a force magnitude of $\|\vec{F}_{\mathrm{GST}}\|$

$$\|\vec{F}_{\mathrm{VL}}\| \cdot d_{jx} = \|\vec{F}_{\mathrm{GST}}\| \cdot r_{jx} \tag{1}$$

$$r_{jx} = \frac{\|\vec{F}_{\mathrm{VL}}\| \cdot d_{jx}}{\|\vec{F}_{\mathrm{GST}}\|} \tag{2}$$

where $\vec{F}_{\mathrm{VL}}$ is the force along the virtual leg direction l_{VL} (Fig. 1D) and d_{jx} is the shortest distance between joint j_x and the virtual leg l_{VL}. Equation 1 balances joints j1 and j2 equally. For the shown, EMA-balanced configuration in Fig. 1 (D and E) and a given a virtual leg length change, these joint's angles change equally. Each joint's torque balance depends on its pulley's radius and the joint's perpendicular distance to the virtual axis.

Next, we introduced an imbalance between the torque loading of the distal joint j_{distal} (external) and its extension torque (internal). The imbalance serves to securely and compliantly "lock" the leg structure under external load $\|\vec{F}_{\mathrm{VL}}\| > 0$. The imbalance was achieved by underdimensioning the most distal joint's pulley radius relative to its nominal (balanced) value. In place of an EMA-balanced pulley (Eq. 1) with nominal radius (r_{N}), an "underbalanced" pulley with half the EMA-balancing radius was mounted

$$r_{\mathrm{und}} = \frac{r_{\mathrm{N}}}{2} \tag{3}$$

$$\|\vec{F}_{\mathrm{VL}}\| \cdot d_{j,\mathrm{distal}} > \|\vec{F}_{\mathrm{GST}}\| \cdot r_{\mathrm{und}} \tag{4}$$

The underbalanced joint deflected faster compared with the balanced joints. Consequently, when the leg was loaded, the distal joint rapidly collapsed until the most distal segment touched the ground to establish a flat, foot-style contact (movie S7).

With the selected global spring's stiffness, the leg deflected by 10% under three body weights, approximate to that observed in legged animals (*73*–*75*). The resulting leg structure was balanced for static load but would destabilize when transitioned between leg postures or when torques were applied. Therefore, we further stabilized the leg by embedding a spring-loaded pantograph mechanism into the z-shaped leg structure (Figs. 1E and 3A), which also provides compliance in leg angle direction, benefiting energy economy (*76*).

The GST coordinates the motion of all four leg joints during stance phase and rapid transitions to a slack, flexed position in swing (Figs. 3 and 4 and movie S7). When unloaded, the distal joint is released from its clutched, digital-extended position (Fig. 5). The GST becomes slack and detached from the distal pulley, and all leg joints become loose. A central pattern generator (CPG) swing controller (Eq. 9 and fig. S1) commands the knee actuator to flex the knee joint j1, leading to coordinated flexion of all four joints, coupled by the multiarticular and the compliant pantograph. Simultaneously, distal joints j3 and j4 rapidly rotate from their digital-extended position during stance to a pronounced digital flexion in swing, akin to the tarsometatarsus stance-to-swing phase kinematics in running birds (*62*, *63*).

Thus, active knee flexion causes all four joints to rapidly flex toward mid-swing, shortening the leg length for maximum ground clearance (Fig. 4C). The shortened swing leg also reduces the hip torque required to accelerate the leg forward during protraction.

The amount of leg flexion depends on the length of the GST released by the joint j4 digital flexion. Suppose that the multiarticular tendon is wrapped around the pulley of joint j4 (Fig. 4B). In that case, joint j3-j4 digital flexion creates insufficient tendon slack to substantially shorten the leg. The distal tendons of ratite birds such as emus and ostriches are routed in sheaths (*77*) that permit substantial off-joint motion during digital flexion, which we also observed in cadaver dissection (Fig. 4A). We mimic the bird's sheath morphology with a tendon catch (Fig. 4, C and D, and fig. S7) for the otherwise loosely mounted multiarticular tendon. The tendon catch allows for substantial tendon slack during digital flexion and guides the tendon back onto its pulley after digital flexion.

An ideal swing-to-stance transition involves a rapid switch from a slack swing leg to an engaged, load-carrying stance leg that supports body weight and cycles elastic energy. In the late swing phase, the leg length actuator stops flexing the knee joint j1, which effectively lengthens the leg as a result of gravity and the leg's angular momentum. Two distal, biarticular tendons (digit-1 extensor and digit-2 extensor; Fig. 3B) couple the ankle j2 extension to the rotation of the distal joints j3 and j4, into their digital-extended position (Fig. 6A). At the leg's most forward position and while still in air, all leg joints are extended (Fig. 6A, still frame $t = 0.08$ s). Next, the hip actuator pulls the leg backward, into touchdown. As soon as the foot contacts the ground, the GST propagates back the joint j4 lever action to all leg joints. The leg is again locked as a springy strut and ready to carry high mechanical loads throughout stance phase.

An ideal stance-to-swing transition involves a rapid switch from a load-carrying leg to a configuration with all joints slack, allowing rapid leg shortening with low resistance to create ground clearance. In practice, the GST clutching mechanism disengages under the following conditions. The global spring reaches its slack length, which occurs when the leg reaches the disengagement angle (Fig. 5A), and the foot rotates from a digital-extended position to a digital-flexed position to release the GST. Alternatively, disengagement can be

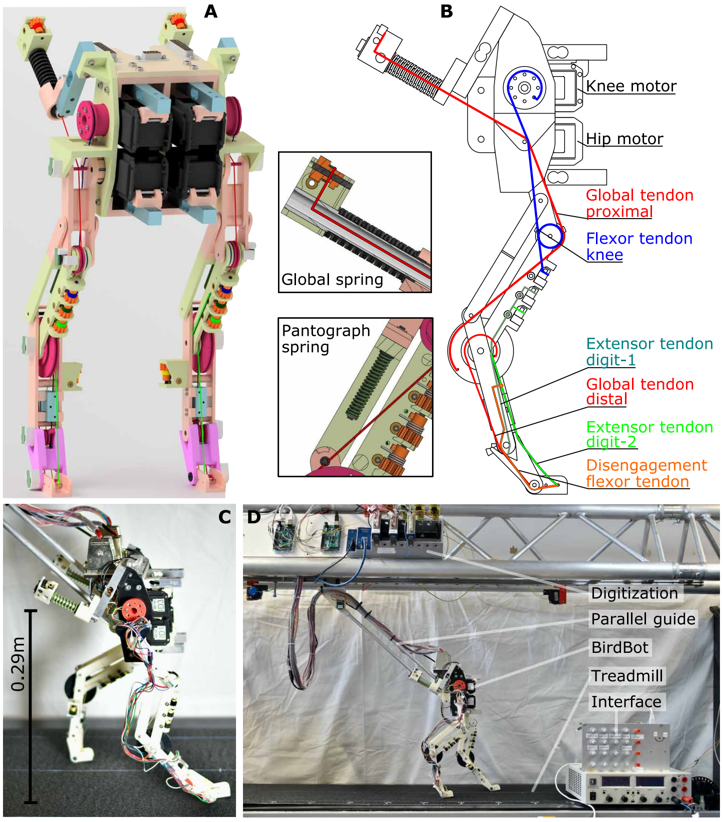

Fig. 3. BirdBot leg design and spring tendon network. (**A**) Computer-aided design drawing of BirdBot. The pantograph spring (spring-12p) is mounted as one-directional elasticity, and the global spring tensions the global multiarticular tendon. Tendon lengths are individually adjusted. (**B**) The GST not only functionally acts across four joints (j1 to j4) but is also guided over hip joint j0. The GST is implemented as two tendons, proximal and distal, connected in the ankle j2 pulley, with different pulley radii. The knee flexor tendon (blue) connects the knee flexion actuator with the tibiotarsus segment, to elevate and shorten the leg during swing. The digit extensors (dark and light green for digit-1 and digit-2) are coupled to ankle j2 action—extension of the ankle pulls both digits into a digital-extended position. The DFT (orange) spans joints j3 and j4 and is actuated by the stance rotation of joint j4 to apply a buckling force at the bistable joint j3 at toe-off to disengage the GST. (**C**) Photo of the BirdBot prototype in side-view, overlaid scale bar. BirdBot's hip height is 0.29 m. (**D**) Experimental setup: treadmill and robot sensor acquisition system. We set gait control parameters through a physical control interface. BirdBot was guided by a four-bar mechanism to constrain pitching, while allowing free fore-aft and vertical translations.

forced through actuation of the distal joint j3 (fig. S11B). At fast speeds, the feedforward actuation patterns cycle the leg length through clutch engagement, mid-stance, and take-off lengths, with the leg lifting off the ground through the robot's momentum. However, at lower speeds, the momentum is insufficient to drive foot lift-off. Consequently, with a digital-extended foot coupled to the global spring through the GST, the foot remains in contact with the GST clutching mechanism engaged. Rotating the foot into a vertical orientation with $\alpha_{j3} > 180°$ angle will reliably disengage the clutch and allow shortening of the slacked leg (fig. S12A). To enable end-stance disengagement with minimal leg work, our aim was to avoid raising the foot to disengage the leg spring. Instead, we added a joint j3 with a disengagement mechanism mediated by a distally mounted, biarticular tendon ["disengagement flexor tendon" (DFT); Fig. 5C and fig. S12B]. The tendon-based disengagement mechanism reduces the work and power required for leg disengagement and works as follows. During stance phase, a joint j3 hard stop only allows joint angles above 160° close to its snap-through angle (Fig. 5C). A biarticular DFT wraps around the joints j3 and j4 (Fig. 5C, DFT, orange tendon). The joint j4 loads the DFT increasingly during stance phase with its joint flexing action. In late stance, the DFT's force pushes the joint j3 over its snap-through angle of 180°. Collapsing joint j3 also slacks the in-parallel GST, which then rapidly slacks all remaining joints into the swing leg configuration (Figs. 4C and 6F and fig. S1).

Both actuators are feedforward controlled by a CPG with two outputs that are interpreted as commanded hip angle and knee angle over time (Eqs. 13 to 16). The hip actuator directly actuates both directions, leg protraction and retraction, whereas the knee actuator transmits flexion torques but no extension torque (fig. S1). The hip output is a sine-like pattern with amplitude A^h oscillating around the femur angle offset O^h. A commanded duty factor adjusts the ratio of swing and stance duration; a duty factor of 0.6 commands a stance phase of 60% of total cycle time. We observe emergent gait patterns with the robot foot already in the air when the femur angle switches from protraction to retraction (end of the commanded swing phase). Consequently, just before touchdown, the hip actuator retracts the leg briefly in air. Similar end-swing characteristics have been shown in underactuated robots with strong natural dynamics (*45*). BirdBot's observed duty factor is 0.49 at a stride frequency of 1.5 Hz (Fig. 6B). In stance, the hip actuator continues to retract the stance leg, propelling the robot forward. As the hip actuator reaches its most posterior angle, leg spring disengagement occurs. The knee actuator starts flexing the knee at the time of leg spring disengagement and, upon disengagement, rapidly flexes the entire leg into the raised swing-leg configuration. The knee actuator starts to release the knee joint

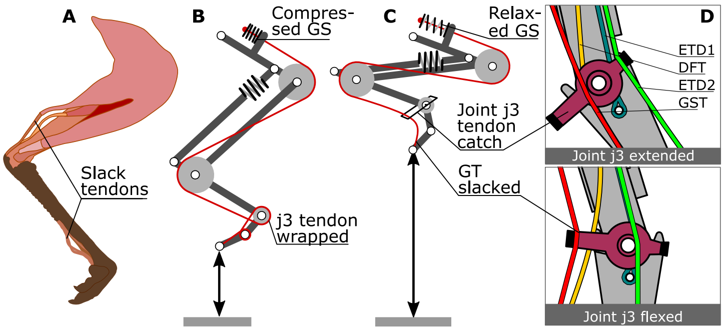

Fig. 4. Enabling tendon slack for low-resistance flexion in swing. (**A**) The distal tendons in the emu and ostrich ratites move loosely within their sheaths at the TMP joint during digital flexion (*77*). (**B**) At the transition from stance to swing, j3 and j4 undergo large digital flexion, which releases the global tendon (GT) length needed to flex the ankle j2 and knee j1. The global tendon can be guided by direct tendon wrapping as shown. However, tight wrapping only releases tendon proportionally to digital flexion angles. Further leg flexion will then load the global spring (GS), which we want to avoid. (**C**) We mimic biological tendon slacking in the robot leg with a detachment and realignment "tendon catch" mechanism at joint j3. This allows full leg flexion without loading the global spring, to achieve low resistance knee flexion without feedback control. (**D**) Mechanism detail: In swing (joint j3 flexed), the global tendon detaches from the j3 pulley. The detachment creates enough tendon slack for full leg shortening.

around mid-swing, and the leg reextends toward the ground. Full leg length is reached at the end of the commanded swing phase, with the leg still in the air and the digital joints extended.

At a 1.5-Hz stride frequency, BirdBot reaches a speed of 0.75 m/s (Froude number Fr = 0.20). In stance phase, a peak retraction torque (leg angle direction) of −1.70 ± 0.05 N·m [confidence interval (CI)] occurred just before midstance (Fig. 6C). During swing phase, the leg angle torque fluctuated between 0.5 N·m at in-air protraction and −0.5 N·m at in-air leg retraction about one-third of the applied leg angle torque during stance (table S5). The torque flexing the knee joint during swing phase reached a maximum of 0.31 ± 0.03 N·m (CI; Fig. 6E, solid line), caused by dynamics of lifting the slack lower leg. This peak torque is comparable in magnitude to the knee-flexing torque required during standing (0.09 N·m statically applied torque; fig. S4 and table S5). In Fig. 6E, we also compare the knee flexing torque of BirdBot with that of a modeled robot with the same morphology but a permanently engaged (nonclutching) knee spring, similar to (*45*). With the additional torque required by the constantly engaged, in-parallel knee spring, the actuator would require 3.7 N·m of torque, or more than 10 times the measured torque of BirdBot's knee, assuming the same knee joint j1 kinematics (Fig. 6G, dashed line, and table S5).

In Fig. 6B, we observe signs of power amplification in the distal tendon work profile, indicated by an asymmetric rate of elastic energy storage and release (*78*). Specifically, the biarticular DFT stored 0.037 ± 0.001 J (CI) elastic energy in the first 82% of the stance phase and released it in the remaining 18% of stance phase, corresponding to an asymmetry ratio of 4.6:1. In comparison, the multiarticular GST stored and released 0.34 ± 0.02 J (CI), on average, about nine times the DFT energy, with relatively symmetric timing around the peak (Fig. 6D and table S3). BirdBot's combined actuators drew in average 15.7 ± 0.4 W and 16.8 ± 0.4 W of electrical net power at 1.0- and 1.5-Hz locomotion, respectively (table S4). The instantaneous electrical power consumption of the hip actuator shows one distinct peak at stance-phase leg retraction (Fig. 7B). The power consumption of the knee actuator peaked twice, following the step-like knee flexion and extension CPG signal (Fig. 7A and fig. S1, A_K). According to Eq. 7, the COT of a natural runner with BirdBot's weight is 1.45 (table S1), and the robot's power consumption at a speed of v = 0.75 m/s corresponds to a net COT of 1.32. It is notoriously hard to compare COT among robots—numerous factors can influence COT including use of mechanical guides (planar four-bar mechanism, rotating boom), varied walking substrate (laboratory surface, treadmill, and outside terrain), power supply (onboard and tethered), control (on-board and remove), motor type (brushes and brushless), gearing, and robot size. BirdBot is guided in-plane by a four-bar while walking on a treadmill, with a pitch-locked trunk, actuated by brushed and high-geared motors, and powered and controller by tether. A freely

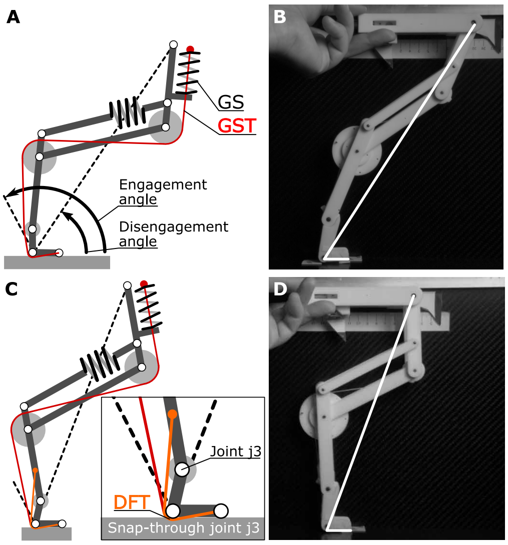

Fig. 5. End stance disengagement. We experimentally measured the disengagement angles with and without the DFT, by manually pushing the hip along a horizontal guide at near-constant speed. (**A**) Without the DFT, leg kinematics unloaded the GST at a virtual leg angle of 59.0° ± 0.3° ("disengagement angle"). (**B**) Snapshot of disengaged leg, like in (A). (**C**) With the DFT, the joint j3 snapped through and unloaded the GST already at a 69.0° ± 1.2° angle, showing a 10° difference caused by the DFT. (**D**) Snapshot of disengaged leg, like in (C). The global spring in the hardware leg is mounted above the hip joint, the modified golden spring schematics in (A) and (C) are shown for simplification.

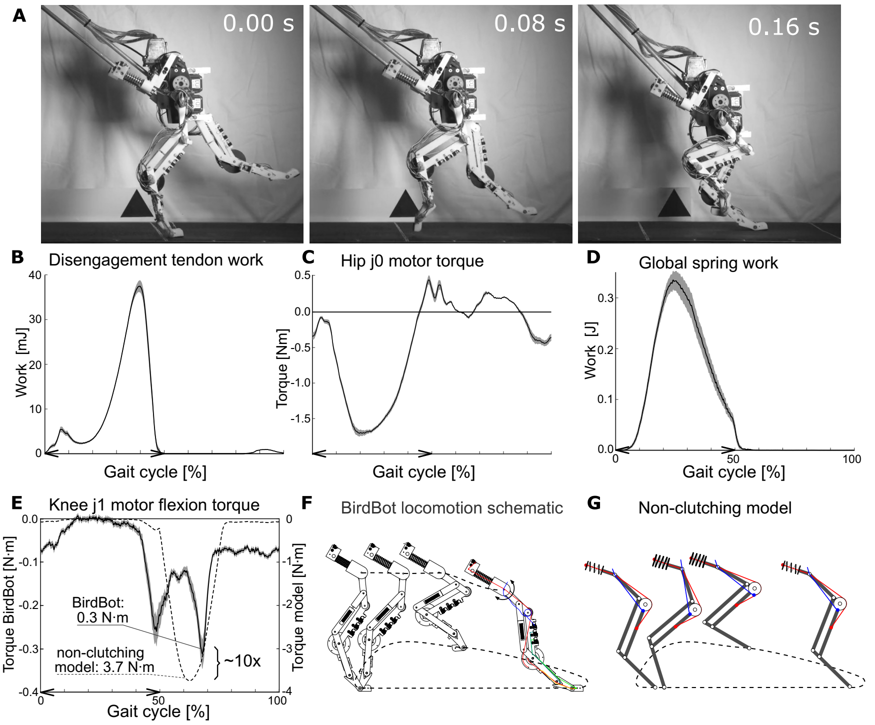

Fig. 6. BirdBot running at a stride frequency of 1.5 Hz, with a speed of 0.75 m/s (Froude number of 0.20). Data are averaged from 70 strides, with a 95% CI shown as a shaded area. The stance period is indicated by "< >" on the *x* axes. (**A**) Side-view video still frames of BirdBot running on the treadmill, with a four-bar guide to restrict rotation. (**B**) The cumulative work applied at the DFT. The tendon stores and releases 0.037 ± 0.001 J (CI) per cycle. The loading and unloading times are asymmetric, indicating power amplification. (**C**) Hip actuator for joint j0 with a peak torque of −1.71 ± 0.05 N·m (CI) during leg retraction at mid-stance. (**D**) The cumulative work applied at the GST, stored and released by the spring as elastic energy. The GST stores on average 0.34 ± 0.02 J (CI) per deflection in this gait. (**E**) The knee flexing actuator applies a peak torque of 0.31 ± 0.03 N·m (CI) at mid-swing to lift the lower leg and create foot-ground clearance (solid line). We modeled a nonclutching, parallel leg spring [dashed line, model shown in (G)] and assumed the same knee joint kinematics as BirdBot. The nonclutched knee actuator model would require 3.7 N·m, which is more than 10 times higher torque than in BirdBot. (**F**) Schematic of BirdBot's leg and foot trajectory over a gait cycle. (**G**) Schematic of the leg and foot trajectory of the nonclutching model.

walking BirdBot would likely consume more power. Nonetheless, BirdBot shows economical locomotion, particularly in comparison with the similarly actuated, freely running robot Cheetah-cub (*45*). To allow indirect comparison between robots, we defined a relative COT in Eq. 8 as the ratio between the robot's COT and that of a natural runner of equal weight, resulting in a relative net COT of 91% for BirdBot.

DISCUSSION

Animals vastly outperform current legged robots, achieving agile movement in natural terrain with robust balance and low metabolic COT, compared with legged robots (*6*, *26*, *79*–*85*). We used an iterative design process and a physical robot to test the hypothesis that a bird-inspired multiarticular linkage mechanism can replace most of the neural circuitry required for joint coordination and stance-swing transition control. The multiarticular spring tendon in the five-segment leg creates a whole-leg clutch, which transitions upon loading into a high stiffness configuration for stance and transitions upon unloading to a slack configuration for swing. The leg design achieves consistent interjoint coordination of a complex leg trajectory, compliant bodyweight support with elastic energy cycling, and rapid, automatic control of swing/stance transitions. The rapid transition to swing is achieved by action of the spring tendon network on a bistable joint, which disengages the stance leg spring. These mechanisms enable bipedal gait with just four actuators under simple, model-free feedforward control. In addition to providing robust mechanics with simple control, the leg design achieves economical COT by reducing knee-flexing torque to $^{1}/_{10}$ of that of nonclutching leg designs similar to Cheetah-cub (*45*).

Research on running ground birds suggested that their remarkable agility and robustness benefit from intrinsic mechanical control (*6*, *26*, *27*, *83*, *86*). BirdBot's leg clutch relies on a digitigrade posture, in which the toe becomes flat against the ground. To freely shorten its leg in swing, the distal segment rotates from a digital-extended

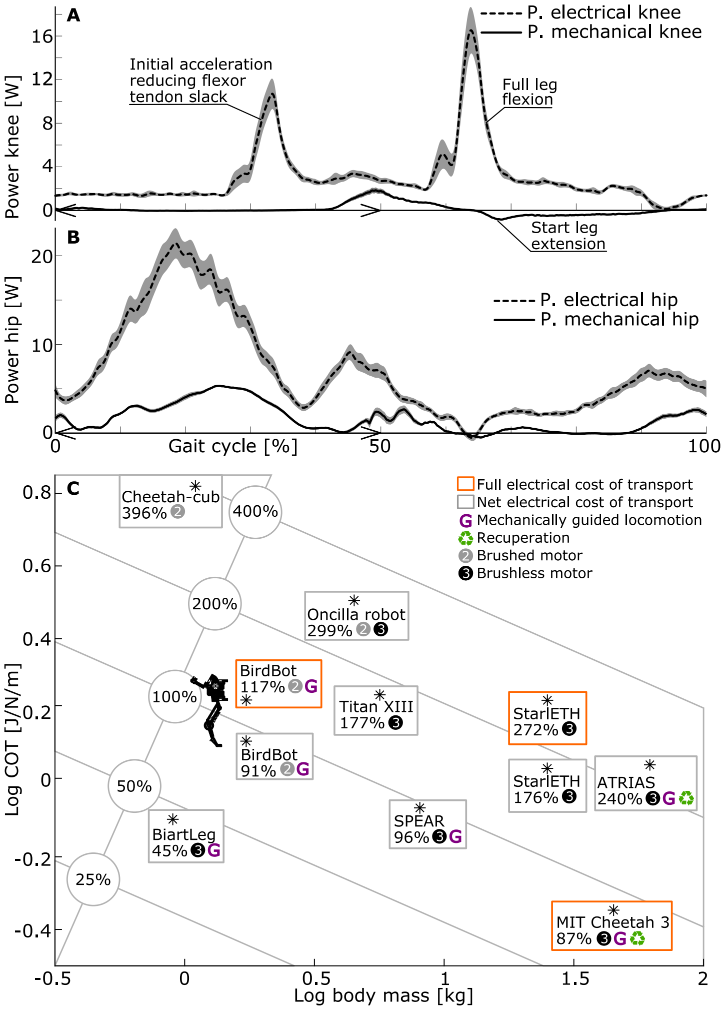

Fig. 7. Robot energetic performance and comparative COT. (**A**) Knee mechanical power (solid line) and instantaneous electrical power of the knee flexing actuator (dashed line). The two electrical power peaks indicate an initial acceleration to reduce tendon slack at the end of stance, and a second burst to fully lift the lower leg in swing. "< >" indicates the observed stance period. (**B**) Hip mechanical power (solid line) and actuator electrical power (dashed line). The highest power consumption occurs during leg retraction in the stance phase. In comparison, swing leg protraction requires considerably less power. (**C**) The electrical COT of selected legged robots, plotted relative to body mass, on a logarithmic scale. As a general reference, the 100% COT line indicates the metabolic cost of animal runners, according to (*120*). Brushless motor–actuated robots that recuperate negative power are indicated with a green recycle symbol. Hopping robots, such as BiartLeg, require no leg shortening for ground clearance in the swing phase, reducing their COT. BirdBot's net COT is slightly below that of a running animal with a similar body mass (1.73 kg). This places BirdBot's net COT in the range of the hopping SPEAR robot and MIT Cheetah 3.

to a digital-flexed posture, which slacks the stance spring. Our analysis suggests a suite of structural features required for the mechanism: elevated, digitigrade posture with a long tarsometatarsus segment, a multiarticular network of ligaments and tendons from femur to toe (Fig. 1C), sesamoid bones creating the appropriate cam dimensions, sheaths to guide slack tendons, and a bistable configuration in the distal joint.

This analysis helps to identify where similar function is likely to be found among diverse animals. Although BirdBot's leg design is inspired by large ratite birds such as emus and ostriches, the structural elements are present to varying degrees among many birds (*6*, *23*, *24*, *30*, *61*–*67*, *87*–*89*). BirdBot is an abstracted and simplified model: Complex bone surface interactions are approximated as hinge joints, and sesamoid structures are approximated as constant radius cams. The model integrates several features: cam radii, distance from the joint center to the virtual leg, segment lengths, and ratios of leg segments. Equations 1 and 3 assume a loading of the virtual leg and establish the required joint moments based on the assumption that all leg joints are mechanically coupled and balanced, resulting in a similar joint velocity for all but the distal joint, which is underdimensioned. Joint coupling propagates loading from proximal and distal and, likewise, distal to proximal. Equations 1 and 4 are indifferent to leg postures (erect or crouched), suggesting that small birds with crouched postures could have a leg clutch. The cam of the distal joint must be underdimensioned, resulting in larger distal joint deflections compared with the knee and ankle. Rapid deflection of the distal joint upon loading creates a flat "foot" contact with the ground and engages the stance leg spring. Disengagement of the stance leg spring is triggered by loading a distal, biarticular tendon, leading to a sudden digital flexion at toe-off. The distal tendon sheath allows tendon detachment and slacking in the swing phase, enabling shortening of the swing leg with low resistance.

Across bird species, the degree to which the leg clutch exists as a passive mechanism likely varies. Ostrich legs have high capacity to support weight and recycle elastic energy in distal tendons (*65*, *67*) and exhibit the distal structures required for the bistable mechanism (*23*, *24*). Running ostriches also have distal joint kinematics consistent with the leg clutch (*88*). In large ratites, the elastic tissues in the distal leg might passively support body weight, but, in most species, engagement of the leg clutch likely requires active muscle contraction.

The BirdBot model challenges the idea of joint myotatic control, in which antagonistic pairs of flexor and extensor muscles control individual joints (*11*–*13*, *90*). A more modern perspective suggests that muscle synergies control functional modules for whole-leg tasks, such as leg stiffness, bodyweight support, propulsion, leg angular cycling, and balance correction (*8*). Control via functional modules is consistent with observed muscle activation patterns in guineafowl, a terrestrial bird with size similar to BirdBot (*91*, *92*). Coactivation of functional modules could actively engage a leg clutch in species where the mechanism is not passive. In terrestrial birds, for example, isometric contraction of ankle extensors might engage the distal tendon network and facilitate proximodistal energy transfer (*27*, *37*, *93*).

The BirdBot leg is a specific implementation of a geometric latch-mediated spring actuation mechanism, as defined by Longo and colleagues (*94*). A diverse range of animals use latch-mediated spring actuation to effectively control high-power, spring-mediated movements (*94*, *95*). In BirdBot, the distal bistable joint supports rapid disengagement of the stance leg spring, actuated by the leg angular rotation in stance. It results in a rapid release of stored energy, similar to the asymmetric joint power profile observed at the TMP joint in running turkeys (*62*). High ground clearance for swing is achieved through rapid, coupled flexion of joints upon clutch disengagement. A similar release of stored elastic energy occurs in horses' legs, triggered by rotation of the ground reaction force vector over leg joint axes, leading to a catapult-like mechanism (*28*). A complex but more direct replication of the tendon network in the horse leg has been recently implemented in a robot by (*96*). Such engagement and disengagement mechanisms enable automatic release of elastic energy over a range of locomotor frequencies and loading conditions, reducing the demand for actuator work and the need for rapid sensory feedback control.

Current legged robots often use direct joint actuation analogous to myotatic unit control, with extension and flexion by joint torque actuators. Transitions between swing and stance must actively be sensed and controlled, using contact, force, or proprioceptive sensors (*46*, *97*, *98*). Although this approach achieves smooth and stable gaits, it relies on precise and high-frequency sensor feedback to detect contact and impact events (*18*, *21*). Paradoxically, existing robots remain clumsy compared with animals, despite using appreciable faster sensing- and information-transfer rates (*22*). Sensor data can be noisy, making it hard to reliably detect contact events, particularly in unstructured terrain (*20*, *21*). To reliably detect contacts and control gait, many robots rely on control architectures that include hybrid feedforward/feedback, model-based prediction and learning strategies (*20*).

In contrast, BirdBot uses a single feedforward motor command at the proximal joint to coordinate complex leg actuation. BirdBot's leg clutch automatically engages and generates ground reaction forces upon loading and disengages upon unloading, without the need for sensors. BirdBot's stance spring passively deflects under load and rebounds after mid-stance, cycling elastic energy. Similar compliant leg robots can operate with no sensors and even stabilize after step-down perturbations (*76*, *99*). Thus, spring-leg designs not only minimize actuator work but can also simplify leg control.

As a consequence of BirdBot's underactuated design, gaits are not directly commanded. Instead, gaits emerge from the interaction between feedforward motor commands and ground reaction forces. This is illustrated by the discrepancy between commanded and observed duty factor. The commanded duty factor of the CPG-driven hip motor is 0.60 at a stride frequency of 1.5 Hz, and the observed gait duty factor is 0.49. This is similar to other robots with elastic legs and CPG control (*45*). Bipeds transition to running gaits at Froude numbers above 0.5 (*100*). BirdBot displayed a grounded gait at slower speed (0.50 m/s; Froude number Fr = 0.09) and brief aerial phases at higher speed, at a Froude number of 0.20 (0.75 m/s). We set the high-level CPG control parameters of amplitude, frequency, and duty factor, and the gait emerged from the robot's elastic leg mechanics.

The structure of Eq. 1 indicates no limitations in scaling BirdBot's leg mechanism to very large sizes. In Fig. 8, we show a large-scale demonstration with a hip height of 1.75 m that carries a human's weight. Once the foot joint j4 is digital-flexed, the knee joint j1 can be flexed without loading the leg's global spring (Fig. 8C). On the

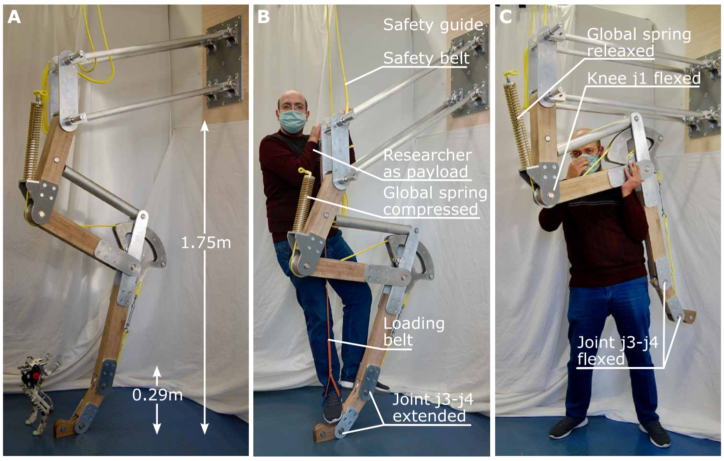

Fig. 8. Scalability of the BirdBot leg design. (**A**) Small-scale (0.29 m) and large-scale (1.75 m) versions of the BirdBot leg. (**B**) The large BirdBot leg supports the weight of a human, hanging by a belt on the hip joint axis. (**C**) With the distal leg digits flexed, the parallel leg spring is disengaged, and knee and ankle joints can be flexed without resistance from the GST.

basis of our analysis and physical demonstrations, we suggest that BirdBot's leg design can become a blueprint for large legged machines.

BirdBot's leg has no direct actuation for leg length extension. Nonsteady locomotion can demand net positive or negative work at distal joints (*6*, *37*, *93*, *101*, *102*). To increase BirdBot's versatility in rough terrain or to facilitate acceleration, a lightweight leg extension actuator could be placed in parallel with the distal extensor tendons (fig. S11). Additional actuators would not only increase versatility and robustness but also increase the leg mass, draw additional power and likely require more complex control with sensory feedback.

Clutch mechanisms, similar to that in BirdBot, need to be lightweight, robust, and of minimal complexity for mobile use in prosthetics, exoskeletons, and other legged robots. Loading conditions change rapidly, and clutches in the drive chain connect and disconnect external and internal forces, from zero to multiple body weights within tens of milliseconds (*103*, *104*). Wiggin *et al.* (*105*) designed a clutch for a human ankle joint exoskeleton that loads its spring in stance and releases the stored energy at push-off, freeing the ankle joint for the swing phase. van den Bogert (*47*) analyzed whole-leg multiarticular passive exoskeleton designs and found that they could substantially reduce joint moments and power; however, no geometry was found to enable a "clutch-like" function, with automatic switching from slack (in swing) to stiff (in stance) [page 6 of (*47*)]. Diller *et al.* (*106*) designed an active exoskeleton with a lightweight and efficient electrostatic adhesion clutch, which altered ankle joint stiffness by selectively engaging parallel rubber springs. Clutches have been integrated into soft exoskeletons, where they hold and release elastic belts (*107*). SPEAR robot's foot features a sprocket-like structure that interlocks with a chain section of a biarticular tendon in stance and disconnects the robot's knee in swing, allowing efficient forward hopping with slacked joints in swing (*108*). The multisegmented leg of FastRunner featured ankle and/or knee clutch mechanisms. Although the 1.4-m-tall FastRunner version did not run in hardware, its simulation reached fast speeds with a single, leg-angle actuator (Froude number Fr = 5 to 7; see table S1) (*109*–*111*). These findings suggest yet-untapped potential for effectively designed elastic clutches to improve robot performance. For future work, we suggest that a hybrid design with BirdBot's clutch mechanism combined with direct actuation and sensory feedback control could merge the benefits of both systems to achieve robust and versatile locomotion.

Recently, multiple advances have improved the economy and performance of legged robots. Robots designed with "quasi-direct" or "proprioceptive" actuation use strong, brushless motors and low-ratio gearboxes (*112*). In these robots, interjoint control is governed by an internal robot model, which matches inter- and intrajoint torque to work against external loads. Joint power is applied directly, with extensor and flexor actuation demanding negative and positive work as the leg compresses and extends. These robots can benefit from power regeneration during negative power phases and redistribute recouped power to other actuators or back into the battery (*17*, *112*).

Another approach is to use compliant legs with parallel or serial springs to cycle energy and reduce actuator work (*45*, *99*). Previous robots with pantograph, spring-loaded legs, and in-parallel knee flexing actuation (*45*, *99*) were designed as quadruped robots. Under feedforward control, Cheetah-cub achieved self-stable trot gait patterns with relatively high speeds (Froude number Fr = 1.3). However, without a disengagement mechanism, the stiff extensor spring requires large and rapid torques to shorten the leg for ground clearance in swing. Consequently, Cheetah-cub demanded high electrical power, resulting in a metabolic COT of 6.6 J/N·m, almost four times that of an animal of equal weight (Fig. 7C and table S1) (*45*, *76*).

BirdBot shares several features with Cheetah-cub, including spring-loaded legs, a proximal pantograph, small-sized, brushed-motor actuators, and a similar weight. BirdBot features an important improvement—its foot-triggered clutch slacks the leg joints during swing. With the stance spring disengaged, the knee torque required to flex the leg for ground clearance decreases from 3.7 N·m for a Cheetah-cub leg design to 0.1 N·m with a BirdBot leg (static loading conditions; table S5). BirdBot's distal tendon also stores energy in stance and releases it at the end of stance (Fig. 6B), similar to the ankle actuation of passive walkers (*57*). Both characteristics contribute to BirdBot's low COT—low knee-flexing torque and tendon elastic recoil of the distal tendon. As a result, BirdBot's COT—one-quarter that of Cheetah-cub—is within the range of an animal of equal weight.

Although comparing robots with different morphologies and numbers of legs is imprecise, it nonetheless provides a general perspective on how energetic performance can be improved by design. BirdBot, MIT Cheetah 3 (*113*), and SPEAR (*108*) cluster below the COT of natural runners (Fig. 7C). Hence, legged robots with power regeneration and low-ratio gearing can achieve exceptional energy economy (MIT Cheetah 3; table S1) (*113*, *114*). Specialized hopping robots can be especially economical, because they operate with a single leg angle actuator, achieving a relative COT of 45% (Fig. 7C and table S1) (*76*).

BirdBot's guidance system keeps the trunk from translating sideways and rotating in any direction. Hence, the trunk will not pitch if torque is applied (fig. S5). Immediately before swing-stance transition engagement, the robot's digits require clearance to rotate from digital-flexed to digital-extended. A forward pitching trunk could reduce ground clearance. To compensate for trunk pitching in an unguided version, higher clearance could be achieved by increasing leg angular velocity to reach an earlier maximum forward leg angle with its required posture for clutch-initialization. Implementing a fully three-dimensional version of BirdBot will also require dedicated actuation and control for balance correction to move in three-dimensional environments (*115*–*117*). In general, pitching moments can be reduced by supporting BirdBot's hip-powered actuation with actuator-powered leg extension, with dedicated designs (fig. S11). Alternatively, the robot's trunk design can be adapted for hip-only actuation (*118*).

Conclusion

Legged robot designers tend to neglect typologies and mechanisms observed in animal legs and often prefer high-powered actuation and relatively simple leg structures. Despite the limitations of biological tissues, the agile and robust performance of animals suggests that robot designs can benefit from a rigorous understanding of more complex multiarticular, strategically geared spring mechanisms to achieve simple, fast, and economic leg control. An additional benefit of the mechanism demonstrated here is the potential for more effective foot-substrate interactions. Many robots still use point-foot designs, which simplifies internal model computation. A clear advantage of the mechanism proposed here is its ability to stand upright, with all actuators switched off. The torque-loaded foot-segment creates a range of viable center of pressure points, where the robot's center of mass can be balanced above, reminiscent of a flamingo standing while sleeping (Fig. 8A and fig. S2) (*30*). The functional implications of a foot acting as an effective leg-clutching mechanism in a multisegment elastic leg remain unexplored. The proposed mechanism allows rapid mechanical control of swing-stance transitions, which can be particularly beneficial for navigating uneven, unpredictable, or soft terrains. The leg clutch and foot segment enable rapid spring engagement and adjustment of the center of pressure in direct response to altered loading. Additional research is needed to understand how foot function contributes to locomotion in animals and to make effective use of foot-mediated control of legged robot locomotion.

MATERIALS AND METHODS

Robot prototype

BirdBot is designed to be left-right symmetric. The robot's design parameters are provided in table S2, and its design is shown in Fig. 3 (A and B). Most of the robot's trunk and leg parts are printed from Acrylonitrile Butadiene Styrene on a fused deposition printer (uPrint SE Plus). The nomenclature for segments and angles can be found in fig. S3. Each leg features two springs. The global spring is mounted serially to the global tendon. We simplify the mounting of force sensors and mount the global spring to the robot's trunk, instead of, for example, the leg segment s01 (fig. S3D). As a consequence, the GST also spans over joint j0. A second, pantograph spring (Fig. 3A) is mounted within the segment s12p. The pantograph spring exerts forces when both parts of segment s12p are pulled apart, for example, when leg retraction torque is exerted at the hip joint (*76*). Hence, the pantograph spring acts as a functional rotatory compliant element in response to hip torques. In emus, the gastrocnemius muscle is positioned similar to the spring-12p. Two off-the-shelf robot actuators (Dynamixel, MX-64 AT, RS485) actuate each leg; the hip actuator directly attaches to the leg and swings it forward (protraction) and backward (retraction). The knee actuator shortens the leg's knee joint j1 through the knee flexor tendon. Leg lengthening is not actively supported, meaning the leg lengthens fully after swing phase, only supported by gravity and the leg's angular momentum. The robot's hip axes and knee flexor pulleys are connected to the trunk by large-diameter, thin-section ball bearings. Low friction bushings guide the remaining joint axes, which are cut from steel stock material.

Spring tendon network

A network of four tendons and spring tendons is mounted to each leg, shown in Fig. 3B. The GST splits into a proximal and a distal part (red). The DFT supports j3 and leg disengagement (orange). The knee flexor tendon lifts the slack leg (blue). A last pair of tendons rotates both digits into digital extension (digit-1 extensor and digit-2 extensor, light and olive green). Each tendon is tensioned through a tendon adjustment mechanism (TAM; fig. S9). TAMs are custom-made, from a plastic worm gear driving a drum winding up the tendon, and work similar to a violin's string tensioning mechanism. The multiarticular GST extends joints j1 to j4 against loads in leg length direction during stance phase (Fig. 3B). The GST also spans over joint j0 to simplify mounting the spring's force sensor. The biarticular DFT runs parallel to the GST but spans only over the leg's two distal joints j3 and j4. When tensioned by joint j4 flexion through stance phase, the DFT pushes joint j3 from one stable joint position, over its unstable, collinear position of segment s23 and digit-1 (Fig. 5, C and D). The DFT action "collapses" joint j3 and with it the in-parallel mounted GST. The DFT does not insert into a spring; instead, we directly use the tendon's intrinsic elasticity, similar to a very stiff spring. We estimated the tendon's spring-like stiffness (k = 60 N/mm) in its built-in configuration. The knee flexor tendon flexes the knee joint j1. Its proximal end inserts into the knee actuator pulley. The tendon is then routed over the hip j0 axis, into the knee flexing pulley, and lastly into its TAM mounted to the s23 segment (tibiotarsus; Fig. 3B and fig. S3D). A pair of dorsiflexion tendons span over joints j2 to j4. When joint j2 extends just before touchdown (Fig. 3B), the dorsiflexion tendons rotate digit-1 and digit-2 into a digital-extended position. The dorsiflexion tendon TAMs are integrated into segment s23. The DFT and the GST are mounted antagonistically to the dorsiflexion tendons, and hence, we adjusted each tendons' slack carefully. All tendons are made from 1-mm-thick cables (Dyneema). Tendon ends are manually cut to length. The tendon's tail is inserted into the standing part of the tendon to create an eye. Both twines are lock-stitched together by hand.

The left and right leg GSTs were initially set to zero slack length, with the robot's legs in the air and all the leg segments extended. The robot was placed on the ground, and the GSTs were adjusted for an equal joint j1 angle between the left and the right leg. We adjusted the DFTs on the standing robot with femur segments set vertically by the hip actuator (joint j0, 0°). The tension of the DFTs was adjusted to a force of F = 100 N, just before the joint j3 snap-through. The knee flexor tendon's slack was removed with the femur segment positioned vertically. Both dorsiflexion tendons were adjusted to create joint j4 digital extension when joint j2 is extended. Knee and hip torque sensors and the GST force sensor were calibrated with an external load cell. The robot's legs were placed horizontally to avoid the effect of gravity. The tendon buckle sensor was calibrated with a defined external load pulling on the DFT.

Actuators and low-level actuator control

Four off-the-shelf robot actuators drive the robot's legs (Dynamixel, MX-64 AT; Fig. 3, A and B). One hip actuator per leg is mounted between the trunk and the femur segment s01; it directly moves the femur. The knee actuator flexes the knee joint j1 by pulling on the knee flexor tendon (Fig. 3B). We controlled the actuators in position mode, from a control PC with an update frequency of f = 125 Hz. All four actuators are connected through a single RS485 communication bus. A U2D2 universal serial bus (USB) communication converter connects the communication bus via USB to the control PC. We modified the MATLAB Dynamixel software development kit for this use (SDK, v.3.5.4). All control commands were sent as feedforward signals.

Instrumentation

Each leg is instrumented with four sensors measuring force or torque. A custom-designed sensor measures the hip actuator's reaction torque. The reaction force F is measured by an off-the-shelf beam-type load cell (TAL220; 100 N), at a lever arm length of l = 47 mm, and we calculate the hip reaction torque $\tau = F \cdot l$ (Fig. 6C). A second, identically constructed sensor measures the reaction torque of the knee actuator, and we calculate the torque acting at the knee flexor tendon (Fig. 6E). The GST's force is measured with an identical force sensor (fig. S9). We measure the DFT's force with a custom-designed tendon buckle sensor. All joint positions are measured with absolute magnetic encoders (AS 5045, AMS), recorded at f = 333 Hz, and time-stamped with a microcontroller board (Arduino Mega), individually for the right and left leg. Both microcontrollers were connected to a PC with USB. Force data were sampled by a data acquisition system (cDAQ-9189, National Instruments) at $f = 1$ kHz, with strain bridge input modules (NI-9237). A custom-written LabVIEW program recorded the NI MAX module data, including the trigger line status. The current supplied to the actuators was captured with an external current sensor (LA 25, 25 A, LEM), mounted to a custom amplifier. The amplifier's voltage output signal was recorded with an analog-to-digital converter (NI-9205). The current sensor was calibrated with a 1-ohm precision resistor. Current data were time-stamped and trigger-synchronized. An external power supply provided the robot's actuator voltage (12.0 V) through a power cable.

Video

Gait experiments were recorded with a high-speed camera (MiroLab 110, Phantom) at a frame rate of $f = 400$ frames/s, and still frames were extracted from video material for Fig. 6A. High-speed videos were synchronized to the data on the basis of an optical and electrical trigger event. Touchdown and toe-off events were determined manually from high-speed videos. Further videos and photos were recorded with a camcorder (FDR-AX 100, Sony) and a digital camera (D5500, Nikon).

Calculation of Froude number, COT, and electrical and mechanical power

We calculate the Froude number as

$$\mathrm{Fr} = v^2/\mathrm{gl} \tag{5}$$

according to (*119*), where v is the robot's speed v in meters per second on the treadmill, averaged over in the sum of 70 strides from five experiments with each 14 strides. The robot's standing hip height is $l = 0.29$ m, and the gravitational acceleration is $g = 9.81$ m/s^2. The mechanical power P (in watts) was calculated as the product of velocity v (in meters per second) and force F (in newtons), or angular velocity ω (in radian per second) and torque τ (in newton-meter). The robot's electrical (metabolic) COT was calculated according to (*120*). We measured the instantaneous current I (in amperes) with current clamps for each actuator individually, calibrated the data, and kept the positive values only, from 70 strides. We then summed up the data of the four actuators and derived the means and SD (table S4). We then calculated the net electrical COT

$$\mathrm{COT}_{\mathrm{en}} = ((U \cdot I) - P_{\mathrm{SB}})/(m \cdot g \cdot v) \tag{6}$$

where we removed the standby actuator power $P_{\mathrm{SB}} = 4.8$ W. The actuator's manual specifies 100-mA standby current, which we confirmed by own measurement. The robot's weight mounted to the rail is $m = 1.73$ kg, the average robot speeds were $v = 0.50$ m/s at $f = 1$ Hz stride frequency, and $v = 0.75$ m/s for $f = 1.5$ Hz stride frequency. COT is normalized (in joules per newton-meter) to evaluate the energy efficiency during locomotion. However, animal locomotion data indicate that the COT decreases with increasing animal mass m, also shown with the "natural runner" down-sloping trend line in (*120*). To compare BirdBot's COT to legged hoppers, bipedal robots, and quadrupedal robots of different body masses, we first digitized Tucker's trend line [figure 2 of (*120*)], which leads to the following COT reference line (Fig. 7C, 100% line)

$$\log_{10}(\mathrm{COT}_{\mathrm{nr}}) = -0.3138 \cdot \log_{10}(m) + 0.2346 \tag{7}$$

We added indicator lines (25, 50, 100, 200, and 400%) for a "relative COT" (in percentage), calculated as the ratio between the natural runner's COT and the robot's electrical net or total COT to Fig. 7C, to indicate COT grouping of robots of different types and sizes

$$\mathrm{COT}_{\mathrm{re}} = \frac{\mathrm{COT}_{\mathrm{nr}}}{\mathrm{COT}_{\mathrm{en}}} \cdot 100\% \tag{8}$$

The above COT comparison is based on allometric relationships; we are comparing BirdBot with an average animal of the same body weight. Specific costs of transport values of similar sized birds at similar locomotion speeds are 0.81 J/N·m [guineafowl (*Numida meleagris*), 1.5 kg, between 0.5 and 3 m/s] (*121*), 1.30 J/N·m [leghorns (*Gallus gallus domesticus*), 2.0 kg, 0.7 m/s] (*122*), and 1.4 and 2.0 J/N·m (guineafowl, 1.3 kg, 0.5 and 1.0 m/s) (*123*).

Locomotion control pattern generation

We generated locomotion control patterns with a CPG, similar to (*45*, *124*). We applied CPG control to generate smooth hip joint angle trajectories, which is important when initializing the gait patterns. Custom-designed CPGs require only few driving parameters, such as amplitude, offset, phase shift, and duty factor. The CPG was implemented on a PC in MATLAB; the trajectories were sent to the actuators as feedforward signals. Stride frequencies of $f = 1.0$ and 1.5 Hz were set, resulting in robot speeds of 0.50 and 0.75 m/s, respectively. The left and the right leg received phase-shifted but otherwise identical trajectories

$$\dot{\phi}_i = 2\pi f + \sum_{i \neq j} c_{ij} \sin(\phi_j - \phi_i - \varphi_{ij}) \tag{9}$$

$$\dot{a}_i^h = \alpha(A_i^h - a_i^h) \tag{10}$$

$$\dot{o}_i^h = \alpha(O_i^h - o_i^h) \tag{11}$$

where ϕ_i is the i-oscillator's phase; $c_{12} = 1$ and $c_{21} = 0$ are coupling terms; f is the stride frequency, $\varphi_{12} = \pi$ and $\varphi_{21} = 0$ are phase shifts between the hip oscillators, a^h and A^h are the instantaneous and the commanded hip amplitude, respectively; o^h and O^h are the instantaneous and the commanded hip offset, respectively; and α is a convergence gain. The commanded duty factor D adapts the phase Θ_i^h of the hip joint of leg i, leading to the hip actuator set position h_i

$$\Theta_i^h = \begin{cases} \dfrac{\phi_i}{2D} & 0 \leq \phi_i \leq 2\pi D \\ \dfrac{\phi_i + 2\pi(1-2D)}{2(1-D)} & \end{cases} \tag{12}$$

$$h_i = a_i^h \cos(\Theta_i^h) + o_i^h \tag{13}$$

The active shortening of the leg length by the knee actuator is coupled to the hip oscillator's phase ϕ_i by the phase shift S_F (begin, flexing) and S_E (end, release and passive extension)

$$S_F = 2\pi S_f(1 - D) \tag{14}$$

$$S_E = 2\pi S_e(1 - D) \tag{15}$$

Table 1. The CPG parameters for gait 1 ($f = 1$ Hz) and gait 2 ($f = 1.5$ Hz).

Parameter	Gait 1	Gait 2	Parameter	Gait 1	Gait 2
f (Hz)	1	1.5	D_{vir}	0.6	0.6
A^h (°)	32	35	α	1	1
O^h (°)	22	30	S_f	0	0
A^k (°)	120	120	S_e	0.22	0.22

where S_F and S_e are the fraction of flexion and extension delay of swing phase, respectively. The knee i actuator angle is set as k_i, with the commanded knee amplitude A^k

$$k_i = \begin{cases} 0 & 0 \le \phi_i \le 2\pi D + S_F \\ A_i^k & 2\pi D + S_F \le \phi_i \le 2\pi - S_E \end{cases} \tag{16}$$

We observe that the commanded duty factor ($D = 0.60$) differs from the observed duty factor ($D = 0.49$, $f = 1.5$ Hz stride frequency). A typical CPG output for one stride of a single leg is provided in fig. S1. CPG parameters are provided in Table 1.

Cadaver studies

Emu cadavers were obtained from a prior study of emu ontogenetic biomechanics (*125*) at the Royal Veterinary College (RVC) Structure and Motion Laboratory. The animals were housed and reared at the RVC, and all procedures and humane euthanasia were conducted with ethical approval under a U.K. Home Office license: PPL707122. Cadavers were stored in a −20°C freezer after euthanasia and thawed slowly to room temperature before experiments.

Treadmill and guide setup

The robot walked on a recreational treadmill (model Christopeit TM500S), modified for speed control by setting a directly connected power supply voltage. The treadmill's speed was measured by a custom mounted encoder (AS 5045, AMS) and recorded by a microcontroller (Arduino Mega). A linear guide (Misumi SVR) was degreased and loosened for minimal sliding friction. The slider is mounted to an overhead rail, $h = 0.53$ m above the belt. Rail and robot are connected by a parallel four-bar guide, with segment lengths $l = 0.51$ m and $l = 0.04$ m. The rail and four-bar restrict the robot to translations in the sagittal plane (fore-aft and up-down) and prohibit trunk pitching. The linear guide's position is measured by a pair of countermounted draw-wire sensors (Waycon LX-PA-20), read out by an analog-digital converter (NI 9205).

Static knee joint torque in swing and stance

For static conditions, we calculated the torque required to extend the knee joint when standing on a single leg and holding the robot's weight and while lifting the lower leg. We simulated three different robot spring and actuator configurations (fig. S4, A to C). All three modeled robot configurations have an equal mass of $m = 1.73$ kg, identical to BirdBot. The robots' center of mass and their hip joints align vertically, and no hip torque is induced during standing. In the lifted leg scenario, the lower leg mass and the horizontal distance between its segments' center of gravity and the knee joint are assumed to be identical for all three designs ($m_{\mathrm{lower}} = 0.092$ kg, $l_{\mathrm{distance}} = 0.056$ m).

Single leg disengagement experiment

The joint positions at leg disengagement and leg unloading were determined on the basis of visual cues, tracked manually from high-speed video footage. Angles were extracted in ImageJ software. The virtual leg angle was defined by the joints j0 and j4 and a third point at the trunk. For the leg with the DFT mounted, we determined the disengagement leg angle when $\alpha_{j3} > 180°$.

Disengagement tendon work calculation

We estimate a spring-like behavior of the DFT. We calculated the tendon's stiffness (k_{DET}) by measuring a known tendon force F_{DET} and the tendon's change in length $\Delta(l_{\mathrm{DET}})$, in its built-in state. For the plot Fig. 6B, we calculate the DFT work W_{DET} from the recorded tendon force, and the change of tendon length l_{DET} wrapping around the pulleys of joints j3 and j4

$$W_{\mathrm{DET}} = \frac{1}{2} F_{\mathrm{DET}} \cdot \Delta l_{\mathrm{DET}} \tag{17}$$

GST work calculation

The work W_{GST} of the GST is calculated from the tendon's force, which is identical to the spring force, and the spring stiffness (Fig. 6D)

$$W_{\mathrm{GST}} = \frac{1}{2} \frac{F_{\mathrm{GST}}^2}{k} \tag{18}$$

Data processing

Data were processed in MATLAB (MathWorks). Joint speeds were derived from joint encoder data, applying the "sgolay_t" MATLAB function to joint position data (author: T. Ramos, settings: $N = 4$, $F = 51$, DIM = 1). Current data were filtered with a zero-phase digital filter (30-Hz low pass, second order, 0.2 PassbandRipple).

Statistics

Unless otherwise indicated, uncertainty bounds are provided as means and SD (means ± SD). Data from continuous data plots are presented as means and 95% CI (means ± CI), averaged over 70 strides. Single leg disengagement data are presented as mean of 20 repetitions per leg configuration. Mean disengagement angles of 69.0° ± 1.2° and 59.0° ± 0.3° (means ± SD) were recorded for the leg with and without the DFT, respectively (Fig. 5). The 10° difference was statistically significant according to a Mann-Whitney *U* test, $n1 = n2 = 20$, $P = 0.01$. Correlation coefficients for j2 and j3 joint trajectories (Fig. 2) were calculated as r = correff(j2, j3) (MATLAB), with 2001 data points from five joint extensions and flexions. The flexion correlation coefficient is $r_{\text{flex}} = 0.99$, and the extension correlation coefficient is $r_{\text{ext}} = 0.96$ (Fig. 2C). Correlation coefficients $r > 0.8$ are considered an indicator for strong coupling.

SUPPLEMENTARY MATERIALS

www.science.org/doi/10.1126/scirobotics.abg4055
Text S1 to S5
Figs. S1 to S14
Tables S1 to S5
Movies S1 to S7
References (*127*–*133*)

REFERENCES AND NOTES

1. J. Delmerico, S. Mintchev, A. Giusti, B. Gromov, K. Melo, T. Horvat, C. Cadena, M. Hutter, A. Ijspeert, D. Floreano, L. M. Gambardella, R. Siegwart, D. Scaramuzza, The current state and future outlook of rescue robotics. *J. Field Robot.* **36**, 1171–1191 (2019).
2. F. Iida, A. J. Ijspeert, Biologically inspired robotics, in *Springer Handbook of Robotics* (Springer, 2016), chap. 75, pp. 2015–2034.
3. N. Kashiri, A. Abate, S. J. Abram, A. Albu-Schaffer, P. J. Clary, M. Daley, S. Faraji, R. Furnemont, M. Garabini, H. Geyer, A. M. Grabowski, J. Hurst, J. Malzahn, G. Mathijssen, D. Remy, W. Roozing, M. Shahbazi, S. N. Simha, J. B. Song, N. Smit-Anseeuw, S. Stramigioli, B. Vanderborght, Y. Yesilevskiy, N. Tsagarakis, An overview on principles for energy efficient robot locomotion. *Front. Roboti. AI* **5**, 129 (2018).
4. G.-Z. Yang, J. Bellingham, P. E. Dupont, P. Fischer, L. Floridi, R. Full, N. Jacobstein, V. Kumar, M. McNutt, R. Merrifield, B. J. Nelson, B. Scassellati, M. Taddeo, R. Taylor, M. Veloso, Z. L. Wang, R. Wood, The grand challenges of Science Robotics. *Sci. Robot.* **3**, eaar7650 (2018).
5. K. Nishikawa, A. A. Biewener, P. Aerts, A. N. Ahn, H. J. Chiel, M. A. Daley, T. L. Daniel, R. J. Full, M. E. Hale, T. L. Hedrick, A. K. Lappin, T. R. Nichols, R. D. Quinn, R. A. Satterlie, B. Szymik, Neuromechanics: An integrative approach for understanding motor control. *Integr. Comparative Biol.* **47**, 16–54 (2007).
6. M. A. Daley, Understanding the agility of running birds: Sensorimotor and mechanical factors in avian bipedal locomotion. *Integr. Comparative Biol.* **58**, 884–893 (2018).
7. L. H. Ting, H. J. Chiel, R. D. Trumbower, J. L. Allen, J. L. McKay, M. E. Hackney, T. M. Kesar, Neuromechanical principles underlying movement modularity and their implications for rehabilitation. *Neuron* **86**, 38–54 (2015).
8. L. H. Ting, H. J. Chiel, Muscle, biomechanics, and implications for neural control. *Neurobiol. Motor Control. Fund. Concepts New Direct.* 365–416 (2017).
9. M. Plooij, G. Mathijssen, P. Cherelle, D. Lefeber, B. Vanderborght, Lock your robot: A review of locking devices in robotics. *IEEE Robot. Autom. Mag.* **22**, 106–117 (2015).
10. H. L. More, J. R. Hutchinson, D. F. Collins, D. J. Weber, S. K. H. Aung, J. M. Donelan, Scaling of sensorimotor control in terrestrial mammals. *Proc. R. Soc. B Biol. Sci.* **277**, 3563–3568 (2010).
11. T. R. Nichols, T. C. Cope, T. A. Abelew, 8 rapid spinal mechanisms of motor coordination. *Exerc. Sport Sci. Rev.* **27**, 255–284 (1999).
12. R. Poppele, C. Terzuolo, Myotatic reflex: Its input-output relation. *Science* **159**, 743–745 (1968).
13. A. A. Sharp, E. Ma, A. Bekoff, Developmental changes in leg coordination of the chick at embryonic days 9, 11, and 13: Uncoupling of ankle movements. *J. Neurophysiol.* **82**, 2406–2414 (1999).
14. Y. P. Ivanenko, R. E. Poppele, F. Lacquaniti, Five basic muscle activation patterns account for muscle activity during human locomotion. *J. Physiol.* **556**, 267–282 (2004).
15. S. Aoi, T. Ohashi, R. Bamba, S. Fujiki, D. Tamura, T. Funato, K. Senda, Y. Ivanenko, K. Tsuchiya, Neuromusculoskeletal model that walks and runs across a speed range with a few motor control parameter changes based on the muscle synergy hypothesis. *Sci. Rep.* **9**, 369 (2019).
16. L. Righetti, J. Buchli, M. Mistry, M. Kalakrishnan, S. Schaal, Optimal distribution of contact forces with inverse-dynamics control. *Int. J. Rob. Res.* **32**, 280–298 (2013).
17. C. Hubicki, J. Grimes, M. Jones, D. Renjewski, A. Spröwitz, A. Abate, J. Hurst, ATRIAS: Design and validation of a tether-free 3D-capable spring-mass bipedal robot. *Int. J. Rob. Res.* **35**, 1497–1521 (2016).
18. S. Seok, A. Wang, D. Otten, S. Kim, Actuator design for high force proprioceptive control in fast legged locomotion, in *Proceedings of the 2012 IEEE/RSJ International Conference on Intelligent Robots and Systems (IROS)* (IEEE, 2012), pp. 1970–1975.
19. D. J. Hyun, S. Seok, J. Lee, S. Kim, High speed trot-running: Implementation of a hierarchical controller using proprioceptive impedance control on the MIT Cheetah. *Int. J. Rob. Res.* **33**, 1417–1445 (2014).
20. G. Bledt, P. M. Wensing, S. Ingersoll, S. Kim, Contact model fusion for event-based locomotion in unstructured terrains, in *Proceedings of the 2018 IEEE International Conference on Robotics and Automation (ICRA)* (IEEE, 2018), pp. 4399–4406.
21. F. Grimminger, A. Meduri, M. Khadiv, J. Viereck, M. Wüthrich, M. Naveau, V. Berenz, S. Heim, F. Widmaier, T. Flayols, J. Fiene, A. Badri-Spröwitz, L. Righetti, An open torque-controlled modular robot architecture for legged locomotion research. *IEEE Robot. Autom. Lett.* **5**, 3650–3657 (2020).
22. M. S. Ashtiani, A. Aghamaleki Sarvestani, A. Badri-Spröwitz, Hybrid parallel compliance allows robots to operate with sensorimotor delays and low control frequencies. *Front. Robot. AI* **8**, 645748 (2021).
23. N. U. Schaller, thesis, University of Heidelberg (2008).
24. N. U. Schaller, B. Herkner, R. Villa, P. Aerts, The intertarsal joint of the ostrich (*Struthio camelus*): Anatomical examination and function of passive structures in locomotion. *J. Anat.* **214**, 830–847 (2009).
25. M. A. Daley, A. Voloshina, A. A. Biewener, The role of intrinsic muscle mechanics in the neuromuscular control of stable running in the guinea fowl. *J. Physiol.* **587**, 2693–2707 (2009).
26. M. A. Daley, A. A. Biewener, Running over rough terrain reveals limb control for intrinsic stability. *Proc. Natl. Acad. Sci. U.S.A.* **103**, 15681–15686 (2006).
27. M. A. Daley, G. Felix, A. A. Biewener, Running stability is enhanced by a proximo- distal gradient in joint neuromechanical control. *J. Exp. Biol.* **210**, 383–394 (2007).
28. A. M. Wilson, J. C. Watson, G. A. Lichtwark, A catapult action for rapid limb protraction. *Nature* **421**, 35–36 (2003).
29. M. P. McGuigan, A. M. Wilson, The effect of gait and digital flexor muscle activation on limb compliance in the forelimb of the horse Equus caballus. *J. Exp. Biol.* **206**, 1325–1336 (2003).
30. Y.-H. Chang, L. H. Ting, Mechanical evidence that flamingos can support their body on one leg with little active muscular force. *Biol. Lett.* **13**, 20160948 (2017).
31. J.-M. Denoix, J.-P. Pailloux, *Physiotherapie und Massage bei Pferden Bewegungstherapie nach den Gesetzen der Biomechanik ; 4 Tabellen* (Stuttgart: Ulmer, 2000).
32. R. Pfeifer, M. Lungarella, F. Iida, Self-organization, embodiment, and biologically inspired robotics. *Science* **318**, 1088–1093 (2007).
33. H. Elftman, The function of muscles in locomotion. *Am. J. Physiol. Leg. Content* **125**, 357–366 (1939).
34. G. J. van Ingen Schenau, M. F. Bobbert, R. H. Rozendal, The unique action of bi-articular muscles in complex movements. *J. Anat.* **155**, 1–5 (1987).
35. G. Jan Van Ingen Schenau, On the action of bi-articular muscles, a review. *Nethe. J. Zool.* **40**, 521–543 (1989).
36. A. D. Kuo, The action of two-joint muscles: The legacy of WP Lombard, in *Classics in Movement Science* (Human Kinetics, 2001), pp. 289–316.
37. M. A. Daley, A. A. Biewener, Leg muscles that mediate stability: Mechanics and control of two distal extensor muscles during obstacle negotiation in the guinea fowl. *Philos. Trans. R. Soc. B Biol. Sci.* **366**, 1580–1591 (2011).
38. J. C. Gordon, N. C. Holt, A. Biewener, M. A. Daley, Tuning of feedforward control enables stable muscle force-length dynamics after loss of autogenic proprioceptive feedback. *eLife* **9**, e53908 (2020).
39. A. J. Ijspeert, Biorobotics: Using robots to emulate and investigate agile locomotion. *Science* **346**, 196–203 (2014).
40. W. P. Lombard, The tendon action and leverage of two-joint muscles of the hind leg of the frog, with special reference to the spring movement. *Contributions to medical research. Wahr, Ann Arbor* (1903), pp. 280–301.
41. M. Hildebrand, The mechanics of horse legs. *Am. Sci.* 594–601 (1987).
42. K. Arikawa, S. Hirose, Development of quadruped walking robot TITAN-VIII, in *Proceedings of the 1996 IEEE/RSJ International Conference on Intelligent Robots and Systems* '96 *(IROS 96)* (IEEE, 1996), vol. 1, pp. 208–214.
43. H. Witte, R. Hackert, K. Lilje, N. Schilling, D. Voges, G. Klauer, W. Ilg, J. Albiez, A. Seyfarth, D. Germann, M. Hiller, R. Dillmann, M. Fischer, Transfer of biological principles into the construction of quadruped walking machines, in *Proceedings of the Second International Workshop on Robot Motion and Control* (IEEE, 2001), pp. 245–249.
44. D. C. Kar, Design of statically stable walking robot: A review. *J. Robot. Syst.* **20**, 671–686 (2003).
45. A. Spröwitz, A. Tuleu, M. Vespignani, M. Ajallooeian, E. Badri, A. Ijspeert, Towards dynamic trot gait locomotion: Design, control and experiments with Cheetah-cub, a compliant quadruped robot. *Int. J. Robot. Res.* **32**, 932–950 (2013).
46. S. Seok, A. Wang, M. Y. Chuah, D. Otten, J. Lang, S. Kim, Design principles for highly efficient quadrupeds and implementation on the MIT Cheetah robot, in *Proceedings of the 2013 IEEE International Conference on Robotics and Automation* (IEEE, 2013), pp. 3307–3312.
47. A. J. van den Bogert, Exotendons for assistance of human locomotion. *Biomed. Eng. Online* **2**, 17 (2003).

48. J. Pratt, G. Pratt, Intuitive control of a planar bipedal walking robot, in *Proceedings of the IEEE International Conference on Robotics and Automation (ICRA '98)* (IEEE, 1998), vol. 3, pp. 1–12.
49. R. M. Alexander, H. C. Bennet-Clark, Storage of elastic strain energy in muscle and other tissues. *Nature* **265**, 114–117 (1977).
50. R. M. Alexander, Elastic energy stores in running vertebrates. *Am. Zool.* **24**, 85–94 (1984).
51. T. A. McMahon, The role of compliance in mammalian running gaits. *J. Exp. Biol.* **115**, 263–282 (1985).
52. A. Ananthanarayanan, M. Azadi, S. Kim, Towards a bio-inspired leg design for high-speed running. *Bioinspir. Biomim.* **7**, 046005 (2012).
53. K. Kurokawa, R. Sato, S. Hiasa, A. Ming, F. Meng, H. Liu, X. Fan, X. Chen, Z. Yu, Q. Huang, Introduction of toe mechanism with bi-articular tendon into legged robot, in *Proceedings of the 2018 IEEE International Conference on Mechatronics and Automation (ICMA)* (IEEE, 2018), pp. 1597–1602.
54. W. Roozing, Z. Li, D. Caldwell, N. Tsagarakis, Design optimisation and control of compliant actuation arrangements in articulated robots for improved energy efficiency. *IEEE Robot. Autom. Lett.* **1**, 1110–1117 (2016).
55. H. Barazesh, M. Ahmad Sharbafi, A biarticular passive exosuit to support balance control can reduce metabolic cost of walking. *Bioinspir. Biomim.* **15**, 036009 (2020).
56. T. McGeer, Passive dynamic walking. *Int. J. Rob. Res.* **9**, 62–82 (1990).
57. S. Collins, A. Ruina, R. Tedrake, M. Wisse, Efficient bipedal robots based on passive-dynamic walkers. *Science* **307**, 1082–1085 (2005).
58. R. Tedrake, T. W. Zhang, M.-f. Fong, H. S. Seung, Actuating a simple 3D passive dynamic walker, in *Proceedings of the IEEE International Conference on Robotics and Automation, ICRA'04. 2004* (IEEE, 2004), vol. 5, pp. 4656–4661.
59. S. H. Collins, M. Wisse, A. Ruina, A Three-dimensional passive-dynamic walking robot with two legs and knees. *Int. J. Rob. Res.* **20**, 607–615 (2001).
60. S. Collins, A. Ruina, A bipedal walking robot with efficient and human-like gait, in *Proceedings of the 2005 IEEE International Conference on Robotics and Automation, ICRA 2005* (IEEE, 2005), pp. 1983–1988.
61. G. E. Weissengruber, G. Forstenpointner, D. Gangl, Gut zu Fuß - funktionell-anatomische Aspekte des bipeden Laufens beim Afrikanischen Strauß (*Struthio camelus* Linné, 1758). *Vet. Med. Austria* **90**, 67–78 (2003).
62. T. J. Roberts, J. A. Scales, Adjusting muscle function to demand: Joint work during acceleration in wild turkeys. *J. Exp. Biol.* **207**, 4165–4174 (2004).
63. J. Rubenson, D. G. Lloyd, T. F. Besier, D. B. Heliams, P. A. Fournier, Running in ostriches (*Struthio camelus*): Three-dimensional joint axes alignment and joint kinematics. *J. Exp. Biol.* **210**, 2548–2562 (2007).
64. P. J. Bishop, K. B. Michel, A. Falisse, A. R. Cuff, V. R. Allen, F. D. Groote, J. R. Hutchinson, Computational modelling of muscle fibre operating ranges in the hindlimb of a small ground bird (*Eudromia elegans*), with implications for modelling locomotion in extinct species. *PLOS Comput. Biol.* **17**, e1008843 (2021).
65. J. Rubenson, D. G. Lloyd, D. B. Heliams, T. F. Besier, P. A. Fournier, Adaptations for economical bipedal running: The effect of limb structure on three-dimensional joint mechanics. *J. R. Soc. Interface* **8**, 740–755 (2011).
66. A. Abourachid, E. Höfling, The legs: A key to bird evolutionary success. *J. Ornithol.* **153**, 193–198 (2012).
67. J. R. Hutchinson, J. W. Rankin, J. Rubenson, K. H. Rosenbluth, R. A. Siston, S. L. Delp, Musculoskeletal modelling of an ostrich (*Struthio camelus*) pelvic limb: Influence of limb orientation on muscular capacity during locomotion. *PeerJ* **3**, e1001 (2015).
68. N. Smith, A. Wilson, K. Jespers, R. Payne, Muscle architecture and functional anatomy of the pelvic limb of the ostrich (*Struthio camelus*). *J. Anat.* **209**, 765–779 (2006).
69. J. Gray, Studies in the mechanics of the tetrapod skeleton. *J. Exp. Biol.* **20**, 88–116 (1944).
70. M. S. Fischer, N. Schilling, M. Schmidt, D. Haarhaus, H. Witte, Basic limb kinematics of small therian mammals. *J. Exp. Biol.* **205**, 1315–1338 (2002).
71. H. Witte, J. Biltzinger, R. Hackert, N. Schilling, M. Schmidt, C. Reich, M. S. Fischer, Torque patterns of the limbs of small therian mammals during locomotion on flat ground. *J. Exp. Biol.* **205**, 1339–1353 (2002).
72. A. A. Biewener, Scaling body support in mammals: Limb posture and muscle mechanics. *Science* **245**, 45–48 (1989).
73. R. Blickhan, The spring-mass model for running and hopping. *J. Biomech.* **22**, 1217–1227 (1989).
74. T. A. McMahon, G. C. Cheng, The mechanics of running: How does stiffness couple with speed? *J. Biomech.* **23**, 65–78 (1990).
75. C. Farley, J. Glasheen, T. McMahon, Running springs: Speed and animal size. *J. Exp. Biol.* **185**, 71–86 (1993).
76. F. Ruppert, A. Badri-Spröwitz, Series elastic behavior of biarticular muscle-tendon structure in a robotic leg. *Front. Neurorobot.* **13**, 64 (2019).
77. E. Mahdy, M. Raouf, Normal anatomical and diagnostic imaging techniques of the musculotendinous structures of the ostrich (*Struthio camelus*) foot. *J. Adv. Vet. Anim. Res.* **7**, 242–252 (2020).
78. S. N. Patek, B. N. Nowroozi, J. E. Baio, R. L. Caldwell, A. P. Summers, Linkage mechanics and power amplification of the mantis shrimp's strike. *J. Exp. Biol.* **210**, 3677–3688 (2007).
79. M. A. Fedak, H. J. Seeherman, Reappraisal of energetics of locomotion shows identical cost in bipeds and quadrupeds including ostrich and horse. *Nature* **282**, 713–716 (1979).
80. R. L. Marsh, D. J. Ellerby, H. T. Henry, J. Rubenson, The energetic costs of trunk and distal-limb loading during walking and running in guinea fowl *Numida meleagris*: I. Organismal metabolism and biomechanics. *J. Exp. Biol.* **209**, 2050–2063 (2006).
81. D. J. Ellerby, M. Cleary, R. L. Marsh, C. I. Buchanan, Measurement of maximum oxygen consumption in guinea fowl *Numida meleagris* indicates that birds and mammals display a similar diversity of aerobic scopes during running. *Physiol. Biochem. Zool.* **76**, 695–703 (2003).
82. J. Rubenson, D. B. Heliams, D. G. Lloyd, P. A. Fournier, Gait selection in the ostrich: Mechanical and metabolic characteristics of walking and running with and without an aerial phase. *Proc. R. Soc. Lond. B Biol. Sci.* **271**, 1091–1099 (2004).
83. A. V. Birn-Jeffery, C. M. Hubicki, Y. Blum, D. Renjewski, J. W. Hurst, M. A. Daley, Don't break a leg: Running birds from quail to ostrich prioritise leg safety and economy on uneven terrain. *J. Exp. Biol.* **217**, 3786–3796 (2014).
84. R. M. Alexander, G. M. O. Maloiy, R. Njau, A. S. Jayes, Mechanics of running of the ostrich (*Struthio camelus*). *J. Zool. Lond.* **187**, 169–178 (1979).
85. M. A. Daley, A. J. Channon, G. S. Nolan, J. Hall, Preferred gait and walk–run transition speeds in ostriches measured using GPS-IMU sensors. *J. Exp. Biol.* **219**, 3301–3308 (2016).
86. Y. Blum, H. R. Vejdani, A. V. Birn-Jeffery, C. M. Hubicki, J. W. Hurst, M. A. Daley, Swing-leg trajectory of running guinea fowl suggests task-level priority of force regulation rather than disturbance rejection. *PLOS ONE* **9**, e100399 (2014).
87. D. Gangl, G. E. Weissengruber, M. Egerbacher, G. Forstenpointner, Anatomical description of the muscles of the pelvic limb in the ostrich (*Struthio camelus*). *Anat. Histol. Embryol.* **33**, 100–114 (2004).
88. R. Zhang, Q. Ji, G. Luo, S. Xue, S. Ma, J. Li, L. Ren, Phalangeal joints kinematics during Ostrich (*Struthio camelus*) locomotion. *PeerJ* **4**, e2324v1 (2016).
89. V. R. Allen, R. E. Kambic, S. M. Gatesy, J. R. Hutchinson, Gearing effects of the patella (knee extensor muscle sesamoid) of the helmeted guineafowl during terrestrial locomotion. *J. Zool.* 178–187 (2017).
90. N. S. Bradley, A. Bekoff, Development of coordinated movement in chicks: I. Temporal analysis of hindlimb muscle synergies at embryonic days 9 and 10. *Dev. Psychobiol.* **23**, 763–782 (1990).
91. J. C. Gordon, J. W. Rankin, M. A. Daley, How do treadmill speed and terrain visibility influence neuromuscular control of guinea fowl locomotion? *J. Exp. Biol.* **218**, 3010–3022 (2015).
92. S. M. Gatesy, Guineafowl hind limb function. II: Electromyographic analysis and motor pattern evolution. *J. Morphol.* **240**, 127–142 (1999).
93. T. J. Roberts, R. L. Marsh, P. G. Weyand, C. R. Taylor, Muscular force in running turkeys: The economy of minimizing work. *Science* **275**, 1113–1115 (1997).
94. S. Longo, S. Cox, E. Azizi, M. Ilton, J. Olberding, R. St Pierre, S. Patek, Beyond power amplification: Latch-mediated spring actuation is an emerging framework for the study of diverse elastic systems. *J. Exp. Biol.* **222**, jeb197889 (2019).
95. S. W. Lipfert, M. Günther, D. Renjewski, A. Seyfarth, Impulsive ankle push-off powers leg swing in human walking. *J. Exp. Biol.* **217**, 1218–1228 (2014).
96. K. Miyashita, Y. Masuda, M. Gunji, A. Fukuhara, K. Tadakuma, M. Ishikawa, Emergence of swing-to-stance transition from interlocking mechanism in horse hindlimb, in *Proceedings of the 2020 IEEE/RSJ International Conference on Intelligent Robots and Systems (IROS)* (IEEE, 2021), pp. 7860–7865.
97. C. Semini, N. G. Tsagarakis, E. Guglielmino, M. Focchi, F. Cannella, D. G. Caldwell, Design of HyQ—A hydraulically and electrically actuated quadruped robot. *Proc. Inst. Mech. Eng. I J. Syst. Control Eng.* **225**, 831–849 (2011).
98. M. Hutter, C. Gehring, D. Jud, A. Lauber, C. D. Bellicoso, V. Tsounis, J. Hwangbo, K. Bodie, P. Fankhauser, M. Bloesch, R. Diethelm, S. Bachmann, A. Melzer, M. A. Höepflinger, ANYmal - a highly mobile and dynamic quadrupedal robot, in *Proceedings of the 2016 IEEE/RSJ International Conference on Intelligent Robots and Systems (IROS)* (IEEE, 2016), pp. 38–44.
99. A. Spröwitz, A. Tuleu, M. Ajallooeian, M. Vespignani, R. Möckel, P. Eckert, M. D'Haene, J. Degrave, A. Nordmann, B. Schrauwen, J. Steil, A. J. Ijspeert, Oncilla robot: A versatile open-source quadruped research robot with compliant pantograph legs. *Front. Robot. AI* **5**, 67 (2018).
100. S. Gatesy, A. Biewener, Bipedal locomotion: Effects of speed, size and limb posture in birds and humans. *J. Zool.* **224**, 127–147 (1991).
101. T. J. Roberts, E. Azizi, Flexible mechanisms: The diverse roles of biological springs in vertebrate movement. *J. Exp. Biol.* **214**, 353–361 (2011).

102. J. W. Rankin, J. Rubenson, J. R. Hutchinson, Inferring muscle functional roles of the ostrich pelvic limb during walking and running using computer optimization. *J. R. Soc. Interface* **13**, 20160035 (May 2016).
103. E. J. Rouse, L. M. Mooney, H. M. Herr, Clutchable series-elastic actuator: Implications for prosthetic knee design. *Int. J. Rob. Res.* **33**, 1611–1625 (2014).
104. M. Plooij, M. Wisse, H. Vallery, Reducing the energy consumption of robots using the bidirectional clutched parallel elastic actuator. *IEEE Trans. Robot.* **32**, 1512–1523 (2016).
105. M. Wiggin, G. Sawicki, S. Collins, presented at the 2011 IEEE International Conference on Rehabilitation Robotics (ICORR) (IEEEE, 2011), pp. 1–5.
106. S. Diller, C. Majidi, S. H. Collins, A lightweight, low-power electroadhesive clutch and spring for exoskeleton actuation, in *Proceedings of the 2016 IEEE International Conference on Robotics and Automation (ICRA)* (IEEE, 2016), pp. 682–689.
107. C. Di Natali, A. Sadeghi, A. Mondini, E. Bottenberg, B. Hartigan, A. De Eyto, L. O'Sullivan, E. Rocon, K. Stadler, B. Mazzolai, D. G. Caldwell, J. Ortiz, Pneumatic quasi-passive actuation for soft assistive lower limbs exoskeleton. *Front. Neurorobot.* **14**, 31 (2020).
108. X. Liu, A. Rossi, I. Poulakakis, A switchable parallel elastic actuator and its application to leg design for running robots. *IEEE ASME Trans. Mechatron.* **23**, 2681–2692 (2018).
109. S. Cotton, I. Olaru, M. Bellman, T. van der Ven, J. Godowski, J. Pratt, Fastrunner: A fast, efficient and robust bipedal robot. Concept and planar simulation, in *Proceedings of the 2012 IEEE International Conference on Robotics and Automation (ICRA)* (IEEE, 2012), pp. 2358–2364.
110. S. Cotton, J. Godowski, C. Schmidt-Wetekam, N. Payton, I. M. C. Olaru, J. Pratt, Bipedal running: When leg architecture influences speed, efficiency and robustness, in *Proceedings of the 2012 IEEE International Conference on Robotics and Automation (ICRA)* (IEEE, 2012), pp. 216–217.
111. J. Godowski, U.S. Patent US2013/0192406A1 (2013).
112. S. Seok, A. Wang, M. Y. Chuah, D. J. Hyun, J. Lee, D. M. Otten, J. H. Lang, S. Kim, Design principles for energy-efficient legged locomotion and implementation on the MIT Cheetah robot. *IEEE ASME Trans. Mechatron.* **20**, 1117–1129 (2015).
113. G. Bledt, M. J. Powell, B. Katz, J. Di Carlo, P. M. Wensing, S. Kim, in *Proceedings of the 2018 IEEE/RSJ International Conference on Intelligent Robots and Systems (IROS)* (IEEE, 2018), pp. 2245–2252.
114. F. Roos, H. Johansson, J. Wikander, Optimal selection of motor and gearhead in mechatronic applications. *Mechatronics* **16**, 63–72 (2006).
115. X. Da, R. Hartley, J. W. Grizzle, Supervised learning for stabilizing underactuated bipedal robot locomotion, with outdoor experiments on the wave field, in *Proceedings of the 2017 IEEE International Conference on Robotics and Automation (ICRA)* (IEEE, 2017), pp. 3476–3483.
116. M. van den Broek, thesis, Delft University of Technology (2019).
117. Ö. Drama, A. Spröwitz, Trunk pitch oscillations for energy trade-offs in bipedal running birds and robots. *Bioinspir. Biomim.* **15**, 036013 (2020).
118. S. Cotton, J. C. Godowski, N. R. Payton, M. Vignati, I. Olaru, C. Schmidt-Wetekam, C. Black, U.S. Patent US20160001831A1 (2016).
119. R. Alexander, Optimization and gaits in the locomotion of vertebrates. *Physiol. Rev.* **69**, 1199–1227 (1989).
120. V. A. Tucker, The energetic cost of moving about. *Am. Sci.* **63**, 413–419 (1975).
121. R. L. Marsh, D. J. Ellerby, J. A. Carr, H. T. Henry, C. I. Buchanan, Partitioning the energetics of walking and running: Swinging the limbs is expensive. *Science* **303**, 80–83 (2004).
122. K. A. Rose, R. L. Nudds, J. R. Codd, Intraspecific scaling of the minimum metabolic cost of transport in leghorn chickens (*Gallus gallus domesticus*): Links with limb kinematics, morphometrics and posture. *J. Exp. Biol.* **218**, 1028–1034 (2015).
123. C. P. McGowan, H. A. Duarte, J. B. Main, A. A. Biewener, Effects of load carrying on metabolic cost and hindlimb muscle dynamics in guinea fowl (*Numida meleagris*). *J. Appl. Physiol.* **101**, 1060–1069 (2006).
124. A. J. Ijspeert, A. Crespi, D. Ryczko, J.-M. Cabelguen, From swimming to walking with a salamander robot driven by a spinal cord model. *Science* **315**, 1416–1420 (2007).
125. L. P. Lamas, R. P. Main, J. R. Hutchinson, Ontogenetic scaling patterns and functional anatomy of the pelvic limb musculature in emus (*Dromaius novaehollandiae*). *PeerJ* **2**, e716 (2014).
126. T. J. Roberts, M. S. Chen, C. R. Taylor, Energetics of bipedal running. II. Limb design and running mechanics. *J. Exp. Biol.* **201**, 2753–2762 (1998).
127. M. Ahmadi, M. Buehler, The ARL monopod II running robot: Control and energetics, in *Proceedings of the 1999 IEEE International Conference on Robotics and Automation* (IEEE, 1999), vol. 3, pp. 1689–1694.
128. J. E. Pratt, thesis, Massachusetts Institute of Technology (2000).
129. J. A. Smith, I. Poulakakis, Rotary gallop in the untethered quadrupedal robot scout II, in *Proceedings of the 2004 IEEE/RSJ International Conference on Intelligent Robots and Systems, 2004. (IROS 2004)* (IEEE, 2004), vol. 3, pp. 2556–2561.
130. M. Hutter, C. Gehring, M. A. Höpflinger, M. Blosch, R. Siegwart, Toward combining speed, efficiency, versatility, and robustness in an autonomous quadruped. *IEEE Trans. Robot.* **30**, 1427–1440 (2014).
131. H.-W. Park, S. Park, S. Kim, Variable-speed quadrupedal bounding using impulse planning: Untethered high-speed 3D Running of MIT Cheetah 2, in *Proceedings of the 2015 IEEE International Conference on Robotics and Automation (ICRA)* (IEEE, 2015), pp. 5163–5170.
132. S. Kitano, S. Hirose, A. Horigome, G. Endo, TITAN-XIII: Sprawling-type quadruped robot with ability of fast and energy-efficient walking. *Robomech J.* **3**, 8 (2016).
133. X. Liu, A. Rossi, I. Poulakakis, SPEAR: A monopedal robot with switchable parallel elastic actuation, in *Proceedings of the 2015 IEEE/RSJ International Conference on Intelligent Robots and Systems (IROS)* (IEEE, 2015), pp. 5142–5147.

Acknowledgments: A.A.S. thanks the International Max Planck Research School for Intelligent Systems (IMPRS-IS) for support. We would like to thank E. Badri for discussions and support developing the coupling mechanism concept and processing data, L.P. Lamas and J.R. Hutchinson for providing access to the emu cadaver, and the members of the MPI-IS mechanical workshop for manufacturing the large BirdBot model leg. **Funding:** This work was funded by the Max Planck Society, and by a Human Frontier Science Program grant (RGY0062/2010) to M.A.D. **Author contributions:** M.A.D. contributed to conceptualization and planning, materials, and resources for biology experiments. A.B.-S. conceived and planned the research, developed the nonmotorized prototype, performed cadaver experiments, and analyzed data. A.A.S. designed and implemented the robot and the experimental setup, performed the robot experiments, and analyzed the robot data. M.S. contributed to research planning, materials and resources, and editing. M.A.D., A.B.-S., and M.S. supervised the research. M.A.D. and A.B.-S. wrote the manuscript with assistance from A.A.S. and M.S. All authors contributed to the interpretation and discussion of the data. **Competing interests:** A European and international patent (no. EP 19157793.1) related to this work has been submitted. The authors declare that they have no other competing interests. **Data and materials availability:** All data needed to evaluate the conclusions of the paper are available in the paper or the Supplementary Materials. Additional data and the BirdBot's computer-aided design model are available as MPDL Edmond dataset.

Submitted 11 January 2021
Accepted 22 February 2022
Published 16 March 2022
10.1126/scirobotics.abg4055

ScienceRobotics

BirdBot achieves energy-efficient gait with minimal control using avian-inspired leg clutching

Alexander Badri-SpröwitzAlborz Aghamaleki SarvestaniMetin SittiMonica A. Daley

Sci. Robot., 7 (64), eabg4055. • DOI: 10.1126/scirobotics.abg4055

Science Robotics (ISSN) is published by the American Association for the Advancement of Science. 1200 New York Avenue NW, Washington, DC 20005. The title *Science Robotics* is a registered trademark of AAAS.

2 BirdBot 2: Investigating parallel elasticity disengagement mechanism effect on efficient legged locomotion

1

Distal disengagement of parallel leg elasticity improves BirdBot-2 locomotion efficiency

Alborz Aghamaleki Sarvestani and Alexander Badri-Spröwitz

***Abstract*—In nature we observe that animals evolved complex, multi-articulate legs controlled with arguably low computational power. Yet legged robots are mostly developed with simpler leg designs, and are controlled with complex algorithms instead. Here we develop BirdBot-1, designed with five-segment legs where joints are mechanically and compliantly coupled by spring-tendons. Specifically in this work, we focus on function and characteristics of the disengagement tendon mechanism (DE-tendon). The robot's bioinspired DE-tendon supports the disengagement of the leg's parallel elasticity, during push-off, just before swing phase. We study sets of gait parameter with for two configurations with and without the DE-tendon. When the DE-tendon is mounted, we report a robot's cost of transport and peak hip torques that are reduced by 30 % and 40 %, respectively. The DE-tendon further supports mechanical energy transfer into center of mass energy. Mounting the DE-tendon increases BB2's speed increases by 28 %. *Index Terms*—bioinspired robot, leg clutch, ankle power amplification, energy-efficient locomotion**

I. INTRODUCTION

Albeit technological improvements over the last years, legged animals still outperform robots in terms of locomotion agility, robustness, versatility, and efficiency [1]. Each animal leg is a complex structures with tens of serial and parallel muscle-tendon units (MTU). Previous research indicated that certain leg functions are directly supported by passive, non-controlled action of legs' compliantly coupled linkage mechanisms [2], [3], [4]. Perturbation experiments with running birds revealed that these animals robustly overcome unforeseen obstacles albeit limited nerve conduction velocity, also indicating that physically acting mechanisms contribute to locomotion robustness [5], [6].

Consequently, we assume that locomotion robustness is supported by adaptive mechanisms that act immediately, and without needing feedback, control, or an accurate terrain or robot estimation. Intrinsic mechanical robustness is especially valuable in the case of uncertain leg loading conditions where sensor data is unavailable, sparse, or delayed [7]. Recent robot leg designs proof that appropriate mechanical joint coupling can lead to energy efficient designs that act robustly during standing, squatting, and walking [8], [9], [7].

Locomotion pattern generation requires actuators to supply a range of speed-torque combinations, spanning an area within the actuator's speed-torque (power) space. Typically, actuators are designed with some amount of overload capacity. Yet sudden, rapid perturbations may demand an increase both in torque and velocity, and exceed actuator design specifications. Higher-performant actuators can supply more power, but are typically more heavy and complex, with more expensive mechanical and electrical components [10], [11].

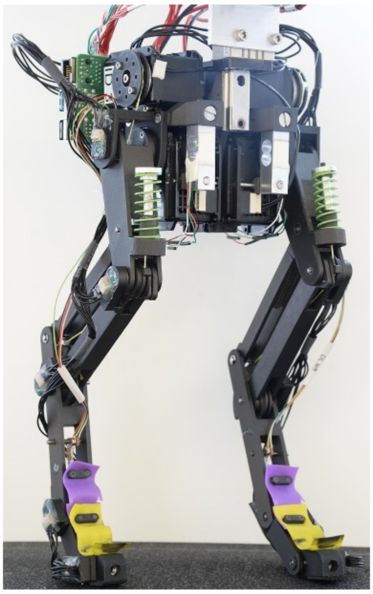

Fig. 1. BirdBot-2 features five-segmented legs with parallel leg elasticity (PLE) that is disengaged in swing phase. A dedicated DE-tendon in the lower, distal leg supports disengagement of PLE.

Alternatively, mechanisms exist that act physically and can rapidly respond to more demanding perturbation loads. Spring- and damper-based mechanisms both function without control input, instantaneously, and with high force and torque output [12], [13], [14], [15], [16]. Hence, physically compliant mechanisms can reject perturbations at low cost [17]. The previous scenario is one possible cause of why animals are still more efficient than robots with high-performance motors [18], [14], even though animals are limited by a low-efficient biochemical to mechanical muscle power conversion [19].

A somewhat neglected design choice are robot legs with more than three segments, which are ubiquitously found in animals. Instead, most robot legs are two- or three-segmented [17], [14], [20], [21]. More leg segments poten-

Dynamic Locomotion Group, Max Planck Institute for Intelligent Systems, 70569 Stuttgart, Germany. Corresponding author: sarvestani@is.mpg.de

tially increase mobility, but also allow storing and releasing energy both in leg length and leg angle direction leading to higher locomotion robustness [17], [15]. Muscle-tendons can actively produce forces and displacements, but also act as a serial and parallel elasticities consuming only small amounts of energy [22], [23]. To virtually model spring action, robots consume electrical energy [11]. Consequently, robotics aims to mimic muscle with physical springs [17], [24], [25], dampers [16], and artificial muscles [26].

Birds and other animals are potentially capable to partially or fully lock leg joints, and stand energy-efficiently [3], [4], [27]. Robotic parallel elastic (parallel elasticity) legs passively carry the robot's weight during standing, and in the stance-phase part of the gait cycle [28], [17], [29]. In contrast, leg designs where actuators bear the robot's mass consume electrical power for the same task [30], [31]. PE legs are energy efficient and robust in stance phase, but compressing a PE leg spring is energy inefficient. The leg-extending PE (extensor) and the leg shortening actuator (flexor) are co-contracting the same joints [32], [17].

Clutches that engage and disengage parallel elasticity dissolve the problem of co-contraction [33], [7]. Clutched, parallel elastic leg designs bear the robot's weight with the parallel leg elasticity and allow leg lifting (flexing) without co-contraction of actuators. Hence, clutched parallel elasticity's allow energy efficient locomotion, and passive standing. Several options exist to activate clutches. Clutches can be actuated by closed-loop-control, or be of the mechanical, self-engaging type [34], [35]. Implementations are ideally light-weight, simple, engage robustly and rapidly, consuming little power [34], [36]. Yet actuated clutch activation can be susceptible to sensor noise, and relies on robust and rapid ground detection.

BB1 features a self-engaging mechanical clutch, with a toe-triggered mechanism that is inspired by the muscle-tendon network of birds' segmented legs. The clutch engages when the robot's toe touches the ground in the intended orientation (digit-extended), and disengages when the robot's toe is digit-flexed [7]. At the end of stance phase, the toe is oriented in locomotion direction, and its tendon insertion retains some amount of toe torque which in turn keeps the global spring-tendon under tension.

A dedicated DE-tendon work in combination with a snap-through joint to robustly disengage the leg's parallel elasticity. The disengagement mechanism consists of a fixed-length tendon of high stiffness, and one additional joint which is designed to snap-through. The biarticular DE-tendon constraints the two distal joints J3 and J4. The tendon wraps around joint J4, and triggers a snap-through of joint J3, into a leg posture that slacks the parallel leg elasticity (global spring-tendon). Movements of joints J3 and J4 are powered by the leg angle progression of the stance leg. With the leg slacked, the leg flexor motor can shorten the leg into swing phase. The DE-tendon acts like a highly stiff spring. The tendon charges in stance and release energy at the transition from stance to swing phase (Fig. 5). In BB1, mounting the DE-tendon allowed an earlier onset disengagement of the global spring-tendon, into swing phase [7].

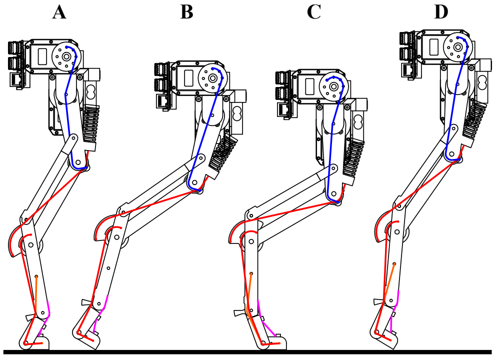

Fig. 2. Four types of global spring-tendon disengagement: A) **Distal tendon-triggered disengagement**: The DE-tendon-action triggers joint J3's snap through at the designed leg angle. B) **Disengagement at high leg angle and full leg length**: The leg reaches its unloaded, full length at high leg angle, and the global spring-tendon becomes fully relaxed. Here, the parallel leg elasticity is typically only partially disengaged; the toe segment still needs to rotate into its digit-flexed posture. C) **Knee flexion triggered disengagement**: The knee motor forces a disengagement by flexing the knee joint against the force of the global spring-tendon. The forced disengagement requires high motor torques and power. D) **Disengagement at low leg angle and full leg length**: Disengagement occurs at a low leg angle and full leg length, caused by an early onset of flight phase at fast locomotion.

The disengagement of the leg's parallel elastic can be grouped into the following four categories, for BirdBot-style legs (Fig. 3). **DE-tendon triggered disengagement** (orange tendon, Fig. 2) leads to controlled and repeatable disengagement characteristics. The DE-tendon's length and pretension define the disengagement (virtual) leg angle [7]. The **disengagement at high leg angle and full leg length** is independent of the DE-tendon. This scenario occurs when the global spring-tendon becomes relaxed at slack length due to leg extension at a high leg angle. If the virtual leg reaches a high leg angle at toe-off, extensor torques and forces drop to zero. Partial or full joint J3 snap-through can occur in this scenario. Because the global spring-tendon may disengage only partially, this is an undesired disengagement type. **Knee flexion triggered disengagement** occurs when while the leg is not fully unloaded, J3 snap-through did not yet trigger, but the knee motor starts lifting the leg. With the global spring-tendon partially engaged, the knee motor flexing the knee joint works against the leg's parallel elasticity. With sufficient motor power, this scenario will eventually flex the leg. Like scenario 3, this is an undesired disengagement type. **Disengagement at low leg angle and full leg length** occurs at highly dynamic, fast locomotion. High locomotion speeds cause trunk velocities at toe-off that are sufficient to pull the leg off the ground, once accelerated. Hence, DE-tendon action is not required, and the global spring-tendon becomes slack at it fully extended posture. Contrary, without explicit DE-tendon disengagement, joint J3 snap-through occurs partially or later, leading specific lower-leg dynamics at toe-off, and potentially with lower mechanical energy recuperation of the DE-tendon.

Elastic mechanism evolved that increase locomotion performance, albeit limited muscle output power or muscle size. Such mechanisms act not unlike engineering clutches or catapults. For example, the monoarticular and biarticular muscle-tendons in the human ankle joint store energy during stance phase, and rapidly release energy during ankle push-off [37], [38]. The longer charging and the rapid release lead to an ankle power amplification [38], [39]. It is still a matter of discussion whether positive ankle power drives leg swing motion, center of mass motion (CoM), or both [40], [41], [38], [42]. Wilson et al. describe a catapult in horse legs, where leg joints below the elbow are rapidly buckled at the end of stance phase. Instead of contracting the biceps with its limited muscle power, this catapult's action recruits muscle-tendon elasticity for more rapid and powerful limb protraction, into leg swing [43].

This study builds upon developing BB1, where the DE-tendon was inserted to disengage the leg's parallel elasticity [7]. With BB2 we aim to answer the following fundamental question; To what extend contributes the buckling of joint J3 to the robot's locomotion dynamics? Inspired also from human ankle joint research, we look at the DE-tendon's functionality as a power amplification mechanism contributing to locomotion performance. Specifically, we hypothesize that the main parameter affecting the performance of the DE-mechanism is robot speed. Hence, here we develop BB2 which is more light-weight, runs faster, and can sustain the higher leg forces compared to BB1. We characterize BB2's performance at three locomotion speeds (walking, running, and transitioning to running), and we alter the robot's leg configuration between with and without DE-tendon.

The following section explains BB2's design; its main components, tendon mechanism, instrumentation, and how we measure the robot kinematics and kinetics. In the methods section, we describe the robot's locomotion leg phases, and two experiment sets characterizing the robot's performance with and without DE-tendon, at three speeds. A second experimental set describes the disengagement performance of BB2 for multiple gait parameters. We discuss results and experimental findings, and how they fit our main two hypotheses, before we conclude.

II. METHODS

BB2 robot is designed with two legs, each feature five segments. The robot's body is mechanically limited to translations in the sagittal plane by two linear guides (SSVRL24) without body rotation (Fig. 3). Knee and hip motors are mounted to the trunk. Hip motor torques are measured by a beam-type load cell connecting motor and body. Hip motors' output axes are supported by thin section ball bearings. We calculate hip motor output torque by multiplying load cell forces and effective lever arm lengths. A single board computer (SBC) is mounted to the trunk as well.

Each **leg features** five segments [S1, S2, S3, S4, S5] connected by five revolute joints [J0, J1, J2, J3, J4]. Each joint features a cam [cam1, cam2, cam3, cam4GS, cam4DE, cam5]; cams act as fixed-radius tendon lever arms of the spring-tendon network [44]. Cam2 and cam3 are compound cams with two radii. The hip's motor output directly drives segment S1.

The knee motor pulls up the segment S2 with the **knee tendon**, which flexes the knee and shortens the leg. The knee flexing tendon passes over the hip axis. Joint J1 rotation (flexion) and knee motor output rotation are linearly related.

The **global spring-tendon** hold the robot's weight in stance phase, and provide the forces to keep the robot standing upright. The global spring-tendon are developed to replace an active, leg extending motor. We implemented the global spring-tendon from two connected tendons. The global spring-tendon is length- and force-adjusted by a tensioning system integrated into the trunk-mounted spring. The proximal part of the global spring-tendon wraps over the extending side of cam2 and over the larger cam3 diameter. The distal part of the global spring-tendon inserts into the smaller cam3 diameter. The remaining distal global spring-tendon passes over cam4 and cam5, and is fixed into segment S5.

The **DE-tendon** supports disengaging the global spring tendon, when mounted (configuration DET-on). The tendon buckles the leg at the end of the stance phase, prepares for push-off, and readies the leg for leg swing. A single-axis force sensor mounts to hing joint S3 and measures the DE-tendon force. On its other end, the DE-tendon inserts into segment S5. The DE-tendon functions as a kinematic constraint between joints J3 and J4—it mechanically couples both joints. During stance phase the robot pivots over the foot of its stance leg with an increasing joint J4 angle. This pivoting J4 motion increases the DE-tendon tendon wrapping around cam5. The stiff DE-tendon builds a tendon force which starts pushing joint J3 and cam3 over its equilibrium point. Once joint J3 snapped over, the global spring-tendon slacks, which in turn slacks the remaining leg.

A **tendon tensioning mechanism** is built with stiff tendons made from Dyneema lines. Tendon lengths are adjusted to set their initial length and to counter tendon creep with individual tensioning mechanisms (Fig. 3).

The robot is **instrumented to electronically record its internal states**. For each robot leg, we record five joint angles, two motor output torques (hip and knee), and three tendon forces (global spring-tendon, knee flexor-tendon, DE-tendon). All data is synchronously recorded on the SBC (Fig. 3). The SBC further runs the robot's **software stack**, its a locomotion controller. A custom-written data monitoring framework allows us monitoring the robot's performance for a given actuator input.

An external **host computer** (Lenovo workstation P 51) runs a custom-written GUI python wrapper. The GUI input receives CPG parameters frequency, duty factor, hip amplitude, hip offset, knee amplitude, phase gains, and phase shifts. The GUI python wrapper generates CPG trajectories from CPG input parameters and sends these via Ethernet to the robot's **SBC** (Raspberry Pi, Model 4). The host computer also runs Labview NI MAX, which records and timestamps all remaining incoming sensor data as a TXT file for post-processing. The python GUI visualizes the robot's data as a live graph, and stores data as a JSON file for post-processing. The onboard SBC receives CPG parameters and sends these to motor controllers. The SBC also receives robot joint encoder data through the SSI interface. It sends data over Ethernet to

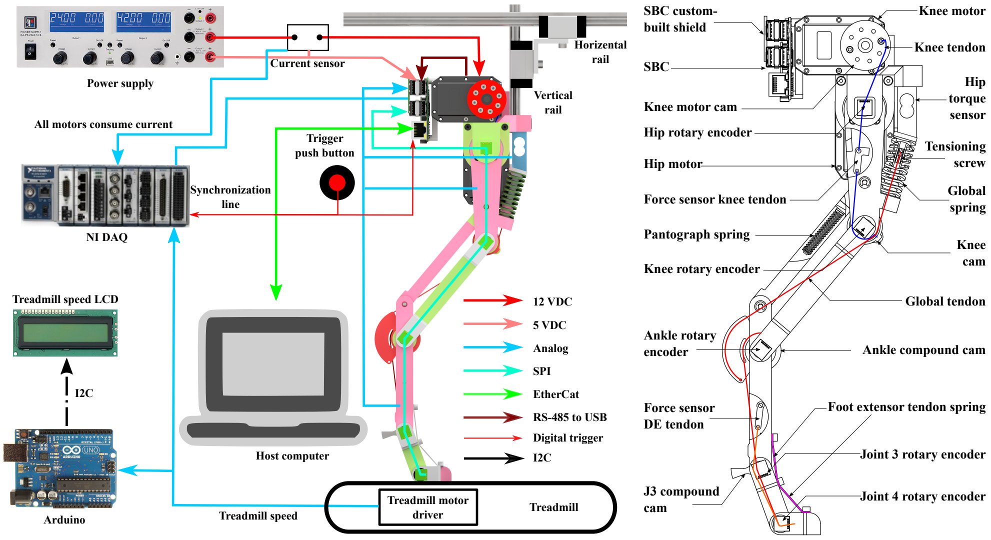

Fig. 3. BB2 robot and its parts (black outlined), the leg's tendon network (overlaid, color) are shown schematically on the right. The experimental setup with data and power connectivity are shown on the left.

the host computer's python GUI. One digital input of the SBC is connected to the physical trigger. It synchronizes all encoder data.

Joint angles are measured with magnetic **joint encoders** (16-bit, absolute encoder, AEAT 8800-Q24). These are mounted on a custom-PCB and are installed at each joint axis measuring the orientation of a diametrical magnet. Joint encoders send joint angle data with the parallel SSI interface at 500 Hz updated frequency to the SBC.

Two **force sensors** are mounted to BB2. The first is a customized, beam-type load cell (TAL 220). It measures the motor's reaction torque. Its data is sampled by a DAQ force sensor module (Fig. 3). The second force sensor measures global spring-tendon and DE-tendon forces. The tendon force sensor is a custom-built, single-axis tension force type sensor (Fig. 3). Force and hip torque data are sent to a DAQ force sensor module.

The SBC sends **motor control** commands via USB to a RS-485 converter (U2D2, Robotis) to servomotors. Motor parameters can be accessed through the SBC, for example for motor calibration.

A **data acquisition system** (DAQ, compactDAQ-9189, National Instruments) collects force data from the DE-tendon, hip and knee force sensors, with strain and bridge modules (NI-9237, National Instruments) at 24-bit resolution, at a sample frequency of 1 kHz. An analog input module (9205, National Instruments) interfaces the current sensor (ACS723) to read motor currents, and the treadmill speed output by the motor driver (DPCANIE-015S400), at 1 kHz sample frequency.

We customized an **off-the-shelf treadmill** (Christopeit TM500S) with a programmable motor driver (DPCANIE-015S400, advance motion controller). We set treadmill velocity by a rotary potentiometer interface interfaced with the motor driver. The analog speed indicator of the motor driver is recorded through the DAQ (CompactDAQ). We live-display the treadmill speed on a display (LCD-1602) interfaced with a microcontroller board (Arduino Uno).

All sensor and video data are synchronized with a multi-contact switch distributing trigger signals either as a digital, rising-edge or falling-edge signal.

Power supplies: Current sensors and the SBC are supplied with 5 V. 12 V are supplied to the robot's four servomotors.

A. *Experiments*

We characterize the influence of the DE-tendon by running BB2 with and without its DE-tendon mounted (DET-on and DET-off, respectively). For both configurations we characterize the robot's gait based on locomotion speed and hip amplitude. In all experiments we recorded BB2's energy consumption and speed, and general gait parameters. The robot ran on a treadmill and was held in the sagittal plane by a guide system with a fixed-pitch trunk posture. We implemented robot gaits at four gait frequencies $f = 0.5$ Hz, 1.0 Hz, 1.5 Hz, and 2.0 Hz. Each locomotion frequency was tested with one low and one high hip amplitude that provided successful locomotion. For each experiment we recorded 20 strides (left and right steps). Each experimental condition was repeated three times leading to in sum 60 strides per experimental condition. This includes 16 experimental conditions: 4 frequencies, 2 tendon configurations, and 2 hip amplitudes.

a) Date post-processing: Tucker defines the **cost of transport (CoT)** as a non-dimensional number that measures a system's energy consumption for a given locomotion distance [45]:

$$CoT = \frac{\sum_{i=1}^{n} P_i}{mgv_{CoG}} \tag{1}$$

with n being the number of actuators, P_i the average actuator power consumption i, m the robot's mass, g the gravitational acceleration, and v_{CoM} the average speed of the center of mass (CoM). We measure the latter in form of the treadmill speed. We calculate the motor input power as:

$$\sum_{i=1}^{n} P_i = \sum_{i=1}^{n} I_i V_i = V \sum_{i=1}^{n} I_i \tag{2}$$

where I_i is the average current of a motor, read by individual current sensors, and V is the motor input voltage. While CoT is a normalized value (J/J), Tucker and others report that large and heavy animals exhibit a low CoT, compared to small and lightweight animals with high CoT values. The underlying trend can be expressed with the following fit: $\log CoT_{NR} = -0.3138 \log m + 0.2346$ [7]. Hence, we normalized the BB2's CoT with respect to that of an average animal of the same body weight. We then document the resulting relative cost of transport ($\mathrm{CoT_{rel}}$), which allows comparing BB2's to that of other, legged robots.

The robot's **linear leg momentum** is expressed by:

$$L = \sum_{i=1}^{n} m_i \, v_{CoG_i} \tag{3}$$

where L is the total linear momentum of leg, n is the number of leg segments, m_i is the segment i mass, and v_{CoG_i} is the linear speed of the center of mass segment i.

We derive the robot's **kinematics and kinetics** from recorded joint angle sensor data. We calculate internal leg forces through joint sensor data and resulting spring deflections with known spring stiffness coefficients. This allows us to calculate the robot's ground reaction forces and the foot's center of pressure. We simplify our calculations by assumptions that leg segment masses and inertias create forces that are negligible, compared to other system forces. We assume that the segment S5 remains flat on the ground, during the entire stance phase, which we confirm experimentally. We assume the leg's state is fully defined, with a full set of joint angles. We calculate: 1) the ground reaction force angle α_{GRF}, as the angle between the GRF vector and the vertical axis, 2) the magnitude of the ground reaction forces $\|F_{GRF}\|$, 3) the center of pressure distance CoP in reference to joint J4. Parameters are shown in Fig. 4. We calculate joint positions from joint encoder data, with the hip joint as a reference:

$$P_{J_0} = \begin{bmatrix} 0 \\ 0 \end{bmatrix}, \; P_{J_1} = \begin{bmatrix} l_1 \sin(\theta_0) \\ -l_1 \cos(\theta_0) \end{bmatrix} \tag{4}$$

The remaining joint positions $i = \{1, \ldots, 4\}$ are:

$$P_{J_{i+1}} = P_{J_i} + l_i \frac{P_{J_{i-1}} - P_{J_i}}{l_{i-1}} \begin{bmatrix} \cos(\theta_i) & -\sin(\theta_i) \\ \sin(\theta_i) & \cos(\theta_i) \end{bmatrix} \tag{5}$$

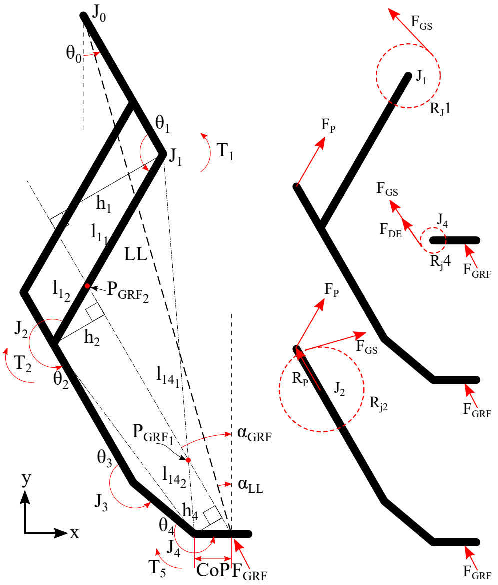

Fig. 4. Schematics showing joint angles and leg geometry that define BB2 leg kinematics and dynamics.

Spring forces and pantograph constraints are calculated based on the pantograph geometry and robot kinematics:

$$F_P = \begin{cases} K_P\left(l_P - l_2 \frac{l_P}{\|l_P\|}\right) & \|l_P\| > l_2 \\ 0 & \|l_P\| \le l_2 \end{cases} \tag{6}$$

$$T_1 = F_{GRF} h_1 \quad , \quad T_1 = F_{GS} R_{J_1} - R_P \times F_{PS} \tag{7}$$

$$T_2 = F_{GRF} h_3 \quad , \quad T_2 = F_{GS} R_{J_2} + R_P \times F_{PS} \tag{8}$$

$$T_4 = F_{GRF} h_5 \quad , \quad T_4 = F_{GS} R_{J_4} + F_{DE} R_{J_{5DE}} \tag{9}$$

The magnitude of the global spring force $\|F_{GS}\|$ is calculated as:

$$\begin{aligned} \|F_{GS}\| = k_{GS} \Delta x_{GS} = k_{GS}(R_{j_1}(\theta_{1_0} - \theta_1) + R_{j_2}(\theta_2 - \theta_{2_0}) \\ + R_{j_3}(\theta_3 - \theta_{3_0}) + R_{j_4}(\theta_4 - \theta_{4_0})) \end{aligned} \tag{10}$$

The DE-tendon force $\|F_{DE}\|$ is calculated as:

$$\begin{aligned} \|F_{DE}\| = k_{DE} \Delta x_{DE} = k_{DE}(R_{j_{3DE}}(\theta_3 - \theta_{3_0}) \\ + R_{j_{4DE}}(\theta_4 - \theta_{4_0})) \end{aligned} \tag{11}$$

Based on the triangle similarity theorem:

$$\frac{h_1}{h_2} = \frac{l_{1_1}}{l_{1_2}} \tag{12}$$

Combining Eqns. (7) and (8):

$$\frac{T_1}{T_2} = \frac{h_1}{h_2} = \frac{l_{1_1}}{l_{1_2}} \tag{13}$$

$$\frac{T_1}{T_2 + T_1} = \frac{l_{1_1}}{l_1} \tag{14}$$

$$\frac{T_1}{T_4+T_1}=\frac{l_{14_1}}{l_{14}} \tag{15}$$

Combining Eqns. (7) to (9), (14) and (15):

$$\begin{aligned} l_{1_1} &= \frac{l_1 F_{GS}(R_{J_2}+R_{J_1})}{F_{GS}R_{J_1}-R_P\times F_{PS}} \\ l_{14_1} &= \frac{\|P_4-P_1\|\,F_{GS}(R_{J_2}+R_{J_1})-R_P\times F_{PS}+F_{DE}R_{J_{4DE}}}{F_{GS}R_{J_1}-R_P\times F_{PS}} \end{aligned} \tag{16}$$

Based on segment lengths l_{1_1} and l_{14_1}, we calculate the ground reaction force direction F_{GRF}:

$$\begin{aligned} P_{GRF_1} &= \frac{P_{J_4}l_{25_1}+P_{J_1}(l_{14}-l_{14_1})}{l_{14}} \\ P_{GRF_2} &= \frac{P_{J_2}l_{1_1}+P_{J_1}(l_1-l_{1_1})}{l_1} \\ F\hat{_{GRF}} &= \frac{P_{GRF_2}-P_{GRF_1}}{\|P_{GRF_2}-P_{GRF_1}\|} \\ \alpha_{GRF} &= \tan^{-1}(\frac{F\hat{_{GRF}}_y}{F\hat{_{GRF}}_x})-\frac{\pi}{2} \end{aligned} \tag{17}$$

Force magnitude is calculated from the torque T_4 and joint-loading distance h_4:

$$\|F_{GRF}\|=\frac{T_4}{h_4} \tag{18}$$

The product of magnitude $\|F_{GRF}\|$ and unit vector $F\hat{_{GRF}}$ leads to the instantaneous ground reaction force $F_{GRF}=\|F_{GRF}\|F\hat{_{GRF}}$. The length h_4 is:

$$h_4=F\hat{_{GRF}}\cdot(P_{GRF_1}-P_{J_4}) \tag{19}$$

We calculate the center of pressure (CoP):

$$CoP=\frac{h_4}{\cos(\alpha_{GRF})} \tag{20}$$

Leg length and angle are calculated as MORE PRECISE, which LL and LA:you mean add ”more precise” or something else?

$$\begin{aligned} LL &= \sqrt{(X_{J_4}+CoP-X_{J_0})^2+(Y_{J_4}-Y_{J_0})^2} \\ \alpha_{LL} &= \tan^{-1}(\frac{Y_{J_0}-Y_{J_1}}{X_{J_0}-CoP-X_{J_1}})-\frac{\pi}{2} \end{aligned} \tag{21}$$

III. RESULTS

We report experimental results to characterize function and performance of the disengagement mechanism.

a) Leg phases: The robot's leg cycles continuously through four phases (Fig. 5). The CPG controller sends identical trajectories to left and right knee and hip motors, with a 50 % phase shift between both sides.

The **stance phase breaking** starts at the moment the leg touches the ground, and lasts until mid-stance. The global spring charges and converts the robot's potential and kinetic energy into spring deflection. The global spring mechanically provides leg length force - no motor is required to extend any leg joints, which is a significant advantage of BirdBot's parallel elastic leg design, in comparison to leg designs with motors and or springs mounted serially. The stance breaking phase continues until mid-stance, where the global spring reaches its maximum deflection caused by maximum leg loading.

Stance phase acceleration starts from the mid-stance till the leg loses ground contact. During this phase, all the energy stored in the global spring will discharge into the system and provide push off for the leg. By having the CPG parameter that matches the natural dynamic of the robot (e.g., matching given and observed duty factor), we can use global spring energy to extend the leg and make the leg ready for the flight phase without applying knee torque. Spring discharge will reduce the hip torque required for pushing the robot body forward (Fig. 7). This phase will continue till the foot loses ground contact.

The **disengagement** (DE) phase overlaps with the stance phase and the early flight phase. Disengagement is the most significant phase of these types of leg design. During disengagement, the DE-tendon wraps around cam5 while the leg rotates forward. As a result, the tendon will extend and store energy. The source of this stored energy is the forwarding motion of the robot. The DE-tendon force increases as the leg get to the end of the stance phase due to the lean forward orientation of the leg and reduced GRF. The DE-tendon force applied on cam4DE will push the J3 out of the locked position. As a result of this snapping of J3 from its hard stop. Global spring-tendon will be disengaged, and the knee motor can lift the leg and start the swing phase without working against global spring.

Knee pull-up: At the end of the stance phase, the knee motor via a cam and tendon will flex the knee joint and create enough leg clearance to swing the leg forward and start the next gait cycle. The ideal case for pulling the knee up is after disengagement happens, then the leg can be lifted and provide enough ground clearance without too much knee motor energy consumption. However, lifting the leg after the disengagement is complete can cause the robot to fall to the ground, especially if there is no double stance phase. Therefore, we usually pull the knee-tendon before disengagement is complete to avoid this situation. By doing so, it is a trade-off between successful locomotion and consuming more knee motor power.

Swing phase: this phase starts from the moment that leg is losing ground contact till the leg establishes ground contact again. During the swing phase leg need to provide ground clearance to avoid a ground collision before the leg does the full swing forward. In this phase, both the global and the DE-tendon are relaxed. The knee motor holds the leg up until the end of the swing phase. Then, the knee releases the leg and establishes ground contact.

Knee release: happens at the end of the swing phase that the knee motor unwraps its tendon, and due to the gravity effect and angular momentum of the leg created during swing forward, the leg will extend and gets ready for the next gait cycle.

Leg engaging: happens at the end of the swing phase and coincides with passive knee extension. During leg engagement, the knee extends and provides slacking into the global tendon. Soft extensor springs extend J3 and J4. By doing so, the global spring engages, and the robot can start the next stance phase.

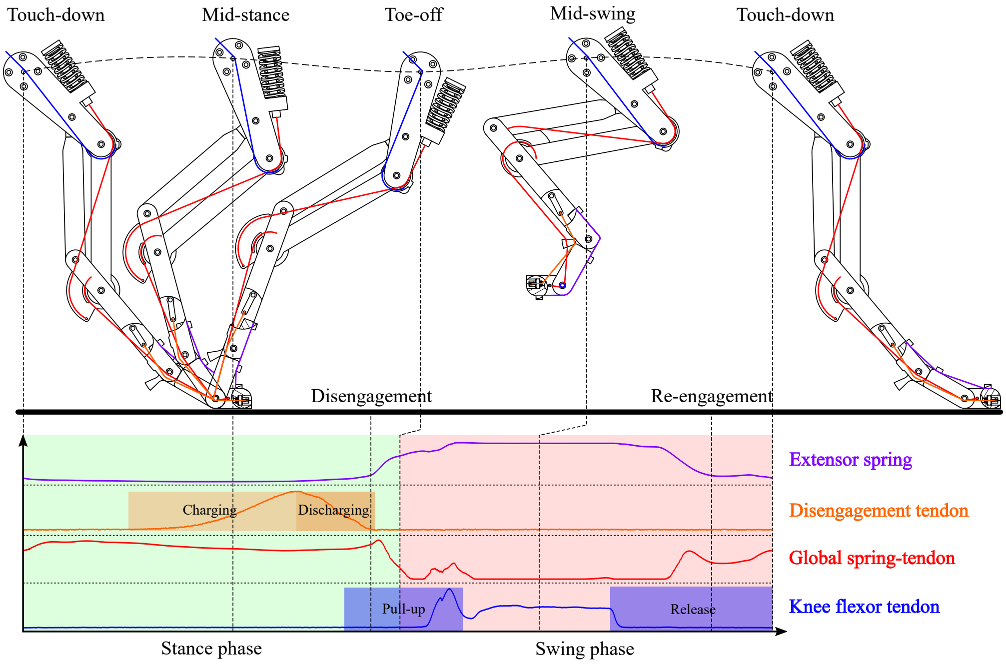

Fig. 5. Leg states and their tendon activations within the locomotion gait cycle. The cycle starts at **touch-down**, with the leg touching the ground and all tendons except the global tendon slack. Around **mid-stance** the hip torque drives the leg forward, and the global tendon bears the leg's peak load. The DE-tendon starts being loaded. At **toe-off** the leg lifts off the ground. The DE-tendon discharges and de-clutches the global spring. The knee motor starts flexing the knee joint, to lift the lower leg. The knee is fully flexed at **mid-Swing** where the global tendon is unloaded. The knee motor starts releasing the knee in preparation for the next touch-down event.

b) Disengagement angle: The DE-tendon act as an angular constrains between J3 and J4 and guarantees disengagement at a certain angle of the virtual leg. However, due to loading on leg charging of tendon varies under different gait parameters, we expect different behavior from the tendon at different speeds. We measure the virtual leg angle at disengagement for three different gait speeds of 0.5 Hz, 1.0 Hz, and 2.0 Hz and two amplitudes: 30° and 40°, for cases, with and without DE-tendon. Results are plotted over virtual leg length (Fig. 6). By increasing speed, the virtual leg angle at disengagement reduces. Leg length increases at disengagement by the increasing hip amplitude, for a given gait frequency. We observe that disengagement occurs in a more narrow range of leg angle, in the DE-tendon-configuration.

c) Torque requirement: We compare robot configuration DE-tendon and no-DE-tendon for actuator torque requirements and robot performance. Fig. 7 shows that the DE-tendon robot requires larger hip torque at low and high speed, more than without its DE-tendon. At low-speed, the no-DE-tendon configuration shows a peak torque of 1.3 Nm in stance, which is 37 % higher than the DE-tendon configuration. Hip torques are similar at intermediate speeds, for DE-tendon and no-DE-tendon. At high-speed, the no-DE-tendon configuration shows a hip torque maximum amplitude of 2.5 Nm in stance, 103 % higher than configuration DE-tendon.

In the leg without the DE mechanism, we do not coordinate the disengagement of the global spring. Hence, leg disengagement happens either via leg orientation or force disengagement via knee flexing motion. These cases combined with speed change cause a random behavior for knee torque. However, we can observe two main peaks in knee motor torque. The first peak coincides with disengagement (either force or with DE tendon), and the second is for pulling the leg up to the most flex position.

The first peak at low and intermediate speed is visible around 1.0 Nm (1DE-tendon), by increasing speed and entering to flight phase first knee torque peak decrease to 0.4 Nm and merge into the second peak for the robot with DE tendon. For configuration DE-tendon and at low speeds, the low-speed first peak is around 1.2 Nm, caused by the forced disengagement. At intermediate speed the peak drops to 0.5 Nm—likely the center of mass motion supports auto-disengagement. At high speed, we measure a peak of 0.7 Nm, near to the 0.5 Nm at intermediate speed.

Meanwhile, knee torque second peak for the robot with DE tendon at low speed is around 0.6 Nm this torque is holding torque of leg mass during the swing. For intermediate speed second peak drop to around 0.5 Nm, the reduction is due to the speed of gait motor cannot flex knee completely, so the holding torque is smaller than low speed. At high-speed gait, second knee torque is around 0.8 Nm, an increase in knee torque caused by fast flexing the leg. Peak caused by dynamic flexing of the leg is larger than holding leg inertia torque at the lower speed.

The second peak for the experiment without DE tendon is much higher than with DE tendon. For the low-speed case, the knee torque at the second peak saturated the sensor due to exceeding the limit of knee torque. The reason for that is the knee motor and global spring co-contract the knee joint and cause huge knee torque in comparison with the case with DE tendon. In intermediate and high-speed gait, the second peak for the case without DE tendon is much higher than the one with DE tendon due to partial co-contraction.

d) Power amplification: A key task of the DE tendon is to store locomotion energy during the stance phase and release that energy at the end of the stance phase. The ratio of charging time of extensor tendon (DE tendon) to discharging time of extensor energy is a metric for power amplification. The DE tendon amplifies power by 1.3, 2.1 and 1.7 for low, intermediate and high speed, respectively (Fig. 8). Power amplification values of DE-tendon configurations indicate they assist both the hip and knee motor energetically. Both motors feature lower peak torques over a longer period of time and maintain an overall higher locomotion energy. The higher parallel elastic is the energetic source leading to locomotion efficiency, compared to leg designs without a mechanically augmented push-off. The DE-tendon configuration recuperated mechanical energy back (Fig. 7). Also, this recuperated energy can help achieve a lower cost of transport and higher speed.

e) Center of mass behavior: No-DE-tendon configurations show more oscillations in the vertical direction (Fig. 7), indicating that the robot decelerates and accelerate more, compared to DE-tendon configurations. More movements increase energetic losses during locomotion. In case of BB2, hip actuators draw more power in the no-DE-tendon configuration.

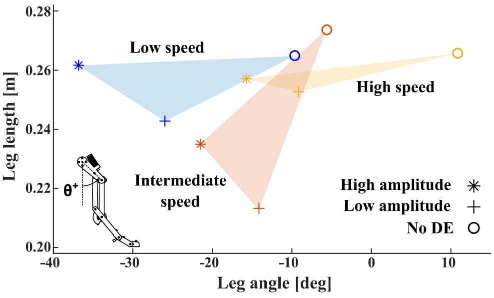

Fig. 6. Resulting leg length plotted over leg angles at the point of disengagement. Three experimental sets are shown: low, medium, and high speed locomotion. A leg angle of zero is defined as the vertical axis, and positive leg angle values are counted in CCW direction, as shown in the schematic on the bottom left. Sets of a speed range (same locomotion frequency) are indicated by the same color.

f) Cost of transport: We measure BB2's cost of transport in configurations DE-tendon and no-DE-tendon. Fig. 9 shows the ratio of BB2's cost of transport, as a fraction of the cost of transport of a natural runner of equal mass.

g) Configuration DET-on: BB2 shows a relative COT of 86 % and 123 % for configurations with and without the disengagement mechanism. Hence, the disengagement mechanism improves the robot's relative COT by 30 %. Compared to a robot with a fixed, parallel leg elasticity (Cheetah-cub), BB2 shows an over four times improved relative cost of transport. DET-on's reduced power consumption is caused majorly by a knee power reduction, compared to DET-off (Fig. 9).

h) Configuration DET-off: Without the support from the disengagement tendon, the foot segment of DET-off only partially disengages the leg's parallel elasticity into swing phase (Fig. 2). As a result, the knee flexing motor work against the parallel elasticity in swing, which increases the robot's energetic cost (Fig. 9). This effect depends on the robot's locomotion speed. At low-speed locomotion, foot segments are insufficiently flexed and we observe incomplete disengagement. At intermediate speeds self-disengagement are observed. At high speed locomotion, we observe incomplete disengagement, likely because of the brief contact time, with high leg loading. At high speed locomotion, early toe-off is observed, where the leg is not yet at its proper self-disengagement angle. Hence, we record a higher COT at low and high locomotions speeds. At intermediate locomotion speeds self disengagement is observed, resulting in a comparably low knee flexing torque with lower power consumption (Fig. 9).

IV. DISCUSSION

a) Disengagement angle: To achieve higher speed with lower power consumption, not only do we need to have concise timing between disengagement of parallel elasticity and knee pull-up, but also we need to define a good Disengagement angle. Recuperated energy can't help the body push-off or knee flexing during the swing phase if the leg is fully unloaded at disengagement point. Hence, for bigger leg lengths, the possibility of passive push-off is reduced (Fig. 6). Equally, for more positive leg disengagement angles the leg is more likely to push-off, since it is more loaded. An early push-off leads to an early flight phase with higher vertical oscillations and less forwarding motion in high-speed gaits. The robot configuration no-DE-tendon shows more center of mass oscillations (Fig. 7). All DE-tendon configurations are faster than their no-DE-tendon counterparts.

With BB2's disengagement mechanism, hip amplitude and the disengagement are coupled. We observe that the virtual leg angle variation increases with increasing hip amplitude. The chance of full disengagement without the help of the knee flexing motor increases, and the energy required to pull the leg up decreases. As a result, robot speed increases and power consumption decreases. At higher commanded hip amplitudes, the leg angle decreases and leg length increases at disengagement, with the leg being closer to resting length. resting length

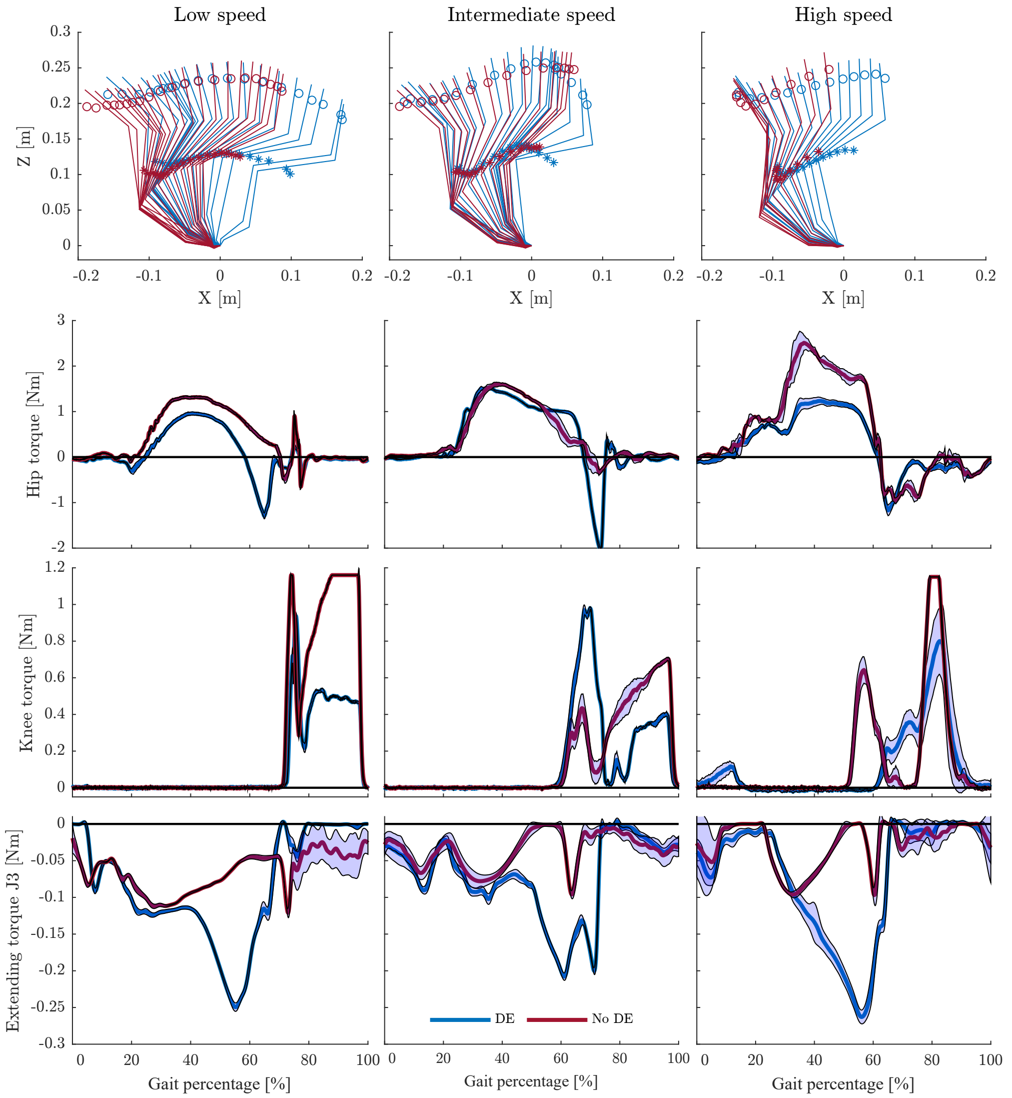

Fig. 7. By comparing motor torque for the case with and without DE-tendon at the low and high speeds, we see an increase in hip torque requirement for the case without DE mechanism at the stance phase. Leg kinematic and center of mass for cases with and without DE mechanism (blue and red, respectively).

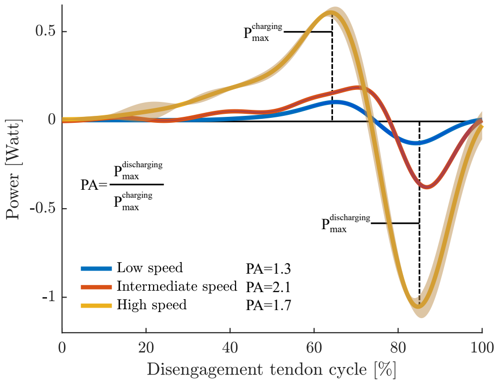

Fig. 8. Power amplification of leg in case of with DE tendon for three cases of low, intermediate and high speed

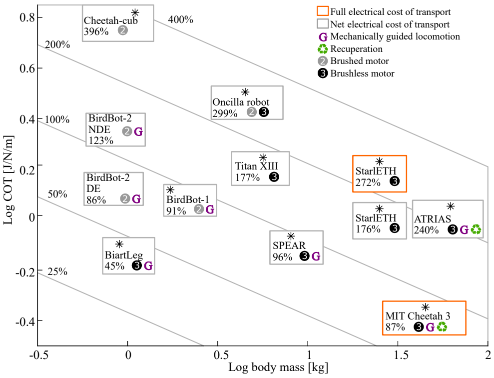

Fig. 9. Cost of transport (CoT) of BB2, for configuration DE-off and DE-on, compared to state-of-the-art legged robots. The diagonal, 100 %-line is Tucker's CoT line for natural-runners (animals), which we converted with the following equation $\log_{10} y = -0.3138 \log_{10} x + 0.2346$ into its logarithmic scale. This line presents the ratio of robot CoT versus animal CoT of the same mass. BB2 in configuration DE-on shows a better performance, compared to the DE-tendon configuration. BB2 shows the most energy-efficient, compared to other bipedal and quadrupedal robots, in terms of $\mathrm{CoT}_{\mathrm{rel}}$. Robot references: [45], [46], [17], [29], [47], [31], [14], [33], [15], [20].

as in: touch-down length?resting length as length of leg when leg is hanging without any leg force

b) Torque requirement: Based on the equation of leg, by having the leg joint angles, we can calculate hip torque at that point under the assumption of zero leg mass. The leg length of the robot is coupled to leg extending mechanisms: 1) global spring and pulley system, which is passively extending the leg. 2) pantograph spring, when it is activated, makes the leg shorter. 3) DE-tendon, which by extending the tendon increases the moment at J4, decreases global spring tension and then causes leg extension.

Leg equations show that decreasing the leg length for a given leg angle requires less hip torque. So when we remove the DE-tendon, we reduce extension torque at J4. Without a DE-tendon, both the ground reaction force and angle will change, and hip torque reduces (Fig. 7). With a DE-tendon, hip motor torques are reduced by 37 % to 103 % in stance phase, when compared to the non-DE-tendon configuration.

Removing the DE-tendon introduces co-contraction between the knee motor and global spring during leg pull-up, which causes the knee motor to apply more than double the torque necessary for the leg pull-up compared to the robot with the DE-tendon.

To discuss the effect of the knee torque for the case with the DE-tendon at the different speeds, we can observe that we generally have two main peaks, which, by increasing speed, these two peaks will merge into each other. The first peak is caused by co-contraction of the knee with global spring during disengagement. This peak for low and intermediate speed is roughly around 1.0 Nm, but for high speed due to leg disengagement via flight phase peak reduced to 0.4 Nm. The knee second peak torque is caused by the leg dynamic, which is required to lift the minimum knee angle and hold it at the position for a portion of the swing phase while the leg is retracting.

Fig. 7 shows for the low-speed gait, the second knee torque peak is at 0.6 Nm, which is a bit higher than 0.4 Nm second peak for intermediate speed. The reason is at the low-speed motor has enough time to lift the leg to minimum knee angle, but at intermediate speed, due to short retraction time motor cannot flex the knee completely, and the second peak is a bit lower. However, the duration of the second peak for high speed is even shorter, and since the error in knee position controller increases, it provides sudden torque to flex the knee, then we have a peak around 0.8 Nm.

c) Power amplification: The DE-tendon charges slowly during stance phase and release the energy at short period of time to snap J3 and clutch global spring tendon (Fig. 8). The power amplification of the DE-tendon reduces hip torques at steady state locomotion and maintain locomotion energy as a result reducing peak hip torque reduce by hip motor to vault the leg forward and also reducing knee torque for lifting the leg. Power amplification depends on charging and discharging time and loading of leg during charging and discharging. At low locomotion speed we show symmetrical loading and unloading as a result of the power amplification $PA = 1.3$, which is close to no power amplification at 1.0. At intermediate speeds the DE-tendon's charging time increases and the discharging time decreases. We observe power amplifications of $PA = 2.1$ at these intermediate speeds (Fig. 8). At high locomotion speed we observe flight phases; it means leg unloaded via robot dynamic as a result DE-tendon charging reduce and as a result timing between charging and discharging changes. At high speeds, we observe a decrease in power amplification $PA = 1.7$. In sum, all DE-tendon configurations improved locomotion efficiency through DE-tendon power amplification.

d) Cost of transport: BB2 reduces power through passive recuperation through global spring, pantograph spring, and DE-tendon. Global spring reduces the necessity of the knee actuator during the stance phase and DE-tendon and pantograph spring provide push-off at the end of stance and help the hip motor to generate less power for swing leg forward and less knee power to pull the leg up. Although DE-tendon positively affects locomotion via amplifying power during the stance and releasing it at the end of the stance. The other effect of the DE-tendon is to clutch the parallel elasticity and help the leg freely start the next cycle and have more leg retraction angle, and as a result, the robot achieves higher speed. Combining these two behavior gives us a better CoT for the robot equipped with a DE-tendon. We observe a 50 % reduction in the cost of transport, with respect to natural-runners (Fig. 9).

V. CONCLUSION

The DE-tendon plays an important role in bipedal locomotion not only to provide robust parallel elasticity disengagement but also it helps to amplify power during leg roll-over motion and use the recuperated energy to have faster leg retraction with large ground clearance. As a result, the robot runs 28 % faster at 2.0 Hz gait frequency. Furthermore, the leg with the DE-tendon has a robust PE disengagement at the end of stance independent of the gait parameter as long as the virtual leg angle reaches to set disengagement angle. This behavior lets the robot avoid co-contraction during leg pull-up and helps improve the robot consumption energy by 10 %. Furthermore, the improvement in energy consumption and increasing speed for a given input parameter improve the robot's CoT by 50 % compared to natural-runner data.

The other important aspect of this study was the necessity of the DE-tendon for different speeds. We observe that DE-tendon for low and high speed have two different functions. At low speed, the co-contraction torque reduction caused by the disengagement is a more significant characteristic of having the DE-tendon. We have a reduction of up to 40 % in hip peak torque and a reduction of more than 60 % in knee peak torque. However, for high-speed gait, the important characteristic of the DE-tendon besides the reducing peak torque for hip and knee motors is to increase robot speed by lengthening the robot's push-off time before entering the swing phase. Also, provide rapid leg retraction in the short time window of flight phase for high-speed gait.

Combined effects of clutching and mechanical recuperation of energy are vital for efficient bipedal legged locomotion. New leg designs need to exploit this disengagement mechanism in their future leg design to reduce and simplify locomotion controllers and make a robot that can walk on uneven terrain with minimum computational cost and minimum sensory data.

ACKNOWLEDGMENT

We thank the International Max Planck Research School for Intelligent Systems (IMPRS-IS) for supporting the academic development of Alborz Aghamaleki Sarvestani. This research was funded by the Max Planck Society through a Max Planck Group Leader grant awarded to ABS.

REFERENCES

[1] A. J. Ijspeert, "Biorobotics: Using robots to emulate and investigate agile locomotion," *science*, vol. 346, no. 6206, pp. 196–203, 2014.

[2] H. Witte, R. Hackert, K. Lilje, N. Schilling, D. Voges, G. Klauer, W. Ilg, J. Albiez, A. Seyfarth, D. Germann, M. Hiller, R. Dillmann, and M. Fischer, "Transfer of biological principles into the construction of quadruped walking machines," in *Robot Motion and Control, 2001 Proceedings of the Second International Workshop on*, 2001, pp. 245 –249.

[3] J.-M. Denoix and J.-P. Pailloux, "Physiotherapie und Massage bei Pferden," *Stuttgart: Ulmer*, 2000.

[4] N. U. Schaller, B. Herkner, R. Villa, and P. Aerts, "The intertarsal joint of the ostrich (struthio camelus): anatomical examination and function of passive structures in locomotion," *Journal of anatomy*, vol. 214, no. 6, pp. 830–847, 2009.

[5] M. A. Daley, G. Felix, and A. A. Biewener, "Running stability is enhanced by a proximo-distal gradient in joint neuromechanical control," *Journal of Experimental Biology*, vol. 210, no. 3, pp. 383–394, 2007.

[6] H. L. More, J. R. Hutchinson, D. F. Collins, D. J. Weber, S. K. H. Aung, and J. M. Donelan, "Scaling of Sensorimotor Control in Terrestrial Mammals," *Proceedings of the Royal Society B: Biological Sciences*, vol. 277, no. 1700, pp. 3563–3568, Dec. 2010.

[7] A. Badri-Spröwitz, A. Aghamaleki Sarvestani, M. Sitti, and M. A. Daley, "BirdBot achieves energy-efficient gait with minimal control using avian-inspired leg clutching," *Science Robotics*, vol. 7, no. 64, p. eabg4055, Mar. 2022.

[8] W. Roozing, Z. Li, D. Caldwell, and N. Tsagarakis, "Design Optimisation and Control of Compliant Actuation Arrangements in Articulated Robots for Improved Energy Efficiency," *IEEE Robotics and Automation Letters*, no. 99, pp. 1–1, 2016.

[9] K. Miyashita, Y. Masuda, M. Gunji, A. Fukuhara, K. Tadakuma, and M. Ishikawa, "Emergence of Swing-to-Stance Transition from Interlocking Mechanism in Horse Hindlimb," in *2020 IEEE/RSJ International Conference on Intelligent Robots and Systems (IROS)*. Las Vegas, NV, USA: IEEE, Oct. 2020, pp. 7860–7865.

[10] F. Roos, H. Johansson, and J. Wikander, "Optimal selection of motor and gearhead in mechatronic applications," *Mechatronics*, vol. 16, no. 1, pp. 63–72, Feb. 2006.

[11] S. Seok, A. Wang, D. Otten, and S. Kim, "Actuator design for high force proprioceptive control in fast legged locomotion," in *2012 IEEE/RSJ International Conference on Intelligent Robots and Systems*. IEEE, 2012, pp. 1970–1975.

[12] Z. H. Shen and J. E. Seipel, "A fundamental mechanism of legged locomotion with hip torque and leg damping," *Bioinspiration & Biomimetics*, vol. 7, no. 4, p. 046010, Dec. 2012.

[13] N. Kashiri, M. Laffranchi, D. Caldwell, and N. Tsagarakis, "Dynamics and Control of an Anthropomorphic Compliant Arm equipped with Friction Clutches," *IEEE/ASME Transactions on Mechatronics*, vol. PP, no. 99, pp. 1–1, 2015.

[14] C. Hubicki, J. Grimes, M. Jones, D. Renjewski, A. Spröwitz, A. Abate, and J. Hurst, "ATRIAS: Design and validation of a tether-free 3D-capable spring-mass bipedal robot," *The International Journal of Robotics Research*, vol. 35, no. 12, pp. 1497–1521, Oct. 2016.

[15] F. Ruppert and A. Badri-Spröwitz, "Series Elastic Behavior of Biarticular Muscle-Tendon Structure in a Robotic Leg," *Frontiers in Neurorobotics*, vol. 13, p. 64, Aug. 2019.

[16] A. Mo, F. Izzi, D. F. Haeufle, and A. Badri-Spröwitz, "Effective viscous damping enables morphological computation in legged locomotion," *arXiv preprint arXiv:2005.05725*, 2020.

[17] A. Spröwitz, A. Tuleu, M. Vespignani, M. Ajallooeian, E. Badri, and A. Ijspeert, "Towards Dynamic Trot Gait Locomotion: Design, Control and Experiments with Cheetah-cub, a Compliant Quadruped Robot," *International Journal of Robotics Research*, vol. 32, no. 8, pp. 932 – 950, 2013.

[18] M. Hutter, C. Gehring, D. Jud, A. Lauber, C. D. Bellicoso, V. Tsounis, J. Hwangbo, K. Bodie, P. Fankhauser, M. Bloesch, R. Diethelm, S. Bachmann, A. Melzer, and M. Hoepflinger, "ANYmal - a highly mobile and dynamic quadrupedal robot," in *2016 IEEE/RSJ International Conference on Intelligent Robots and Systems (IROS)*. IEEE, Oct. 2016, pp. 38–44, iSSN: 2153-0866.

[19] T. Ryschon, M. Fowler, R. Wysong, A.-R. Anthony, and R. Balaban, "Efficiency of human skeletal muscle in vivo: comparison of isometric, concentric, and eccentric muscle action," *Journal of applied physiology*, vol. 83, no. 3, pp. 867–874, 1997.

[20] G. Bledt, M. J. Powell, B. Katz, J. D. Carlo, P. M. Wensing, and S. Kim, "MIT Cheetah 3: Design and Control of a Robust, Dynamic Quadruped Robot," in *2018 IEEE/RSJ International Conference on Intelligent Robots and Systems (IROS)*, Oct. 2018, pp. 2245–2252, iSSN: 2153-0866.

[21] F. Grimminger, A. Meduri, M. Khadiv, J. Viereck, M. Wüthrich, M. Naveau, V. Berenz, S. Heim, F. Widmaier, T. Flayols, J. Fiene, A. Badri-Spröwitz, and L. Righetti, "An Open Torque-Controlled Modular Robot Architecture for Legged Locomotion Research," *IEEE Robotics and Automation Letters*, vol. 5, no. 2, pp. 3650–3657, Apr. 2020.

[22] H. Geyer and H. Herr, "A muscle-reflex model that encodes principles of legged mechanics produces human walking dynamics and muscle activities," *IEEE Transactions on neural systems and rehabilitation engineering*, vol. 18, no. 3, pp. 263–273, 2010.

[23] K. Nishikawa, "Titin: A Tunable Spring in Active Muscle," *Physiology*, vol. 35, no. 3, pp. 209–217, May 2020.

[24] S. Heim, F. Ruppert, A. A. Sarvestani, and A. Spröwitz, "Shaping in practice: training wheels to learn fast hopping directly in hardware," in *2018 IEEE International Conference on Robotics and Automation (ICRA)*. IEEE, 2018, pp. 5076–5081.

[25] M. S. Ashtiani, A. A. Sarvestani, and A. Badri-Spröwitz, "Hybrid parallel compliance allows robots to operate with sensorimotor delays and low control frequencies," *Frontiers in Robotics and AI*, vol. 8, p. 170, 2021.

[26] D. R. Higueras-Ruiz, K. Nishikawa, H. Feigenbaum, and M. Shafer, "What is an artificial muscle? A comparison of soft actuators to biological muscles," *Bioinspiration & Biomimetics*, 2021.

[27] Y.-H. Chang and L. H. Ting, "Mechanical evidence that flamingos can support their body on one leg with little active muscular force," *Biology letters*, vol. 13, no. 5, p. 20160948, 2017.

[28] R. M. Alexander, "Three Uses for Springs in Legged Locomotion," *The International Journal of Robotics Research*, vol. 9, no. 2, pp. 53–61, Apr. 1990.

[29] A. Spröwitz, A. Tuleu, M. Ajallooeian, M. Vespignani, R. Möckel, P. Eckert, M. D'Haene, J. Degrave, A. Nordmann, B. Schrauwen, J. Steil, and A. J. Ijspeert, "Oncilla Robot: A Versatile Open-Source Quadruped Research Robot With Compliant Pantograph Legs," *Frontiers in Robotics and AI*, vol. 5, 2018.

[30] S. Seok, A. Wang, D. Otten, and S. Kim, "Actuator design for high force proprioceptive control in fast legged locomotion," in *2012 IEEE/RSJ International Conference on Intelligent Robots and Systems (IROS)*, 2012, pp. 1970–1975.

[31] M. Hutter, C. Gehring, M. Bloesch, M. A. Hoepflinger, C. D. Remy, and R. Siegwart, "Starleth: A compliant quadruped robot for fast, efficient, and versatile locomotion," in *Adaptive Mobile Robotics*. World Scientific, 7 2012, pp. 483–490.

[32] R. Van Ham, T. G. Sugar, B. Vanderborght, K. W. Hollander, and D. Lefeber, "Compliant actuator designs," *IEEE Robotics & Automation Magazine*, vol. 16, no. 3, pp. 81–94, 2009.

[33] X. Liu, A. Rossi, and I. Poulakakis, "SPEAR: A monopedal robot with Switchable Parallel Elastic actuation," in *2015 IEEE/RSJ International Conference on Intelligent Robots and Systems (IROS)*, Sep. 2015, pp. 5142–5147.

[34] D. F. Häufle, M. Taylor, S. Schmitt, and H. Geyer, "A clutched parallel elastic actuator concept: Towards energy efficient powered legs in prosthetics and robotics," in *2012 4th IEEE RAS & EMBS International Conference on Biomedical Robotics and Biomechatronics (BioRob)*. IEEE, 2012, pp. 1614–1619.

[35] M. Plooij, W. Wolfslag, and M. Wisse, "Clutched elastic actuators," *IEEE/ASME Transactions on Mechatronics*, vol. 22, no. 2, pp. 739–750, 2017.

[36] E. J. Rouse, L. M. Mooney, and H. M. Herr, "Clutchable series-elastic actuator: Implications for prosthetic knee design," *The International Journal of Robotics Research*, vol. 33, no. 13, pp. 1611–1625, 2014.

[37] A. Hof, B. Geelen, and J. Van den Berg, "Calf muscle moment, work and efficiency in level walking; role of series elasticity," *Journal of biomechanics*, vol. 16, no. 7, pp. 523–537, 1983.

[38] S. W. Lipfert, M. Günther, D. Renjewski, and A. Seyfarth, "Impulsive ankle push-off powers leg swing in human walking," *Journal of experimental biology*, vol. 217, no. 8, pp. 1218–1228, 2014.

[39] B. Kiss, E. C. Gonen, A. Mo, A. Buchmann, D. Renjewski, and A. Badri-Sprwitz, "Investigation on a bipedal robot: Why do humans need both Soleus and Gastrocnemius muscles for ankle push-off during walking?" in *Submitted to IROS 2022, arXiv abs/2203.01588*, 2022, p. 7.

[40] M. Meinders, A. Gitter, J. Czerniecki, and others, "The role of ankle plantar flexor muscle work during walking." *Scandinavian journal of rehabilitation medicine*, vol. 30, no. 1, p. 39, 1998.

[41] A. D. Kuo, J. M. Donelan, and A. Ruina, "Energetic Consequences of Walking Like an Inverted Pendulum: Step-to-Step Transitions." *Exercise & Sport Sciences Reviews*, vol. 33, no. 2, pp. 88–97, Apr. 2005.

[42] K. E. Zelik and P. G. Adamczyk, "A unified perspective on ankle push-off in human walking," *Journal of Experimental Biology*, vol. 219, no. 23, pp. 3676–3683, Dec. 2016. [Online]. Available: http://jeb.biologists.org/content/219/23/3676

[43] A. M. Wilson, J. C. Watson, and G. A. Lichtwark, "A catapult action for rapid limb protraction," *Nature*, vol. 421, no. 6918, pp. 35–36, Jan. 2003.

[44] A. A. Biewener, "Scaling Body Support in Mammals: Limb Posture and Muscle Mechanics," *Science*, vol. 245, no. 4913, pp. 45–48, Jul. 1989.

[45] V. A. Tucker *et al.*, "Energetic cost of locomotion in animals." *Comparative Biochemistry and Physiology*, vol. 34, pp. 841–846, 1970.

[46] V. A. Tucker, "The Energetic Cost of Moving About: Walking and running are extremely inefficient forms of locomotion. Much greater efficiency is achieved by birds, fishand bicyclists," *American Scientist*, vol. 63, no. 4, pp. 413–419, Jul. 1975.

[47] S. Kitano, S. Hirose, A. Horigome, and G. Endo, "TITAN-XIII: sprawling-type quadruped robot with ability of fast and energy-efficient walking," *ROBOMECH Journal*, vol. 3, no. 1, pp. 1–16, Mar. 2016.

[48] A. J. Ijspeert, A. Crespi, D. Ryczko, and J.-M. Cabelguen, "From Swimming to Walking with a Salamander Robot Driven by a Spinal Cord Model," *Science*, vol. 315, no. 5817, pp. 1416–1420, Mar. 2007.

Alborz Aghamaleki Sarvestani Received a B.Sc and M.Sc degree in mechanical engineering with a major in applied design, dynamics, vibrations, and control from Shiraz University in 2012 and 2015, respectively. He is now a Ph.D. researcher in the Dynamic Locomotion Group at the Max Planck Institute for Intelligent Systems. He is interested in legged locomotion, assistive robotics, bioinspired robotics, robotics, mechanism design, and sensor fusion.

Alexander Badri-Spröwitz Received his Diploma in Mechatronics from Ilmenau Technical University in Germany in 2005, and a Ph.D. in manufacturing systems and robotics from the Swiss Federal Institute of Technology, Lausanne, in Switzerland in 2010. Since 2016, he is Max Planck Research Group Leader heading the Dynamic Locomotion Group and IMPRS-IS Faculty at the Max Planck Institute for Intelligent Systems in Stuttgart, Germany. Badri-Sprwitz and his team develop legged research mechanics and control of animal and machine legged locomotion.

APPENDIX

a) Central Pattern Generator: We implemented a Central Pattern Generator similar to [48], [17], [7]. The CPG outputs hip and knee motor trajectories for the left and right leg, as feedforward trajectories interpreted as motor positions. We chose this CPG model to directly input gait parameters hip and knee amplitude, hip offset, phase shift between legs, and gait duty factor. Actuator trajectories are calculated with the following Central Pattern Generator;

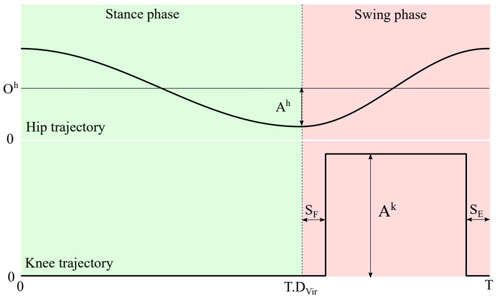

Fig. 10. CPG trajectories.

$$\dot{\phi_i} = 2\pi f + \sum_{i \neq j} c_{ij} sin(\phi_j - \phi_i - \varphi_{ij}) \tag{22}$$

$$\dot{a_i^h} = \alpha(A_i^h - a_i^h) \tag{23}$$

$$\dot{o_i^h} = \alpha(O_i^h - o_i^h) \tag{24}$$

ϕ_i is the i-oscillator's phase. $c_{12} = 1, c_{21} = 0$ are coupling terms. f is the locomotion frequency. $\varphi_{12} = \pi, \varphi_{21} = 0$ are phase shifts between hip oscillators. a_i^h and A_i^h are the instantaneous and the commanded hip amplitude, respectively. o_i^h and O_i^h are the instantaneous and the commanded hip offset, respectively. α is a convergence gain. The commanded duty factor D adapts the phase Θ_i^h of the hip joint of leg i, leading to the hip actuator set position h_i:

$$\Theta_i^h = \begin{cases} \frac{\phi_i}{2D} & 0 \leq \phi_i \leq 2\pi D \\ \frac{\phi_i + 2\pi(1-2D)}{2(1-D)} & \end{cases} \tag{25}$$

$$h_i = a_i^h cos(\Theta_i^h) + o_i^h \tag{26}$$

The active flexion and extension of knee is coupled to the hip phase ϕ_i by the phase shift S_F and S_E, respectively:

$$S_F = 2\pi S_f(1-D) \tag{27}$$

$$S_E = 2\pi S_e(1-D) \tag{28}$$

Where S_f and S_e are the fraction of flexion and extension delay of swing phase, respectively. The knee i actuator angle is set as k_i, with the commanded knee amplitude A_i^k:

$$k_i = \begin{cases} 0 & 0 \leq \phi_i \leq 2\pi D + S_F \\ A_i^k & 2\pi D + S_F \leq \phi_i \leq 2\pi - S_E \\ 0 & 2\pi - S_E \leq \phi_i \leq 2\pi \end{cases} \tag{29}$$

b) Robot and system properties:

c) Nomenclature:

d) Robot locomotion screenshot:

Part	Mass [g]	Part	Mass [g]
Robot	1200	S1	32
Trunk	980	S2	39
Leg	110	S3	19
Actuator	165	S4	11
Force sensor	20	S5	9
Tendon force sensor	1		

Abbreviation	Definition	Abbreviation	Definition
BB1	BirdBot-1	l_p	Length pantograph segment
BB2	BirdBot-2	K_p	Pantograph spring stiffness
DE	Disengagement	K_{GS}	Global spring stiffness
GS	Global spring	R_{J_i}	Cam radius join i
PE	Parallel elasticity	R_P	Offset parallel pantograph
CPG	Central Pattern Generator	F_{GRF}	Ground reaction force
CoT	Cost of transport	F_{GS}	Force global spring
m	Robot mass	F_{DE}	Force disengagement tendon
g	Gravitational acceleration	h_i	Distance joint i to GRF
v_{CoG}	Robot velocity	α_{GRF}	GRF angle to z direction
J_i	Joint i	LL	Leg length
S_i	Segment i	α_{LL}	LL angle to z direction
cam_i	Cam i	f	Gait frequency
cam4DE	Cam disengagement J_4	ϕ_i	Phase motor i
cam4GS	Cam global spring J_4	φ_{ij}	Phase shift matrix
SPI	Serial peripheral interface	A_i^h	Hip amplitude, commanded
SSI	Synchronous Serial Interface	A_i^k	Knee amplitude, commanded
I_i	Current motor i	a_i^h	Hip amplitude, instantaneous
V_i	Voltage motor i	O_i^h	Hip offset, commanded
L	Total linear momentum	o_i^h	Hip offset, instantaneous
θ_i	Joint angle i	D	Duty factor, gait
m_i	Mass segment i	S_F	Phase shift, knee flexing
T_i	Torque joint i	S_E	Phase shift, knee extending
P_{J_i}	Coordinate joint i	S_f	Delay, knee flexing
l_i	Length segment i	S_e	Delay, knee extending

3 Effect of passive extensor tendon on performance of front and hind legs in quadrupeds

Effect of passive extensor tendon on performance of front and hind legs in quadrupeds

Alborz Aghamaleki Sarvestani[1,*], **Robin Petereit**[1], **and Alexander Badri-Spröwitz**[1]

[1]Max Planck Institute for Intelligent Systems, Dynamic Locomotion, Stuttgart, Germany
[*]Corresponding Author: sarvestani@is.mpg.de

ABSTRACT

Some animals have less mobility in their distal joints for the hind leg compared to the front leg. For example, studies show that the hind leg distal joint can have 50 % less motion during trot gait than the front leg distal joint. This difference is rooted in the development of extensor muscle at distal joints. To show the different functionality of extensor muscles in the front and hind legs, we designed an experiment to measure the performance of a robot with a leg similar to mammalian leg morphology. Then we simplified all extensor muscle with high stiffness tendon called DE tendon. And measure the performance of our quadruped robot, RoboManul, with and without this DE tendon.
We increased robot speed by 56 % under the same gait parameter by adding the DE tendon. At the same time, we also reduced input power by 60 %.this improvement resulted in the reduction of CoT by 20 % compared to the robot without the DE tendon. However, adding the DE tendon increase performance of the front leg. In walking scenarios front leg recuperate energy nine times more than the hind leg. Higher leg loading due to trunk pitch down and front leg loading allow front leg DE tendon to store more energy compared to the hind leg.

Introduction

quadruped animals have a complex Leg morphology[1]. Leg morphology for the front and hind leg evolve differently depending on morphology, the animal center of mass, segmentation, muscle-tendon network[2,3]. The front and hind leg can have different equivalent elements between the front and hind such as muscle size[3], segment length[4] or joint angular limits[5]. One of the important differences between the front and hind leg is in the distal mechanism of the leg[6].In dogs, we have a different range of motion for foot joints between the front and hind leg[5,7]. As you can see in Fig. 1, the front leg creates up to 50 % more foot flexing rather than the hind leg[8] during symmetric gait such as trot gait.
Studies show that distal leg muscles are recuperating locomotion energy[9,10] during walking via a catapult mechanism[6,11,12]. And also study from Wilson et al.[6] shows that foot flexion can help animals slack extensor muscles and protract faster during the swing phase.
Asymmetric leg for front and hind combined by hip torque propulsion animal forward cause pitch motion in the trunk which is an unwanted source of energy loss [13]. Most of the optimization algorithm for path planning of quadruped robots try to minimize body pitch which narrows the range of acceptable trajectory, which increase robot speed and efficiency. Recently, a new robotic leg design was developed[14] that includes a passive distal mechanism similar to what we observe in avians and mammals. With the help of this robotic setup, we can take a deeper look into the functionality of the distal mechanism in quadruped with respect to other parameters during locomotion such as hip torque, weight distribution, and asymmetric front and hind leg design.

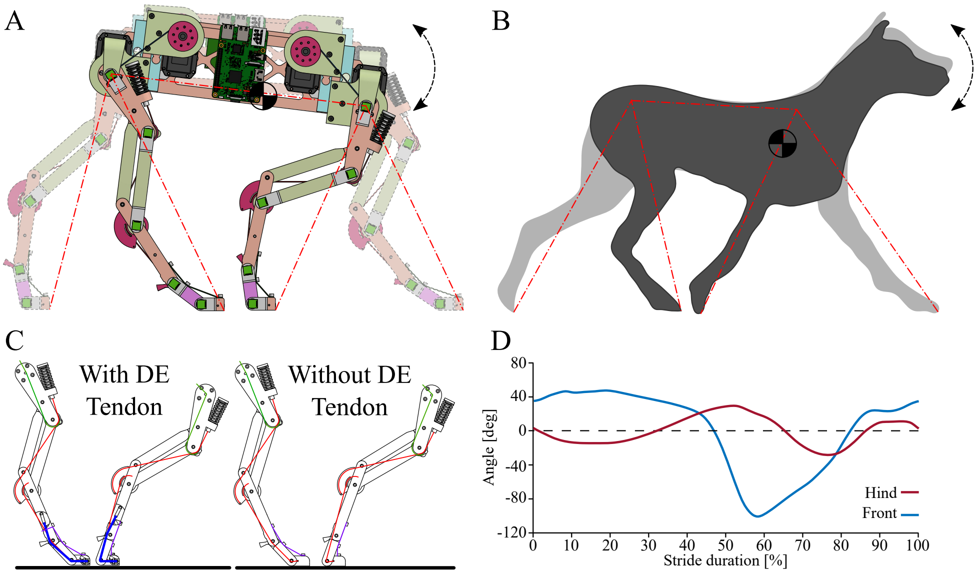

Figure 1. A. Quadruped robot in trot has a wider stance angle for the front leg than the hind leg. B. Dog has a wider stance angle for the front leg rather than the hind leg, foot joint range for front legs is wider than hind legs.[7] C.leg with and without DE Tendon(blue tendon) D.foot joint angle for front and hind leg of dog during trot[5]

To explain the functionality of the distal leg mechanism, we simplify the leg and keep the necessary part of the complex leg. In this study, we use a quadruped robot with a newly designed leg mechanism[14](Fig. 1) we test the robot under two different scenarios. The first scenario is a leg with a disengagement tendon that acts as an extensor muscle during foot roll-over. The second scenario is a leg without a disengagement tendon. We test the robot in three different gait frequencies for each set. Then we measure the speed and motor consumption of each scenario. Based on the power consumption of the motor and DE tendon activation, evaluate the performance of the front and hind legs. And the necessity of a disengagement tendon in the leg for the quadrupedal scenario.

Results

in this section, we present experimental results for the quadruped robot for two cases with and without disengagement tendon to show the performance of the leg distal mechanism.

Hip torque: according to Fig. 2 Average hip torque for front leg reduced by 39 %, 38 % and 56 % when disengagement tendon is active for gait frequencies of 1.0 Hz,1.1 Hz and 1.5 Hz respectively. Reduction for hind leg average hip torque is 92 %, 98 % and 138 %. It means at the first part of the stance, elastic energy recuperation drives the hind leg forward. As a result average hip torque change sign from negative to positive. It means the part of torque that protracts the leg forward is higher than the part pushing the body forward.

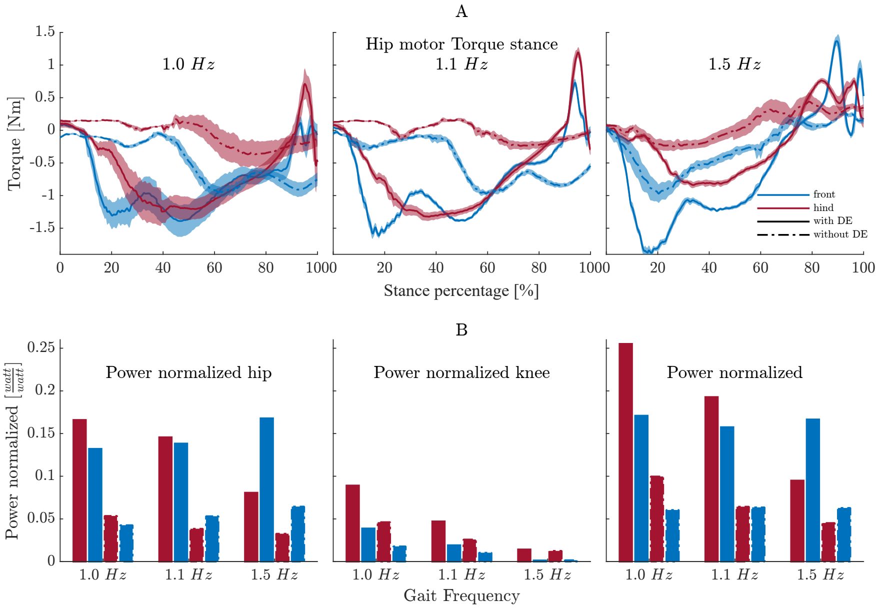

Figure 2. A. Hip motor torque during the stance phase of robot averaged with confidence 95% for the front (solid blue) and the hind (solid red) leg for two cases with DE tendon (solid) and without DE tendon (dashed-dot). B. Power consumption of hip, knee and total of robot for the front (blue) and the hind (red) leg for the scenario with DE tendon (solid) and without DE tendon (dashed-dot),

Hip and knee power: According to Fig. 2 we can observe that by increasing speed, we have a reduction of power consumption in knee motor for all scenarios. For cases with DE tendon, knee power for the front leg reduced by 56 %, 59 % and 91 % compared to the hind leg for gait frequencies of 1.0 Hz,1.1 Hz and 1.5 Hz respectively. Reduction in power for the similar parameters by removing DE tendon is 61 %, 60 % and 87 %. It shows that DE Tendon reduces knee power requirement for the leg but does not change the ratio of knee power consumption for the front and hind leg.

From Fig. 2 we can see that by increasing speed, hip power consumption for the front leg increase, but hind hip power consumption decrease. We can see a portion of hip power consumption between the hind leg and front leg goes from 56 % : 44 % to 32 % : 68 % for speed increase from 1.0 Hz to 1.5 Hz. It means we use more hind hip power at the low speed, but at high speed, we use more front hip power.

In Fig. ,2 we can see the front leg almost apply a certain amount of energy into the robot between 1.0 Hz and 1.5 Hz for both with and without DE tendon cases, but, at the same time, we can see a reduction in energy that the hind leg applies into the robot. Interestingly, by increasing speed, motors insert less energy into the system.

General disengagement via foot segmentation helps the front leg more than the hind leg. We can see more energy consume for the hind leg to flex the knee. This energy would be minimal if the DE tendon acts properly and disengages the global spring.

DE tendon Work: DE tendon act as a reservoir of locomotion energy that charge during stance and return that energy to the system at the beginning of the flight phase. We can see that by increasing speed from 1.0 Hz to 1.5 Hz, the ratio of the power of the front leg DE tendon to the hind DE tendon reduces from 90%:10% to 60%:40%. This number shows that the robot relay mostly on front leg disengagement more than hind leg at the lower speed. By increasing, speed dependency of the leg on the DE tendon for disengagement is generally reduced by 60 %.

Trunk pitch: When the robot applies hip torque in any direction reaction torque will pitch the trunk beside that leg forces for front and hind can also pitch the robot in the positive (upward) or negative (downward) direction. Robots with lesser body oscillation are dissipating less locomotion energy. By adding DE tendon, we reduce body oscillation by 19 %, 21 % and 24 % for gait frequencies of 1.0 Hz,1.1 Hz and 1.5 Hz respectively. By increasing speed, trunk pitch gets smaller.

Speed: As you can see in Fig. 3 we increase robot speed by 56%, 28% and 12% for gait frequencies of 1.0 Hz,1.1 Hz and 1.5 Hz, respectively, by adding DE tendon to the leg. Even though we send the same command to the hip and knee motor, we have a larger angle of contact for the front leg, which means the distal mechanism makes less interference with a knee lift-off and provides more swing push for the front leg.

Cost of transport: Total cost of transport of robot calculate as $CoT = \frac{P_{In}}{m.g.v}$ where P_{in} is input motor power, m is robot mass, v is robot speed. COT is a metric for showing the robot's efficiency. To compare robots to other robots and animal efficiency, we use the natural runner line presented by Tucker[15,16]. The ratio of robots COT to COT of the natural runner of the same mass would be a metric to compare the energy efficiency of different size robots. This metric shows that adding the DE tendon reduces robot COT by 20%. This increase in efficiency happens by reducing hip and knee input power and achieving higher speed. You can see the COT of RoboManul compared to other state-of-the-art robots.

Optimized motor gearbox selection: In Robomanul, we use a servo drive motor. These motors and gearbox systems are inefficient in energy consumption due to losses because of acceleration and deceleration of gearbox inertia. We know that input electrical energy equals mechanical output energy plus losses.

$$P_{Input\ motor} = P_{Mechanical} + P_{Joule\ heating} = \mathrm{T}\omega + RI^2 \tag{1}$$

Roos shows that we always have mechanical losses in the motor gearbox system because of the accelerating inertia of the motor shaft and gearbox. We also have electrical losses due to joule heating of coil in motor[17]. Roos framework shows that to achieve the minimum cost of transport for the robot. We need to optimize the combination of the motor parameter(select appropriate motor), gearbox ratio, and effective inertia.

$$P_{Inputmotor} = (J_{Motor} + J_{Gears})\ddot{\theta}_{load}\dot{\theta}_{load}n^2 + \frac{\tau_{load}(t))}{\eta_{gearbox}}\dot{\theta}_{load} + R_{Motor}\frac{T_m^2}{K_T^2} \tag{2}$$

By applying this equation to various low inertia gearboxes and off-the-shelf brushless motors, we can get to optimal motor and gearbox to achieve minimum COT for the robot. In our case, if we use brushless motor MN-7005 (T-motor) and gear ratio 8:1, we can get to a normalized COT of 10%.

Discussion

DE tendon performance is influenced by many parameters for the front and hind leg. Parameters such as leg loading and angle of roll-over at joint define the amount of the DE tendon mechanical charging and recuperation of locomotion energy during a gait cycle. Trunk oscillation can strongly influence both of these parameters. On the other hand, increasing body oscillation increases locomotion energy costs. By observing the power and torque difference of front and hind leg motors under similar input parameters

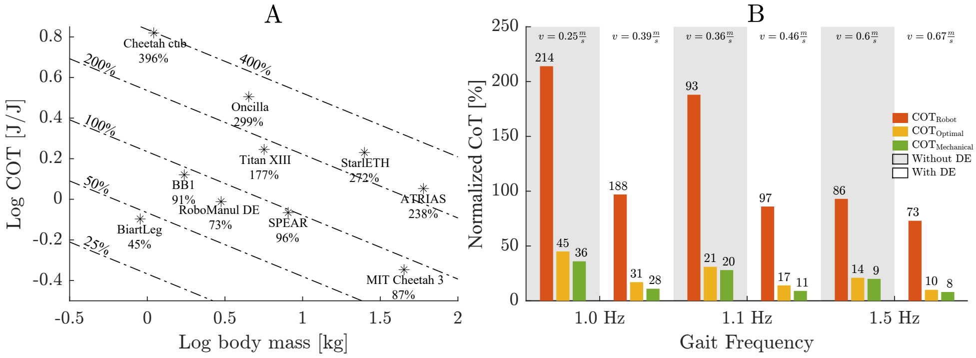

Figure 3. A. CoT of Robomanul in comparison to the state of the art robots[14, 18–25] on Tucker graph of normalize CoT to natural runners[15, 16] B. Cost of transport mechanical (orange), electrical (green) and optimized (yellow) one base on roos framework[17] for six experiments with DE tendon (white shadow) and without DE tendon (gray shadow) and robot achieve speed.

such as leg design and control and changing DE tendon, we identify DE tendon's role for the front and hind leg during locomotion. The first effect is adding DE tendon was to reduce trunk oscillation by 24%. Also, by adding the DE tendon, we introduce a third elastic element that allows us to compensate for one source of energy loss. The task of the global tendon is to recuperate mechanical energy in leg length direction[26]. The task of the pantograph spring is to recuperate energy in leg angle direction[24]. And the DE tendon task is to act as some form of memory elasticity that depends on ground contact store energy during the stance phase and release that energy as push at the stance phase and knee flexing at the beginning of the sewing phase.

from data we can see the front leg DE tendon recuperate nine times higher than the hind leg and also hind leg use more knee energy to lift of from ground which means clutch behaviour didn't happen properly in back joint one of the conclusion is that DE tendon at hind leg in quadruped is not functioning as it should do it could be a source why hind leg foot segment in quadruped (segment 3-4) are more fixed during stance phase. the other reason that quadruped robot doesn't need clutching parallel elasticity via DE tendon is the main purpose of disengagement is to lift the leg and create leg clearance during swing phase. If we can clear that clearance via other source the robot or animal doesn't knee to flex knee during swing. As we can see these clearance can provide at higher speed when robot has flight phase means center of mass push into air during leg push off and create leg clearance or it can create for low speed via trunk oscillation and specificaly head down motion of trunk at hind leg toe off. on the other hand we can observe DE tendon in front leg due to higher leg loading and wider roll over angle charge more and release more energy to extend proximal underactuated part of leg to sweep higher angle during stance and as a result during swing phase. this effect again can amplify by head up motion of trunk on the front leg at the point of toe off.

beside these difference between front and hind leg adding DE tendon and mechanism into the leg design change natural dynamic of system.specifically be introducing more serial spring into system reduce natural frequency of system. this reduction in natural frequency help us to walk/run at higher locomotion energy at lower gait frequency for given input energy.

result shows that by adding DE tendon despite increase total mechanic energy of the robot by 56%, 28% and 12% for gait frequencies of 1.0 Hz,1.1 Hz and 1.5 Hz, respectively, we reduce input energy by almost

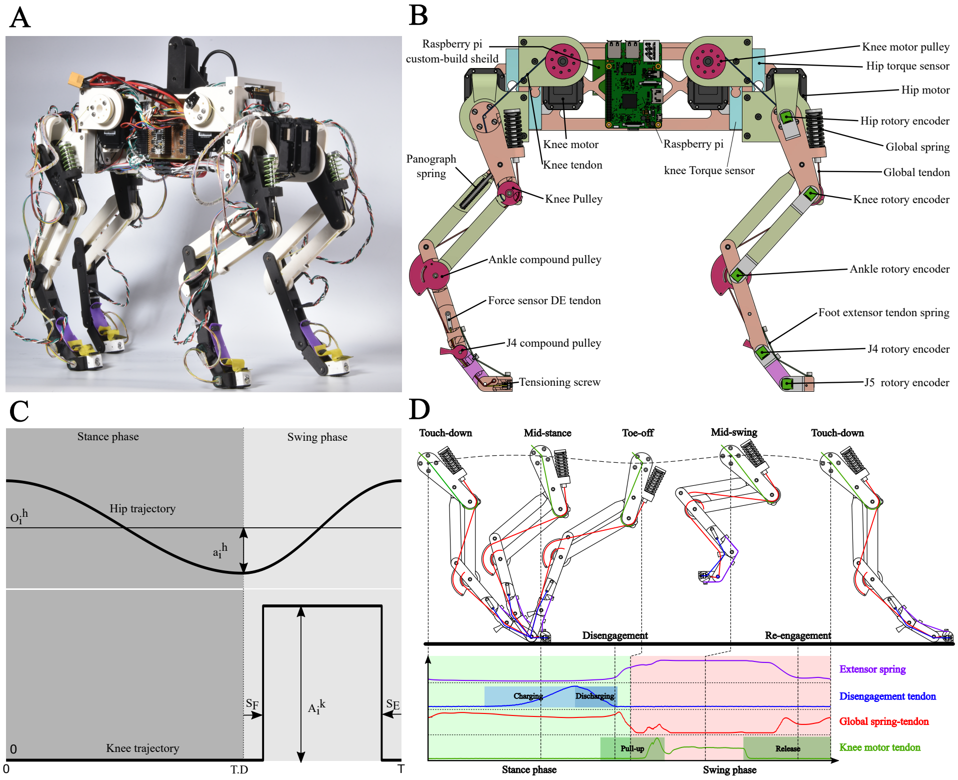

Figure 4. A. Picture of RoboManul stand with off motor. B. schematic of RoboManul with internal component C. Cpg Pattern apply as position control to robot motor. D. leg phases during locomotion and activation pattern of different tendons

60% for all speed.

Methods

Robot Structure: RoboManul consists of four identical legs and a trunk Fig. 4. Each leg has five segments and five revolute joints and one spring-loaded parallel pantograph segment that keep segment 1 and segment 3 parallel under no-load scenarios. each leg connects to the hip motor (Dynamixel, MX-64 AT). The knee joint connects through a fixed pulley and a tendon to the knee motor (Dynamixel, MX-64 AT). The knee motor can flex the knee joint. all robot joints except the hip coordinate passively via the global spring and tendon system. this tendon allows the robot leg to load passively without consuming energy. At robot foot, we have extensor Disengagement tendon (DE tendon) which connect on one side to segment 3 and after wrapping around joint 4 and 5 connect to set screw at segment 5. this tendon act as a charging spring which can recuperate locomotion energy back to leg especially at the end of stance phase. DE tendon also acts as clutch activation to disengage global spring and lif unloaded leg to flight phase

Fig. 4. Besides the DE tendon at the robot foot, we have two elastic latex band springs that flex joints four and five at all times. The purpose of this tendon is to passively engage the global spring as knee joint release.

Instrumentation: RoboManul has many sensors to measure the performance of the leg during the experiment. Each leg has five 16-bit magnetic rotary encoders (AEAT8800-Q24) to measure each joint angle. each leg has three force sensors, two of them measure the torques of the hip and knee motor, and one tensile force sensor measures tension in the DE tendon. Besides this force and position instrumentation, we have a current sensor (ACS723) to measure the input power of each motor separately and we have one rugged IMU (VN-100) to measure trunk movement. all force sensors read via custom-built shield for Itsybitsy microcontroller that communicates all data to onboard computer (Raspberry Pi 4+). All encoders and the IMU data read directly via a custom-built Raspberry Pi shield. Onboard computer has the responsibility to communicate with motors via U2D2 converter.

Software: RoboManul software runs on the host computer and onboard computer. On the host computer, there is a python base GUI that users can set gait parameters and observe online data from sensors. Users can also save experiment results into JSON files for further process in other programs. the other computer is Raspberry Pi 4 B which runs low-level codes for reading from different sensors on the robot and also receives actuator trajectory from the host computer to send to motor drivers. The onboard computer sends sensors and motors data back to host computer for saving and further post-processing.

Gaits and Motion Control: We send a feed-forward position control command to hip and knee motor if robot to generating trot gait [18,27]. We can set CPG parameters such as gait frequency, hip amplitude, knee amplitude, knee offset, hip phase shift and knee phase shift via python GUI on the host computer. later generated pattern sent to the onboard computer to apply on robot actuators.

$$\dot{\phi}_i = 2\pi f + \sum_{i \neq j} C_{ij} sin(\phi_j - \phi_i - \varphi_{ij}) \tag{3}$$

$$\dot{a}_i^h = \alpha(A_i^h - a_i^h) \ , \ \dot{o}_i^h = \alpha(O_i^h - o_i^h) \tag{4}$$

where ϕ_i is the i-oscillator's phase. $C = \begin{pmatrix} 0 & 0 & 0 & 0 \\ 1 & 0 & 0 & 0 \\ 1 & 0 & 0 & 0 \\ 1 & 0 & 0 & 0 \end{pmatrix}$ is coupling matrix. f is the gait frequency. $\varphi = \begin{pmatrix} 1 & 0 & 0 & 0 \\ 0 & 0 & 0 & 0 \\ 1 & 0 & 0 & 0 \\ 0 & 0 & 0 & 0 \end{pmatrix}$ are phase shifts matrix, a_i^h and A_i^h are the instantaneous and the desired hip amplitude, respectively. o_i^h and O_i^h are the instantaneous and the desired hip offset, respectively. α is a convergence gain.

$$\Theta_i^h = \begin{cases} \frac{\phi_i}{2D} & 0 \leq \phi_i \leq 2\pi D \\ \frac{\phi_i + 2\pi(1-2D)}{2(1-D)} & \end{cases} \tag{5}$$

$$h_i = a_i^h cos(\Theta_i^h) + o_i^h \tag{6}$$

where D is commanded duty factor. h_i is desired hip angle of i'th leg.
The active shortening of the leg length by the knee actuator is coupled to the hip oscillator by the phase

shift S_F for flexing and S_E for passive extension:

$$S_F = 2\pi S_f(1-D) \ , \quad S_E = 2\pi S_e(1-D) \tag{7}$$

The knee i actuator angle is set as k_i, with the commanded knee amplitude A_i^k:

$$k_i = \begin{cases} 0 & 0 \leq \phi_i \leq 2\pi D + S_F \\ A_i^k & 2\pi D + S_F \leq \phi_i \leq 2\pi - S_E \end{cases} \tag{8}$$

A CPG output trajectory for one stride is shown in Fig. 4.

Experiments: to measure the performance of the DE tendon in the front and hind leg we design two sets of experiments. The first set robot has a disengagement tendon and in the second set, we remove the disengagement tendon. and measure joints angle, tendon forces and motors torque and power. to identify the effect of robot dynamic and leg loading on the performance of the passive DE mechanism for each set we measure 15 strides of the robot at three different gait input frequencies of 1 Hz,1.1 Hz and 1.5 Hz. in order to perform continuous walking of the robot and record multiple strides of robot data, we put the robot on a treadmill with a linear guide and harness that allows the robot to move and rotate in the sagittal plane. the hole experiments were recorded with a high-speed camera (mirolab 110) with 400 fps.

Acknowledgments

We thank the International Max Planck Research School for Intelligent Systems (IMPRS-IS) for supporting the academic development of Alborz Aghamaleki Sarvestani.

Author contributions statement

AAS and RP conceived and conducted the experiments, AAS and ABS analyzed the results. All authors reviewed the manuscript.

References

1. Jones, K. E., Angielczyk, K. D. & Pierce, S. E. Stepwise shifts underlie evolutionary trends in morphological complexity of the mammalian vertebral column. *Nature communications* **10**, 1–13 (2019).
2. Kubo, T., Sakamoto, M., Meade, A. & Venditti, C. Transitions between foot postures are associated with elevated rates of body size evolution in mammals. *Proceedings National Academy Sciences* **116**, 2618–2623 (2019).
3. Wilson, A. & Lichtwark, G. The anatomical arrangement of muscle and tendon enhances limb versatility and locomotor performance. *Philosophical Transactions Royal Society B: Biological Sciences* **366**, 1540–1553 (2011).
4. Young, N. M. & HallgrÍmsson, B. Serial homology and the evolution of mammalian limb covariation structure. *Evolution* **59**, 2691–2704 (2005).
5. Lorke, M. *et al.* Comparative kinematic gait analysis in young and old beagle dogs. *Journal Veterinary Science* **18**, 521–530, DOI: https://doi.org/10.4142/jvs.2017.18.4.521 (2017).

6. Wilson, A. M., Watson, J. C. & Lichtwark, G. A. A catapult action for rapid limb protraction. *Nature* **421**, 35–36, DOI: https://doi.org/10.1038/421035a (2003).

7. Fischer, M. S., Lilje, K., Lauströer, J. & Andikfar, A. *Dogs in motion* (VDH Service, 2011).

8. Fischer, M. S., Lehmann, S. V. & Andrada, E. Three-dimensional kinematics of canine hind limbs: in vivo, biplanar, high-frequency fluoroscopic analysis of four breeds during walking and trotting. *Scientific reports* **8**, 1–22, DOI: https://doi.org/10.1038/s41598-018-34310-0 (2018).

9. Alexander, R. M. Storage of elastic strain energy in muscle and other tissues. *Nature* **265**, 114–117 (1977).

10. Alexander, R. M. Walking and Running: Legs and leg movements are subtly adapted to minimize the energy costs of locomotion. *American Scientist* **72**, 348–354 (1984).

11. Hof, A., Geelen, B. & Van den Berg, J. Calf muscle moment, work and efficiency in level walking; role of series elasticity. *Journal biomechanics* **16**, 523–537, DOI: https://doi.org/10.1016/0021-9290(83)90067-2 (1983).

12. Lipfert, S. W., Günther, M., Renjewski, D. & Seyfarth, A. Impulsive ankle push-off powers leg swing in human walking. *Journal experimental biology* **217**, 1218–1228, DOI: https://doi.org/10.1242/jeb.097345 (2014).

13. Usherwood, J. R. & Granatosky, M. C. Limb work and joint work minimization reveal an energetic benefit to the elbows-back, knees-forward limb design in parasagittal quadrupeds. *Proceedings Royal Society B* **287**, 20201517 (2020).

14. Badri-Spröwitz, A., Aghamaleki Sarvestani, A., Sitti, M. & Daley, M. A. Birdbot achieves energy-efficient gait with minimal control using avian-inspired leg clutching. *Science Robotics* **7**, eabg4055 (2022).

15. Tucker, V. A. *et al.* Energetic cost of locomotion in animals. *Comparative Biochemistry Physiology* **34**, 841–846, DOI: https://doi.org/10.1016/0010-406X(70)91006-6 (1970).

16. Tucker, V. A. The Energetic Cost of Moving About: Walking and running are extremely inefficient forms of locomotion. Much greater efficiency is achieved by birds, fish—and bicyclists. *American Scientist* **63**, 413–419 (1975).

17. Roos, F., Johansson, H. & Wikander, J. Optimal selection of motor and gearhead in mechatronic applications. *Mechatronics* **16**, 63–72 (2006).

18. Spröwitz, A. *et al.* Towards Dynamic Trot Gait Locomotion: Design, Control and Experiments with Cheetah-cub, a Compliant Quadruped Robot. *International Journal Robotics Research* **32**, 932 – 950, DOI: 10.1177/0278364913489205 (2013).

19. Spröwitz, A. *et al.* Oncilla Robot: A Versatile Open-Source Quadruped Research Robot With Compliant Pantograph Legs. *Frontiers Robotics AI* **5**, DOI: 10.3389/frobt.2018.00067 (2018).

20. Kitano, S., Hirose, S., Horigome, A. & Endo, G. TITAN-XIII: sprawling-type quadruped robot with ability of fast and energy-efficient walking. *ROBOMECH Journal* **3**, 1–16, DOI: 10.1186/s40648-016-0047-1 (2016).

21. Hutter, M. *et al.* Starleth: A compliant quadruped robot for fast, efficient, and versatile locomotion. In *Adaptive Mobile Robotics*, 483–490, DOI: 10.1142/9789814415958_0062 (WORLD SCIENTIFIC, 2012).

22. Hubicki, C. *et al.* ATRIAS: Design and validation of a tether-free 3D-capable spring-mass bipedal robot. *The International Journal Robotics Research* **35**, 1497–1521, DOI: 10.1177/0278364916648388 (2016).

23. Liu, X., Rossi, A. & Poulakakis, I. SPEAR: A monopedal robot with Switchable Parallel Elastic actuation. In *2015 IEEE/RSJ International Conference on Intelligent Robots and Systems (IROS)*, 5142–5147, DOI: 10.1109/IROS.2015.7354101 (2015).

24. Ruppert, F. & Badri-Spröwitz, A. Series Elastic Behavior of Biarticular Muscle-Tendon Structure in a Robotic Leg. *Frontiers Neurorobotics* **13**, 64, DOI: 10.3389/fnbot.2019.00064 (2019).

25. Bledt, G. *et al.* MIT Cheetah 3: Design and Control of a Robust, Dynamic Quadruped Robot. In *2018 IEEE/RSJ International Conference on Intelligent Robots and Systems (IROS)*, 2245–2252, DOI: 10.1109/IROS.2018.8593885 (2018). ISSN: 2153-0866.

26. Alexander, R. M. Elastic energy stores in running vertebrates. *American Zoologist* **24**, 85–94 (1984).

27. Ijspeert, A. J., Crespi, A., Ryczko, D. & Cabelguen, J.-M. From swimming to walking with a salamander robot driven by a spinal cord model. *science* **315**, 1416–1420 (2007).

4 Hybrid Parallel Compliance Allows Robots to Operate With Sensorimotor Delays and Low Control Frequencies

frontiers
in Robotics and AI

ORIGINAL RESEARCH
published: 16 June 2021
doi: 10.3389/frobt.2021.645748

Hybrid Parallel Compliance Allows Robots to Operate With Sensorimotor Delays and Low Control Frequencies

Milad Shafiee Ashtiani†, Alborz Aghamaleki Sarvestani† and Alexander Badri-Spröwitz*

Dynamic Locomotion Group, Max Planck Institute for Intelligent Systems, Stuttgart, Germany

Animals locomote robustly and agile, albeit significant sensorimotor delays of their nervous system and the harsh loading conditions resulting from repeated, high-frequent impacts. The engineered sensorimotor control in legged robots is implemented with high control frequencies, often in the kilohertz range. Consequently, robot sensors and actuators can be polled within a few milliseconds. However, especially at harsh impacts with unknown touch-down timing, controllers of legged robots can become unstable, while animals are seemingly not affected. We examine this discrepancy and suggest and implement a hybrid system consisting of a parallel compliant leg joint with varying amounts of passive stiffness and a virtual leg length controller. We present systematic experiments both in computer simulation and robot hardware. Our system shows previously unseen robustness, in the presence of sensorimotor delays up to 60 ms, or control frequencies as low as 20 Hz, for a drop landing task from 1.3 leg lengths high and with a compliance ratio (fraction of physical stiffness of the sum of virtual and physical stiffness) of 0.7. In computer simulations, we report successful drop-landings from 3.8 leg lengths (1.2 m) for a 2 kg quadruped robot with 100 Hz control frequency and a sensorimotor delay of 35 ms.

Keywords: legged robots, parallel and passive compliance, hybrid actuation and leg design, sensorimotor delay, Feedback, latency, parallel elastic actuation

OPEN ACCESS

Edited by:
Dai Owaki,
Tohoku University, Japan

Reviewed by:
Takashi Takuma,
Osaka Institute of Technology, Japan
Thiago Boaventura,
University of São Paulo, Brazil
Philipp Stratmann,
Technical University of Munich, Germany

****Correspondence:***
Alexander Badri-Spröwitz
sprowitz@is.mpg.de

†These authors have contributed equally to this work

Specialty section:
This article was submitted to Computational Intelligence in Robotics, a section of the journal Frontiers in Robotics and AI

Received: *23 December 2020*
Accepted: *26 May 2021*
Published: *16 June 2021*

Citation:
Ashtiani MS, Aghamaleki Sarvestani A and Badri-Spröwitz A (2021) Hybrid Parallel Compliance Allows Robots to Operate With Sensorimotor Delays and Low Control Frequencies. Front. Robot. AI 8:645748. doi: 10.3389/frobt.2021.645748

1 INTRODUCTION

Animals use muscle-tendon networks, which they control by spinal circuits, the brainstem, and with sensory feedback to produce joint torque and work for legged locomotion (Forssberg et al., 1977; Grillner and Wallen, 1985; Biewener, 1989; Ijspeert, 2008; Takakusaki et al., 2016; Stratmann et al., 2018). The response time for muscle action caused by an external stimulus is related to axonal conduction velocity and animal body weight, and the resulting sensorimotor delay can be as slow as 41 ms in a 4 kg, cat-sized animal (More et al., 2010; Franklin and Wolpert, 2011; More and Donelan, 2018). House cats run with up to 5 Hz locomotion frequency (Bertram et al., 2014). At an assumed duty cycle of 0.4 the stance phase lasts 80 ms, and the animal would be sensor-blind for half its stance phase, i.e., during the entire force ramp-up time. We often assume feedback to be critical in challenging conditions like in rough terrain locomotion. However, running birds and other animals traverse hidden perturbations with ease, albeit limited sensorimotor capabilities (Daley et al., 2006; Ernst et al., 2018).

Animal locomotion control is simplified by a morphology with tendons and muscles with intrinsic physical stiffness (Alexander, 1990; Blickhan et al., 2007a). Physical elasticities mounted serially like tendons can lead to under-actuation and reduced controllability. However, animals show no obvious signs of decline in robustness, responsiveness, or agility. Many muscle-tendons are part of more extensive networks with parallel muscle-tendon units, requiring sensorimotor coordination (Lombard, 1903; Hutchinson et al., 2005). This raises two questions: For parallel mounted active and passive stiffness, how do animals deal with significant sensorimotor delays (**Figure 1A**)? And how are legged robots impacted (**Figure 1B**)? This section briefly reviews concepts from biomechanics and legged robotics dealing with sensorimotor delays, the control of leg forces, especially at leg impacts, and active and passive joint stiffness. In the main part of this work we present a robotic proof-of-concept characterizing parallel active and passive stiffness as one source of robustness against adverse conditions for feedback controllers.

Inspired by animal morphology and passive and active leg stiffness, legged robot designs often include mechanical springs (Nasiri et al., 2016; Ambrose and Ames, 2020). Series elastic actuation (SEA) can simplify control, improve robustness and interaction safety, and protect actuators from overloads (Raibert et al., 1984; Robinson et al., 1999; Pratt and Krupp, 2004; Hutter et al., 2011; Calanca et al., 2015; Hutter et al., 2016; AhmadSharbafi et al., 2020). Designs with parallel mounted springs and actuators (parallel elastic actuation, PEA) can increase leg forces, improve locomotion energy efficiency, and reduce actuator loading (Gunther et al., 2015; Niehues et al., 2015; Plooij et al., 2016; Yesilevskiy et al., 2016; Liu et al., 2018; Toxiri et al., 2018; Yesilevskiy et al., 2018; Roozing et al., 2019; Ambrose and Ames, 2020). Combined parallel and serial elastic designs have been proposed, leading to reduced peak torques and improved locomotion applicability (Grimmer et al., 2012). Leg stiffness is altered mechanically in several ways; decoupling actuator and spring action during the locomotion cycle can simplify control and improve energy efficiency (Wiggin et al., 2011; Spröwitz et al., 2013). Variable elastic mechanisms augment physical stiffness for efficient actuation (Choi et al., 2011; Mathijssen et al., 2014; Braun et al., 2016). Until today, it remains challenging to effectively alter and rapidly manipulate compliance under high loads while keeping the mechanisms compact, robust, and lightweight.

Serial and parallel elastic-legged robots can locomote by feed-forward control and without system knowledge from feedback (Iida and Pfeifer, 2004; Narioka et al., 2012; Spröwitz et al., 2018; Ruppert and Spröwitz, 2019). However, passive, compliant designs are under-actuated and show limited controllability. Parallel elastic designs can maintain good control authority; when controllability is more needed than spring-based natural dynamics, the actuator overrides the spring's action (Verstraten et al., 2016). Usually, parallel elastic legs are designed with strong springs providing all essential torques and forces. Consequently, strong, relatively heavy, and fast actuators are required to override springs.

Legged robots with proprioceptive actuation and sensing and quasi-direct drives feature the highest control authority, compared to passive and partially actuated designs (Seok et al., 2012; Ding and Park, 2017; Park et al., 2017). These legged machines are agile and fast, they jump high, and land robustly (Park et al., 2017; Grimminger et al., 2020). From a sensorimotor perspective, proprioceptive actuators require 1) low communication and control delays in the range of a few milliseconds allowing 2) high-frequency control above 500 Hz, 3) accurate force and joint speed sensing, 4) and precise touch-down sensing (Bledt et al., 2018; Grimminger et al., 2020; Li et al., 2020). Not all conditions are always met, especially in unknown terrain and during harsh touch-downs, when actuator gains are changed, and when sensor noise indirectly causes feedback delays (Hubicki et al., 2016; Hammoud et al., 2020).

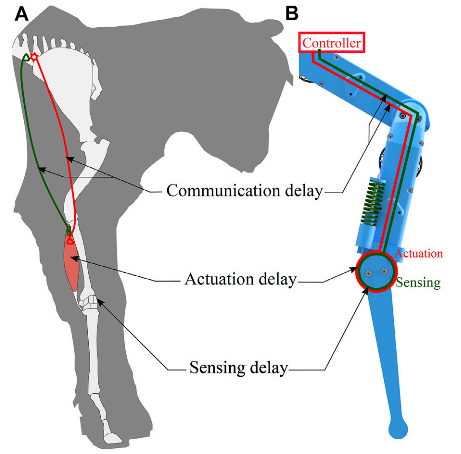

FIGURE 1 | (A) Animal locomotion control is subject to sensorimotor delays from sensing, communication, and actuation. The drawing is loosely inspired by Figure 1 of More and Donelan (2018). **(B)** Robots typically have lower intrinsic delays from electronic sensing and communication. Instead, delays are caused, for example, by filtering noisy data. We systematically tested robot controllers with varying sensorimotor delay and control frequency. We hypothesized that a hybrid system comprised of passive joint elasticity and parallel active joint stiffness can reject sensorimotor delays robustly, for appropriate compliance ratios.

Robot force sensors are affected by leg impacts loading legs from zero to multiple body weights in a few ten milliseconds, and leading to wobbling masses (Günther et al., 2003; Mo et al., 2020). Impact vibrations transfer to the sensor's mechanics and appear as sensor noise requiring processing (Spröwitz et al., 2018; Grimminger et al., 2020). Low-noise leg force sensors are being developed, yet there remains a trade-off between sensitivity and specificity, sensor noise from impacts, and sensor weight and complexity (Ananthanarayanan et al., 2012; Hutter et al., 2014; Grimminger et al., 2020; Ruppert and Badri-Spröwitz, 2020). Noisy force data can be filtered to identify touch-down and leg loading uniquely, but filtering adds to the overall sensorimotor delay; for example, delays of 31 ms are documented to uniquely identify touch down with proprioceptive sensing (Grimminger et al., 2020). Monitoring the deflection of physical joint elasticity provides alternative leg loading information, for example, for virtual model control (Pratt et al., 1997). Virtual damping assumes precise speed estimation, but numerically differentiating noisy signals requires filtering for sufficiently smooth signals, leading to feedback delay (Flacco et al., 2012; Hammoud et al., 2020).

Robot-internal electrical communication is limited only by the speed of light, and with relatively short wire lengths communication delays are minimal. Contrary, teleoperation between operator and legged robot over long-distance can lead to significant feedback delays (Varkonyi et al., 2014). Dedicated force feedback control can robustly deal with limited delays; beyond that, control destabilizes (Lee and Spong, 2006; Shafiee-Ashtiani et al., 2017; Shafiee et al., 2019). The applicability of high-level locomotion planners is related to control frequency and therefore also to sensorimotor delay; current planners run on time for control frequencies above 100 Hz (Ponton et al., 2018; Mastalli et al., 2020). Legged robots intrinsically tolerating low control frequencies are therefore good candidates for complex online locomotion planners.

Besides virtual and physical springs, both virtual and physical damping have been applied to control legged locomotion, also as part of impedance control (Seok et al., 2012; Boaventura et al., 2013; Nagayama et al., 2016; Park et al., 2017; Heim et al., 2020; Mo et al., 2020). By dissipating excess potential and kinetic energy and producing damping forces, leg reaction forces are adapted, and post-impact oscillations are reduced (Blickhan et al., 2007a; Haeufle et al., 2014; Semini et al., 2015). Virtual damping control requires precise speed estimation, which makes the method brittle in the presence of sensor noise (Bledt et al., 2018; Hammoud et al., 2020). Mechanical leg dampers are immune to feedback delays and sensor noise but must actively be switched off when not required (Mo et al., 2020).

In animals, upper limb control is subject to sensorimotor delays, like during manipulation tasks. Humans and other animals manipulate objects by exploiting muscle-tendon elasticities, effectively changing joint stiffness (Franklin et al., 2004). Antagonistic pairs of muscle-tendons can be prestressed by feed-forward ('preflex') control, leading to increased joint stiffness for a given posture independent from feedback delay, but with limited movement range (Hogan, 1984; Crevecoeur and Scott, 2014). Alternatively, reflexes can alter joint stiffness. Mouel and Brette (2019) show that increased joint stiffness should be compensated for by reduced sensorimotor gains; otherwise, delayed feedback leads to unstable behavior. Setting joint impedance through feed-forward sensorimotor commands might allow stable upper limb postures with noisy state estimation (Berret and Jean, 2020). Upper limb manipulation and lower limb locomotion tasks differ in their respective loading scenarios. Most manipulation tasks are continuous, while legged locomotion is always hybrid and non-continuous. Leg forces and loading times depend on body weight and drop height. The leg forces in this work ramp up from zero to body weights within 0.1 s and lead to joint angle changes above 45°. End-effector forces during manipulation are typically within the range of the object's weight instead of the user's body weight (Crevecoeur and Scott, 2014).

In this work, we aim to merge two diametrical principles while maintaining their best properties; 1) Passive leg joint compliance that works without feedback and at low control frequency, and 2) active joint compliance providing control authority. We hypothesize that, for a given robot design and locomotion task, there exists a range of compliance ratios—a 'hybrid' range—that works best despite significant feedback delays and low control frequencies.

This work uniquely contributes as follows; We systematically characterized the full range of active-to-passive parallel compliance ratios for a given total leg joint compliance. We simulate adverse controller conditions in simulated and hardware drop landings, including significant feedback delays, low control frequencies, and varying duty cycles. Previous work in parallel-elastic legged robotics typically investigated parallel compliance with high-frequency and low delay actuation (Mazumdar et al., 2016).

In **Section 2**, we present a stability analysis of a simplified model in the presence of sensorimotor delays, for two ratios of parallel compliance. We then present computer simulations and hardware experiments and investigate the effect of control frequencies, sensorimotor delays, and duty cycles on a robot leg with varying ratios of parallel compliance, for drop-landings (**Section 3**). We also characterize a simulated quadruped robot made of four of these legs, for multiple drop-landing heights. We discuss the work in **Section 4**, and conclude in **Section 5**.

2 MATERIALS AND METHODS

We quantify the total (sum of) system compliance as active compliance in parallel to passive (spring-based) compliance, acting at the knee joint (**Figure 1B**):

$$K_{\text{total}} = K_{\text{active}} + K_{\text{passive}} \tag{1}$$

where K_{passive} [Nm/rad] is the joint's passive rotational stiffness, K_{active} [Nm/rad] is the joint's active, virtual, rotational stiffness produced by the actuator. K_{total} [Nm/rad] is the summed up rotational joint stiffness. We define a 'compliance ratio' λ_{passive} as the ratio of passive stiffness and total stiffness:

$$\lambda_{\text{passive}} = K_{\text{passive}} \big/ K_{\text{total}} \tag{2}$$

Hence, for a compliance ratio $\lambda_{\text{passive}} = 0.1$ the knee spring supplies 10% of the knee torque to carry the robot, and the knee actuator supplies the remaining 90%. A λ_{passive} of 1.0 indicates a knee joint with a physical spring and no motor.

2.1 Theoretical Analysis of a Simplified, Reduced Model of an Actuated Pendulum

We analyzed a simplified system with parallel compliance, to analytically quantify the effects of sensorimotor delays. The reduced order model consists of a strut-like leg mounted as a single degree-of-freedom pendulum and represents a simplified robot lower leg (**Figure 4A**). The equations governing the pendulum motion are:

$$I\ddot{\theta} \; + \; mgL \cdot sin\left(\theta - \theta_0\right) + K_{\text{passive}}\left(\theta - \theta_0\right) + D\dot{\theta} = \tau_{\text{m}} \tag{3}$$

where $D = 0.14$ Nms/rad is the system damping, K_{passive} is the stiffness of the parallel compliant element, $L = 0.16$ m is the center of mass distance to the pivot point, $m = 0.5$ kg is the mass, $I = mL^2$ is the moment of inertia, g is the standard gravity, and θ_0 is the equilibrium joint angle of the relaxed spring. We set a total stiffness of $K_{\text{total}} = 1.15$ Nm/rad. The instantaneous joint angle is θ, and τ_{knee} is the knee joint control torque input, implemented as active compliance:

$$\begin{aligned} I\ddot{\theta} \ + mgL \cdot sin\left(\theta - \theta_0\right) + K_{\text{passive}}\left(\theta - \theta_0\right) + D\dot{\theta} \\ = -K_{\text{active}}\left(\theta_{\text{feedback}} - \theta_0\right) \end{aligned} \qquad (4)$$

where K_{active} is the active motor compliance. The sensor reads the joint angle θ_{feedback}. We assume a small enough angular deviation of the pendulum around the equilibrium point: $\sin(\theta - \theta_0) \simeq (\theta - \theta_0)$, which allows to write **Eq. 4** as a linear differential equation. We converted **Equation 4** to the Laplace domain and incorporated a fixed feedback time delay t_d of the control input (active compliance). The resulting closed-loop system transfer function can be presented in the frequency domain as:

$$\frac{\Theta_s}{\Theta_{ds}} = \frac{K_{\text{active}}e^{-t_d s} + mgL + K_{\text{passive}}}{s^2 I + Ds + K_{\text{active}}e^{-t_d s} + K_{\text{passive}} + mgL} \qquad (5)$$

We linearized the system's exponential time delay term with a third-order Padé approximation. A system pole analysis of this simple system provides an intuitive understanding of the effects of two compliance ratios for a given total joint stiffness on closed-loop stability, and for given sensorimotor delays.

2.2 Computer Simulation of Articulated Robot Legs

We characterized a single, articulated robot leg with hybrid joint compliance. Drop landings are one of the most challenging tasks due to high, impulse-like ground reaction forces, and nonlinear and hybrid leg loading. Drop landing is similar to a step response perturbation, which is a conventional control theory tool to characterize black box systems. We computer simulated the robot leg in PyBullet (Coumans and Bai, 2019), and performed extensive drop-landing simulations for a broad range of sensorimotor delays, duty cycle frequencies, and λ_{passive}. We simulated a single leg and a quadruped robot, both modified from the open-source quadruped robot Solo (Grimminger et al., 2020).

In **Figure 2**, we show the control and sensorimotor strategies tested. The black curve is the schematic, desired knee motor torque trajectory. The control frequency (step-like, brown line) is measured in commands per second. For reference, the control frequency of proprioceptive actuation in legged robots is often around 1 kHz, i.e., a cycle period takes $dt_{\text{control}} = \frac{1}{f} = 1$ ms. We are especially interested in investigating scenarios with control frequencies well below 1 kHz.

Torque is applied with three strategies; First, the activation duration $dt_{\text{activation}}$ is defined as the time period between control commands, i.e., $dt_{\text{activation}} = DC \times dt_{\text{control}}$. The activation duration lasts at least 1 ms and at most $\frac{1}{f}$. For $dt_{\text{activation,min}}$, the control command is applied for a period of 1 ms and then reset to zero. For $dt_{\text{activation,max}}$, the actuator will maintain its value until the control command is updated (**Figure 2A**, brown line). Second, we applied a sensorimotor delay to the control command (**Figure 2B**). Third, the force-activity relationship of muscles is not fully understood (Roberts and Gabaldón, 2008), and we included tests with varying duty cycles, defined as the fraction of dt_{control} with a non-zero actuator torque (**Figure 2C**).

The active compliance controller knee joint input is:

$$\tau_{\text{knee,motor}} = K_{\text{total}}\left(1 - \lambda_{\text{passive}}\right)\left(\theta_{\text{feedback,knee}} - \theta_{0,\text{knee}}\right) \qquad (6)$$

To simulate the spring in PyBullet, we implemented a knee joint spring torque:

$$\tau_{\text{knee,spring}} = K_{\text{total}}\left(\lambda_{\text{passive}}\right)\left(\theta_{\text{knee}} - \theta_{0,\text{knee}}\right) \qquad (7)$$

2.3 Setup Hardware Experiments

We modified a single leg of the eight degree-of-freedom (8-DOF), open-source, quadruped robot 'Solo' (Grimminger et al., 2020). The leg has two active degrees of freedom, one at the hip and one at the knee. Both leg segments are 0.16 m long, the lower leg mounts a semi-circular foot of 15 mm radius. A brushless motor (Antigravity MN4004-kv380, T-Motor) drives a two-stage belt transmission with an overall 9 : 1 gear ratio for each active joint. An optical encoder (AEDT-9810-T00, Avago) measures the motor's rotor position, which is recalculated into joint angles. We mounted physical springs in parallel to the knee joint (SWY 16.5–30 for $\lambda_{\text{passive}} = 1.0$, SWY 16.5–45 for $\lambda_{\text{passive}} = 0.67$, SWY 16.5–80 for $\lambda_{\text{passive}} = 0.37$, Misumi). The spring's tendon inserts into a knee joint pulley with radius 18.9 mm (**Figure 3B**). The spring mount allows rapid exchange of springs between experiments.

To simplify the touch-down scenario, the robot leg was dropped guided by a vertical rail (**Figure 3A**). The hip joint was constrained to follow half of the knee joint angle at all times, controlled by a position controller creating foot contact vertically below the hip joint. We recorded the vertical hip position with two draw-wire sensors (LX-PA-40, WayCon) mounted above and below the robot, to cancel out single sensor force bias. The hip position allows quantifying the robot's landing behavior and characterizing hybrid compliance. The hip position was sampled by an analog-to-digital (A/D) converter on the brushless motor driver board. The motor board sends motor position and vertical position data to the PC communication board, via a serial peripheral interface (SPI). The PC communication board connects the motor driver board via EtherCAT to a PC (Intel Xeon(R) W-2145 CPU, 3.7 GHz, 16 cores, 64 bit, 62.5 GB Ram, Ubuntu 18.04). We wrote a Python wrapper to control the robot. The Python wrapper timestamps and saves joint angles, motor currents, and hip height into a text file. We analyzed and plotted data in Matlab.

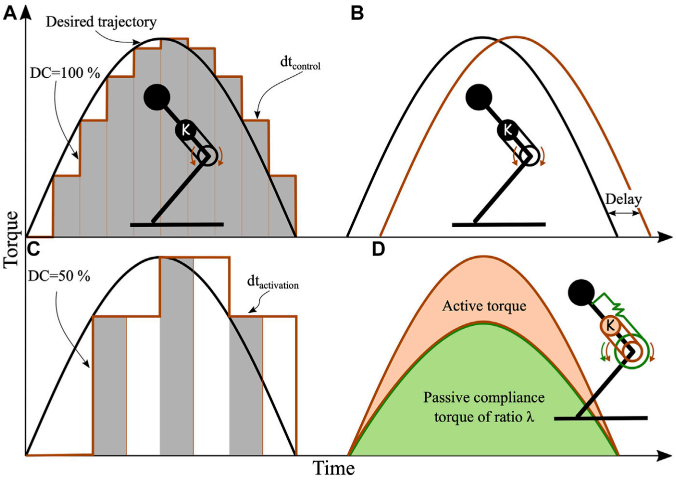

FIGURE 2 | Knee motor command for different combinations of control frequency, duty cycle, and sensorimotor delay. **(A)** A 100% duty cycle at low control frequency. **(B)** A set sensorimotor delay between the desired knee output torque, and the commanded output torque. **(C)** A 50% duty cycle. **(D)** An example for a compliance ratio of $\lambda_{passive} \approx 0.75$ is shown. The mechanical knee spring produces three quarter of the total knee torque (green). The knee actuator is programmed as a virtual spring producing the remaining torque (brown).

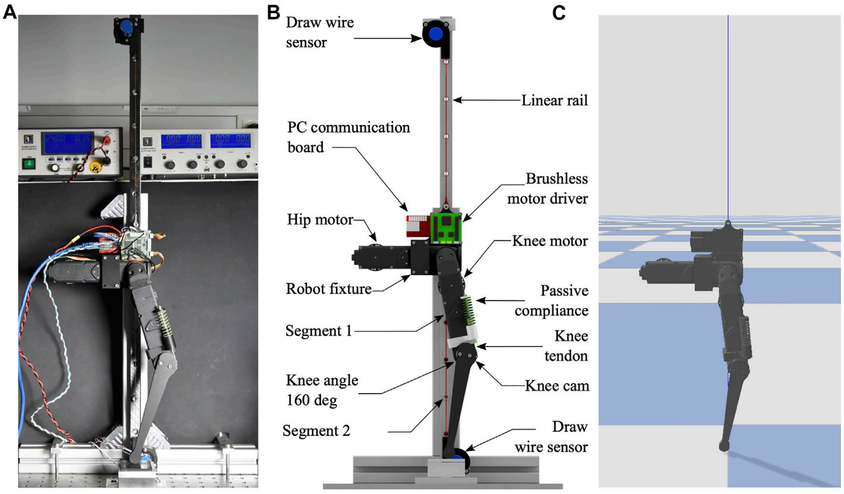

FIGURE 3 | Experimental setup. **(A)** The 2-DOF hybrid compliant leg. The one-directional spring (passive compliance) extends the knee joint via a knee tendon and a knee pulley. Knee springs with varying stiffness were mounted during the experiments, supporting between 0 and 100% robot's weight. A rail guides the robot's vertical drop, and a pair of potentiometers measures the robot's height. The knee motor produces torques in parallel to mounted knee spring. **(B)** Setup details, computer aided drawing. **(C)** The Unified Robot Description Format (URDF)-based model of the hybrid compliant robot leg, simulated in PyBullet.

3 RESULT

This section initially presents results from the pendulum task. We then show computer simulation results with a single robot leg and hybrid joint compliance. We simulated quadruped-robot drops from multiple heights, and we present hardware experiment results with a single leg mounted to a vertical slider.

3.1 Hanging Pendulum Analysis, Simplified Model

The pendulum pole analysis shows that for $\lambda_{\text{passive}} = 0$ and with increasing feedback delay, the dominant system poles move from their stable region toward the unstable region at the imaginary axis (**Figure 4B**). For medium compliance ratios, the rate of divergence is lower. The step response indicates that increasing the sensorimotor delay with active control ($\lambda_{\text{passive}} = 0.0$) leads to continuous oscillations, and resonance eventually destabilizes the system (**Figure 4C**). For hybrid passive compliance and a feedback delay of 20 ms, the closed-loop response is stable and smooth (**Figure 4D**).

The pendulum example is a simplification allowing a pole analysis with few parameters, but with an intuitive interpretation; **Figure 4B** shows when parameters lead to destabilization, with a clear cross-over into the unstable regime. The robot leg computer simulations in the following sections require more elaborate interpretation, but are more precise in terms of mechanics, and less simplified. Instead of continuous time analyses, time-discrete analyses are also applied for simplified systems, and we briefly provide results of a time-discrete analysis of the pendulum example in the **Supplementary Material section** for the interested reader.

3.2 Single-Leg Computer Simulation

We studied the effects of varying combinations of sensorimotor delay, control frequency, and compliance ratio λ_{passive} on controller performance during landing. We initially recorded a reference hip height trajectory dropping the robot leg with $\lambda_{\text{passive}} = 1.0$, which settled after 0.35 s at a hip height of 33 cm (**Figure 5**).

We then performed computer simulations to quantify the viability of the landing task, varying λ_{passive} from 0.0 to 1.0 in steps of 0.05, the sensorimotor delay from 0 to 60 ms in steps of 5 ms, and sensorimotor control frequencies of 20, 50, 100, 250, and 1,000 Hz. We tested duty cycles of 25, 50, and 100%.

In PyBullet, we set joint damping values of 0.01 Nms/rad and 0.05 Nms/rad for hip and knee, respectively. A single leg weighs 0.6 kg, and the quadruped robot 2.0 kg. We chose the total knee joint stiffness so that leg length changed by 10% during the first mid-stance, after dropping it from 42.5 cm. We implemented a $\lambda_{\text{passive}} = 1.0$ with a spring of stiffness $K = 4680$ N/m acting on the knee pulley of radius $r = 18.9$ mm, leading to a rotational stiffness of $Kr^2 = 1.67$ Nm/rad. We defined settling time as the difference between the initiated drop time and the hip position stabilizing within a ±1% margin of the settling hip height after 3 s simulation time. We applied the Matlab function *stepinfo* for this analysis. We used twice the $\lambda_{\text{passive}} = 1.0$ value as the global settling time (0.7 s) and defined 90% of the passive compliant $\lambda_{\text{passive}} = 1.0$ settling hip height as minimum final hip height (30 cm).

In **Figure 5**, the results of 273 drop-landing simulations are shown, with varying sensorimotor delays and λ_{passive} settings, a 100% duty cycle, and a control frequency of 1 kHz. Grey data points represent failed landings with a settling time higher than 0.7 s or too low settling hip heights. For full active actuation ($\lambda_{\text{passive}} = 0.0$), and when increasing the sensorimotor delay above 25 ms, all landings fail. For $\lambda_{\text{passive}} > 0.4$, the leg lands successfully in the presence of 40 ms delays. Results show that the hybrid compliant leg has successful intermediate regimes allowing for relatively large sensorimotor delays, with an appropriate combination of passive and active compliance.

We then investigated the effect of varying control frequency (20, 50, 100, 250, and 1,000 Hz) and duty cycle (25, 50, and 100%, **Figure 6**). Most visible is a decreasing feasible area for all three duty cycles at reduced control frequencies. Comparing duty cycles of 25 and 100% (**Figures 6A,C**) shows that the feasible area did change with reduced duty cycles. Low compliance ratios ($\lambda_{\text{passive}} \approx 0.2$) lead to successful landings combined with a duty cycle of 50% or the highest control frequency (1 kHz). **Figure 6C** shows that duty cycles of 100% at control frequencies of 100, 250, and 1,000 Hz have a similar-sized feasible region. When switching to a low control frequency (20 Hz, black line) the feasible area reduces much. For a 50% duty cycle, the feasible area changes slightly when switching between 50 and 250 Hz control frequency (**Figure 6B**). The biggest changes are visible when changing from 1,000 Hz to 250 Hz, and from 50 to 20 Hz. Typically, higher duty cycle values led to better results, for otherwise identical parameters. An exception is found when comparing duty cycles of 25 and 100%. The hatched area in **Figure 7A** indicates successful landings at low duty cycles, where high duty cycle landings failed because of hip height oscillations beyond the settling time limit (**Figure 7B**). For most compliance ratios above 0.6, we observe successful landings, including critical combinations of 60 ms delay and 20 Hz control frequency. All results indicate successful landing for compliance ratios equal and higher than 0.7.

3.3 Quadruped Computer Simulation

The previous single leg simulation results indicate that with high compliance ratio, robot performance becomes largely independent of sensorimotor delay, and control frequency. But fully passive compliance reduces control authority. In seven drop-landing scenarios, we altered drop height and passive and active stiffness of a quadruped robot, to characterize system and controller performance, but also to emphasize the importance of control authority (**Figure 8**). The duty cycle was set to 100% in all quadruped robot simulations. The simulation parameters are provided in **Table 1**.

The case-1 robot simulated a compliance ratio of 1.0, i.e., fully passive elastic knee joints. The robot was dropped from a height of 0.7 m and landed successfully. The case-2 robot used identical control parameters, was dropped from 1.0 m height, and failed to land successfully. At close observation it becomes visible that its knee joints inverted after the first landing rebound, and the robot landed with inverted knee angles and without spring support.

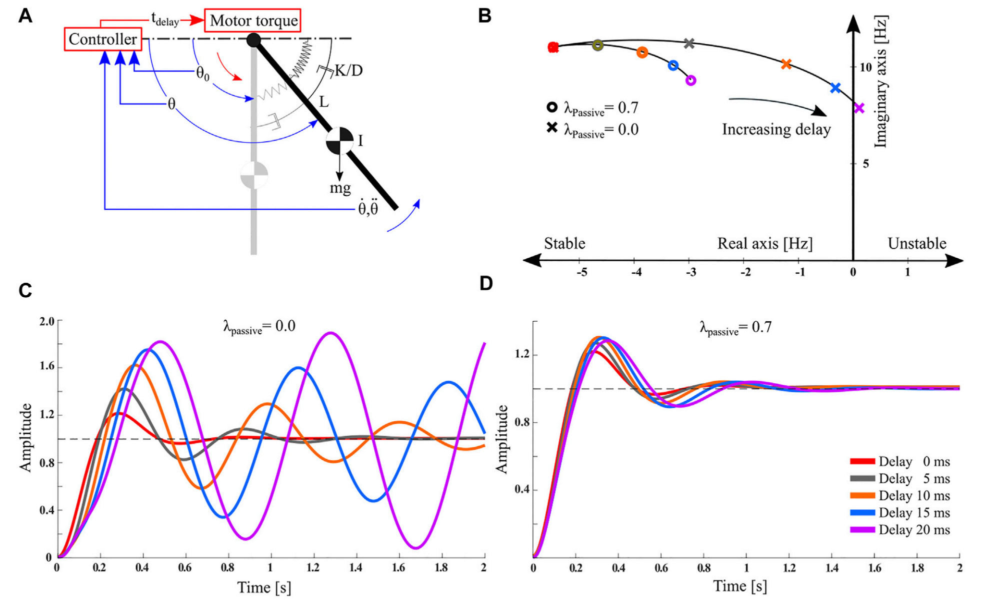

FIGURE 4 | Simulation results of a simplified, single-link pendulum mounted to a parallel motor-spring combination **(A)**. Parameters are provided in **Section 2.1**. **(B)** Graphical pole analysis of the actuated pendulum. The effects of varying delay and compliance ratios on the system stability are shown. **(C)** The system's step response for varying delays with $\lambda_{passive}$ = 0.0, and **(D)** $\lambda_{passive}$ = 0.7. The hybrid parallel compliance controller ($\lambda_{passive}$ = 0.7) is stable for all tested delays, and performs better compared to fully active actuation ($\lambda_{passive}$ = 0.0).

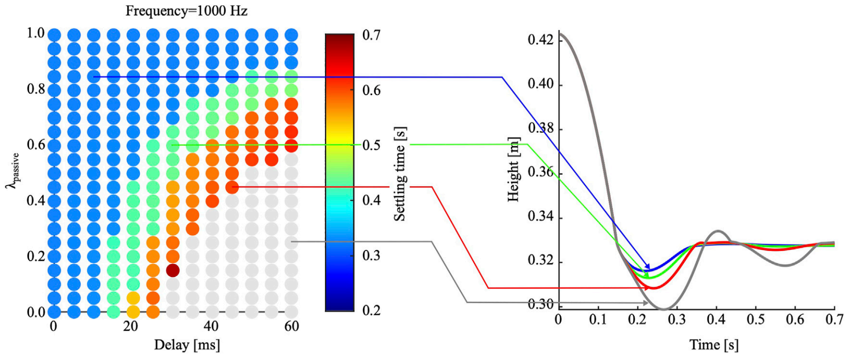

FIGURE 5 | Computer simulation results: 273 drops were simulated, for the robot leg controlled with a control frequency of 1,000 Hz and a duty cycle of 100%. The compliance ratio $\lambda_{passive}$ was varied between 0 and 1 in steps of 0.05, and the sensorimotor delay between 0 and 60 ms in steps of 5 ms. The grey data points and the grey hip height trajectory show failed landings with too large settling times. All colored data points and trajectories show successful landings. Successful landings are visible for sensorimotor delays up to 60 ms, in combination with compliance ratios of $\lambda_{passive}$ = 0.6 and above.

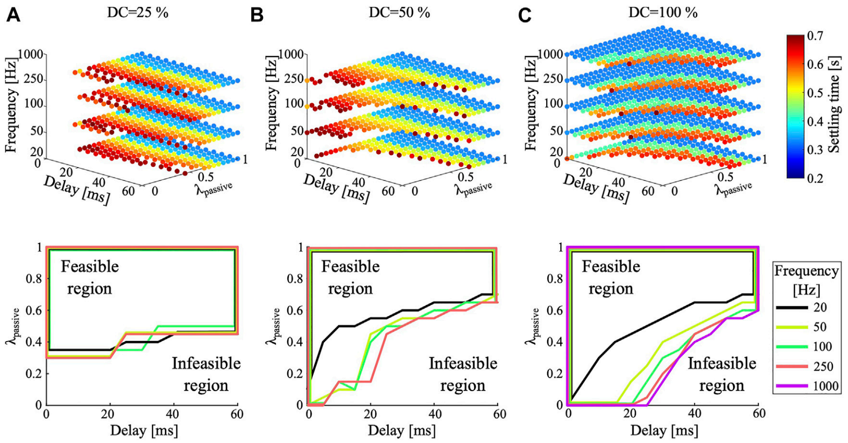

FIGURE 6 | Simulation results: Dropping the hybrid actuated robot leg from a height of 42.5 cm. Parameters varied are duty cycle (DC), control frequency, system delay, and compliance ratio ($\lambda_{passive}$). The reference landing performance is the top left data point in each plot. It presents the behavior of the fully passive leg ($\lambda_{passive}$ = 1.0). Plots for DC = 25% and DC = 50% show no data for 1,000 Hz; with a step time of 1 ms partial duty cycles are not possible.

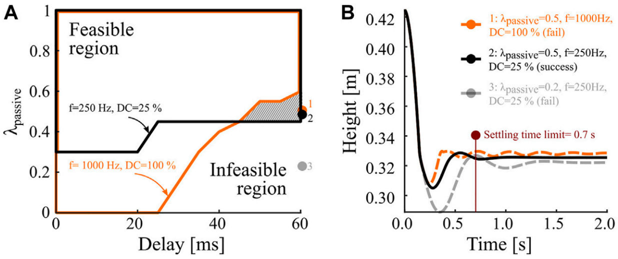

FIGURE 7 | For simulations with a 25% duty cycle and 60 ms feedback delay feasible solutions are visible for compliance ratios of λ = 0.5 **(B**, solid black). In the indicated overlapping parameter area **(A)**, the 100% duty cycle simulation fails with insufficient settling time **(B**, dashed orange).

Case-2 emphasizes the drawback of passive compliance; without control, the knee joint orientation cannot be adjusted prior to rebounding. The case-3 configuration featured a controller with full, bi-directionally active compliance (no passive compliance), and without sensorimotor delay. The controller ran at 1 kHz and successfully guided the landing. In case-4, a fully active compliant robot with 17 ms sensorimotor delay failed to land properly, which shows the vulnerability of active compliance in the presence of sensorimotor delay. Case-5 shows a successful landing scenario by combining passive and active compliance ($\lambda_{passive}$ = 0.67), with 27 ms sensorimotor delay, and reduced control frequency (200 Hz). Case-6 was also configured with a $\lambda_{passive}$ = 0.67, a control frequency of 100 Hz, and failed landing the robot. For case-7, we decreased the compliance ratio to $\lambda_{passive}$ = 0.59, and the robot landed successfully from a height of 1.2 m, and with a sensorimotor delay of 35 ms at a control frequency of 100 Hz. Case-7 shows how an appropriate combination of active and passive compliance at low control frequency maintains good control authority and robustness in the presence of sensorimotor delay.

3.4 Hardware Experiments

We validated the previous single-leg simulations with hardware experiments. We chose compliance ratios of $\lambda_{passive}$ = $[0, 0.37, 0.67, 1]$ and a total rotational knee stiffness of K_{total} = 1.67 Nm/rad. We then varied control frequencies ([1000, 100, 10]Hz) and sensorimotor delays ([0, 10, 20, 30, 50]ms). The duty cycle was set to 50% for 10

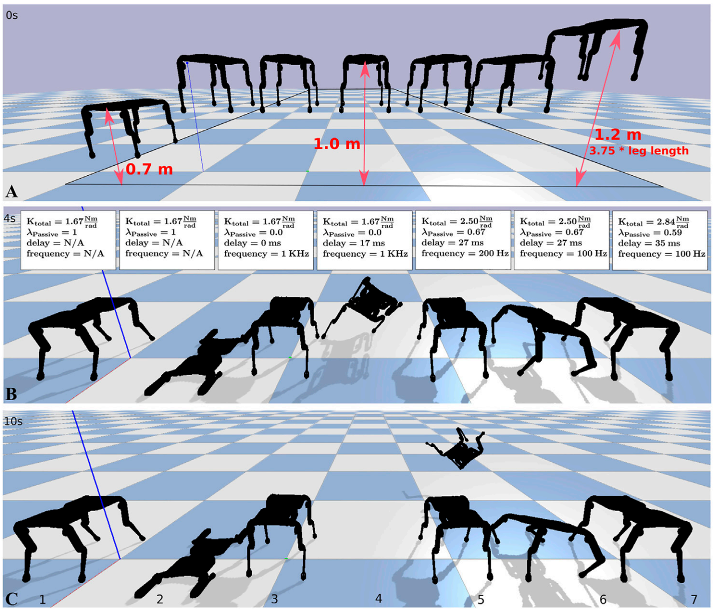

FIGURE 8 | Computer simulated quadruped robots landing, in seven different scenarios, controlled with a duty cycle of 100%. **(A)** The robot's initial drop heights are indicated with red arrows. **(B)** An intermediate robot state at 4 s simulation time. The panels also provide controller parameters. **(C)** Converged robot state after 10 s. Cases 1, 3, 5, and 7 landed successfully.

TABLE 1 | Simulation parameters of the quadrupedal robot, with a duty cycle of 100%.

Case	Total compliance (Nm/rad)	$\lambda_{passive}$ (%)	Control frequency (Hz)	Delay (ms)
1	1.6717	100	1,000	0
2	1.6717	100	1,000	0
3	1.6717	0	1,000	0
4	1.6717	0	1,000	17
5	2.5076	67	200	27
6	2.5076	67	100	27
7	2.8419	59	100	35

and 100 Hz control frequency, and 100% for 1,000 Hz control frequency.

In **Figure 9**, we assess the difference $e_{sim2real}$ between computer simulations and hardware experiments, as the root-mean-square error (RMSE) between two resulting hip trajectories, normalized by the maximum leg length, measured during the settling duration of 0.7 s. The criteria for successful drop landings in hardware and computer simulation are identical (**Section 3.2**). Grey colored data shows failure cases in both experiments and simulations. Viable cases with an RMSE of less than 6% (**Figure 9**) indicate good consistency between hardware experiment and computer simulation. We show four exemplary hip trajectories for varying compliance ratios (**Figure 9**, I–IV). The first two cases are feasible landings with good consistency between simulation and experiments. In case III, the hardware experiment stabilized at a lower-than-simulation hip height but still within the required margin. Case IV is a failed drop, and neither the hardware experiment nor the simulated robot leg showed the necessary settling behavior.

4 DISCUSSION

The single-leg drop results in **Figure 5** show a continuous and gentle decrease of system robustness with increasing feedback

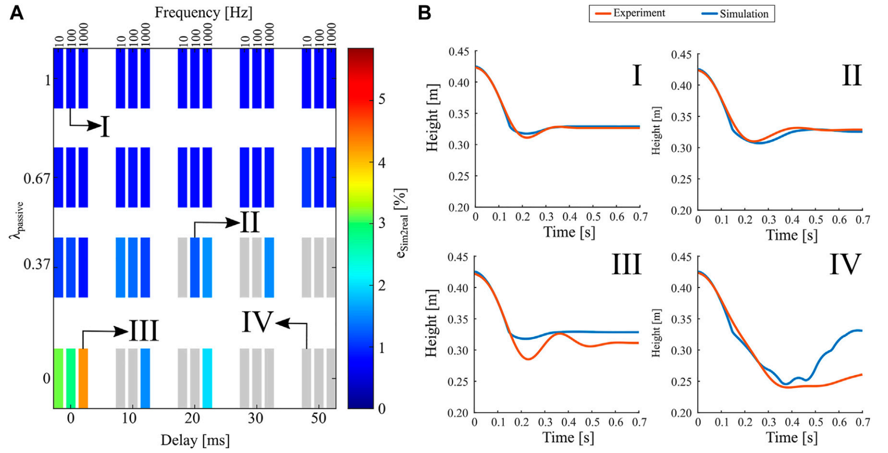

FIGURE 9 | Results comparing computer simulations and hardware experiments, as root-mean-square error of the instantaneous hip height normalized by the initial leg length. **(A)** Good similarities are shown as colored data patches. Grey data patches indicate unsuccessful drop experiments, violating settling time or final height criteria. **(B)** Hip trajectories. (I–III) Successful landings with short settling times and sufficient settling hip heights. (IV) An example of an unsuccessful landing in simulation and hardware.

delay when transitioning from a fully physically springy leg toward a fully actuated leg controlled by a virtual-spring controller. Hence, parallel structures of active compliance with the correct amount of passive compliance offer one possible answer to the question of how animals counteract perturbations in the presence of large sensorimotor delays. The ratio of passive to active compliance could be permanently set genetically, formed over a lifetime by training (Fouré et al., 2012), or set when required by partial or full recruitment of slacked muscle-tendon structures (Hogan, 1984). Legged robots equally benefit from intrinsic robustness against feedback delay. We believe that compliance ratios for other designs will depend on the specific leg and controller design parameters, the locomotion task, and the required controllability. If the available control frequency is limited or high delays are expected, a higher compliance ratio can be used. In the future, we are especially interested in exploring compliance rations of $\lambda_{passive} > 0.5$. One early design choice to consider is the effective spring deflection. Typically, stiffer springs feature a smaller deflection range possibly leading to limited joint movement range, compared to softer springs. We used springs designed for large deflections. One can also balance the knee cam radius with the spring's movement range and stiffness. We suggest the following, general procedure to establish a compliance ratio for a given task and robot:

1. Select a total joint stiffness based on the required steady state leg length, the maximum leg deflection, and the leg geometry (segment lengths, robot mass, cam radius). This step can be executed by test-mounting a $\lambda = 1$ spring (no actuator) with given stiffness and spring slack position, dropping the robot leg, and observing its joint angles.
2. Alternatively, a simplified kinematic model can provide an estimate of the steady-state leg length (**Supplementary Material Section 3**).
3. Select a desired compliance ratio. In the examples shown, compliance ratios between 0.5 and 0.7 worked well. Low compliance ratios provide higher controllability, as long as control frequencies are high and feedback delays are low, and vice versa. Duty cycles should be set to maximum (100%), unless they are specifically exploited.
4. Check that the parallel mounted actuator has the capacity to supply the required torque and speed. Low compliance ratios (≈ 0.5) require an actuator providing a higher work and power output throughout the task. With higher compliance ratios (> 0.7) the parallel spring carries more base load. When spring dynamics must be overwritten, high actuator torques are required but typically for shorter time. For a motor-gearbox design methodology we refer to Roos et al. (2006).

This work centers around adjusting the ratio of physical, passive compliance for a given total joint compliance. Online-adjustable spring stiffness mechanisms have been proposed, but many are still bulky and heavy (Yamaguchi and Takanishi, 1997; Vanderborght et al., 2013; Wolf et al., 2015). If a locomotion task requires large changes of total joint stiffness with a constant ratio of passive compliance (Ferris et al., 1998), robust and light-weight adjustable stiffness designs will be needed. For versatile locomotion sequences like jumping, landing and fast running, learning-based methods could extract a 'best' range of compliance ratios from large locomotion data sets.

We see at least three applications for hybrid compliance ratios in legged robots; 1) For legged robots which exploit natural dynamics of mechanical springs but require intermittent, high controllability for tasks like jumping or acceleration (Spröwitz et al., 2013; Lakatos et al., 2017). 2) For legged robots without access to high-frequency control or low-noise and low-latency sensors, which are expensive and time-consuming to develop (Nam et al., 2020). 3) For motion planners featuring update frequencies in the low sub-kilohertz range, in need of a legged robot with intrinsic robustness when controlled at these frequencies (Ponton et al., 2018).

5 CONCLUSION AND SUMMARY

We systematically characterized combinations of parallel mounted passive and active joint compliance for their ability to control the robot's leg length after landing. We tested against detrimental effects of significant feedback delays, low control frequencies, and low duty cycles in the full range of compliance ratios. Our goal was to find a compliance ratio for one given total knee compliance that works well with the above controller limitations. In comparison, previous work in parallel-elastic legged robotics typically investigated parallel compliance with high-frequency and low delay actuation (Batts et al., 2016; Mazumdar et al., 2016).

Our computer simulations show successful single-leg drop-landings for sensorimotor delays up to 60 ms, and control frequencies as low as 20 Hz in combination with a compliance ratio of $\lambda_{\text{passive}} = 0.7$. For a 'hybrid' setting between λ_{passive} 0.4 and 0.7; the partially active compliance ensures good control authority, and the remaining passive, spring-based compliance reacts immediately and independently from the controller. We verified single-leg computer simulations with hardware experiments for a range of parameters and showed good agreement between both.

We ran computer simulations of quadruped robots with varying total leg stiffness values when landing from multiple drop heights. Compliance ratios in the hybrid range (around 0.5) worked better in the presence of adverse controller settings (delays, control frequency) than active compliance, and allowed for the necessary amount of controllability compared to pure passive compliance. We finally note that the engineered compliance ratios were robustly handling feedback delays similar to the neuromuscular sensorimotor delays reported of running animals of equal size to the presented hybrid robot leg.

DATA AVAILABILITY STATEMENT

The raw data supporting the conclusion of this article will be made available by the authors, without undue reservation.

AUTHOR CONTRIBUTIONS

MA and AS contributed to the concept, robot design, experimental setup, simulation, and experimentation. AB-S developed the original hybrid active/passive compliant concept. All authors discussed the data, agreed with the presented results, and contributed to the writing.

ACKNOWLEDGMENTS

The authors thank the International Max Planck Research School for Intelligent Systems (IMPRS-IS) for supporting AAS. We thank Felix Grimminger and Jad Saud for support developing the robot leg and the spring mechanism, the Robotic ZWE for prototyping support, and Julian Viereck for providing the quadruped robot URDF file.

SUPPLEMENTARY MATERIAL

The Supplementary Material for this article can be found online at: https://www.frontiersin.org/articles/10.3389/frobt.2021.645748/full#supplementary-material

REFERENCES

AhmadSharbafi, M., Yazdanpanah, M. J., Ahmadabadi, M. N., and Seyfarth, A. (2020). Parallel Compliance Design for Increasing Robustness and Efficiency in Legged Locomotion-Theoretical Background and Applications. *IEEE/ASME Trans. Mechatronics*. doi:10.1109/TMECH.2020.3019686

Alexander, R. (1990). Three Uses for Springs in Legged Locomotion. *Int. J. Robotics Res.* 9, 53–61. doi:10.1177/027836499000900205

Ambrose, E., and Ames, A. D. (2020). Improved Performance on Moving-Mass Hopping Robots with Parallel Elasticity. *2020* IEEE Int. Conf. Robotics Automation (Icra) *(Ieee)*, 2457–2463. doi:10.1109/ICRA40945.2020.9197070

Ananthanarayanan, A., Foong, S., and Kim, S. (2012). A Compact Two DOF Magneto-Elastomeric Force Sensor for a Running Quadruped. 2012 *IEEE Int. Conf. Robotics Automation (Icra)*, 13981403. doi:10.1109/ICRA.2012.6225201

Batts, Z., Kim, J., and Yamane, K. (2016). Design of a Hopping Mechanism Using a Voice Coil Actuator: Linear Elastic Actuator in Parallel (LEAP). 2016 *IEEE Int. Conf. Robotics Automation (Icra)*, 655–660. doi:10.1109/ICRA.2016.7487191

Berret, B., and Jean, F. (2020). Stochastic Optimal Open-Loop Control as a Theory of Force and Impedance Planning via Muscle Co-contraction. *PLOS Comput. Biol.* 16, e1007414. doi:10.1371/journal.pcbi.1007414

Bertram, J. E. A., Gutmann, A., Randev, J., and Hulliger, M. (2014). Domestic Cat Walking Parallels Human Constrained Optimization: Optimization Strategies and the Comparison of normal and Sensory Deficient Individuals. *Hum. Mov. Sci.* 36, 154–166. doi:10.1016/j.humov.2014.05.008

Biewener, A. A. (1989). Scaling Body Support in Mammals: Limb Posture and Muscle Mechanics. *Science* 245, 45–48. doi:10.1126/science.2740914

Bledt, G., Wensing, P. M., Ingersoll, S., and Kim, S. (2018). Contact Model Fusion for Event-Based Locomotion in Unstructured Terrains. 2018 *IEEE Int. Conf. Robotics Automation (Icra)*, 4399–4406. doi:10.1109/ICRA.2018.8460904.ISSN: 2577-087X

Blickhan, R., Seyfarth, A., Geyer, H., Grimmer, S., Wagner, H., and Günther, M. (2007a). Intelligence by Mechanics. *Phil. Trans. R. Soc. A: Math. Phys. Eng. Sci.* 365, 199–220. doi:10.1098/rsta.2006.1911

Boaventura, T., Medrano-Cerda, G. A., Semini, C., Buchli, J., and Caldwell, D. G. (2013). *IEEE/RSJ International Conference on Intelligent Robots and Systems*

(IROS).Stability and Performance of the Compliance Controller of the Quadruped Robot Hyq

Braun, D. J., Apte, S., Adiyatov, O., Dahiya, A., and Hogan, N. (2016). Compliant Actuation for Energy Efficient Impedance Modulation. *2016 IEEE Int. Conf. Robotics Automation (Icra)*, 636–641. doi:10.1109/ICRA.2016.7487188

Calanca, A., Muradore, R., and Fiorini, P. (2015). A Review of Algorithms for Compliant Control of Stiff and Fixed-Compliance Robots. *IEEE/ASME Trans. Mechatronics* 21, 613–624. doi:10.1109/TMECH.2015.2465849

Choi, J., Hong, S., Lee, W., Kang, S., and Kim, M. (2011). A Robot Joint with Variable Stiffness Using Leaf Springs. *IEEE Trans. Robotics* 27, 229–238. doi:10.1109/TRO.2010.2100450

Coumans, E., and Bai, Y. (2019). Pybullet, a python Module for Physics Simulation for Games, Robotics and Machine Learning. Available at: http://pybullet.org.

Crevecoeur, F., and Scott, S. H. (2014). Beyond Muscles Stiffness: Importance of State-Estimation to Account for Very Fast Motor Corrections. *PLoS Comput. Biol.* 10, e1003869. doi:10.1371/journal.pcbi.1003869

Daley, M. A., Usherwood, J. R., Felix, G., and Biewener, A. A. (2006). Running over Rough Terrain: guinea Fowl Maintain Dynamic Stability Despite a Large Unexpected Change in Substrate Height. *J. Exp. Biol.* 209, 171–187. doi:10.1242/jeb.01986

Ding, Y., and Park, H.-W. (2017). Design and Experimental Implementation of a Quasi-Direct-Drive Leg for Optimized Jumping. 2017 *IEEE/RSJ Int. Conf. Intell. Robots Syst.* (Iros), 300–305.

Ernst, M., Götze, M., Blickhan, R., and Müller, R. (2018). Humans Adjust the Height of Their center of Mass within One Step when Running across Camouflaged Changes in Ground Level. *J. Biomech.* doi:10.1016/j.jbiomech.2018.12.036

Ferris, D. P., Louie, M., and Farley, C. T. (1998). Running in the Real World: Adjusting Leg Stiffness for Different Surfaces. *Proc. R. Soc. Lond. Ser. B: Biol. Sci.* 265, 989–994. doi:10.1098/rspb.1998.0388

Flacco, F., Luca, A. D., Sardellitti, I., and Tsagarakis, N. G. (2012). On-line Estimation of Variable Stiffness in Flexible Robot Joints. *Int. J. Robotics Res.* 31, 1556–1577. doi:10.1177/0278364912461813

Forssberg, H., Grillner, S., and Rossignol, S. (1977). Phasic Gain Control of Reflexes from the Dorsum of the Paw during Spinal Locomotion. *Brain Res.* 132, 121–139. doi:10.1016/0006-8993(77)90710-7

Fouré, A., Nordez, A., and Cornu, C. (2012). Effects of Eccentric Training on Mechanical Properties of the Plantar Flexor Muscle-Tendon Complex. *J. Appl. Physiol.*, 114, 523–537. Publisher: American Physiological Society. doi:10.1152/japplphysiol.01313.2011

Franklin, D. W., So, U., Kawato, M., and Milner, T. E. (2004). Impedance Control Balances Stability with Metabolically Costly Muscle Activation. In *J. Neurophysiol.*, 92. American Physiological Society, 3097–3105. doi:10.1152/jn.00364.2004.Publisher

Franklin, D. W., and Wolpert, D. M. (2011). 72. Publisher: Elsevier, 425–442. doi:10.1016/j.neuron.2011.10.006Computational Mechanisms of Sensorimotor Control*Neuron*

Grillner, S., and Wallen, P. (1985). Central Pattern Generators for Locomotion, with Special Reference to Vertebrates. *Annu. Rev. Neurosci.* 8, 233–261. doi:10.1146/annurev.ne.08.030185.001313

Grimmer, M., Eslamy, M., Gliech, S., and Seyfarth, A. (2012). A Comparison of Parallel-And Series Elastic Elements in an Actuator for Mimicking Human Ankle Joint in Walking and Running. In Robotics and Automation (ICRA), 2012 IEEE International Conference on. (IEEE), 2463–2470.

Grimminger, F., Meduri, A., Khadiv, M., Viereck, J., Wüthrich, M., Naveau, M., et al. (2020). An Open Torque-Controlled Modular Robot Architecture for Legged Locomotion Research. *IEEE Robotics Automation Lett.* 5, 3650–3657. doi:10.1109/LRA.2020.2976639

Gunther, F., Shu, Y., and Iida, F. (2015). Parallel Elastic Actuation for Efficient Large Payload Locomotion. *2015 IEEE Int. Conf. Robotics Automation (Icra)*, 823–828. doi:10.1109/ICRA.2015.7139273

Günther, M., Sholukha, V. A., Kessler, D., Wank, V., and Blickhan, R. (2003). Dealing with Skin Motion and Wobbling Masses in Inverse Dynamics. *J. Mech. Med. Biol.* 3, 309–335.

Haeufle, D. F. B., Günther, M., Wunner, G., and Schmitt, S. (2014). Quantifying Control Effort of Biological and Technical Movements: An Information-Entropy-Based Approach. *Phys. Rev. E* 89, 012716. doi:10.1103/PhysRevE.89.012716

Hammoud, B., Khadiv, M., and Righetti, L. (2020). *Impedance Optimization for Uncertain Contact Interactions through Risk Sensitive Optimal Control* arXiv: 2011.04684 [cs, eess].

Heim, S., Millard, M., Le Mouel, C., and Badri-Spröwitz, A. (2020). A Little Damping Goes a Long Way: a Simulation Study of How Damping Influences Task-Level Stability in Running. *Biol. Lett.* 16, 20200467. doi:10.1098/rsbl.2020.0467Publisher: Royal Society

Hogan, N. (1984). Adaptive Control of Mechanical Impedance by Coactivation of Antagonist Muscles. *IEEE Trans. automatic Control* 29, 681–690. Publisher: IEEE.

Hubicki, C., Grimes, J., Jones, M., Renjewski, D., Spröwitz, A., Abate, A., et al. (2016). ATRIAS: Design and Validation of a Tether-free 3D-Capable spring-mass Bipedal Robot. *Int. J. Robotics Res.* 35, 1497–1521. doi:10.1177/0278364916648388

Hutchinson, J. R., Anderson, F. C., Blemker, S. S., and Delp, S. L. (2005). Analysis of Hindlimb Muscle Moment Arms in Tyrannosaurus rex Using a Three-Dimensional Musculoskeletal Computer Model: Implications for Stance, Gait, and Speed. *Paleobiology* 31, 676–701. doi:10.1666/04044.1

Hutter, M., Gehring, C., Hopflinger, M., Blosch, M., and Siegwart, R. (2014). Toward Combining Speed, Efficiency, Versatility, and Robustness in an Autonomous Quadruped. *IEEE Trans. Robotics* 1–14. doi:10.1109/TRO.2014.2360493 PP,

Hutter, M., Gehring, C., Jud, D., Lauber, A., Bellicoso, C. D., Tsounis, V., et al. (2016). Anymal-a Highly mobile and Dynamic Quadrupedal Robot. *2016 IEEE/RSJ Int. Conf. Intell. Robots Syst. (Iros) (Ieee)*, 38–44.

Hutter, M., Remy, C. D., Hoepflinger, M. A., and Siegwart, R. (2011). Scarleth: Design and Control of a Planar Running Robot. In 2011 IEEE/RSJ International Conference on Intelligent Robots and Systems (IEEE), 562–567. doi:10.1142/9789814415958_0062

Iida, F., and Pfeifer, R. (2004). Cheap Rapid Locomotion of a Quadruped Robot: Self-Stabilization of Bounding Gait. *Intell. Autonomous Syst.* 8, 642–649.

Ijspeert, A. J. (2008). Central Pattern Generators for Locomotion Control in Animals and Robots: A Review. *Neural Networks* 21, 642–653. doi:10.1016/j.neunet.2008.03.014

Lakatos, D., Friedl, W., and Albu-Schaffer, A. (2017). Eigenmodes of Nonlinear Dynamics: Definition, Existence, and Embodiment into Legged Robots with Elastic Elements. *IEEE Robotics Automation Lett.* 1–1. doi:10.1109/LRA.2017.2658018

Lee, D., and Spong, M. W. (2006). Passive Bilateral Teleoperation with Constant Time Delay. *IEEE Trans. robotics* 22, 269–281. (Publisher: IEEE.

Li, C., Ding, Y., and Park, H.-W. (2020). Centroidal-momentum-based Trajectory Generation for Legged Locomotion. *Mechatronics* 68, 102364. doi:10.1016/j.mechatronics.2020.102364

Liu, X., Rossi, A., and Poulakakis, I. (2018). A Switchable Parallel Elastic Actuator and its Application to Leg Design for Running Robots. *IEEE/ASME Trans. Mechatronics* 23, 2681–2692. doi:10.1109/TMECH.2018.2871670

Lombard, W. P. (1903). The Tendon Action and Leverage of Two-Joint Muscles of the Hind Leg of the Frog, with Special Reference to the spring Movement. In Contributions to medical research. Ann Arbor: Wahr, 280–301.

Mastalli, C., Budhiraja, R., Merkt, W., Saurel, G., Hammoud, B., Naveau, M., et al. (2020). Crocoddyl: An Efficient and Versatile Framework for Multi-Contact Optimal Control. In 2020 IEEE International Conference on Robotics and Automation (ICRA), 2536–2542. doi:10.1109/ICRA40945.2020.9196673.ISSN:2577-087X

Mathijssen, G., Furnemont, R., Brackx, B., Van Ham, R., Lefeber, D., and Vanderborght, B. (2014). Design of a Novel Intermittent Self-Closing Mechanism for a MACCEPA-Based Series-Parallel Elastic Actuator (SPEA). 2014 *IEEE/RSJ Int. Conf. Intell. Robots Syst. (IROS 2014)*, 2809–2814. doi:10.1109/IROS.2014.6942947

Mazumdar, A., Spencer, S. J., Hobart, C., Salton, J., Quigley, M., Wu, T., et al. (2016). Parallel Elastic Elements Improve Energy Efficiency on the STEPPR Bipedal Walking Robot. *IEEE/ASME Trans. Mechatronics* 1–1. doi:10.1109/TMECH.2016.2631170

Mo, A., Izzi, F., Haeufle, D. F. B., and Badri-Spröwitz, A. (2020). Effective Viscous Damping Enables Morphological Computation in Legged Locomotion. *Front. Robotics AI* 7. doi:10.3389/frobt.2020.00110

More, H. L., and Donelan, J. M. (2018). Scaling of Sensorimotor Delays in Terrestrial Mammals. *Proc. R. Soc. B: Biol. Sci.* 285, 20180613. doi:10.1098/rspb.2018.0613

More, H. L., Hutchinson, J. R., Collins, D. F., Weber, D. J., Aung, S. K., and Donelan, J. M. (2010). Scaling of Sensorimotor Control in Terrestrial Mammals. *Proc. R. Soc. B: Biol. Sci.* 277, 3563–3568. doi:10.1098/rspb.2010.0898

Mouel, C. L., and Brette, R. (2019). Anticipatory Coadaptation of Ankle Stiffness and Sensorimotor Gain for Standing Balance. *PLOS Comput. Biol.*, 15. e1007463, 2019 . Publisher: Public Library of Science. doi:10.1371/journal.pcbi.1007463

Nagayama, T., Ishihara, H., Tomori, H., Yamada, Y., and Nakamura, T. (2016). Vertical Jumping Motion Simulation with Consideration for landing Using a Monopedal Robot with Artificial Muscles and Magnetorheological Brakes. *IECON 2016 - 42nd Annu. Conf. IEEE Ind. Elect. Soc.*, 660–665. doi:10.1109/IECON.2016.7794022

Nam, H., Xu, Q., and Hong, D. (2020). A Reliable Low-Cost Foot Contact Sensor for Legged Robots. *2020 17th Int. Conf. Ubiquitous Robots (Ur)*, 219–224. doi:10.1109/UR49135.2020.9144878.ISSN:2325-033X

Narioka, K., Rosendo, A., Spröwitz, A., and Hosoda, K. (2012). Development of a Minimalistic Pneumatic Quadruped Robot for Fast Locomotion. In Proceedings of IEEE International Conference on Robotics and Biomimetics (ROBIO). Guangzhou, China, 307–311. doi:10.1109/ROBIO.2012.6490984

Nasiri, R., Khoramshahi, M., Shushtari, M., and Ahmadabadi, M. N. (2016). Adaptation in Variable Parallel Compliance: Towards Energy Efficiency in Cyclic Tasks. *IEEE/ASME Trans. Mechatronics* 22, 1059–1070. doi:10.1109/TMECH.2016.2637826

Niehues, T. D., Rao, P., and Deshpande, A. D. (2015). Compliance in Parallel to Actuators for Improving Stability of Robotic Hands during Grasping and Manipulation. *Int. J. Robotics Res.* 34, 256–269. doi:10.1177/0278364914558016

Park, H.-W., Wensing, P. M., and Kim, S. (2017). High-speed Bounding with the MIT Cheetah 2: Control Design and Experiments. *Int. J. Robotics Res.* doi:10.1177/02783649176942440278364917694244

Plooij, M., Wisse, M., and Vallery, H. (2016). Reducing the Energy Consumption of Robots Using the Bidirectional Clutched Parallel Elastic Actuator. *IEEE Trans. Robotics* 32, 1512–1523. doi:10.1109/TRO.2016.2604496

Ponton, B., Herzog, A., Del Prete, A., Schaal, S., and Righetti, L. (2018). On Time Optimization of Centroidal Momentum Dynamics. *2018* IEEE Int. Conf. Robotics Automation (Icra) *(Ieee)*, 5776–5782.

Pratt, J., Dilworth, P., and Pratt, G. (1997). Virtual Model Control of a Bipedal Walking Robot. *1997 IEEE Int. Conf. Robotics Automation, Proc.* 1, 193–198. doi:10.1109/ROBOT.1997.620037

Pratt, J. E., and Krupp, B. T. (2004). Series Elastic Actuators for Legged Robots. In Unmanned Ground Vehicle Technology Vi, 5422 (Orlando, FL: International Society for Optics and Photonics), 135–144.

Raibert, M. H., Brown Jr, H. B., and Murthy, S. S. (1984). Machines that Walk. In Robotics and Artificial Intelligence. Springer, 345–364.

Roberts, T. J., and Gabaldón, A. M. (2008). Interpreting Muscle Function from EMG: Lessons Learned from Direct Measurements of Muscle Force. *Integr. Comp. Biol.* 48, 312–320. doi:10.1093/icb/icn056

Robinson, D. W., Pratt, J. E., Paluska, D. J., and Pratt, G. A. (1999). Series Elastic Actuator Development for a Biomimetic Walking Robot. In 1999 IEEE/ASME International Conference on Advanced Intelligent Mechatronics (Cat. No. 99TH8399). IEEE, 561–568.

Roos, F., Johansson, H., and Wikander, J. (2006). Optimal Selection of Motor and Gearhead in Mechatronic Applications. *Mechatronics* 16, 63–72. doi:10.1016/j.mechatronics.2005.08.001

Roozing, W., Ren, Z., and Tsagarakis, N. G. (2019). An Efficient Leg with Series–Parallel and Biarticular Compliant Actuation: Design Optimization, Modeling, and Control of the Eleg. *Int. J. Robotics Res.* doi:10.1177/02783649198937620278364919893762

Ruppert, F., and Badri-Spröwitz, A. (2020). FootTile: a Rugged Foot Sensor for Force and Center of Pressure Sensing in Soft Terrain. In 2020 IEEE International Conference on Robotics and Automation (ICRA). IEEE, 4810–4816. doi:10.1109/ICRA40945.2020.9197466

Ruppert, F., and Spröwitz, A. (2019). Series Elastic Behavior of Biarticular Muscle-Tendon Structure in a Robotic Leg. *Front. neurorobotics* 13, 64. doi:10.3389/fnbot.2019.00064

Semini, C., Barasuol, V., Boaventura, T., Frigerio, M., Focchi, M., Caldwell, D. G., et al. (2015). Towards Versatile Legged Robots through Active Impedance Control. *Int. J. Robotics Res.* doi:10.1177/02783649155788390278364915578839

Seok, S., Wang, A., Otten, D., and Kim, S. (2012). Actuator Design for High Force Proprioceptive Control in Fast Legged Locomotion. In 2012 IEEE/RSJ International Conference on Intelligent Robots and Systems (IROS). 1970–1975. doi:10.1109/IROS.2012.6386252

Shafiee, M., Romualdi, G., Dafarra, S., Chavez, F. J. A., and Pucci, D. (2019). Online Dcm Trajectory Generation for Push Recovery of Torque-Controlled Humanoid Robots. In 2019 IEEE-RAS 19th International Conference on Humanoid Robots (Humanoids). IEEE, 671–678. doi:10.1109/Humanoids43949.2019.9034996

Shafiee-Ashtiani, M., Yousefi-Koma, A., and Shariat-Panahi, M. (2017). Robust Bipedal Locomotion Control Based on Model Predictive Control and Divergent Component of Motion. In 2017 IEEE International Conference on Robotics and Automation (ICRA). IEEE, 3505–3510. doi:10.1109/ICRA.2017.7989401

Spröwitz, A. T., Tuleu, A., Ajallooeian, M., Vespignani, M., Möckel, R., Eckert, P., et al. (2018). Oncilla Robot: A Versatile Open-Source Quadruped Research Robot with Compliant Pantograph Legs. *Front. Robotics AI* 5. doi:10.3389/frobt.2018.00067

Spröwitz, A., Tuleu, A., Vespignani, M., Ajallooeian, M., Badri, E., and Ijspeert, A. J. (2013). Towards Dynamic Trot Gait Locomotion: Design, Control, and Experiments with Cheetah-Cub, a Compliant Quadruped Robot. *Int. J. Robotics Res.* 32, 932–950. doi:10.1177/0278364913489205

Stratmann, P., Albu-Schäffer, A., and Jörntell, H. (2018). Scaling Our World View: How Monoamines Can Put Context into Brain Circuitry. *Front. Cell Neurosci.* 12. doi:10.3389/fncel.2018.00506

Takakusaki, K., Chiba, R., Nozu, T., and Okumura, T. (2016). Brainstem Control of Locomotion and Muscle Tone with Special Reference to the Role of the Mesopontine Tegmentum and Medullary Reticulospinal Systems. *J. Neural Transm.* 123, 695–729. doi:10.1007/s00702-015-1475-4

Toxiri, S., Calanca, A., Ortiz, J., Fiorini, P., and Caldwell, D. G. (2018). A Parallel-Elastic Actuator for a Torque-Controlled Back-Support Exoskeleton. *IEEE Robotics Automation Lett.* 3, 492–499. doi:10.1109/LRA.2017.2768120

Vanderborght, B., Albu-Schaeffer, A., Bicchi, A., Burdet, E., Caldwell, D. G., Carloni, R., et al. (2013). Variable Impedance Actuators: A Review. *Robotics Autonomous Syst.* 61, 1601–1614. doi:10.1016/j.robot.2013.06.009

Varkonyi, T. A., Rudas, I. J., Pausits, P., and Haidegger, T. (2014). Survey on the Control of Time Delay Teleoperation Systems. In IEEE 18th International Conference on Intelligent Engineering Systems INES 2014. IEEE, 89–94. doi:10.1109/INES.2014.6909347

Verstraten, T., Beckerle, P., Furnémont, R., Mathijssen, G., Vanderborght, B., and Lefeber, D. (2016). Series and Parallel Elastic Actuation: Impact of Natural Dynamics on Power and Energy Consumption. *Mechanism Machine Theor.* 102, 232–246.

Wiggin, M., Sawicki, G., and Collins, S. (2011). An Exoskeleton Using Controlled Energy Storage and Release to Aid Ankle Propulsion. In 2011 IEEE International Conference on Rehabilitation Robotics (ICORR). 1–5. doi:10.1109/ICORR.2011.5975342

Wolf, S., Grioli, G., Friedl, W., Grebenstein, M., Hoeppner, H., Burdet, E., et al. (2015). *Variable Stiffness Actuators: Review on Design and Components*. IEEE/ASME Transactions on Mechatronics. 1. doi:10.1109/TMECH.2015.2501019

Yamaguchi, J., and Takanishi, A. (1997). Design of Biped Walking Robots Having Antagonistic Driven Joints Using Nonlinear spring Mechanism. In , Proceedings of the 1997 IEEE/RSJ International Conference on Intelligent Robots and Systems, 1997. IROS '97. vol. 1, 251–259 vol.1. doi:10.1109/IROS.1997.649062

Yesilevskiy, Y., Gan, Z., and David Remy, C. (2018). Energy-optimal Hopping in Parallel and Series Elastic One-Dimensional Monopeds. *J. Mech. Robotics* 10. doi:10.1115/1.4039496

Yesilevskiy, Y., Gan, Z., and Remy, C. D. (2016). Optimal Configuration of Series and Parallel Elasticity in a 2D Monoped. In 2016 IEEE International Conference on Robotics and Automation (ICRA). 1360–1365. doi:10.1109/ICRA.2016.7487269

Conflict of Interest: The authors declare that the research was conducted in the absence of any commercial or financial relationships that could be construed as a potential conflict of interest.

5 An Open Source Modular Treadmill for Dynamic Force Measurement with Load Dependant Range Adjustment

An Open Source Modular Treadmill for Dynamic Force Measurement with Load Dependant Range Adjustment

Alborz Aghamaleki Sarvestani[1], Felix Ruppert[1], and Alexander Badri-Spröwitz

Abstract— **Ground reaction force sensing is one of the key components of gait analysis in legged locomotion research. In order to measure continuous force data during locomotion we present a novel compound instrumented treadmill design. The treadmill is 1.7 m long, with a natural frequency of 170 Hz and an adjustable range that can be used for humans and small robots alike. Here, we present the design methodology for the treadmill and characterize the treadmill in its natural frequency, noise behavior and real life performance. Additionally, we contribute an ISO 376 norm conform calibration procedure for all spatial force directions and center of pressure position. We achieve a force accuracy of ≤ 5.6 N for the ground reaction forces and ≤ 13 mm in center of pressure position.**

I. INTRODUCTION

In biomechanics and locomotion research one keystone data is ground reaction force data [1][cite me harder]. Ground reaction force (GRF) data enables locomotion research in humans and animals [1, 2], where no internal measurement of dynamics is possible. In robotic research, ground reaction forces can be used to validate bio-inspired leg designs [3, 4] as well as control designs [5, 6].

The gold standard sensor modality for locomotion research are stationary force plates [7]. While force plates are a great tool to measure the forces exerted onto the floor during a step, their major drawback is, that they can only capture one step due to their stationary nature and small size. Solutions to this problem are either wearable sensor solutions [8, 9] or force plates with moving substrate [10].

By incorporating force sensors into a treadmill, continuous data can be captured. With a split-belt treadmill, where each foot steps on its own treadmill, gaits with double stance phases can be characterized [11]. Even treadmills with three belts can be realized [12].

The driving factor in the design of force sensors is the natural frequency of the sensor as well as the whole measuring system. The high natural frequency is required, so that the treadmill does not oscillate in the frequency spectrum examined in gait analysis, usually ≈ 30 Hz (cite???).This is especially important when measuring subjects with a low body mass like rodents or small robots [13]. To adapt to the different requirements for light and heavy subjects, different size treadmills can be implemented (cite??). However, different implementations increase the cost drastically since two systems have to be manufactured.

Instrumented treadmills, that were previously reported, can be divided into categories based on several criteria. The sensor concept commonly used are strain gauge sensors [14–16]. While strain gauge sensors a good solution to measure static loads, piezo based sensors are more suited for measuring dynamic load under high static pre-load [17]. While piezo sensors are more expensive, they are stiffer, because the deflection measured in the force transducer is on an atomic level. The higher stiffness also enables piezo sensors to measure extremly fast signals above 1 kHz due to their higher natural frequency.

An alternative, simpler solution is to place a recreational treadmill on top of factory made force plates [10, 18]. While the effort in design and production is small, store bought treadmills with plywood surfaces can not provide the stiffness and rigidity needed to measure forces with high temporal solutions.

A general design decision is the placement of components with respect to the force sensors. To reduce weight, the motor can be placed outside the treadmill and connected with a flexible drive shaft to minimize motor vibrations in the sensor signal [14]. Alternatively the motor can be placed on top of the force sensors so the sensors are the only connection of the treadmill to the ground [17, 18]. While an external motor reduces weight, it is also a parasitic connection to the ground that can degrade the sensor signal since not all forces are recorded through the force sensor.

In addition to ground reaction forces, the center of pressure (COP) is an important measurement in legged locomotion research [19–21]. The COP describes the point where the GRF vector applies on the foot [19]. In order to calculate the COP from the force vectors of the individual sensors an accurate measuring system is required. Both the force data, as well as the dimensions of the treadmill have to have a high accuracy to achieve accurate COP estimations [22].

To calibrate the instrumented treadmill, several different methods have been reported. A straight forward way is to use calibrated dead weights to compare the sensor output [10, 12, 14, 16]. While this method is simple to implement and norm conform, it only allows calibration in the vertical direction. To calibrate all three force directions an instrumented stick with a force sensor can be used [18]. With this method, application of forces in three dimensions is possible but since the stick is pushed manually, the results are not reproducible which is mandatory in norm conform calibration. The calibration results are therefore not comparable in between different treadmill designs.

---

[1] The authors contributed equally to the paper

Dynamic Locomotion Group, Max Planck Institute for Intelligent Systems, Stuttgart, Germany

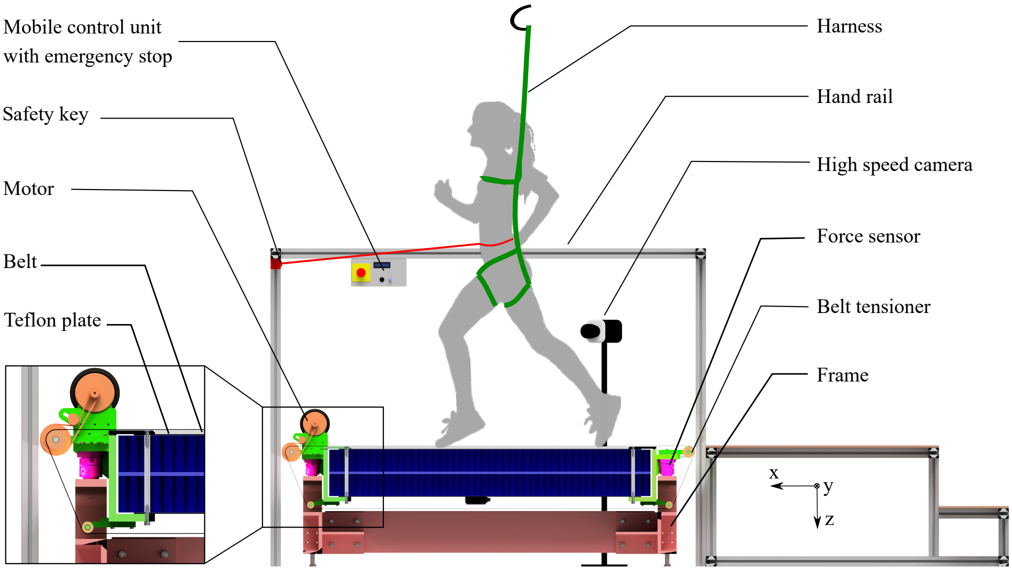

Fig. 1: Cut view of the treadmill render with base frame (red), force sensors (purple), compound plate fixture (green), actuation (orange), compound plate consisting of sandwich plate (dark blue), carbon fiber plate (light blue) handrail (grey) and mobile control unit with emergency stop and treadmill safety key (red) on top. The compound plate, fixture and actuator are floating on the force sensors to ensure that all internal forces are measured. The hand rail is not connected to the treadmill to not compromize the natural frequency.

In this paper we present an open source, modular, instrumented treadmill with a compound plate. We first provide a framework to estimate the natural frequency of a similar system for different geometric design parameters. To achieve maximum stiffness at reduced weight we design a novel compound surface structure made from aluminium and carbon fiber. We then quantify the treadmill, showing improved natural frequency, noise behavior and accuracy in force and center of pressure sensing. We also present a norm conform protocol to calibrate treadmills based on international norms and standards. Last we showcase the ability of our treadmill to measure ground reaction forces over a wide measuring range. We evaluate the treadmill performance for a small robot of 4 kg as well as a human subject of 90 kg body weight.
The novelty of this work is fourfold:

- We present a design methodology for achieving high natural frequencies based only on the dimensions of the surface area. We validate our approach and achieve a natural frequency only 4% off the model calculation. The high required stiffness is achieved through a compound surface structure made from an aluminium honey comb plate and carbon fiber plates for increased tensile strength.
- We present a modular, compound, instrumented treadmill design. The high natural frequency with adjustable range enables the use for heavy subjects (90 kg human) as well as for small, light subjects (5 kg robot)
- We present a calibration routine that is conform with ISO 376 and DKD 3-3 to achieve accurate and reproducible calibration results that are not possible with previously presented approaches. Our calibration approach allows a standardized comparison of different treadmill designs.
- We present a calibration method to increase the COP measurement on the treadmill through a reproducible calibration that increases the COP accuracy to less than 1 mm. We showcase the importance of this calibration approach in scenarios where the sensor plane and the surface plane are not in the same plane.

II. TOOLS AND METHODS

A. *Mechanical Design*

The basic concept of this instrumented treadmill (Figure 1) is to float all moving parts that are in contact with the treadmill surface on top of the force sensors. In this design all forces from the actuator and the measuring forces are recorded. The treadmill is constructed so that two treadmills can be placed side by side to form a split belt treadmill with a belt gap of 44 mm. The treadmill base consists of a frame made from steel and longitudinal aluminium profiles. The frame acts as the fixture point for the force sensors. Additionally the heavy

TABLE I: Comparison of key features for different instrumented treadmills presented in literature.

Parameter	Belli [17]	Bundle [14]	Collins [18]	Kram [10]	Paolini [12]	Verkerke [16]	Sarvestani et. al.
Natural frequency [Hz]	58 Hz	113 Hz	41 Hz	87 Hz	210 Hz	120 Hz	170 Hz
Sensor type	Piezo	Strain gauge	Strain gauge	Strain gauge	-	Strain gauge	Piezo
Sample rate [Hz]	800	2000	1200	1000	1080	100	10 000
Noise	5 N at 17 Hz	-	50 N at 40 Hz	80 N at 46 Hz	5.1 N std. dev.	-	6 N at 70 Hz
Floating mass [kg]	250	-	140	90	-	-	45
Calibration	Instrumented leg	Weight	Instrumented pole	Weight	Weight	Weight	ISO 376 and DKD 3-9 conform in all spatial directions.

TABLE II: Maximum force ranges and resolutions for different amplifier settings

Amplifier range [pC]	Force range x,y [N]	Resolution x,y [N]	Force range z [N]	Resolution z [N]
1000	129.9	0.0019	256.4	0.0039
5000	649.4	0.0099	1282.1	0.0195
10 000	1298.7	0.0198	2564.1	0.0391
50 000	6493.5	0.0991	12820.5	0.1956

TABLE III: Instrumented Treadmill parameters

Parameter	Value
Treadmill size l×b×h	1744×640×520 mm
Treadmill surface l× b	1522×510 mm
Height from ground	520 mm
Total weight	270 kg
Floating weight	45 kg
Max speed	$4.7\,\frac{m}{s} \approx 17\,\frac{km}{h}$
Max subject weight	500 kg
Height handrail	1100 mm
Max. force	F_x, F_y = 25 kN F_z = 60 kN
Max. sampling frequency	10 000 Hz
Safety features	Emergency stop button and safety key Handrail at 1100 mm height Adjustable lanyard with harness attached to the ceiling

frame acts as a counterweight to the ground reaction forces exerted on the treadmill during locomotion. The surfaces in contact with the force sensors are precision ground to ensure a plane connection between the sensor and the frame. The force sensors sit on top of the base frame and connect the treadmill compound plate and the compound fixture to the base frame.

To achieve maximum stiffness at low mass, the compound plate consists of two honey comb sandwich plates (10 mm thickness, 35μm honey comb thickness) and two carbon fiber plates bonded with an epoxy resin for aluminium-carbon connections (2015B, *Araldite*). The compound plate is clamped into two c-shaped compound fixtures made from aluminium, that also include the connection for the force sensors. To decouple the whole treadmill assembly from the frame, the actuator is also placed on the compound fixture to ensure that all internal forces are captured in the sensors. The actuator is connected to a standard conveyor belt running over four rollers (ROFAWT50-15-L400, *Misumi*). The top rollers are barreled to ensure self centering of the belt. The surface of the treadmill in contact with the underside of the conveyor belt is covered with a teflon plate to reduce gliding friction between belt and treadmill. The roller in the back of the treadmill is equipped with a custom built tensioning mechanism based on a lead screw to adjust the belt tension to remove belt slippage on the rollers.

The motor is a brushed DC treadmill motor taken from a commercial treadmill (*Christopeit-Sport*). It has 0.92 kW continuous power at 180 V bus voltage and a maximum motor speed of 5400 rpm. The motor is geared with a 3:1 ribbed V-belt (PJ, 483x5 mm, **zahnriemen24** and is connected to a motor controller (DPCANIE-015S400, *a-m-c*). The ribbed V-belt was chosen because the timing belt in the initial design introduced vibrations into the system. Because of the undercut between the small motorside timing pulley (8 teeth) and the belt an unacceptable noise source at a frequency of $f_{noise} = \omega_{motor} \cdot n_{teeth}$ was visible in the Fourier transform of the force signal.

The secondary motor axis is equipped with a flywheel to increase inertia and stabilize motor speed. Motor position is measured with a magnetic angular encoder (AEAT8800, *Broadcom*) and fed back to the motor controller. To use the treadmill at a constant speed the motor controller can be set to speed control mode. The motor controller also has a torque control mode with direct access to the desired current. In this mode it is possible to run perturbation experiments with reproducible speed perturbations.

The force sensors (9366CCSP, *Kistler*) are connected to a summation box under the compound plate. The summation box is connected to a charge amplifier (9865, *Kistler*) and a data acquisition system (85695B, *Kistler*). The charge amplifier can automatically switch its amplification stage depending on the amount of charges coming from the sensors. The sensors have sensitivities of $\approx 7.7\,\frac{pC}{N}$ in x- and y-direction and $\approx 3.9\,\frac{pC}{N}$ in z-direction. The system can therefore be used for loads ranging from 129 - 6493 N in x- and y-direction and 256 - 12820 N in z-direction(Table II).

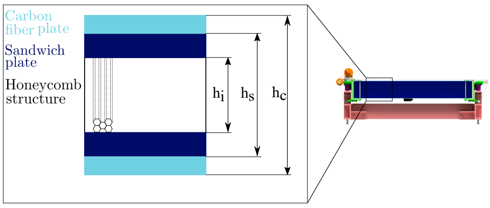

Fig. 2: Sketch of a longitudinal cut through the sandwich (black) and carbon fiber (blue) compound treadmill plate.

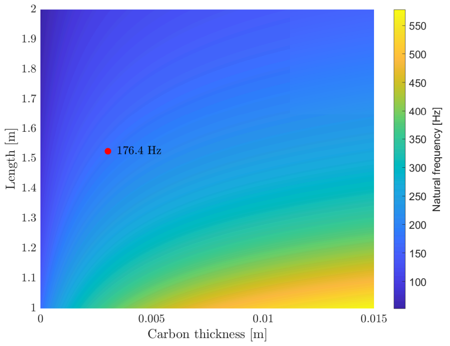

Fig. 3: Heat map of the effects of treadmill plate length and carbon fiber plate thickness on the natural frequency of the instrumented treadmill. The red dot marks the selected value pair.

To ensure safe experiments a handrail is placed around the treadmill at 1100 mm height according to DIN 18065. The handrail constructed from aluminium profiles (*Bosch*) ensures safe experiments in the event of an accident. To not compromise the natural frequency of the treadmill, the handrail is not connected to the treadmill but rather placed on the ground. The handrail has cantilevers on the ground to prevent it from tipping over sideways. The treadmill has a mobile control unit with a display for the current speed, a potentiometer to set the desired speed and an emergency stop button. On the handrail there is also a safety key. If the subject moves too far from the front of the treadmill, the safety key attached to the subject is pulled from its base on the handrail and breaks the safety circuit. Both emergency stops are connected to the "Safe torque off" feature on the motor driver that enables safe error handling and immediately turns off the motor in case of an emergency.
Additionally an adjustable lanyard (FAR1104-51 „*JSP*) is attached to the ceiling above the treadmill to prevent injuries in case an experiment participant stumbles on the treadmill. A wooden runway with a step is placed behind the treadmill for easier access as well as a safe area should a subject reach the end of the treadmill.

TABLE IV: Sensor accuracy as a function of frequency based on natural frequency f_n [23, p. 47]

Accuracy [%]	10	5	1
f_{max}	$0.3 \cdot f_n$	$0.2 \cdot f_n$	$0.1 \cdot f_n$

For synchronization, the charge amplifier, the high speed camera and the treadmill motor controller are equipped with a custom made trigger device.

B. Theoretical Design Considerations

The primary design criterion for instrumented treadmills is the natural frequency of the system. The higher the natural frequency, the higher the sensor accuracy (Table IV). Under load the treadmill will oscillate at its natural frequency. To not degrade the sensor signal, the natural frequency has to be higher than the frequency spectrum of the measured signal. The higher the natural frequency of the measuring systems is compared to the sensor signal spectrum, the cleaner the measured data will be.
In this section we provide a simple model to estimate the natural frequency of our instrumented treadmill design for different design parameters. This way the design is modular and can easily be modified for individual applications and desired dimensions. The maximum measurable frequency with a certain accuracy is defined by the force sensor. In this case, a piezoelectric force sensor (9366CCSP, *Kistler*,[23]) defines the accuracy as a function of frequency based on the natural frequency f_n of the measuring setup (Table IV). The natural frequency is defined as:

$$f_n = \frac{1}{2 \cdot \pi} \sqrt{\frac{c}{m}} \tag{1}$$

where m is the system mass and c is the system stiffness. The part of the treadmill that has the biggest effect on the natural frequency is the plate the subject is running on (Figure 1). The design process is a trade off between increasing stiffness, which is beneficial, and in doing so increasing the mass, which is disadvantageous. The goal is to find a material with high bending stiffness and low weight. To increase the stiffness of the plate [14] implemented a honey comb core sandwich panels (Compocel EL, *CEL components*). Two aluminium plates provide a high area moment of inertia while the hollow honey comb structure provides rigidity with little increase to the system mass. We adapt the same principle but combine it with a epoxy-bonded compound carbon fiber plate on top of the aluminium plates. The carbon fiber plates increase the tensile strength on the surface of the treadmill plate to increase bending stiffness. At the same time the lower density of carbon fiber adds less weight to the system compared to a thicker aluminium plate.

The driving equation for bending stiffness and natural frequency is

$$\sigma = \frac{F \cdot l^3}{48 \cdot E \cdot I} \tag{2}$$

where σ is the deformation, F is the applied force, E is the E-modulus and I is the area moment of inertia. With Hooke's law

$$c = \frac{F}{\sigma} \tag{3}$$

this results in:

$$f_n = \frac{1}{2 \cdot \pi} \sqrt{\frac{48 \cdot E \cdot I}{m \cdot l^3}} \tag{4}$$

$$I_s = \frac{b \cdot (h_s^3 - h_i^3)}{12} \tag{5}$$

$$I_c = \frac{b \cdot (h_c^3 - h_s^3)}{12} \tag{6}$$

$$f_n = \sqrt{\frac{b \cdot (E_s \cdot (h_s^3 - h_i^3) + E_c \cdot (h_c^3 - h_s^3))}{\pi^2 \cdot m \cdot l^3}} \tag{7}$$

where I_s is the area moment of inertia of the sandwich plate, I_c is the area moment of inertia of the carbon fiber plates, E_s is the E-modulus of aluminium, E_c is the E-modulus of a carbon fiber plate, b is the width of the treadmill surface, l is the length of the treadmill surface, h_s is the thickness of the sandwich plate, h_i is the thickness of the inside of the sandwich plate and h_c is the thickness of the sandwich carbon fiber compound plate as shown in Figure 2. From the equation we see that the stiffness of the treadmill is dominantly dependent on the length and height of the substrate. With a longer treadmill substrate and thinner carbon fiber plates the natural frequency reduces as shown in Figure 3. To find a good balance between low mass and high stiffness we chose a treadmill area of $\approx 1400 \times 500$ mm. With these measures we expect a natural frequency of $f_x = 630$ Hz, $f_y = 250$ Hz, and $f_z = 176$ Hz with minimal cost of material and weight. This natural frequency corresponds to the natural frequency of the gold standard force plate usually used for biomechanical experiments [24].

C. Calibration

While the force sensors in the treadmill are factory calibrated, the treadmill has to be recalibrated after assembly to ensure the required natural frequency and accuracy are achieved.

1) Natural frequency: To test the natural frequency an impact test is used as described in the literature with either a wooden ball [12] or an instrumented hammer [20]. We tap the treadmill in all three Cartesian coordinate directions with a hammer, while the data acquisition system is running. We measure the transient response to the impact, sampled at 10 kHz, and use fast fourier transform (FFT) to visualize the frequency response spectrum. The natural frequency f_0 for each direction shows as the prominent peak in the frequency response spectrum.
To determine the damping rate of the system, we calculate the envelope function of the transient response by fitting an exponential function to the peaks of each impact response. From the envelope function we calculate the damping ratio ξ and the Q-factor for each force direction.

$$y(t) = A \cdot e^{-\lambda \cdot t} \cdot \cos(\omega t) \tag{8}$$

$$\omega = 2\pi \cdot f_0 \tag{9}$$

$$\xi = \frac{\lambda}{\sqrt{(\lambda^2 + \omega^2)}} \tag{10}$$

$$Q = \frac{1}{2 \cdot \xi} \tag{11}$$

where $y(t)$ is the transient response, A is the amplitude, λ is the time constant, t is time, ω is the oscillation angular velocity, ξ is the damping ratio and Q is the Q-factor.

2) Signal noise: To determine the motor induced noise on the force sensors we first collect force data when the motor is turned off and compare it, to when the motor is running at speeds of 0-2.5 $\frac{m}{s}$ in increments of 0.5 $\frac{m}{s}$. We log the motor speed with the motor driver software at 1 kHz and force data at 1 kHz. We use two standard deviations (95%) as a measure for noise of the signal and display the changes in motor noise dependent on motor speed.

3) Sensor calibration: According to ISO 376 and DKD 3-9 (Figure 6) we calibrate the treadmill with a calibrated normal . To calibrate the treadmill we use an external 3-axis force sensor (K3D60, *ME-Systeme*) and a data acquisition system (cDAQ9189, *National Instruments*). By using an external, calibrated force sensor as ground truth we achieve a norm conform calibration with more reliable data compared to custom built device. To make the calibration reliable and reproducible we use a servo motor (PM54-060-S250-R, *Dynamixel*) to exert forces. The motor is fixed to the handrail in different positions. To connect the motor to the external force sensor, we use a 3 mm Dyneema cable (Dyneema, *Liros*) as well as a serial spring to provide series elastic behavior [25] to protect the external force sensor from shock. The external force sensor is clamped to the top of the treadmill in a grid of 4×3 predefined positions (Figure 4). To determine the force injection point the force sensor position and orientation is recorded with a motion capture system (Prime^{22}, *OptiTrack*) at 200 Hz. Known fixpoints on the treadmill as well as the force sensor and the force sensor plate are equipped with MoCap markers (Figure 4). This way the exact orientation of the force sensor and the force injection points can be recalculated. The motor first exerts maximum force twice for 30 s to preload the sensors. After the force is increased from 0 N to 200 N continuously by 6 $\frac{N}{s}$. The force plate data is sampled at 1000 Hz, the force sensor is sampled at 1600 Hz and the motion capture data is recorded at 200 Hz.

4) Shear compensation: Because the treadmill surface is not in one plane with the force sensor reference plane, shear effects on the center of pressure have to be compensated (Figure 7). Therefore, we calculate an optimal sensor offset that is applied in the COP calculation to minimize the shear influence on the COP position. The equation results from the

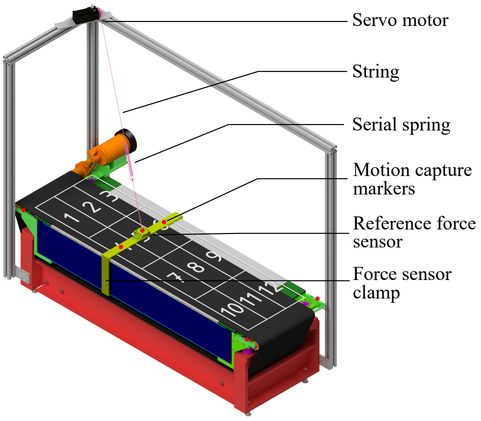

Fig. 4: Calibration setup with treadmill, servo motor and force sensor for reproducible and accurate force insertion into the treadmill. The numbered grid represents the 12 calibration points. To measure orientation and position of the force sensor the treadmill, force sensor and force sensor clamp are equipped with motion capture markers.

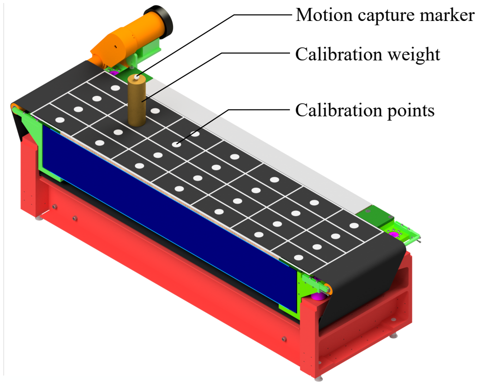

Fig. 5: Setup for calibrating the COP accuracy. A weight is placed on 28 points in an evenly spaced grid on the treadmill surface. The weight is located with a MoCap marker, and the MoCap position is used as the ground truth to characterize the accuracy of the treadmill COP estimation.

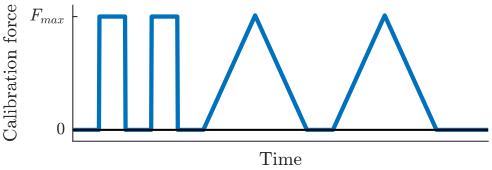

Fig. 6: Calibration routine for the instrumented treadmill based on DKD 3-9 and ISO 376. The sensors are preloaded twice and the force is then ramped up and down continuously twice. From this protocol, accuracy, linearity, repeatability, and hysteresis can be calculated.

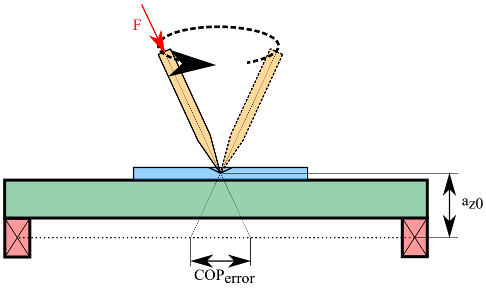

Fig. 7: Sketch of the shear calibration procedure. A pointed rod (orange) induces a force F in different directions into the treadmill surface (green) through a conic hole in an aluminium plate (blue). Dependant on the sensor offset a_{z0}, the influence of shear force components on the COP error in the sensor plane (red) can be minimized.

moment equilibrium around the treadmill centers:

$$a_x = \frac{F_x * a_z - M_y}{F_z} \tag{12}$$

$$a_y = \frac{F_y * a_z + M_x}{F_z} \tag{13}$$

where a_i is the COP position, F_i are forces, M_i are moments in the cartesian coordinates. a_z¡0 is the sensor offset. We fix a thin aluminium plate with a conic hole to the treadmill surface and push into the whole with a pointy rod. This way the force direction can change arbitrarily while ensuring, that the force application position does not change. We perform 15 arbitrary motions with different force angles and amplitudes. Because the COP does not depend on the force amplitude, manual force application is acceptable. We then calculate the optimal a_{zO} value that minimizes the change in a_x and a_y when the force direction changes. By finally subtracting the aluminium plate thickness we find the optimal a_{zO} value.

5) *Center of pressure:* To estimate the COP error, we calibrate the COP position using a weight and a motion capture system (Mocap). We place a 15 kg weight at 28 even spaced points on the treadmill. The weight is marked at its center with a reflective Mocap marker. Using 3 Mocap

cameras we locate the weight on the treadmill. We use the Mocap data as ground truth, to compare to the treadmill COP position estimate. The error of the treadmill estimate is calculated with:

$$COP_{error} = COP_{treadmill} - COP_{Mocap} \tag{14}$$

We then fit a 4th order surface polynomial $S(x, y)$ to the COP_{error} in x and y direction. With this polynomial we correct future COP measurements to minimize the estimation error.

$$S(x, y) = \sum_{n=0}^{4} a_n \cdot x^n + b_n \cdot y^n \tag{15}$$

where $S(x, y)$ is the surface polynomial, a_n and b_n are the polynomial coefficients and x and y are the cartesian treadmill coordinates. The COP estimate for each treadmill point (x_0, y_0) can then be corrected with:

$$COP_{corrected_{(x_0,y_0)}} = COP_{Raw_{(x_0,y_0)}} - S(x_0, y_0) \tag{16}$$

D. *Human and Robot Experimentation*

The switchable amplification of the force sensor signals (Table II) in combination with the high natural frequency of the treadmill allows force measurements with constantly high accuracy independent of the force amplitude. To showcase the high accuracy of the treadmill for different loading scenarios, we showcase a human of 90 kg and small robot of 4 kg, walking on the robot. Ground reaction force data is recorded for both subjects at 1 kHz, high speed video of the legs is recorded at 400 Hz. The treadmill speed is set to 0.63 $\frac{m}{s}$.
The human subject walks on the treadmill for 1 minute where 20 s are recorded. The data is then normalized over body mass and is presented unfiltered and averaged for 30 strides. As comparison data for small subjects we use our quadrupedal robot Morti [26]. The robot walks on the treadmill, guided by a linear rail in the sagittal plane for 2 minutes where 20 s are recorded at a speed of 0.15 $\frac{m}{s}$. We normalize the data by body weight and display it over percent of step cycle.

III. RESULTS

A. *Calibration*

1) Natural frequency: The resulting natural frequencies (Figure 8) fit the theoretical values calculated in Figure 3. The natural frequency in x-direction is the highest with $f_{0,x} = 385$ Hz (calculated 635 Hz). The deviation from the calculated frequency stems from the fact, that the calculation is only a rough estimation since the standard equations for bending moment of inertia is only an approximation. The values for $f_{0,y} = 204$ Hz (calculated 350 Hz) and $f_{0,z} = 169$ Hz (calculated 175 Hz) fit well to the calculated values. As expected the value for $f_{0,z}$ is the lowest since the stiffness is lowest in this direction as discussed above. The deviations stem from uncertainty in material, manufacturing and assembly accuracy. All three spacial force directions show minor parasitic peaks in the frequency spectrum. Most noticable a parasitic peak in the z-direction at ≈ 80 Hz. The parasitic peaks in the frequency spectrum stem from non-rigid connections on the drums and actuator that oscillate at their own natural frequencies. The prominent natural frequency peaks of the first harmonic of the treadmill structures are clearly visible at the frequencies mentioned above.
We also see the overall system damping in the time the oscillations fade out. In all three directions the impact force fades after around 0.08 s (Figure 8 a,b,c).
To characterize the signal damping we calculate the damping ratio ξ and the Q-factor. The damping ratios are $\xi_{\mathrm{x}} = 0.0148$, $\xi_{\mathrm{y}} = 0.033$ and $\xi_{\mathrm{z}} = 0.0093$. The respective Q-factors are $Q_{\mathrm{x}} = 33.8$, $Q_{\mathrm{y}} = 15.02$ and $Q_{\mathrm{z}} = 5.3$. All damping rates are below 0.033 which shows that the construction is stiff and has little soft parts that interfere with the signal transfer through the compound plate.

2) Signal noise: The noise behavior of the treadmill at different treadmill speeds is shown in Figure 9. The maximum noise of the force sensors at 0 $\frac{m}{s}$ is -0.76 N, 0.77 N, and -1.8 N in x,y, and z-direction. The 95% confidence interval in all three directions is $\leq$ 1 N. At higher treadmill speed the noise level rises because of vibrations from the actuator. In x- and y-direction the noise is higher with a maximum of 6 and 8 N respectively. Because the belt moves in the x-y plane, this is to be expected. In z-direction the noise is $\leq$ 4 N. Compared to the maximum range, as well as in respect to a human walking on the treadmill the noise is negligible and would only come into play with very light subjects at high speeds.

3) Sensor calibration: The calibration data is compared to the force sensor data (Figure 10). For each calibration point we calculate the maximum difference between the sensor as the normal and the treadmill. The sampled grid with the respective sensor accuracies in x, y and z direction is shown in Figure 11. The maximum errors are $\Delta F_x = 4.6$ N, $\Delta F_y = 5.3$ N and $\Delta F_x = 5.6$ N. Compared to their maximum sensor range the error is around 0.02%. The maximum error in our calibration occurs, when the servo motor starts and stops moving rapidly at the discontinuities of the square functions. This induces oscillations in the serial spring which lead to measuring errors. This can be omitted by using an elastic string to dampen the oscillation but is not necessary for our results since the calculations are only done at steady state behavior according to ISO 376. We therefore ignore the transient behaviors in between the evaluation windows.
The reproducibility was determined from the square function data. The difference between reoccuring sensor signals in Figure 10 is 0.4% of the normalized force. Linearity [27] was determinded from the difference of the data in the slope function to the linearized normal sensor data. It is $\leq$ 1% for all three force directions. The hysteresis [27] was calculated, by fitting a 6th order polynomial to one of the slope functions and the hysteresis effect was calculated in both input-output, as well as in output-input direction. The resulting hysteresis was found to be $\leq$ 0.25% of the normalized force. From all calibration points we calculate a calibration map that shows the accuracy of the force sensing capabilities for every point on the treadmill. The calibration map is shown in Figure 11. The error gets bigger towards the edges of the treadmill

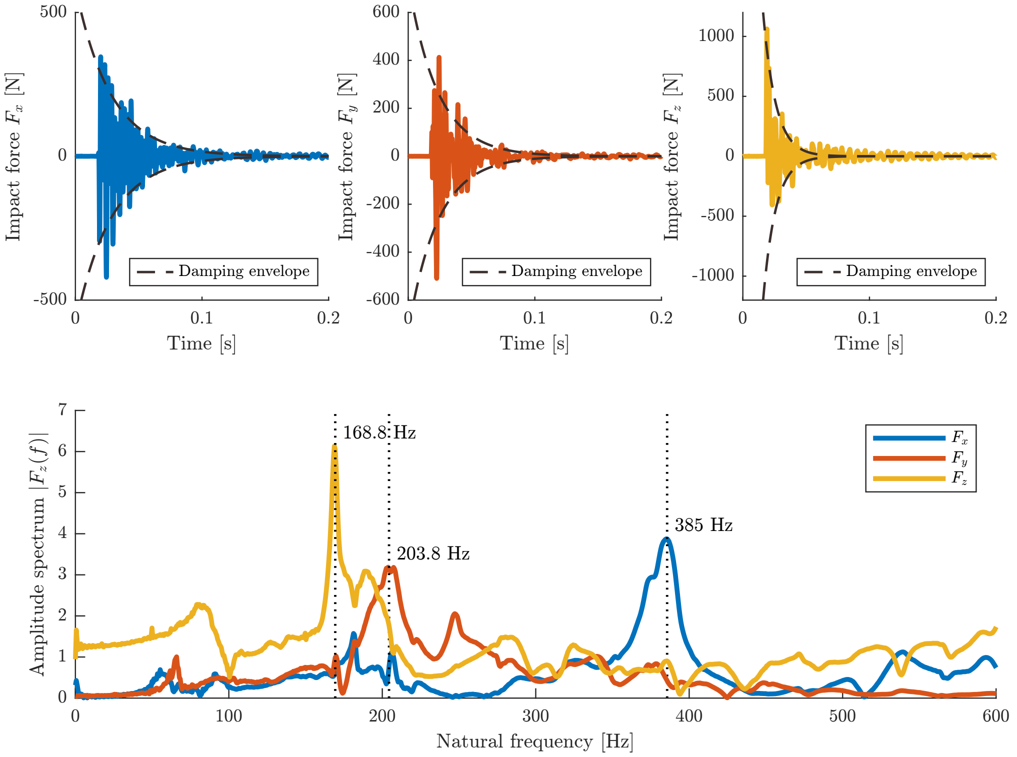

Fig. 8: Unfiltered impact response of tapping the treadmill with a hammer in x-, y- and z-direction (top). Frequency response spectrum from Fast Fourier Transfrom (bottom). F_x shows a prominent peek at 385 Hz, F_y at 203 Hz and F_z at 169 Hz. These values correspond to the values calculated in the beginning of the paper.
The damping envelope (dashed line) is used to characterize the damping behavior. The damping ratios are $\xi_\mathrm{x} = 0.0148$, $\xi_\mathrm{y} = 0.033$ and $\xi_\mathrm{z} = 0.0093$. The respective Q-factors are $Q_\mathrm{x} = 33.8$, $Q_\mathrm{y} = 15.02$ and $Q_\mathrm{z} = 5.3$.

surface. This is to be expected, because the bending of the sandwich plate is more asymmetric the further the force induction point deviates from the middle of the treadmill surface. Theoretically, force sensing is best in the center of polygon spanned by the force sensors. This is especially visible in x and y direction. There is also a shift visible towards the left edge of the treadmill surface. This stems from the fact, that the belt of the treadmill is not running in the center of the treadmill surface. Because the treadmill is designed as a split belt treadmill, both belts are shifted towards one another to minimize the belt gap. The overall error in all three force directions lies well within our expected specifications for a treadmill of this size.

4) Shear Compensation: From the 15 shear calibration experiments, we calculate the minimal sensor offset as described in Figure 7. The optimal sensor offset from 15 experiments is shown in Figure 12 a). The mean sensor offset $a_{z,0}$ is 0.078 m ±0.005 m. The deviation stems from the noise behavior characterized in Figure 9 as well as the measuring error in Figure 11. With the optimized sensor distance, we recalculate the corrected COP from the sampled data. The resulting minimized expected COP error is 0.013 ±0.0012 m in x and 0.003±0.001 m in y-direction as shown in Figure 12 b). Therefore, the relative COP error is $\leq$ 0.8% of the treadmill length in both directions.

5) Center of Pressure: The raw COP error in Figure 13 a) shows a COP estimation error of $\leq$ 20 mm in x-direction and $\leq$ 12 mm in y-direction. The fitted surface polynomial approximates the raw COP error data in Figure 13 b) well with R^2 = 99.86%. With the COP error across the treadmill surface accounted for, the resulting error in the COP estimation is corrected with a remaining uncertainty of ±1 mm in x direction and ±0.5 mm in y direction. The error estimation through a surface polynomial shows to be an effective way of improving the COP estimate of the instrumented treadmill.

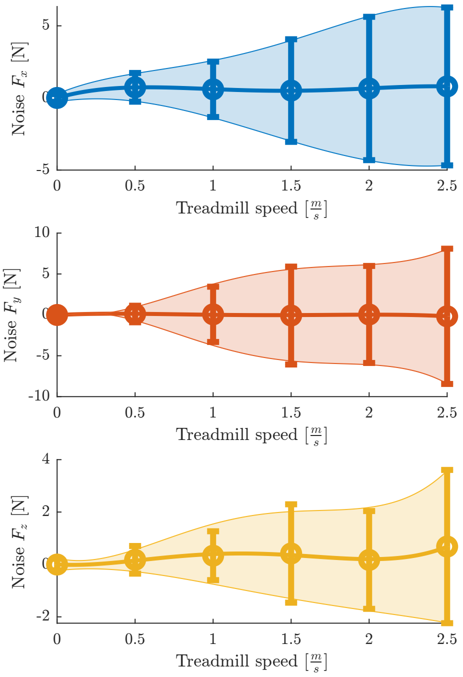

Fig. 9: Noise level of the instrumented treadmill in relation to treadmill speed in x-, y- and z-direction with mean and 95% confidence intercals. Frequency spectrum of the treadmill noise (bottom). The frequency spectrum shows prominent peaks at 50 Hz in all three signals from line voltage.

B. *Human and Robot Experimentation*

In the human walking experiment we see a m-shaped ground reaction force profile expected for a walking gait. The z-direction shows one distinct maximum per step. We believe this to be due to the rigid structure of the treadmill as well as the subject wearing shoes [28]. The overall shape is comparable to data presented in [10] for a similar speed range.

To evaluate the performance of the instrumented treadmill we calculate the confidence interval for both the human and robot experiment over 30 steps. The confidence for the human treadmill are $S_{x,mean} = 8.8 \pm 6.1\,\text{N}$, $S_{y,mean} = 8.4 \pm 2.2\,\text{N}$ and $S_{z,mean} = 16.8 \pm 9.6\,\text{N}$. The confidence is highest during the maximum peak for each leg as well as during

The confidence for the robot experiment are $S_{x,mean} = 0.47 \pm 0.19\,\text{N}$, $S_{y,mean} = 0.38 \pm 0.16\,\text{N}$ and $S_{z,mean} = 0.97 \pm 0.44\,\text{N}$.

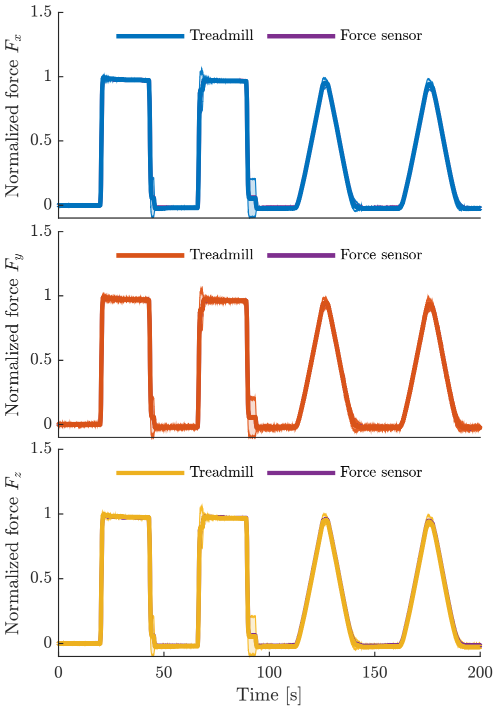

Fig. 10: Averaged data over 12 calibration points from Figure 4 with treadmill data, 95% confidence interval and ground truth force sensor data in purple. The calibration is done according to ISO 376 and DKD 3-9 as described in Figure 6.

IV. CONCLUSION

In this paper we present a modular, instrumented treadmill. We provide a framework to design the natural frequency, the key feature, of such a treadmill. The framework can be used to design a treadmill of similar style with individual geometry and performance criteria. The sensor design in this paper is open source, and can be used as the basis for future development. We validate our design assumptions through experiments and show that, within manufacturing and material uncertainty, our design approach is valid. We reach a natural frequency of 169 Hz which is less than 3% off the calculated value.

We then characterize the sensor performance of the treadmill with a norm conform calibration protocol according to ISO 376 and DKD 3-9. In a first step we calibrate the treadmill sensors against an external normal. This procedure provides a reproducible and accurate dataset that can then be used to calculate standard force sensor characteristics like accuracy, linearity, reproducibility and hysteresis. Since the treadmill is used as a sensor modality, we believe the proper

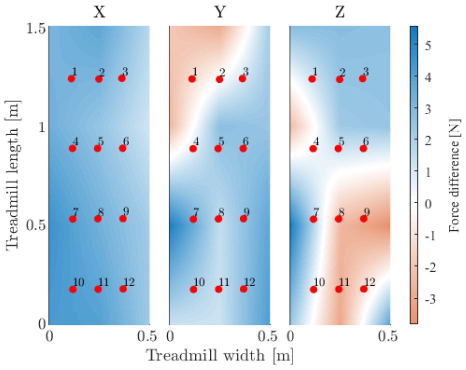

Fig. 11: Calibration result for all calibration points shown in Figure 4. Displayed is the maximum error between the force sensor and the treadmill data from Figure 10. Maximum error is 4.6 N, 5.3 N and 5.6 N in x,y and z direction respectively. The red dots show the 12 calibration points reconstructed from motion capture data.

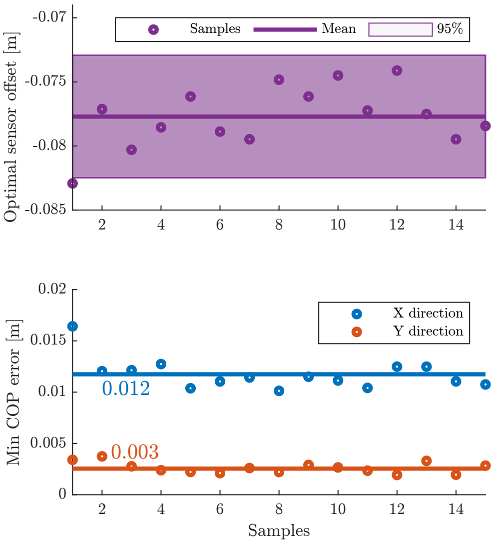

Fig. 12: *a)* Optimal sensor offset for 15 experiments with mean and 95% confidence interval. The mean optimal sensor offset is -0.078 m.
b) Resulting minimal COP estimate errors for the 15 experiments. Mean COP error from shear influence is 0.013 m in x and 0.003 m in y direction.

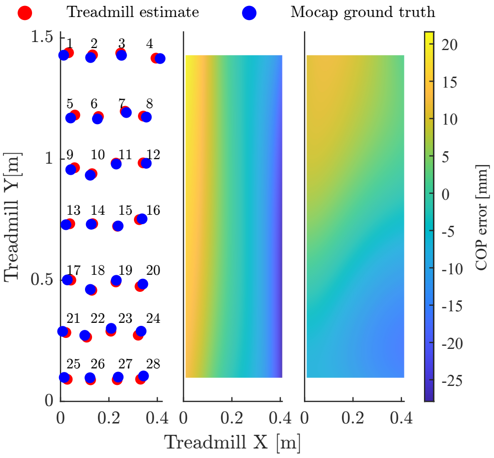

Fig. 13: *a)* COP position from treadmill estimate (red) and ground truth (blue) from Mocap measurement. The raw COP error is ≤ 20 mm. *b)* COP error surface fit after COP calibration with a dead weight on 28 even spaced calibration points across the treadmill surface, original data in orange.

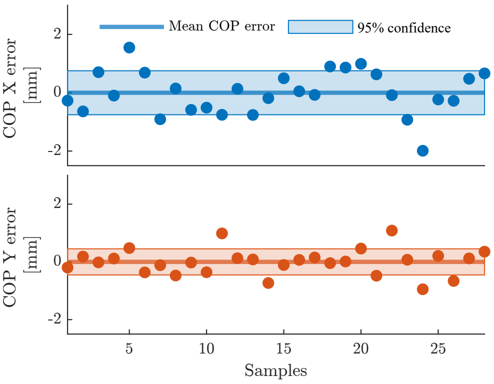

Fig. 14: COP estimation after correction with the surface polynomial error approximation from Figure 13. The COP error is corrected in both directions with a remaining uncertainty of ±1 mm in x direction ±0.5 mm in y direction.

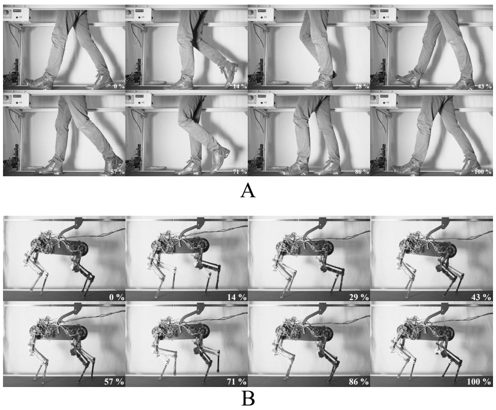

Fig. 15: A. Photo of a human subject walking on the instrumented treadmill. B. Photo of a Robot walking on the instrumented treadmill.

calibration and report of characteristics to be one of the key features of an instrumented treadmill design. By providing a concise framework we hope to improve the comparability and characterization procedure in the future.

Overall the characterization of our treadmill shows values that are comparable to a standard force plate of that size.

We then characterize the COP estimation by placing dead weight on the treadmill surface. With the surface fit correction provided by the force sensor manufacturer we are able to achieve force plate levels of accuracy for the center of pressure estimation even though our treadmill surface is manyfold bigger than a force plate. While the static COP error can be removed with minimal error, the influence of shear forces shows to be a much bigger influence.

We minimize the shear influence and the COP error can be decreased to 13×3 mm which is sufficient for gait analyses. If required the shear influence might be reduced by using appropriate filtering techniques and trying to estimate the force directions more accurately than in this approach.

Additionally we characterize the noise behavior of the treadmill when the belt is actuated for different speeds. Overall the treadmill speed can be neglected and is only visible in high speeds.

Finally we present a real world experiment with a 90 kg human as well as a 4 kg robot to showcase the adjustable range and superior performance of our treadmill for different weight subjects.

The treadmill design presented here, is comparable to the gold standard sensor modality for ground reaction forces, force plates. We achieve a similar natural frequency, good noise performance, and a center of pressure estimation well within the limits of what is typically required in biomechanical studies.

Through the compound plate design, we achieve a lower floating mass compared to other treadmill designs (Table I).

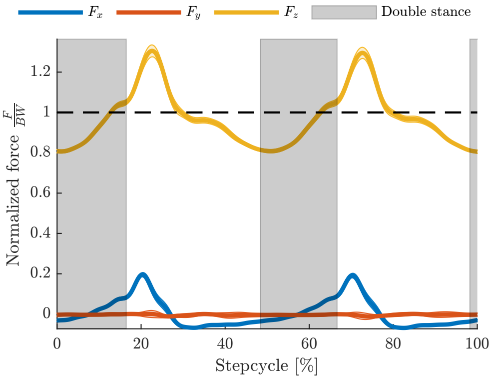

Fig. 16: Normalized ground reaction force data for a human subjects of 90 kg walking on the treadmill at 1.3 $\frac{m}{s}$. Data is shown for one stride consisting of one left and one right step. The double stance phase is shaded grey. All data is shown with 95% confidence intervals, averaged over 30 consecutive steps in a 20 s window. The body weight is shown as a dashed line.

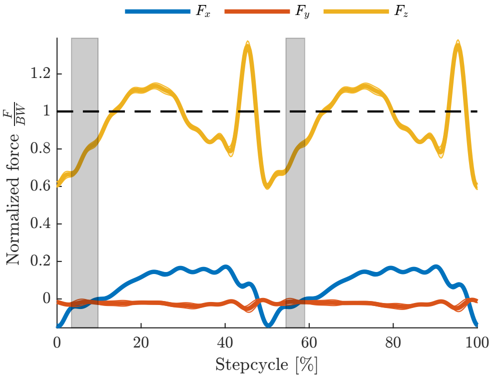

Fig. 17: Normalized round reaction force data for quadruped robot Morti of 4 kg walking on the treadmill at 0.2 $\frac{m}{s}$. Data is shown for one stride consisting of one front-left hind-right and one right-front hind-left step. The double stance phase is shaded grey. All data is shown with 95% confidence intervals, averaged over 30 consecutive steps in a 20 s window. The body weight is shown as a dashed line.

We achieve a much higher sampling frequency, better noise performance and accuracy. Through the norm conform calibration, we can calibrate with a higher accuracy and reproduce our calibration results, which is not possible with other calibration concepts.

CONTRIBUTION

AAS and FR contributed to the concept, developed the mechanical design, the motor control and the experimental setup, conducted all experiments, analyzed the data and wrote the paper. ABS contributed to the concept, feedback, supervision and editing.

AVAILABILITY

The mechanical design and implementation details will made be publically available upon the acceptance of this manuscript. All data used in the paper is available upon request.

ACKNOWLEDGMENT

We would like to thank Bernard Javot for his feedback and help during the mechanical design, Andre Thill and Alessio Atzori for manufacturing and their help with assembly as well as Maren Heuer for implementing the motor controller. We thank the International Max Planck Research School for Intelligent Systems (IMPRS-IS) for supporting the academic development of Felix Ruppert and Alborz A. Sarvestani. This work was made possible thanks to a Max Planck Group Leader grant awarded to ABS by the Max Planck Society.

REFERENCES

[1] M. A. Daley, "Running over rough terrain: Guinea fowl maintain dynamic stability despite a large unexpected change in substrate height," *Journal of Experimental Biology*, vol. 209, no. 1, pp. 171–187, Jan. 2006.

[2] C. Schumacher *et al.*, "A movement manipulator to introduce temporary and local perturbations in human hopping," in *2018 7th IEEE International Conference on Biomedical Robotics and Biomechatronics (Biorob)*, IEEE, Aug. 2018.

[3] F. Ruppert and A. Badri-Spröwitz, "Series elastic behavior of biarticular muscle-tendon structure in a robotic leg," *Frontiers in Neurorobotics*, vol. 13, Aug. 2019.

[4] A. Spröwitz *et al.*, "Towards dynamic trot gait locomotion: Design, control, and experiments with cheetah-cub, a compliant quadruped robot," *The International Journal of Robotics Research*, vol. 32, no. 8, pp. 932–950, Jun. 2013.

[5] C. Semini *et al.*, "Towards versatile legged robots through active impedance control," *The International Journal of Robotics Research*, vol. 34, no. 7, pp. 1003–1020, May 2015.

[6] C. Hubicki *et al.*, "ATRIAS: Design and validation of a tether-free 3d-capable spring-mass bipedal robot," *The International Journal of Robotics Research*, vol. 35, no. 12, pp. 1497–1521, Jul. 2016.

[7] B. Bates *et al.*, "An assessment of subject variability, subject-shoe interaction, and the evaluation of running shoes using ground reaction force data," *Journal of Biomechanics*, vol. 16, no. 3, pp. 181–191, Jan. 1983.

[8] M. Y. Chuah and S. Kim, "Enabling force sensing during ground locomotion: A bio-inspired, multi-axis, composite force sensor using discrete pressure mapping," *IEEE Sensors Journal*, vol. 14, no. 5, pp. 1693–1703, May 2014.

[9] F. Ruppert and A. Badri-Spröwitz, "Foottile: A rugged foot sensor for force and center of pressure sensing in soft terrain," in *Proceedings of the IEEE International Conference on Robotics and Automation*, IEEE, May 2020.

[10] R. Kram *et al.*, "Force treadmill for measuring vertical and horizontal ground reaction forces," *Journal of Applied Physiology*, vol. 85, no. 2, pp. 764–769, Aug. 1998.

[11] P. A. Willems and T. P. Gosseye, "Does an instrumented treadmill correctly measure the ground reaction forces?" *Biology Open*, vol. 2, no. 12, pp. 1421–1424, Nov. 2013.

[12] G. Paolini *et al.*, "Testing of a tri-instrumented-treadmill unit for kinetic analysis of locomotion tasks in static and dynamic loading conditions," *Medical Engineering & Physics*, vol. 29, no. 3, pp. 404–411, Apr. 2007.

[13] H. Witte *et al.*, "Torque patterns of the limbs of small therian mammals during locomotion on flat ground.," *The Journal of experimental biology*, vol. 205, pp. 1339–1353, Pt 9 May 2002, ISSN: 0022-0949.

[14] M. W. Bundle, M. O. Powell, and L. J. Ryan, "Design and testing of a high-speed treadmill to measure ground reaction forces at the limit of human gait," *Medical Engineering & Physics*, vol. 37, no. 9, pp. 892–897, Sep. 2015.

[15] F. Dierick *et al.*, "A force measuring treadmill in clinical gait analysis," *Gait & Posture*, vol. 20, no. 3, pp. 299–303, Dec. 2004.

[16] G. Verkerke *et al.*, "Determining the centre of pressure during walking and running using an instrumented treadmill," *Journal of Biomechanics*, vol. 38, no. 9, pp. 1881–1885, Sep. 2005.

[17] A. Belli *et al.*, "A treadmill ergometer for three-dimensional ground reaction forces measurement during walking," *Journal of Biomechanics*, vol. 34, no. 1, pp. 105–112, Jan. 2001.

[18] S. H. Collins *et al.*, "A simple method for calibrating force plates and force treadmills using an instrumented pole," *Gait & Posture*, vol. 29, no. 1, pp. 59–64, Jan. 2009.

[19] B. Benda, P. Riley, and D. Krebs, "Biomechanical relationship between center of gravity and center of pressure during standing," *IEEE Transactions on Rehabilitation Engineering*, vol. 2, no. 1, pp. 3–10, Mar. 1994.

[20] L. Sloot, H. Houdijk, and J. Harlaar, "A comprehensive protocol to test instrumented treadmills," *Medical Engineering & Physics*, vol. 37, no. 6, pp. 610–616, Jun. 2015.

[21] S. R. Goldberg, T. M. Kepple, and S. J. Stanhope, "In situ calibration and motion capture transformation optimization improve instrumented treadmill measurements," *Journal of Applied Biomechanics*, vol. 25, no. 4, pp. 401–406, Nov. 2009.

[22] R. Pàmies-Vilà *et al.*, "Analysis of different uncertainties in the inverse dynamic analysis of human gait," *Mechanism and Machine Theory*, vol. 58, pp. 153–164, Dec. 2012.

[23] *Multicomponentforce link set*, Type 9366CC, Kistler, Jun. 2009.

[24] *3d force plate portable (0...5kn)*, Type 9260AA, Kistler, Feb. 2014.

[25] G. A. Pratt and M. M. Williamson, "Series elastic actuators," in *Proceedings 1995 IEEE/RSJ International Conference on Intelligent Robots and Systems. Human Robot Interaction and Cooperative Robots*, IEEE Comput. Soc. Press, 1995.

[26] F. Ruppert and A. Badri-Spröwitz, "Learning neuroplastic matching of robot dynamics in closed-loop CPGs," Nov. 2021.

[27] H. Czichos and W. Daum, "Sensors and circuits," in *Dubbel*, Springer Berlin Heidelberg, W1–W37.

[28] S. R. Simon *et al.*, "Peak dynamic force in human gait," *Journal of Biomechanics*, vol. 14, no. 12, pp. 817–822, Jan. 1981.

6 Shaping in Practice: Training Wheels to Learn Fast Hopping Directly in Hardware

Shaping in Practice: Training Wheels to Learn Fast Hopping Directly in Hardware

Steve Heim, Felix Ruppert, Alborz A. Sarvestani, Alexander Spröwitz
Dynamic Locomotion Group
Max Planck Institute for Intelligent Systems, Germany

arXiv:1709.10273v2 [cs.RO] 7 Mar 2018

***Abstract*— Learning instead of designing robot controllers can greatly reduce engineering effort required, while also emphasizing robustness. Despite considerable progress in simulation, applying learning directly in hardware is still challenging, in part due to the necessity to explore potentially unstable parameters. We explore the concept of shaping the reward landscape with *training wheels*; temporary modifications of the physical hardware that facilitate learning. We demonstrate the concept with a robot leg mounted on a boom learning to hop fast. This proof of concept embodies typical challenges such as instability and contact, while being simple enough to empirically map out and visualize the reward landscape. Based on our results we propose three criteria for designing effective training wheels for learning in robotics. A video synopsis can be found at `https://youtu.be/6iH5E3LrYh8`.**

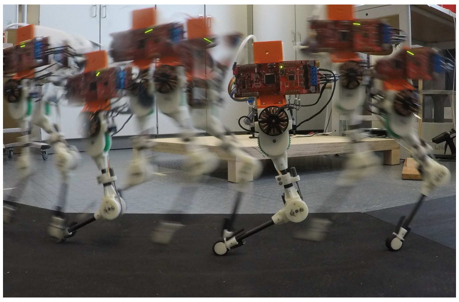

Fig. 1: A multiple-exposure image of our robotic leg mounted on a boom hopping, showing the distinct stance and flight phases.

I. INTRODUCTION

In nature, animals learn to move with a grace and agility that is the envy of robotics engineers. One major challenge is that most algorithms rely on accurate models, which in turn also take a lot of engineering effort. Alternatively, reinforcement learning (RL) is a powerful paradigm that can work both model-based or *model-free*. In addition, reinforcement learning is often able to learn from generic and even highly delayed reward signals: for example a legged robot might receive a reward for reaching a specific target location within a set time limit, and no reward for getting progressively closer. This allows for easy and intuitive assignment of rewards without constraining the behavior for achieving the goal. Despite these attractive features and promising achievements in simulation [1][2], applying RL directly in hardware has proven challenging [3][4][5] with only a handful of successes that actually run model-free [6][7].

One major challenge in hardware comes from the necessity to *explore* the reward landscape. The landscape is usually non-convex, and often only subsets represent behaviors that actually accumulate reward: the rest of the landscape often looks flat, representing different behaviors that all receive the same or even no reward. Sampling from these regions provides no gradient information for the robot to learn from. This is particularly true when the reward is generic and delayed such as in the previous example: a policy that causes the robot to fall over immediately would get the same reward of zero as a policy that hops in place, even though the second policy arguably solves part of the locomotion problem [8]. This problem is even more accentuated in robots that are unstable, since instabilities often quickly lead to direct failure states. These failures generally lead to no reward, and can also damage the hardware. In practice, exploration is executed cautiously, usually locally. This combination means that large parts of the reward landscape are flat, and there is no salient gradient to lead the learning agent in the correct direction.

The exploration challenge can be solved by choosing a more appropriate policy parameterization, or with different exploration strategies such as intrinsic motivation [9]. This can however be difficult to find and does not eliminate the flat regions, or the potentially damaging failures.

Another approach is to shape the reward landscape. A common method of shaping is to encode more information of the task in the reward [10]. The drawback is that it requires more prior knowledge of the task, and goes against the attractiveness of being able to choose rewards based on achieving a task rather than specifying a behavior[1]. It is also possible to shape the landscape by proper mechanical design. For example, walking robots designed after passive-dynamic walkers [11] have good stability properties for a wide range of policy parameters, allowing quick and reliable learning from even poor initializations [6]. The drawback is that designing the system around one specific behavior can

---

contact: lastname@is.mpg.de
Dynamic Locomotion Group, Max Planck Institute for Intelligent Systems, Heisenbergstr. 3, 70569 Stuttgart, Germany

[1] Whether the robot crawls, walks or runs should depend on the context of the situation and not on the goal.

be limiting in terms of versatility and design options.

We build on these ideas with the concept of *training wheels*: shaping the landscape with *temporary mechanical modifications of the robot that allow for easier learning*. To the best of our knowledge, this concept has only been briefly explored in simulation, even though initial results showed promise [12]. We present a proof of concept directly in hardware, applied to learning fast hopping of a monoped robot with a rolling foot: an underactuated, unstable system featuring hybrid dynamics.

We would like to note that we largely use the terminology of the RL community. In particular, the term *environment* signifies everything that is beyond direct control of the learning agent. Take for example an agent whose policy outputs a desired joint position; then the environment includes not only the physical world the robot moves in, but also the robot itself and the PD motor controller used to track the desired joint position. For a more thorough treatment of RL see [5][13].

II. SETUP: MECHANICS, POLICY AND LEARNING SCHEME

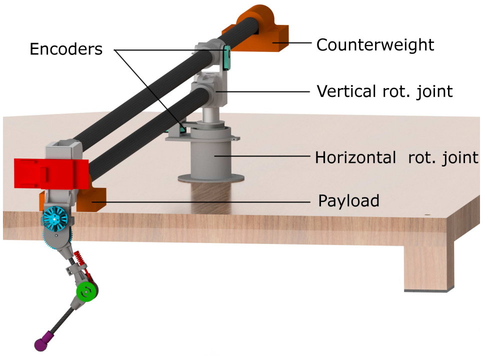

Fig. 2: The entire robot consists of a leg mounted on a boom, with a total of four degrees of freedom. The counterweight balances out the mass of the boom without the leg or payload. The payload represents the mass of the batteries and additional electronics, which are offloaded via a tether.

Our robot platform (Fig. 2) consists of a two-segment leg with a passive compliant ankle joint and an actuated hip joint, mounted on a boom which constrains the body to motion on a 2D surface. The robot thus has four degrees of freedom (DoFs) and a single actuator. The passive compliance at the ankle joint (Fig. 3) results in favorable natural dynamics [14], though the system is still passively unstable.

The learning task is to achieve fast hopping, and the reward for each rollout is the average speed with one additional condition: potentially damaging behavior, such as landing on the ankle instead of the foot, is tagged as a failure and receives no reward. The training wheels for this proof of concept are a simple change of the total mass of the robot body: essentially we allow learning in a reduced gravity environment.

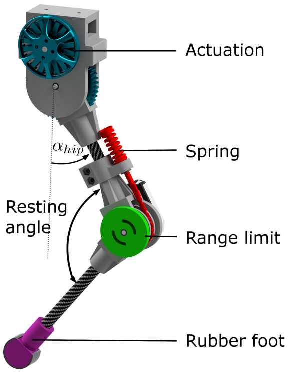

Fig. 3: The two-segment leg has a brushless DC motor at the hip, and a passive compliant ankle joint. The spring is mounted to a cam mechanism, and the joint itself is limited in extension range.

We choose these training wheels for two reasons: first, they should make it easier for the agent to learn the task. Second, they should also be easy to apply in practice, so the final behavior can be achieved with less engineering effort. Based on this we introduce our first criterion in designing training wheels: *how easy are training wheels to apply to a generic set of robots*. For example, the weight of batteries, computation or other payload can easily be offloaded during an initial training phase for most robot designs.

We choose a simple policy with a 2D parameter space: the hip actuator tracks an open-loop sinusoidal position trajectory as follows

$$\alpha_{hip} = \theta_0 + \theta_1 \sin(\omega t) \tag{1}$$

where α_{hip} is the angular position of the hip, ω is a hardcoded angular frequency while θ_0 and θ_1, offset and amplitude parameters respectively, form the parameter space of the policy. This simple policy parameterization serves two purposes: first, a low-dimensional deterministic policy is amenable to the simplest of learning schemes, and thus eliminates the ambiguity of whether the training wheels or the algorithm implementation are responsible for the change in performance. In the results presented we choose $\omega = 9$Hz, based on experience. Higher values achieve higher performance, but failures are also more violent and prone to damaging hardware. Since we also need to sample failure parameters to map out the landscape, we compromise between safety and performance.

We use stochastic gradient descent based on simple finite-difference methods [15]. More importantly, the low dimensionality allows us to empirically map out and inspect the landscape of the learning problem as a 3D surface as seen in Fig. 4. This allows us to compare the landscapes with and without training wheels in detail, and show the change in learning performance across each landscape.

A. Hardware Details

Each DoF of the boom and leg is measured with a rotary encoder (CUI ATM102-V). The boom arm has a length of 1.5[m] from pivot to the leg, and is counterweighted to completely offset its own mass without the leg. The ankle joint of the leg (Fig. 3) is mechanically limited to 130° in one direction, and has a spring with a stiffness of 6 $[\frac{N}{mm}]$ attached to a cam mechanism with a radius of 15 [mm]. This spring is slightly preloaded such that it always returns to the resting angle of 130°. The upper and lower leg segments measure 110 [mm] and 136 [mm] respectively, and the virtual leg length from hip to foot is 223 [mm] at rest. The hip is actuated with a brushless outrunner motor (T-motor MN-4006) with a 1:5 gearbox. The motor control board (Texas Instruments TMS320F28069M with DRV8305EVM booster packs) uses field-oriented control for direct torque control of the motor. A Xenomai real-time linux operating system handles high-level control. Electric power and computational power are both off-loaded via tether. A representative mass is directly attached on the boom just behind the leg. With the entire payload, the robot has a body weight of 600 [g]. For our two training wheel environments the representative mass is replaced with an intermediate mass or completely removed. This results in a body weight of 505 [g] (0.84 g_0) and 415 [g] (0.69 g_0) respectively.

III. RESULTS

We test three environments: the robot with full payload and two environments with training wheels which reduce the weight to 0.69 g_0 and 0.84 g_0, where g_0 is the weight of the robot in the original environment. We will refer to these two environments with training wheels as the *beginner environment* and the *intermediate environment* respectively. We map out the entire reward landscape for each environment by sampling and then interpolating the parameter space (Fig. 4). The parameter space is limited to $\theta_0 = [0\ 40]^\circ$ and $\theta_1 = [10\ 45]^\circ$. Parameters outside this range are either unreachable due to mechanical hard-stops, or in the zero-reward region for all environments, and cropped for clarity. All three landscapes have a mountain-like shape emerging out of a flat surface. While not quite convex, the landscapes each have a prominent peak, making them amenable to stochastic gradient descent. Also present in all three landscapes is a cliff: a sudden sharp drop from high to zero reward. This is found in the upper right quadrant of the parameter space and can be recognized in Fig. 4 by the dense contour lines. This cliff represents the border between parameters which exhibit stable high performance and unstable parameters. In practice it is both difficult as well as dangerous to learn from beyond this cliff: policies with high-amplitude tend to crash violently and damage the hardware. It is interesting to note that the orientation of the cliff does change in each environment, though its proximity to the peak does not.

A. Salient Gradient Sets

We are interested in the region that achieves non-zero reward which we will refer to as a *salient gradient set* (SCS), delimited in the figures by the thicker, outermost contour. This is the set of parameters a learning agent needs to sample from in order to learn. The second criterion for choosing effective training wheels is *how much the training wheels increase the size of the SCS*. Indeed the SCS of the beginner environment covers 46% of the total parameter space, compared to 25% of the intermediate environment and 20% in the original environment. This increase in size is important both for gradient-based and gradient-free methods. With stochastic gradient descent, for example, the gradient is estimated by local sampling. This means the agent must start inside, or at least within local sampling distance of the SCS in order to estimate a gradient. Increasing the size of the SCS directly increases the basin of attraction of the learning system. Other exploration approaches such as eps-greedy can sample from the SCS despite being initialized well away of the SCS. In this case, increasing the size of the SCS increases the probability of sampling from it, thus improving rate of convergence.

B. Funneling Sets

In Randløv's simulated work [12], the training-wheels environment converges gradually to the original environment. In practice, it is often difficult to implement a gradual mechanical change: in many cases it is desirable to have training wheels that are either on or off, or at least require only a few stages. This brings up an important requirement for training wheels: *successive environments must funnel into each other*. In Fig. 5, the peak of the beginner environment, located at $[22.5\ 32.6]^\circ$, lies only barely within the SCS of the original environment. In general, there are no guarantees the peak of the training-wheels will be contained in the SCS of the original problem. If it isn't, or in our case if the policy has not fully converged, there is a good chance that when the training wheels are removed, the policy is still too far from the next SCS to effectively sample from it. This issue is solved by having an intermediate environment, whose SCS contains a large area around the peak of the beginner environment. In other words, each training-wheel environment should easily *funnel into* the SCS of the next environment to be effective. This is particularly important when local exploration strategy is used, and is conceptually similar to designing controller funnels [16][17].

There is a second consideration that should be kept in mind: while the peak of an earlier environment *must*[2] be contained in the SCS of the successive environment, the reverse is not true. This means switching *back* to an earlier training environment must be done only cautiously, especially in hardware. A simple workaround is to keep a memory of previous policies, and switch back to known stable policies when switching back to previous training environments.

---

[2] This condition is necessary when exploration is strictly local, and can be relaxed otherwise.

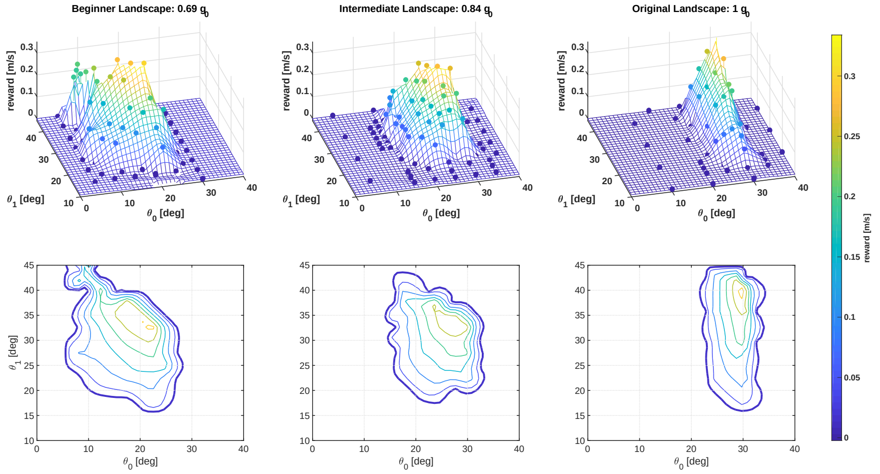

Fig. 4: The landscapes of the beginner, intermediate and original environments are visualized here. The upper row shows the sampled points (circles) and the resulting interpolated mesh, slightly offset for visibility. The more gradual climb in the lower gravity environments is visible. The contour maps in the second column more clearly show the change in shape of the 'reward mountain', the shape of of the cliff and most importantly, the size of the basin of attraction for the learning system. The outer contour showing the set of parameters which can provide a gradient is outlined with a thicker line. If the learning agent only samples outside this set, it will not be able to accurately estimate a gradient.

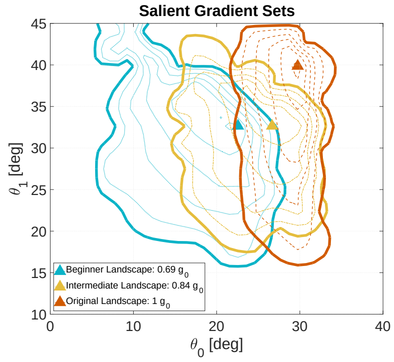

Fig. 5: The salient gradient set (SCS) for each environment is mapped out with contour lines and the peak of each set marked by a triangle. The location of the peak of one training environment with respect to the SCS of the successive environment is very important. To be effective, the training wheels must guide the current policy towards parameters that will sample from the salient gradient set of the next landscape with higher probability.

C. *LEARNING ACROSS LANDSCAPES*

As a proof of concept we use offline stochastic gradient descent with finite-differences, with parameter perturbations ranging between 0.5° and 2°. Gradient estimates tend to be more robust to noise with larger perturbations, especially where the gradient is very shallow such as at the edges of the SCS. On the other hand, they become unstable closer to the peak and especially when close to the cliff. We also choose a constant, relatively large learning rate of 2.5. Again, larger steps have the risk of overshooting and stepping over the cliff, but otherwise perform well. In both cases a cleverer, variable choice of these parameters would help the learning process, but is not relevant to the training-wheels concept and is kept constant.

Several typical learning sessions are shown in Fig. 6a, with the most successful reaching a speed of 0.35 $\left[\frac{m}{s}\right]$. We also purposefully initialize several trials outside the SCS of the original environment, and as expected we observe meandering paths. Examples of agents initialized with parameters outside their respective SCS are shown in Fig. 6b. As expected, without sufficient gradient information the agents will simply take steps in random direction. While this random exploration has a non zero probability of entering the salient gradient set and therefore converging, it can take a large amount of iterations, especially when starting at some distance from the set and with smaller learning step sizes. Especially when learning directly in robot hardware, it is critical to reduce the number of trials necessary.

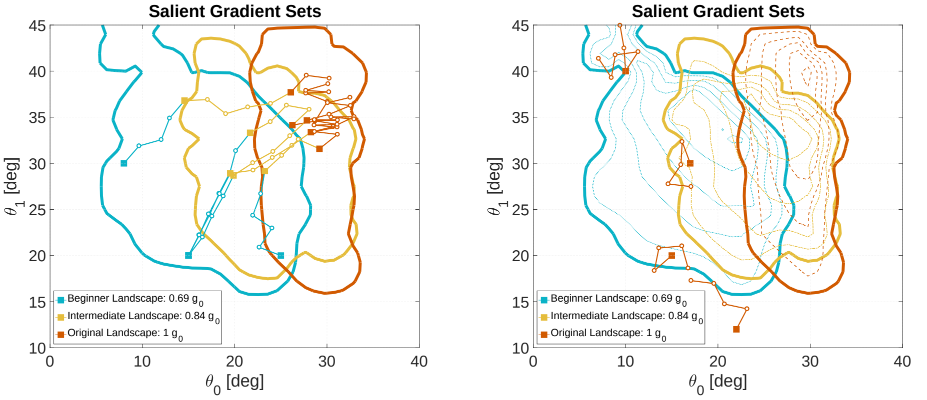

(a) Typical successful learning paths

(b) Unsuccessful learning attempted with the original landscape, marked in red.

Fig. 6: Several typical learning paths are shown here: above, successful learning trials progress from the beginner to an intermediate and finally to the original environment. Contour lines are not shown for visual clarity. One of these learning trials typically took around 10 minutes. Below are trials initialized directly with the original environment but outside its salient gradient set. These take learning steps in random directions without improving.

IV. CONCLUSIONS AND OUTLOOK

We build on the concept of training wheels, temporary mechanical modifications of the system, to shape the learning landscape [12]. We apply it to learning open-loop legged locomotion in a constrained test stand, as a simple, low-dimensional problem that is unstable, underactuated and features impacts. We propose three criteria to designing effective training wheels in practice.

1) Ease of application to a generic set of robots
2) Increase in probability of sampling from the salient gradient set
3) Ease of funneling from a training environment to the successive environment

Since reducing the engineering effort is a main attraction for applying learning to robotics, it is important that training wheels are easy to implement and apply. As an example, we surmise that adding damping to the joints, or to the floating base, of a robot would help stabilize the system and greatly help learning by improving stability [18][19], at a moderate cost to performance and efficiency. Implementing mechanical damping on small joints is however much more difficult than simply temporarily offloading some of the payload, and would require a custom design for each new robot. This partially defeats the purpose of reducing the engineering effort. While we plan to explore solutions to this in future work, there is a lot of merit in solutions as effective yet simple as reducing the payload.

The second criterion is the main qualifier for the effectiveness of the training wheels in shaping the learning landscape. To be more precise, increasing the probability of sampling from the salient gradient set is what makes a training wheel environment easier to learn in. The actual size of the set in relation to the sample space is a good proxy; it is more generalizable to arbitrary exploration strategies, and makes it more intuitive to predict when designing training wheels. In most cases it will be impossible to map out the landscape by brute-force as we have done here. Good methods to approximate the SGS size, or directly estimate the sampling probability, need to be developed to more systematically evaluate potential training wheels.

The final criterion is particularly relevant when local exploration strategies are used. As this strategy is common in robotics, we feel it is an important criterion to include. Training wheels that can be continuously tuned out, until the dynamics converge back to the original environment, would be guaranteed to satisfy this criterion [12]. However the implementation of such training wheels generally goes against the first criteria, and a trade-off will have to be made. To be effective, training wheels will require a strategy to transition from one landscape to the next. In practice, it is helpful to regularly estimate the local gradient of the next landscape before each transition. Ideally, we would want to design a sequence of training wheels that funnel into each other, similar in concept to [16][20].

In this work, when to switch between environments was chosen heuristically. With the actual landscape maps available for reference, we can be very confident that the funnel overlap between environments is large and we do not need to completely converge on one environment before switching to the next. For future work, it will be interesting to find a more general rule for switching environments. Since the number of trials needed to converge is particularly important when learning in hardware, an optimal switching policy to learn with the fewest iterations would be particularly useful.

Although we have presented these landscape shaping results in the context of reinforcement learning, the challenge of traversing a landscape in parameter-space is inherent to optimization problems as a whole. In particular, the concepts we develop should be useful for applying derivative-free optimization in hardware [21] as well.

ACKNOWLEDGMENTS

We would like to thank Özge Drama, Felix Grimminger and Julian Viereck for fruitful discussions, advice and help along the way. We also thank Felix Widmaier who wrote the code to run and interface with the motor control boards. We thank the International Max Planck Research School for Intelligent Systems (IMPRS-IS) for supporting the academic development of Felix Ruppert. This work was partially supported by an MPI Grassroots grant provided to Ludovic Righetti, Felix Grimminger and Alexander Spröwitz in 2017.

REFERENCES

[1] X. B. Peng, G. Berseth, and M. Van de Panne, “Terrain-adaptive locomotion skills using deep reinforcement learning”, *ACM Transactions on Graphics (TOG)*, vol. 35, no. 4, p. 81, 2016.

[2] T. P. Lillicrap, J. J. Hunt, A. Pritzel, *et al.*, “Continuous control with deep reinforcement learning”, *ArXiv preprint arXiv:1509.02971*, 2015.

[3] P. Abbeel, A. Coates, M. Quigley, *et al.*, “An application of reinforcement learning to aerobatic helicopter flight”, in *ADVANCES in neural information processing systems*, 2007, pp. 1–8.

[4] J. Peters and S. Schaal, “Reinforcement learning of motor skills with policy gradients”, *NEURAL networks*, vol. 21, no. 4, pp. 682–697, 2008.

[5] J. Kober, J. A. Bagnell, and J. Peters, “Reinforcement learning in robotics: A survey”, *THE International Journal of Robotics Research*, vol. 32, no. 11, pp. 1238–1274, 2013.

[6] R. Tedrake, T. W. Zhang, and H. S. Seung, “Learning to walk in 20 minutes”, in *PROCEEDINGS of the Fourteenth Yale Workshop on Adaptive and Learning Systems*, Yale University New Haven (CT), vol. 95585, 2005, pp. 1939–1412.

[7] N. Kohl and P. Stone, “Policy gradient reinforcement learning for fast quadrupedal locomotion”, in *ROBOTICS and Automation, 2004. Proceedings. ICRA’04. 2004 IEEE International Conference on*, IEEE, vol. 3, 2004, pp. 2619–2624.

[8] M. H. Raibert, *Legged robots that balance*. MIT press, 1986.

[9] N. Chentanez, A. G. Barto, and S. P. Singh, “Intrinsically motivated reinforcement learning”, in *Advances in neural information processing systems*, 2005, pp. 1281–1288.

[10] V. Gullapalli and A. G. Barto, “Shaping as a method for accelerating reinforcement learning”, in *INTELLIGENT Control, 1992., Proceedings of the 1992 IEEE International Symposium on*, IEEE, 1992, pp. 554–559.

[11] T. McGeer, “Passive dynamic walking”, *The International Journal of Robotic Research*, vol. 9, no. 2, pp. 62–82, 1990.

[12] J. Randløv, “Shaping in reinforcement learning by changing the physics of the problem.”, in *ICML*, 2000, pp. 767–774.

[13] R. S. Sutton and A. G. Barto, *Reinforcement learning: An introduction*, 1. MIT press Cambridge, 1998, vol. 1.

[14] J. Rummel and A. Seyfarth, “Stable running with segmented legs”, *The International Journal of Robotics Research*, vol. 27, no. 8, pp. 919–934, 2008.

[15] J. Peters and S. Schaal, “Policy gradient methods for robotics”, in *INTELLIGENT Robots and Systems, 2006 IEEE/RSJ International Conference on*, IEEE, 2006, pp. 2219–2225.

[16] Q. Cao, A. T. Van Rijn, and I. Poulakakis, “On the control of gait transitions in quadrupedal running”, in *INTELLIGENT Robots and Systems (IROS), 2015 IEEE/RSJ International Conference on*, IEEE, 2015, pp. 5136–5141.

[17] R. Tedrake, I. R. Manchester, M. Tobenkin, *et al.*, “Lqr-trees: Feedback motion planning via sums-of-squares verification”, *THE International Journal of Robotics Research*, vol. 29, no. 8, pp. 1038–1052, 2010.

[18] J. E. Colgate and J. M. Brown, “Factors affecting the z-width of a haptic display”, in *ROBOTICS and Automation, 1994. Proceedings., 1994 IEEE International Conference on*, IEEE, 1994, pp. 3205–3210.

[19] M. Calisti, F. Corucci, A. Arienti, *et al.*, “Dynamics of underwater legged locomotion: Modeling and experiments on an octopus-inspired robot”, *Bioinspiration & biomimetics*, vol. 10, no. 4, p. 046012, 2015.

[20] A. Karpathy and M. Van De Panne, “Curriculum learning for motor skills”, *Advances in Artificial Intelligence*, pp. 325–330, 2012.

[21] A. Spröwitz, R. Moeckel, J. Maye, *et al.*, “Learning to move in modular robots using central pattern generators and online optimization”, *The International Journal of Robotics Research*, vol. 27, no. 3-4, pp. 423–443, 2008.